UNIVERSITY OF SOUTHAMPTON

FACULTY OF NATURAL AND ENVIRONMENTAL SCIENCES
CHEMISTRY

Synthesis, characterisation and charge storage behaviour of some transition metal nitrides

By

Syed Imran Ullah Shah

Supervisor

Prof. Andrew L. Hector

Thesis for the degree of Doctor of Philosophy

August 2015

University of Southampton

Abstract

FACULTY OF NATURAL AND ENVIRONMENTAL SCIENCES

CHEMISTRY

Doctor of Philosophy

Synthesis, characterisation and charge storage behaviour of some transition metal nitrides

By Syed Imran Ullah Shah

The application of nanostructured materials with ordered morphologies and properties to electrochemical capacitors (ECs) is being studied in order to provide enhanced energy density without comprising their inherent high power density and excellent cyclability. In this study we have synthesised some metal nitrides through various routes using non-oxide precursor sources and studied their structure, composition and morphology. As synthesised materials were made in to electrodes and their capacitances were measured using cyclic voltammetry.

Manganese nitrides were obtained in a solvothermal synthesis by reacting $MnCl_2$ and $LiNH_2$. Nanotubes at 350 °C or spherical shape particles were seen at higher temperatures. Capacitances were seen to drop with scan number when run for longer periods at higher scan rates. Molybdenum nitride samples were obtained by solution phase ammonolysis of $MoCl_5$ or $Mo(NMe_2)_4$ to obtain the polymers. Annealing the choloroimide polymer yielded hexagonal MoN at 500 °C, rock salt Mo_2N at 700 °C and above and a mix of both the phases at 600 °C. Imide derivatives yielded distorted cubic up to 800 °C and a mix of hexagonal and rock salt at high temperature. Nanotubes were obtained from imide derivatives up to 900 °C, while spherical particles above this temperature and for chloroimide derivatives at any temperature. CVs obtained for chloroimide derivatives show to double layer supercapacitors dominating over redox reaction, while imide derivatives were found to be redox in nature. Chloroimide samples show high capacities up to 247 F g^{-1} at 2 mV s^{-1} and long cycling lifetime for both the derivatives through 1000 cycles.

Vanadium nitride samples were obtained by solution phase ammonolysis of $V(NMe_2)_4$. Annealing the polymer at various temperatures under NH_3 produced VN with standard rock salt structure at 500-1000 °C while distorted rock salt in the samples obtained at lower temperature. Particles were found to be spherical in shape. Highest capacitance of 128 F g^{-1} was seen for the sample obtained at 600 °C at lower 2 mV s^{-1}. Capacitance was found to be stable through 1000 scans only when a short potential window was used. TiN samples were produced by obtaining a precursor from solution phase ammonolysis of $Ti(NMe_2)_4$ and annealing the precursor under ammonia or through sol-gel route using long chain amines as the templating agents. PXD patterns showed rock salt TiN with broad peaks at 500 °C or highly crystalline at 800 °C. TEM images suggested particles to be spherical in shape. A fairly high surface area of 319 m^2 g^{-1} was observed for the sample obtained from annealing the HDA/$PrNH_2$ polymer at 500 °C. Cyclic voltammograms showed poor charge storage and most of the samples tend to oxidise rapidly in aqueous KOH. VN/C samples were obtained carrying an overnight reaction of $V(NMe_2)_4$ with NH_3 in a hydrothermal bomb at various temperature. PXD reviled rock salt VN, some distortion was in the structure was found in the sample obtained at lower temperature. TEM images show vanadium nitride nano particles with carbon nanotubes. Specific capacitances were observed to be decreased with scan number through 100 cycles in 1 M KOH.

Contents

Chapter 1 Introduction

Chapter 4 Synthesis of molybdenum nitrides and charge storage behaviour 73

Chapter 5 Synthesis of vanadium nitrides and use in supercapacitors 111

List of figures

List of tables

Acknowledgements

I would like to express my deepest gratitude to my supervisor Professor Andrew L. Hector for his continuous support, advice during my research. His friendly attitude and especially his patience in every situation helped me to accomplish my studies. I would like to acknowledge my advisor Professor John R. Owen for his expert advice on my project reports and his kind help with my publications is highly appreciated.

I am thankful to Costa Bassetto Victor and Pangagoulia Danai for helping me in collecting the Raman data and Dr. Shuncai Wang for his help with electron diffraction and high resolution images. I thank all my colleagues Wafa Al-Arjan, Mehboba Hassan, Ben Grey, Xiang Li, Calum Robertson, Jack, Kripa sirdar, for their friendship and help in during my studies. Thanks to all my friends anywhere in the world for being with me as a source of smiles and happiness.

My deepest gratitude goes to my Mom and Dad; their love and prayers were always supporting me in every hardship and every stressful situation during my studies. I heartily dedicate my thesis to my late father Syed Lal Badshah. I thank to all my family members for their moral support at all the times during my PhD. Thanks to my dear wife Syeda Momina Bibi for coming to my life at the end of my PhD.

I am grateful to the University of Southampton, Chemistry for providing me the funding for my PhD studies.

Above all, I would like to thank my Allah for His blessings, giving me strength that made me able to reach to my goals.

Abbreviations

TMNs	Transition Metal Nitrides
TGA	Thermogravimeteric Analysis
PXD	Powder X-ray Diffraction
PDF	Pair distribution function
IR	Infrared
EM	Electron Microscopy
TEM	Transmission Electron Microscopy
CVD	Chemical Vapour Deposition
ALD	Atomic Layer Deposition
THF	Tetrahydrofuran
HDA	hexadecylamine
CTAB	Cetyl trimethylammonium bromide

DECLARATION OF AUTHORSHIP

I Syed Imran Ullah Shah...

declare that this thesis and the work presented in it are my own and has been generated by me as the result of my own original research.

[title of thesis] Synthesis, characterisation and charge storage behaviour of some transition metal nitrides..

I confirm that:

1. This work was done wholly or mainly while in candidature for a research degree at this University;
2. Where any part of this thesis has previously been submitted for a degree or any other qualification at this University or any other institution, this has been clearly stated;
3. Where I have consulted the published work of others, this is always clearly attributed;
4. Where I have quoted from the work of others, the source is always given. With the exception of such quotations, this thesis is entirely my own work;
5. I have acknowledged all main sources of help;
6. Where the thesis is based on work done by myself jointly with others, I have made clear exactly what was done by others and what I have contributed myself;
7. [Delete as appropriate] None of this work has been published before submission [or] Parts of this work have been published as: [please list references below]:

Signed: ....

Date:.........12/08/2015..

1.1 Introduction

Transition metal nitrides (TMNs) and carbides have wide applications in many industrial sectors. TMNs such as TiN, NbN, HfN, and TaN serve as highly corrosion-resistant materials, barrier layers for the semiconductor industry, good electrical conductors and low temperature superconductors as well as hard coatings.[1, 2] Some early transition metal nitrides behave like noble metals (Pt, Pd, Rh and Ru) in the catalysis of some chemical and electrochemical reactions, including oxidation of hydrogen, CO, alcohols and reduction of oxygen.[3] Some of the metal nitrides have also shown hydrogen gas storage capabilities e.g. Li_3N based compositions.[4]
There are numerous reviews on the chemistry of nitride materials including those focused on structure,[5, 6] catalysis,[7] high pressure phases,[8] hard materials,[9] phosphors,[10] s-block nitrides[11] and silicon nitride ceramics.[12]

Application of nitride materials in electronics, opto-electronics, wear resistant coatings, sensors and high temperature ceramics are facilitated by synthesis methods that yield the material in the appropriate form. As a general rule nitrides sinter less readily than oxides due to their high lattice energies, hence nitrides with small particle sizes have long been studied. There is an increasing interest in the size and shape dependent properties of these materials to understand existing properties and develop new ones, e.g. for semiconductors such as GaN, catalytically active compositions like Co_3Mo_3N and hard materials such as TiN.[13]

In this chapter some of the important applications and the synthesis routes for nanocrystalline transition metal nitrides will be discussed.

1.2 Applications of metal nitrides

1.2.1 Catalysis

The interest in binary or ternary metal nitrides as catalysts is due to the similarity in activity of the transition metal nitrides to noble metals[14, 15] and their high surface areas which typically have been obtained through ammonolysis of metal oxides by temperature programmed reaction[16-19] and in some cases have higher activity than commercial catalysts.[20] The morphology of the nanocrystalline material could be varied by changing the flow rate and the heating and the cooling rates.[21] In catalysis, porous nitrides not only offer a large accessible surface area with minimum mass transfer issues.[22] The introduction of nitrogen atoms into the early transition metal leads to the increase of the d electron density of the metal at the Fermi level and induces noble metal like properties to the nitrides.[23, 24] Furthermore during the passivation step following nitride preparation and before exposure to air, oxygen is incorporated into the lattice and as a result an acidic nature can appear.[21] Catalytic studies of nitrides obtained through precursor decomposition are few.[25, 26]

Catalysis with metal nitrides has mainly centred around the transition metal nitrides with special emphasis on groups 5 and 6. These nitrides have been particularly successful with reactions in a hydrogen environment like hydrogenation, de-hydrogenation, hydrodenitrogenation, hydrodesulphurisation, hydrogenolysis, ammonia synthesis, amination, hydride activation and also in photocatalysis.[27] Transition metal nitrides W_2N, Mo_2N, and VN, along with vanadium oxynitride, have been found to be active catalysts for ammonia synthesis.[28-30] N_2 and H_2 are activated on the surface of the nitrides, followed by ammonia synthesis and desorption of NH_3 gas. The phase of the nitrides as well as the acid/base nature of the nitrides becomes important to have facile activation and desorption steps. A ternary nitride Co_3Mo_3N doped with Cs has proven to be more efficient than the commercial Fe/K_2O catalyst in NH_3 synthesis. The effect of doping has not been particularly dependent on the amount of loading and Cs doping on Mo_2N has not been effective.[31] NH_3 synthesis via hydrazine decomposition on Al_2O_3 supported molybdenum nitride shows activities comparable to the traditional Ir/Al_2O_3 catalyst.[32] The catalytic properties of nanocrystalline TiN in hydrogen transfer reactions with complex hydrides like $NaAlH_4$ has also been reported.[33] The reaction between diphenylethyne (DPE) and $NaAlH_4$ is faster in the presence of TiN and decomposes the alanate to AlH_3 and NaH. The AlH_3 then reduces the DPE to stilbine forming an unknown intermediate, which then is further reduced in H_2 to reproduce the alanate.

1.2.2 Photcatalysis

The photocatalytic properties of nanocrystalline Ta_3N_5 have been recently reported. Because of its absorption in the visible region of the solar spectrum, it is potentially more efficient than the more traditional TiO_2 or oxynitrides based on TiO_2. Zhang and Gao[34] studied the photocatalytic properties of $TiO_{2-x}N_x$ in comparison to Ta_3N_5 of different crystallite sizes in the decomposition of methylene blue and observed that the nanoparticles of Ta_3N_5 showed better activity than large particles and exhibited a much higher photocatalytic activity than $TiO_{2-x}N_x$ of the same size. Yang and co-workers[35] recently reported on the increased efficiency of CNT/Ta_3N_5 monocomposites in photocatalysis compared with Ta_3N_5 nanoparticles. Ta_2O_5 was impregnated into the CNT's and was nitrided in NH_3 to form the composites. The better activity of the nanocomposites may be due to the high conductivity of the nanotubes, which helps in scavenging the photogenerated electrons.

1.2.3 Supercapacitors

Energy has become a primary focus of most of the world powers and scientific community due to changing global scenarios. It has created great interest in developing and refining more efficient energy storage devices.[36] The demand for more sustainable, efficient energy storage has provoked a renewed scientific and commercial interest in advanced capacitor designs in which the suite of experimental techniques and ideas that comprise nanotechnology are playing a critical role.[37] Electrochemical capacitors (ECs) are also known as supercapacitors, or ultra-capacitors because of their higher power and energy density (20-200 times greater specific capacitance) compared with conventional capacitors.[38] EC stores electrical charge in the electric double layer capacitors (EDLC) at a surface-electrolyte interface, primarily in high surface area carbon. Because of the high surface area and the thinness of the double layer, these devices can have very high specific and volumetric capacitances. This enables them to have very high energy density for capacitors and essentially unlimited charge/discharge cycle life.[39] In addition to high surface area carbons, even higher capacitance can be achieved by using redox-active materials such as metal oxides and conducting polymers. These materials store electrochemical charge using highly reversible surface redox reactions, commonly described as “pseudocapacitance” in the literature.[40] The energy density of an electric double layer capacitor (EDLC) is small compared to that of rechargeable batteries; one needs to increase the capacitance of EDLC. The double layer capacitance is correlated to the morphological properties of the porous electrodes, which is the surface area and pore size distribution of the electrode material.[41, 42]

1.2.3.1 Models of the EDLC

The complexity of the EDLC models used to describe the interfacial region at an ideally polarized electrode has increased with time. Figure 1.1 shows the models for the case when potentials are negative to the potential zero charge.[43]

The first model was proposed by Helmholtz, who envisaged that all the charge on the metal is balanced by a mono-layer of ions of opposite charge immediately adjacent to the surface. As a result, the potential changes steeply and linearly over the thickness of this monolayer. Outside this layer, the solution will have the composition of the bulk with equal concentrations of anions and cations moving randomly through the solution. Somewhat later, it was noted that the ability of ions to move freely through an electrolyte solution at ambient temperatures should be taken into account. In consequence, a second model was suggested. Again the surface charge is balanced by ions in solution of opposite charge but the ions are now free to move in solution rather than bound to the surface; close to the surface there is a large excess of cations over anions and this difference decreases smoothly over a few nanometers until the composition of the bulk solution is reached. In such a model the potential will drop smoothly across the whole of the layer with a composition different from the bulk, most rapidly at the surface and with a decreasing gradient across this layer. The final model combines the two concepts. This model envisages a compact layer of ions with a gradual change to the bulk solution composition with distance from the surface. Now, a significant fraction of the potential change will occur linearly with distance across the compact layer with the rest dropped as a smooth function of distance across the diffuse layer.

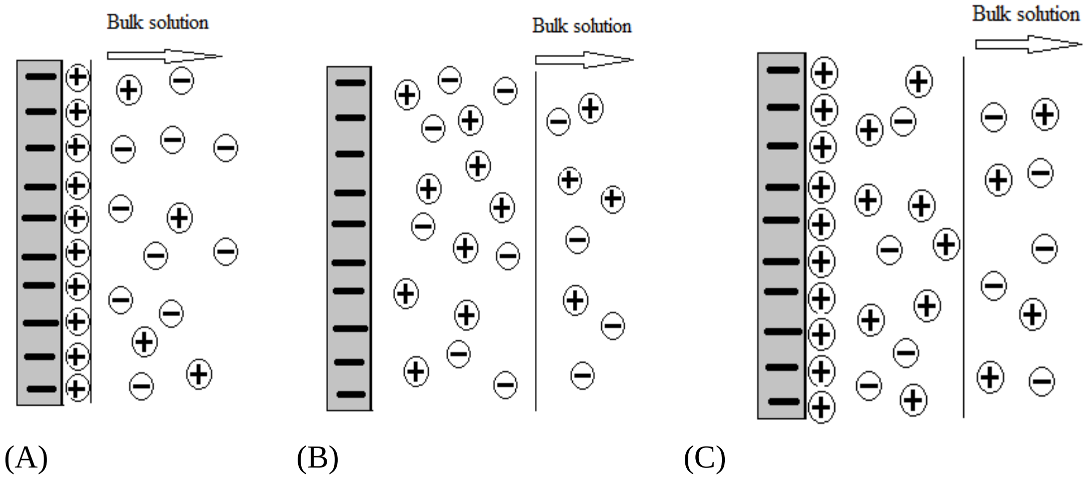

Figure 1.1: (a) Helmholtz model (b) Gouy-Chapman and (c) Gouy-Champan-Stem model

Capacitance C for EDLC can be measured by the equation given below. C is directly proportional to absolute permittivity, relative permittivity and surface area of the electrode, while indirectly proportional to the distance between the electrodes.

$$C = \frac{\varepsilon_o \varepsilon_r A}{d}$$

where C : is capacitance in farads

ε_o : absolute permittivity of free space (vacuum permittivity) which is 8.85×10^{-12}

ε_r : relative electrical permittivity of the dielectric material between the layers

A : A is the area of capacitor plate

d : d is the distance between the electrodes

1.2.3.2 *Transition metal oxides and nitrides for redox supercapacitors*

Redox ECs use redox process at the surface to enhance charge storage capacity, similarly to a battery. Ruthenium oxide (RuO_2) and hydrous ruthenium oxides ($RuO_2 \bullet 0.5H_2O$) have been intensively studied to be used as redox ECs, as they have shown high theoretical specific capacitance of ca. 2000 F g^{-1} in a wide potential window of 1.4 V, and electrical conductivity of the order of 10^5 S cm^{-1}. However, commercial applicability of RuO_2 is so far hindered by its high cost. [44-49] Other metal oxides e.g. manganese,[50] titanium[51] and vanadium[52] have been investigated as alternative to RuO_2.

Transition metal nitrides like VN,[53, 54] TiN,[55-57] WN,[58] MoN_x[59-64] and have also been found to be potential replacements for RuO_2 as supercapacitor electrode materials because of their high conductivity, low cost and high chemical resistance. Further, careful surface oxidation would expose the different oxidation states of the metal for Faradaic reactions leaving the conducting properties of the nitrides under the surface intact.[55, 65, 66] Nano-structured VN synthesised by a two-step ammonolysis reaction of metal halide has also been studied as the electrode material for supercapacitors. Specific capacitance of 1340 F g^{-1} was obtained at a scan rate of 2 mVs^{-1}, with 554 F g^{-1} reported at a high scan rate of 100 mV s^{-1}.[65]

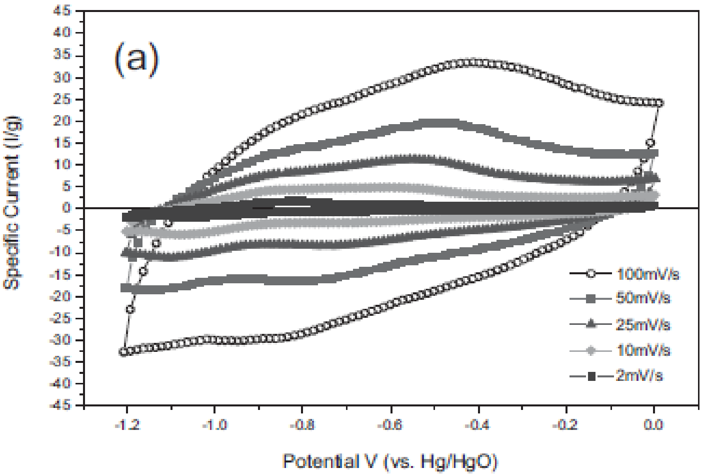

Figure 1.2: Cyclic voltammograms for VN in 1 M KOH at various scan rates.[65]

TiN synthesised by two-step ammonolysis of $TiCl_4$ was tested for ECs. A specific capacitance of 234 F g^{-1} at 2mV s^{-1} or 23.7 F g^{-1} at 100 mV s^{-1} was measured.[55]
A mixture of γ-Mo_2N and Co_3Mo_3N of different Co/(Co+Mo) molar ratios has been synthesised by the reaction between cobalt (III) nitrate and ammonium heptamolybdate. The specific capacitance increased from 30 F g^{-1} to 109 F g^{-1} when the Co/(Co+Mo) ratio was increased from 0 to 0.25 after which the capacitance decreased. The voltage stability window at 0.8 V remained the same as pure nitride, but the kinetics of the redox process became faster with a corresponding increase in the current.

1.2.4 Ultrahard materials

Coatings of high hardness and low coefficient of friction are in demand for applications under severe conditions like high vacuum, high temperature, high loads and low temperatures. Diamond, with hardness of 70-100 GPa (gigapascal), has been used for such coatings. But diamond is expensive, is difficult to form as thin smooth coatings, and alloys with carbide-forming metals like iron and steel at high temperature. Nitrides like c-BN, TiAlN, TiZrN or TiCN are good hard coating materials with hardness in the range of 20-30 GPa, which could further be improved by varying structure and composition of the film.[67-72]

Patscheider[70] examined the hardness of TiN:Si_3N_4 nanocomposites. In the absence of silicon nitride, the TiN nanocrystals are elongated particles in the range of several hundreds of nanometres with a hardness of approximately 27 GPa. The hardness increases to ~35 GPa with the addition of less than 10 atomic percent of Si_3N_4, increasing the amount of Si_3N_4, there is an increasing coverage of the TiN crystallites by Si_3N_4 which impedes the growth of the TiN crystallites and forces them to renucleate. Due to this disturbed growth, the particle size of the TiN crystallites decreases with the increase in hardness and continues till the size of the TiN particles is small enough to prevent any dislocation activity. Such small crystallites are only deformed upon moving single undeformed TiN nanocrystallites against each other and that requires a much higher energy than dislocation movements, hence this increases the hardness. The nanocomposites at this stage consist of grains of nanocrystalline TiN separated by a few monolayers of Si_3N_4. At higher Si_3N_4 concentration, the grain separation becomes such that the hardness of the material becomes similar to that of Si_3N_4.

1.3 Synthesis Routes to TMNs

The distinguishing factor in nitride synthesis over the oxides is the strong N≡N triple bond that requires twice as much energy as the O=O double bond to dissociate, and sensitivity to oxygen/moisture, especially at high temperature. As a result of this the reports on oxides are many more than those on nitrides. Recent developments in the field include on the synthesis of spinel nitrides (e.g. Si_3N_4), and morphologies like nanorods, microporous and mesoporous nitrides (Si_3N_4, Si-Al-N, Si-B-N), nanocrystals of high surface area (Mo_2N, VN, WN, TiN etc.) and self-standing colloids of different band gaps (GaN, AlN, Ga-In-N) to name a few. The TMNs are synthesised using different techniques depending upon the required materials properties for a particular application.

1.3.1 Mechanochemical milling

TMNs are traditionally synthesised via the direct nitridation of metal in N_2, carried out at high temperatures.[73] These high energy processes give rise to the product with metallic impurities and large particle sizes due to fast sintering of the metal. These problems have been solved to some extent in the mechanochemical milling process. This process has been quite successful in synthesising metal nitrides sometimes at RT and sometimes through post-synthesis annealing.[74, 75] The problem with this method is that long reaction times (several days) and a high pressure of N_2/NH_3. Often products are found to contain Fe impurities that have leached out from the metallic balls due to constant grinding of the hard materials. Furthermore the nanocrystals have defect-rich structures due to the constant beating. Modifications have been made to the process to hasten the reaction and hence reduce cost and improve purity of the product. Some TMNs have been reported through enhanced mechanochemical milling techniques, such as synthesis of TiN using an electrical discharge,[76] SiN via combustion synthesis,[77] AlN improving pulverisation by using $LiOH.H_2O$,[78] and liquid-solid reaction for synthesis of TiN.[79]

There are also reports on the synthesis of ternary nitrides via ball milling of the ternary carbides in nitrogen or via the ball milling of the second metal with the binary nitride. The advantage of the latter method is that it is independent of the availability of the ternary carbide. Ternary nitrides of Fe_3Mo_3N and Co_3Mo_3N have been synthesised this way.[80]

1.3.2 Gas-Solid Reactions

Nanoscale metal nitrides are often synthesised via the ammonolysis of nanoscale metal particles, metal chlorides, oxides or sulfides. The nature of the precursor dictates the nature of the product. This method involves high temperature reactions, which can result in agglomerated products with very low surface area. Tsai et al[81] synthesised TMN nanoparticles by reducing the metal halides with a sodide, $[K^+(15\text{-crown-}5)_2Na^-]$. The purified metals or bimetallic nanoparticles were then heated under N_2 or NH_3 to obtain the nanocrystalline nitrides. They synthesised γ-Mo_2N (800 °C in N_2), Ta_3N_5 (650 °C in NH_3) and $NbN_{0.95}$ (800 °C in NH_3) along with the ternary nitrides Fe_3Mo_3N (>650 °C, N_2) and some previously unknown phases of Ba-Nb-N, Fe-Nb-N and Cu-Nb-N. Organic impurities from the alkalides were found, especially when Ba was used as the metal precursor because of its higher reactivity. Li et al.[82] synthesised δ-Mo_2N and γ-Mo_2N by reacting MoO_3 in a N_2/H_2 mixture and NH_3 at 697 and 737 °C, respectively. The latter is formed due to a pseudomorphic relationship to the MoO_3 whereas δ-Mo_2N, is the thermodynamically more stable phase.

Nitridation of aminomolybdate precursors $(NH_4)_6Mo_7O_{24}{\bullet}4H_2O$, $(NH_4)_2MoO_4$ and H_4MoO_3 has also been studied because of their layer structures similar to MoO_3.[83] A molybdenum oxynitride intermediate is formed in NH_3 at lower temperature (325°C). The ammonium paramolybdate and MoO_3 produce oxynitride intermediates when heated in ammonia at 450 and 510 °C, and ultimately produce a mixture of MoN and Mo_2N respectively. High surface area nitrides are produced from the paramolybdate and MoO_3 as they both lead to pseudomorphous products.

Porous crystalline Ta_3N_5 has been synthesised by the ammonolysis of Ta_2O_5 at 850 °C.[84] The surface area increased from 1.8 $m^2\ g^{-1}$ in Ta_2O_5 to 11.4 $m^2\ g^{-1}$ in Ta_3N_5. This was due to the generation of pores in Ta_3N_5 owing to the void created by the replacement of $3O^{2-}$ ions with 2 N^{3-}. Zhang et al.[34] used Ta_2O_5 to obtain Ta_3N_3 with complete nitridation at the lower temperature of 700 °C. Using Ta_2O_5 reduced the reaction temperature of Ta_3N_3 synthesis.

Sulfides have also proved to be good precursors for nitride synthesis and have produced phases which are normally not achieved with the oxide precursor. Ammonolysis of MoS_2 has been shown to produce δ-MoN selectively over γ-Mo_2N.[85] W_5N_6 has been obtained by the ammonolysis of the high surface area WS_2.[85]

1.3.3 Solid state metathesis reaction (SSM)

Solid state metathesis reactions have been particularly effective in generating TMNs. The method has been claimed as a more energy efficient and cost effective synthesis route compared with the classical methods of nitride synthesis through repeated grinding, heating and cooling steps. The method involves the reaction between metal halides and alkali or alkaline earth metal nitrides as nitrogen sources of which Li_3N, Mg_3N_2, Ca_3N_2 and NaN_3 have been most popular. The method, being a solvent free solid state reaction, involves large activation energies to overcome the diffusion barrier. This initiation is achieved either through igniting the reagents at room temperature, grinding reagents together, heating samples in a furnace or igniting the reagent mixture with a filament. After initiation at room temperature, these reactions often reach temperatures well over 1000 °C in seconds or even less.[86, 87] The reactions are highly exothermic and become self-propagating once initiated. The whole process is very brief, with a duration usually of less than 5 s, which keeps the nucleation and growth process very short, resulting in small crystallites and occasionally some metastable phases.[88, 89] The method is effective in generation of early transition metal mono-nitrides (TiN,[90] ZrN[91]) and partially successful with the group 5 mono-nitrides like TaN and NbN, which are contaminated with the sub-nitrides,[92] with particle sizes in the range of 20-50 nm. Metal nitrides such as Mo_2N, W_2N, Cu_3N (decomposition temperature less than 790°C), main group nitrides like AlN, GaN (decomposition temperature 877 °C), and Zn_3N_2 (decomposition temperature around 500 °C).

1.3.4 Solvothermal synthesis

Solvothermal methods for synthesis of metal nitrides can overcome some of the problems involved in solid state metathesis reactions. The solvothermal method may be seen as a modified SSM reaction where the metathetical reaction is carried out in a solvent at a temperature higher than the boiling point of the solvent.[93] This method has been particularly successful in synthesis of metastable phases. Nanocrystalline GaN has been reported via the reaction between $GaCl_3$ and Li_3N in benzene at 280 °C.[94] The product was mainly hexagonal with some rock salt phase. The formation of the rock salt phase at this low temperature is intriguing as rock salt GaN is normally produced only at high temperature and high pressure. Cu_3N,[95] InN,[96] and BN[97, 98] have also been reported from solvothermal methods. Recently nanoparticles of ZrN, HfN, NbN, Ta_3N_5 and TaN have been formed via solvothermal reactions of early transition metal chlorides and dialkylamides with $LiNH_2$ in mesitylene and benzene.[27] All preparations were carried out in autoclaves. The formation of Ta_3N_5 takes place via stepwise substitution of chloride groups and condensation with the elimination of NH_3. The $TaCl_5$ was found to be a little more soluble in benzene than in mesitylene, but is fully consumed in reactions carried out in either solvent. Reduction of $NbCl_5$ was carried in a similar kind of reaction. Reactions below show the synthesis of Ta_3N_5 and of NbN:

$$TaCl_5 \xrightarrow{5LiNH_2,\ -5LiCl} \text{“}Ta(NH_2)_5\text{”} \longrightarrow {}^{1}/_{3}\ Ta_3N_5 + {}^{10}/_{3}\ NH_3$$

$$NbCl_5 \xrightarrow{5LiNH_2,\ -5LiCl} NbN + {}^{10}/_{3}\ NH_3 + {}^{1}/_{3}\ N_2 + 5LiCl$$

Reactions of metal (Zr, Hf or Ta) dialkylamides with $LiNH_2$ led in all cases to crystallization of the MN phase. These reactions suggested that solvothermal reactions are not as clean in mesitylene as they are in benzene. However the main disadvantage of this method is the decomposition of solvent during the nitridation reaction, which can incorporate high level of carbon in the crystal lattice of the final product.

1.3.5 Precursor decomposition

Precursor-based synthesis of metal nitrides has been particularly successful in the synthesis of films via CVD, because of properties like volatility and solubility of precursors in normal organic solvents. Synthesis of colloidal nanocrystalline nitrides via precursor decomposition has also been gaining momentum over the last decade due to the new requirements of the optoelectronic industry that the feature size be reduced from 130 nm in 2002 to 22 nm in 2016.[99] Film development methods based on CVD may also not be able to provide acceptable film coverage in etched trenches and other such reduced features. This prompts different deposition methods like spin coating.[100, 101]

The precursor decomposition methods can be divided into two broad categories. One is the use of metal inorganic precursors involving M-N-H atoms and the other is metal organic precursors containing M-N-R linkages, both of which lead to MN particles. The advantage of the former is that it can produce pure metal nitrides with little or no C contamination. The disadvantage is that the decomposition of these precursors happens at a higher temperature and the lack of organic groups renders the precursors insoluble in all organic solvents preventing the possibility of any reaction in the solution phase. Metal-organic precursors, on the other hand, are soluble in organic solvents and have the potential of producing a colloidal dispersion of nitrides. Ideally the precursor has clusters or a molecular structure similar to that found in the desired final product.

Brown and Maya[102] used the inorganic route to synthesise ZrN, TiN and NbN. They treated metal dialkylamides with NH_3 to obtain a precipitate. The precipitate was then pyrolysed to obtain pure nitrides in the +3 oxidation state. Baxter et. al[103] reacted transition metal dialkylamides or hexamethyldisilyl amides with condensed NH_3 in THF, which resulted in a hydrocarbon-insoluble product that showed a remarkable reduction in the carbon content compared to the starting material. The method can be looked upon as an extrapolation of the sol-gel method, except that the end product is a precipitate. The reactions proceed via transamination of the dialkyl amide. The precipitate was then pyrolysed under He to temperatures of 650-800 °C to obtain nanocrystalline (~30 nm or less) metal nitrides for the early transition metals and lanthanides. The late transition metals like Fe, Co, Cu produced the metals after heating. Reactions with mixed metal amides either produced a solid solution (Nb: Ta) or a mixture of the two nitrides (Ti:V). Kaskel et. al.[104] synthesised TiN nanocrystals by heating different $TiCl_4$ complexes with ligands like aliphatic amines, ethers and bipyridines in NH_3 to temperatures between 700 and 1000 °C, depending on the nature of the precursor. This method is an easy and simple way of producing TiN nanocrystals of different morphologies and high surface area (>200 $m^2\ g^{-1}$) with very little impurity.

ZrN has also been reported by using tris(hexamethyldisilylamido)zirconium.[31] The precursor was pyrolysed under NH_3 or vacuum to obtain pure crystalline ZrN at 1075 °C. Advantages of this method are that the precursor is soluble in organic solvents and therefore has the potential for applications producing films and coatings.

Wolczanski et al.[105] used a single source metallorganic precursor designed to have the correct ratio of atoms needed to form TaN, (Fig. 1.4). They synthesised the precursor

$[(^tBuCH_2)_2TaN]_5$ in three different ways, via reactions of $(^tBuCH_2)_3Ta{=}CH^tBu$ with NH_3, $(^tBuCH_2)_2Ta(NMe_2)_5$ with NH_3, and $(Me_2N)_3$-$Ta{=}N^tBu$ with NH_3.

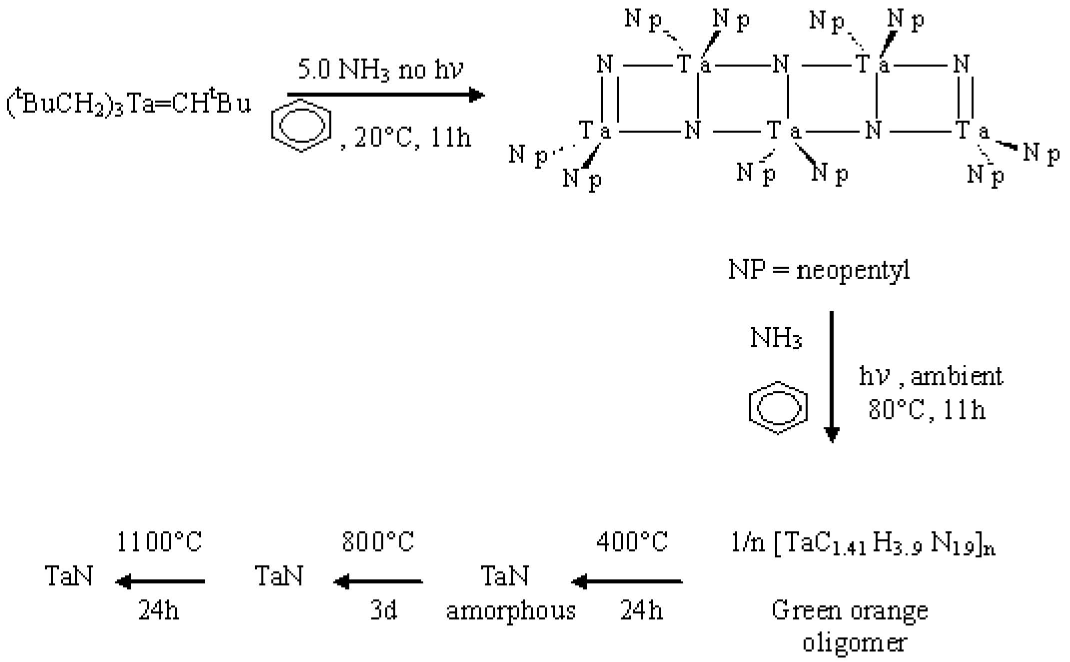

Figure 1.3: Precursor methods for preparation of cubic TaN

Heating the precursor to 400 °C and 800 °C produced amorphous and nanocrystalline TaN, respectively. Formation of the kinetically driven cubic phase in preference to the thermodynamically stable hexagonal phase was related to the structural similarities of the precursor and cubic TaN. Both the precursor and cubic TaN have corner-sharing structures whereas the hexagonal phase has TaN_3 and TaN_6 units, which makes its synthesis infeasible at this temperature.

Nano-crystals of δ–MoN and γ-Mo_2N have been reported[106] by heating two different Mo precursors, nitridotris(neopentyl)molybdenum(V) and its oxo-bridging bis(imido) derivative, in NH_3 to 700 °C. The C content was reduced from 2 to <0.1% by varying the temperature ramp rate between 100-200 °C/min. Nitrogen deficient Mo_2N was obtained when NH_3 was replaced by N_2 between 500 and 700 °C, but the carbon contents were higher than the ammonolysed product suggesting that the hydrocarbon removal was not complete at 500 °C in NH_3.

1.3.6 Non-oxide sol-gel method

The sol-gel method is well known for producing solids of different morphologies. Though the method has traditionally been used for the synthesis of oxides, it has now been successfully extrapolated to nitrides and chalcogenides, especially for formation of highly porous materials. The interesting morphologies produced by sol-gel chemistry (Figure 1.4) have largely contributed towards applications in catalysis and ceramic materials.[107] Sol-gel processing takes place through a series of steps: controlled hydrolysis and condensation, gelation, aging and drying.[108, 109] It is based on the formation of a stable suspension of colloidal particles (amorphous or crystalline) or polymer in a liquid, a sol.[110] This is subsequently linked up to immobilise the liquid phase in a porous, three dimensional solid network; this is referred to as a gel.[111, 112] The rate of condensation is controlled by various parameters, such as the properties of the starting material, e.g. diffusivities, reactivities, etc., their concentrations, reaction temperatures, solvent, and possible additives.[113]

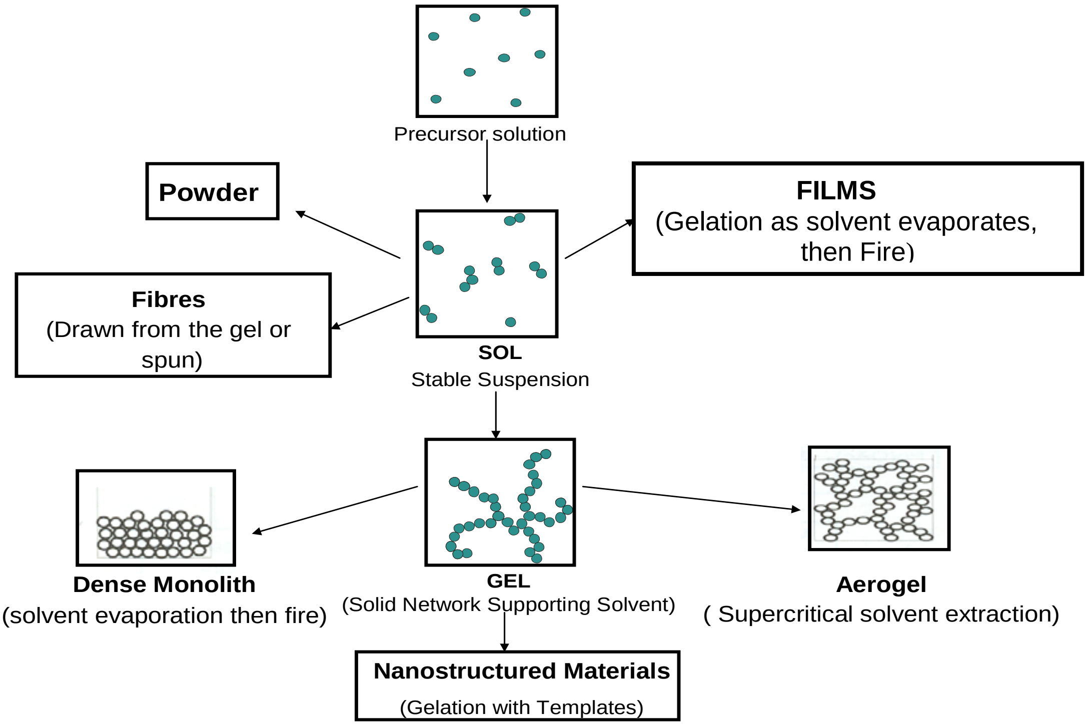

Figure 1.4: Processing route to materials using sol-gel methods

Non-oxide routes have largely developed around silicon nitride. Kaskel[114] and co-workers have demonstrated the possibility to engineer the pore size of amorphous silicon nitride from a microporous framework. The NH and NH_2 groups, especially around the inner surface of the solid, have been functionalised to introduce other metals into the framework and in the process have produced nanocomposites of metal nitrides and silicon nitride. Such materials find use as hard materials and also as gas filters.[115]

Jansen et. al.[116] introduced transition metals into the silicon nitride framework. Three metal dialkyl amides, $Ti(NMe_2)_4$, $Ta(NMe_2)_5$ and $Zr(NMe_2)_4$ were chosen as they had similar ammonolysis rates to $Si(NHMe)_4$ which was considered essential to having a homogeneous distribution of metal and Si in the gel. The reaction can produce tertiary silicon nitrides by dissolving the two amides in a common solvent at low temperature and ammonolysing the solution to create a polymetallosilazane precipitate. The aim of these reactions is described below:

$$M^1\text{-NRR'} + NH_3 \longrightarrow M^1\text{-}NH_2 + \text{HNRR'} \qquad \text{(Ammonolysis)}$$

$$M^1\text{-}NH_2 + M^2\text{-NRR'} \longrightarrow M^1\text{-NH-}M^2 + \text{HNRR'} \qquad \text{(Condensation)}$$

Note that well balanced reactivities of M^1 and M^2 will lead to a statistical mixture of M^1-NH-M^2, M^1-NH-M^1 and M-NH-M^2 linkages.

Heating the dried gels to 1000 °C in NH_3 produced composites of nanocrystalline metal nitrides in an amorphous Si/M/N matrix. The aim of this study was to synthesise a material with improved fracture strength and resistance to oxidation and thermal shock by incorporating transition metals into Si_3N_4. Cheng et al[117] have similarly developed nanocomposites of TiN nanocrystals in an amorphous mesoporous Si/Ti/N framework using the bis(dimethylamino)silylamino-μ-bis[(dimethyl-amino)silylimino] titanium as a precursor. Those composites are of interest as hard materials because of the combination of a nanocrystallites and an amorphous phase.

High surface area silicon aluminium nitride based xerogels have also been reported.[118] A solution of $[EtAl(\mu\text{-NHEt})(\mu\text{-NEt})_2Si(NHEt)]_2$ in pentane was placed in a 100 ml autoclave and ammonia was condensed on to it. The mixture was heated to 413 K (P = 170 bar) for 12 hrs. The resulting solid had a high surface area (795 $m^2\ g^{-1}$) and was mesoporous. Cheng et al[119] produced mesoporous Si-Al-N xerogels by ammonolysis of the alanate $(C_4H_8O)Al[HNSi(NMe_2)_3]_3$ in the presence of triflic acid as a catalyst. The inorganic gel so formed was dried and pyrolysed in NH_3 to 200, 600 and 1000 °C. This procedure did not increase the basicity as intended but did provide an easy way of incorporating another element into silicon nitride.

1.3.6.1 Advantages and limitations of sol-gel processes for nitrides

Sol-gel reactions are low temperature processes and therefore a large degree of control over morphology and composition can be achieved. These processes can produce highly porous nanocrystalline materials or dense ceramic bodies. Pore size can be tailored by the modification of reagents or the control of initial nucleation and/or condensation. The casting of complex shapes can be achieved without the need for melting or machining due to synthesis via a gel. Amorphous materials can be produced if the synthesis is carried out below the material’s crystallisation temperature.

There are a number of challenges to be met in order to make sol-gel processing as useful in nitride synthesis as it is with oxides. The obvious precursors are amides, and these are often expensive, difficult to synthesise and very oxygen/moisture sensitive. Reactions with ammonia often also occur very rapidly and lead to precipitation. The control measures to control hydrolysis and condensation in oxide sol-gel chemistry are not obviously applicable to the amide-based equivalent, though some controlled preparations do exist.[120] Reactions of chlorides or amides with ammonia offer an interesting way to control synthesis of metal nitride powders and potentially to target high surface area or new compositions. These have been explored only superficially to date.

1. 4 Objectives

Solution phase ammonolysis for precursor synthesis presents itself as an effective technique for the synthesis of nitride nanoparticles based on molecular precursor decomposition. This technique could access a variety of morphologies and particle sizes which would be of great interest for their use in catalysis. The use of an oxygen-free precursor source avoids contamination by oxygen and the reactions are carried out at relatively low temperature and over short time scale to produce the metal nitrides, saving energy and reaction time.

This thesis describes the use of solution phase ammonolysis to synthesise polymeric precursors which are decomposed by heating under ammonia to a give amorphous or crystalline products.

The incorporation of transition metals into silicon nitride using a sol-gel approach has previously been used to produce metal/silicon nitride nano-composites aiming for use as hard materials, with improved resistance to oxidation or thermal shock.[115, 116] Both binary nitrides with small particle sizes and well controlled compositions, and silicon nitride with incorporated metal atoms or supported metal nitride nanoparticles, could be of interest for catalysis. Hence this work has concentrated on tantalum and molybdenum nitrides, and the incorporation of these metals into silicon nitride.

1.5 References

1. K. S. Weil, Y. J. Kim and P. N. Kumta, *Mater. Lett.*, 1999, **39**, 292.
2. L. E. Toth, *Refrectory Materials, Transition Metal Carbides and Nitrides*, 1971, **7**, 12.
3. J. B. Christian, S. P. E. Smith, M. S. Hittingham and H. D. Abruna, *Electrochem. Comm.*, 2007, **9**, 2128.
4. Y. H. Hu and E. Ruckenstein, *Industrial Eng. Chem. Res.*, 2007, **47**, 48.
5. S. T. Oyama, The Chemistry of Transition Metal Carbides and Nitrides, Blackie, Glasgow, 1996
6. D. H. Gregory, *J. Chem. Soc., Dalton Trans.*, 1999, 259.
7. J. S. J. Hargreaves and D. Mckay, *Catalysis*, 2006, **19**, 85.
8. E. Horvath-Berdon, R. Riedel, A. Zerr, P. F. McMillan, G. Auffermann, Y. Prots, W. Bronger, R. Kniep and P. Kroll, *Chem. Soc. Rev.*, 2006, **35**, 987.
9. *Handbook of Ceramic Hard Materials*, R. Riedel(Ed.), Wiley, 2000.
10. R.-J. Xie and N. Hirosaki, *Sci. Technol. Adv. Mater*, 2007, **8**, 588.
11. D. H. Gregory, *Coord. Chem. Rev.*, 2001, **215**, 301.
12. F. L. Riley, *J. Amer. Ceram.*, 2000, **83**, 245.
13. B. Mazumder and A. L. Hector, *J. Mater. Chem.*, 2009, **19**, 4673.
14. R. B. Levy and M. Boudart, *Science*, 1973, **181**, 547.
15. A. H. Cowley, R. A. Jones, C. M. Nunn and D. L. Westmoreland, *J. Mater. Chem.*, 1990, **2**, 221.
16. M. Nagai, Y. Goto, A. Miyata, M. Kiyoshi, K. Hada, K. Oshikawa and S. Omi, *J. Catal.* , 1998, **182**, 292.
17. L. Volpe and M. Boudart, *J. Solid State Chem.*, 1985, **59**, 348.
18. L. Volpe and M. Boudart, *J. Solid State Chem.*, 1985, **59**, 332.
19. G. J. Choi, R. L. Curl and L. T. Thompson, *J. Catal.*, 1995, **146**, 218.
20. C. W. Colling and L. T. Thompson, *J. Catal.*, 1996, **146**, 193.
21. J. Trawczynski, *Catal. Today*, 2001, **35**, 343.
22. B. Mazumder and A. L. Hector, *Top. Catal.*, 2009, **52**, 1472.
23. S. T. Oyama, *J. Solid State Chem.*, 1992, **96**, 442.
24. L. Ramqvist, *J. Appl. Phys.*, 1971, **42**, 2113.
25. S. Wang, X. Wang, Z. Zhang and Y. Qian, *J. Mater. Sci.*, 2003, **38**, 3473.

26. R. N. Panda and S. Kaskel, *J. Mater. Sci.*, 2006, **41**, 2465.

27. B. Mazumder, P. Chirico and A. L. Hector, *Inorg. Chem.*, 2008, **47**, 9684.

28. S. T. Oyama, *Catalysis*, 1992, **133**, 358.

29. M. R. Hillis, C. Kemball and M. W. Roberts, *Trans. Faraday Soc.*, 1996, **62**, 3570.

30. R. Kojima and K.-I. Aika, *Appl. Catal. A: Gen.,*, 2001, **215**, 149.

31. C. K. Narula and L. F. Allard, *J. Mater. Chem.*, 1998, **8**, 1881.

32. M. G. Barker, M. G. Francesconi, P. M. O'Meara and F. C. Baker., *J. Alloys Compd.*, 2001, **317-318**, 186.

33. S. Kaskel, K. Schlichte and T. Kratzke, *J. Mol. Catal. A: Chem.*, 2004, **208**, 291.

34. Q. Zhang and L. Gao, *Langmuir*, 2004, **20**, 9821.

35. B. Fu, L. Gao and S. Yang, *J. Amer. Ceram. Soc.*, 2007, **90**, 1309.

36. M. S. Halper and J. C. Ellenbogen, *Supercapacitors: A Brief Overview*, 2006, 1.

37. X. Zhao, B. M. Sanchez, P. J. Dobson and P. S. Grant *Nanoscale*, 2011, **3**, 839.

38. T.-C. Liu, W. G. Pell, B. E. Conway and S. L. Roberson, *J. Electrochem. Soc.*, 1998, **145**, 1882.

39. J. R. Miller and A. F. Bruke, *Electrochem. Soc.*, 2008, **53**.

40. K. Naoi and P. Simon, *Electrochem. Soc. Interface*, 2008, 34.

41. O. Barbieri, M. Hahn, A. Herzog and R. Kotz, *Carbon*, 2005, **43**, 1303.

42. W. Y. Gang and Z. X. Gang, *Electrochem. Acta*, 2004, **49**, 1957.

43. D. Pletcher, *A First Course in Electrode Process*, 2009, **2nd Edition**, 76.

44. S. H. Zhou, M. H. Xhu and I. Honma, *J. Power Sources*, 2003, **122**, 219.

45. D. N. Futaba, K. Hata, T. Yamada, T. Hiraoka, Y. Hayamizu, Y. Kakudate, O. Tanaike, H. Hatori, M. Yumura and S. Iijima, *Nature Mater.*, 2006, **2006**, 987.

46. W. Sugimoto, H. Iwata, Y. Yasunaga, Y. Murakami and Y. Takasu, *Angewandte Chemie International Edition*, 2003, **42**, 4092.

47. W. C. Fang, O. Chyan, C. L. Sun, C. T. Wu, C. P. Chen, K.H. Chen, L.-C. Chen and E. C. J. H. Huang, *Electrochem. Comm.*, 2007, **9**, 239.

48. C. C. Hu, K. H. Chang, M. C. Lin and Y. T. W. N. Lett., *Nano Lett.*, 2006, **6**, 2690.

49. M. W. Mehrens, J. Schenk, P. M. Wilde, E. Abdelmula, P. Axmann and J. Garche, *J. Power Sources*, 2002, **105**, 182.

50. H. Chen, X. Dong, J. Shi, J. Zhao, Z. Hua, J. Gao, M. Ruan and D. Yan, *J. Chem. Mater.* , 2007, **17**, 855.

51. E. M. Sorensen, S. J. Barry, H.-K. Jung, J. M. Rondinelli, J. T. Vaughey and K. R. Poeppelmeier, *J. Chem. Mater.*, 2005, **18**, 482.
52. T. Kudo, Y. Ikeda, T. Watanabe, M. Hibino, M. Miyayama, H. Abe and K. Kajita, *Solid State Ionics*, 2002, **152**, 833.
53. D. Choi, E. Blomgren and P. N. Kumta, *Adv. Mater.*, 2006, **18**, 1178.
54. P. J. Hanumantha, M. K. Datta, K. S. Kadakia, D. H. Hong, S. J. Chung, M. C. Tam, J. A. Poston, A. Manivannan and P. N. Kumta, *J. Electrochem. Soc.*, 2013, **160**, 2195.
55. D. Choi, G. E. Blomgren and P. N. Kumta, *J. Electrochem. Soc.*, 2006, **153**, A2298.
56. D. Choi and P. N. Kumta, *J. Electrochem. Soc.* , 2006, **12**, 2298.
57. X. Liu, Y. Zhang, T. Wu and J. Huang, *Chem. Comm.*, 2012, **48**, 9992.
58. D. Choi and P. N. Kumta, *J. Amer. Chem. Soc.*, 2007, **90**, 3113.
59. C. Z. Deng, R. A. J. Pynenberg and K. C. Tsai, *J. Electrochem. Soc.*, 1998, **145**, L61.
60. S.L.Roberson, D. Finello and R. F. Davis, *J. App. Electrochem.*, 1999, **29**, 75.
61. Li. Xue-Liang, X. Yan, W. Hua, W. Hua-lin, W. Wei-dong and C. Xiang-ying, *Trans. Nonferous Met. Soc. China*, 2009, **19**, 620.
62. D. Finello, New Developments in Ultracapacitor Technology, Report no. WL-TR-95-7024, Wright Laboratory, Eglin Air Force Base, Florida, USA, 1995.
63. T.-C. Liu, W. G. Pell, B. E. Conway and S. L. Roberson, *J. Electrochem. Soc.*, 1998, **145**, 1882.
64. C. Chen, D. Zhao and X. Wang, *Mater. Chem.*, 2006, **97**, 156.
65. D. Choi, G. E. Blomgren and P. N. Kumta, *Adv. Mater.*, 2006, **18**, 1178.
66. C. Z. Deng, R. A. J. Pynenberg and K. C. Tsai, *J. Electrochem. Soc.*, 1998, **153**, L61.
67. S. H. Jhi, J. Ihm, S. G. Louie and M. L. Cohen, *Nature (London)*, 1999, **399**, 132.
68. A. J. Perry, *J. Vac. Sci. Tech.*, 1988, **A 6**, 2140.
69. I. Pollini, A. Mosser and J. C. Parlebas, *Phys. Rep.*, 2001, **355**, 1.
70. J. Patscheider, *Mater. Res. Bull.*, 2003, **28**, 180.
71. H. Hochst, R. D. Bringans, P. Steiner and T. Wolf, *Phys. Rev.* , 1982, **B 25**, 7183.
72. D. J. Kim, Y. B. Jung, M. B. Lee, Y. H. Lee and J. H. Lee, *Thin Solid Films*, 2000, **372**, 276.
73. G. Selvasuray and L. Sheet, *Mater. Sci. Technol.*, 1994, **9**, 463.

74. A. Calka, *Appl. Phys. Lett.*, 1991, **59**, 1568.
75. J. M. Criado, M. D. Alcala and C. Real, *Solid State Ionics.*, 1997, **101**, 1387.
76. A. Mosbah, A. Calka and D. Wexler, *J. Alloys Cmpds.*, 2006, **424**, 279.
77. A. B. Jin, Y. Yang, Y. X. Chen, Z. M. Lin and J. T. Li, *J. Amer. Ceram. Soc.*, 2006, **89**, 1099.
78. Y. Kameshima, M. Irie, A. Yasumori and K. Okada, *Solid State Ionics*, 2004, **172**, 185.
79. F. Zhang, W. A. Kaczmarek, L. Lu and M. O. Lai, *J. Alloys Cmpd.*, 2000, **307**, 249.
80. C. J. H. Jacobsen, J. J. Zhu, H. Lindelov and J. Z. Jiang, *J. Mater. Chem.*, 2002, **12**, 3113.
81. X. Z. Chen, J. L. Dye, H. A. Eick, S. H. Elder and K.-L. Tsai, *Chem. Mater.*, 1997, **9**, 1172.
82. S. Li, W. B. Kim and J. S. Lee, *Chem. Mater.*, 1998, **10**, 1853.
83. C. H. Jaggers, J. N. Michaels and A. M. Stacy, *Chem. Mater.*, 1999, **9**, 150.
84. D. Lu, G. Hitoki, E. Katou, J. N. Kondo, M. Hara and K. Domen, *Chem. Mater.*, 2004, **16**, 1603.
85. R. Marchand, F. Tessier and F. J. Disalvo, *J. Mater. Chem.*, 1999, **9**, 297.
86. P. R. Bonneau, R. F. Jarvis and R. B. Kaner, *Nature*, 1991, **349**, 510.
87. I. P. Parkin, *Chem. Soc. Rev.*, 1996, 199.
88. J. C. Fitzmaurice and I. P. Parkin, *Polyhedron*, 1993, **12**, 1295.
89. R. E. Treece, E. G. Gillan and R. B. Kaner, *Comments Inorg. Chem.*, 1995, **16**, 313.
90. U. A. Joshi, S. H. Chung and J. S. Lee, *J. Solid State Chem.*, 2005, **178**, 755.
91. J. C. Fitzmaurice, A. L. Hector and I. P. Parkin, *J. Chem. Soc. Dalton. Trans.*, 1993, 2435.
92. A. L. Hector and I. P. Parkin, *Chem. Mater.*, 1995, **7**, 1728.
93. G. Demazeau, *J. Mater. Sci.*, 2008, **43**, 2104.
94. Y. Xie, Y. Qian, W. Wang, S. Zhang and Y. Zhang, *Science*, 1996, **272**, 1976.
95. J. Choi and E. G. Gillan, *Inorg. Chem.*, 2005, **29**, 1610.
96. R. A. Janes, M. A. Low and R. B. Kaner, *Inorg. Chem.*, 2003, **42**, 2714.
97. X. Hao, M. Yu, D. Cui, X. Xu, Q. Wang and M. Jiang, *J. Cryst. Growth*, 2002, **241**, 124.

98. L. Chen, Y. Gu, Z. Li, Y. Qian, Z. Yang and J. Ma, *J. Cryst. Growth*, 2005, **273**, 646.
99. *International Technology Roadmap for Semiconductors*, , 2002 Update, Semiconductor Industry Association, 2002.
100. S. J. Martin, J. P. Godschlax, M. E. Mills, E. O. Shaffer and P. H. Townsend, *Adv. Mater.*, 2000, **12**, 1769.
101. K. Mosig, T. Jacobs, K. Brennan, M. Rasco, J. Wolf and R. Augur, *Microelectron. Eng.*, 2002, **64**, 11.
102. G. M. Brown and L. Maya, *J. Amer. Ceram. Soc.*, 1998, **71**, 78.
103. D. V. Baxter, M. H. Chisholm, G. J. Gama, V. F. Distasi, A. L. Hector and I. P. Parkin, *Chem. Mater.*, 1996, **8**, 1222.
104. S. Kaskel, K. Sclichte and G. Chaplais, *J. Mater. Chem.*, 2003, **13**, 1496.
105. M. M. B. Holl, P. T. Wolczanski and G. D. V. Duyne, *J. Amer. Chem. Soc.*, 1990, **112**, 7989.
106. N. A. K. Hansen and W. A. Herrmann, *Chem. Mater.*, 1998, **10**, 1677.
107. A. L. Hector, *Chem. Soc. Rev.*, 2007, **36**, 1745.
108. H. J. Schmidt, *J. Non-Cryst. Solids*, 1988, **100**, 51.
109. D. R. Ulrich, *J. Non-Cryst. Solids*, 1988, **100**, 174.
110. B. E. Yoldas, *Bull. Amer. Ceram. Soc.*, 1975, **54**, 286.
111. U. Schuber and N. Husing, *Synthesis of Inorganic Material*, 2nd edition, WILEY-VCH verlag GmbH & Co. KGaA, Weinheim 2004.
112. L. L. Hench and J. K. West, *Chem. Rev.*, 1990, **90**, 30.
113. A. Hannemann, J. C. Schon and M. Jansen, *J. Mater. Chem.*, 2005, **15**, 1167.
114. S. Kaskel, K. Schlichte and B. Zibrowius, *Phys. Chem. Chem. Phys.*, 2002, **4**, 1675.
115. F. Cheng, B. Toury, F. Lefebvre and J. S. Bradley, *Chem. Comm.*, 2003, 242.
116. J. Loffelholz, J. Engering and M. Jansen, *Z. Anorg. Allg. Chem.*, 2000, **626**, 963.
117. F. Cheng, S. M. Kelly, S. Clark, N. A. Young, S. J. Archibald and J. S. Bradley, *Chem. Mater.*, 2005, **17**, 5594.
118. S. Kaskel, G. Chplais and K. Schlichte, *J. Mater. Chem.*, 2005, **17**, 181.
119. F. Cheng, S. M. Kelly, F. Lefebvre, S. Clark, R. Supplit and J. S. Bradley, *J. Mater. Chem.*, 2005, **15**, 772.
120. A. W. Jackson and A. L. Hector, *J. Mater. Chem.*, 2007, **17**, 1016.

2 Instrumental techniques

2.1 Powder X-Ray Diffraction (PXD)

Powder X-ray diffraction is a widely used non-destructive technique that is used to obtain the information about the crystallographic structures and composition of natural and synthetic materials.

The diffraction pattern is obtained from the powder of material rather than a single crystal. Incident X-rays are reflected by the powder sample with a set of diffraction angles that is unique to the elemental composition and structure of the material, and are collected by the detector. After indexing the reflection positions the information about elemental composition of the material and crystal structure can be retrieved by refining the patterns.

X-rays are generated by a cathode ray tube, a crystal monochromator is used in a diffraction experiment to obtain the desired single X-ray wavelength. The monochromator is placed in series between the radiation source and the powder sample under investigation. The monochromator is usually mounted in the correct orientation to diffract only X-ray photons of the desired wavelength (e.g. Cu K_α at 1.5406 Å). The incident X-ray after contact with the sample is then scattered and produce constructive interference (diffracted ray) to give rise a diffraction pattern, when conditions satisfy the Bragg diffraction. Bragg diffraction occurs when the X-ray of comparable wavelength with atomic spacing are incident upon a crystalline powder sample, scattered by the atoms in the system and undergo constructive interference in accordance to Bragg's law.

$$n\lambda = 2d\sin\theta \qquad (2.1)$$

where λ is the X-ray wavelength

n is an integer (1, 2, 3, ..)

d is the inter-planar separation in the crystalline material

and θ is the angle of incidence (Bragg angle)

Angle of diffraction measured as 2θ, is related to the inter-planar spacing d. The specific atomic arrangement of the crystal structure defines the relative intensities of the diffracted waves.

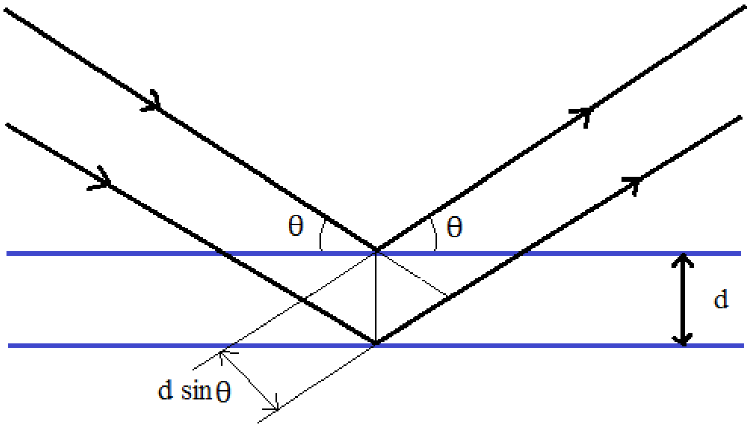

Figure 2.1: Schematic diagram of X-ray diffraction

2.1.1 PXD instrumentation

Powder X-ray diffraction (PXD) data were collected using a Siemens D5000 diffractometer or a Bruker D2 Phaser. X-ray photons for diffraction experiments are produced by bombarding a copper target with a beam of electrons emitted from a heated filament. X-ray of wavelength, λ=1.5406 Å (copper $K_{\alpha 1}$) are selected using a germanium single crystal monochromator. The monochromator beam is collimated by aperture slits and directed onto the sample, while a second set of slits is placed just before the detector (Fig. 2.2).

The relative position of incident beam, sample and detector is described as Bragg-Brentano geometry. Detector is rotated at an angular velocity double than the rotation velocity of the sample to keep a fixed relationship between the incident angle θ and the diffraction angle 2θ during the experiment. The diffractometer is controlled by an external PC for D5000 or built in with Bruker D2 Phaser and the software collects and stores the diffraction data.

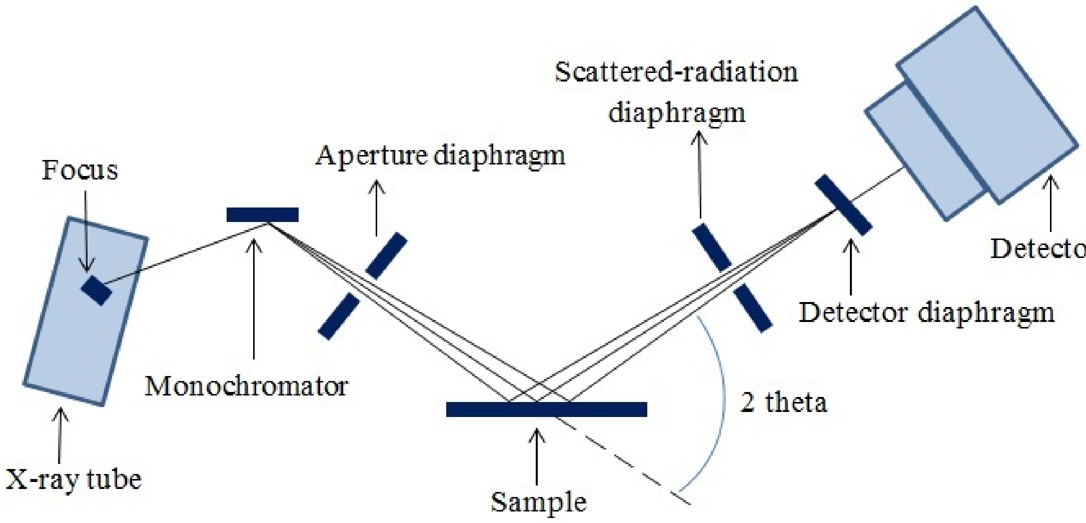

Figure 2.2: Schematic representation of the powder X-ray diffractometer

Air sensitive samples were mounted in an air sensitive sample holder and sealed inside a nitrogen filled glove box to avoid any oxidation. Various phases present in the powder samples were identified by comparison with the JCPDS[1] database through the Bruker "EVA" software package. The structure fitting of the data was performed using the General Structure Analysis Suite (GSAS).[2]

2.1.2 *The Rietveld method*

Structure factor extraction from the PXD data is often difficult due to many overlapping peaks in the diffraction pattern. In order to increase the amount of the information that could be extracted from powder data, H.M. Rietveld realised that although many reflections did overlap and thus could be modelled as single entities, the total intensity and the peak shape of a cluster of reflections could be determined by using simple peak shape parameters.[3, 4]

The typical procedure for the refinement of a structural model with X-ray powder diffraction data involved:

- Determination of an approximate model of the structure (e.g. using the ICSD database)
- Refinement of the lattice parameters and zero point
- Refinement of the atom positions in the structure
- Refinement of the isotropic thermal parameters
- Full refinement of peak shape parameters, in addition to any asymmetry or preferred orientation parameters which might be necessary.

A detailed description about the Rietveld structure refinement with solved examples is given in the GSAS manual.[2]

.

2.1.3 Particle size estimation from GSAS Refinement

Particle size can be related to peak shape for a diffraction pattern. For constructive interference to produce a strong peak the number of lattice planes contributing needs to be large. Destructive interference just off the Bragg angle is the reason why peaks are sharp, and reducing the correlation length also weakens this effect, hence with small particles the peaks become broader. GSAS[2] uses a treatment that incorporates the broadening into the Lorentzian terms, resulting in a modified version.
Information on particle size can be extrapolated from the complex expressions derived to model the Gaussian and Lorentzian contributions of the peak shape. Mathmatically particle size can be calculated using a modified form of the Scherrer equation.

$$p = \frac{1800K\lambda}{\pi L_x} \qquad (2.2)$$

where K is the Scherrer constant, λ is the X-ray wavelength (1.54 Å) and L_x is the value of the Lorentzian component extracted from GSAS refinement.

The equation 2.2 has been used to calculate the particles size of all materials prepared in this work. PXD patterns were collected with a Siemens D5000 using a sample holder for air sensitive material for (chapter 3 and 4) while Bruker D2 Phaser (chapter 6 and 7) and high intensity diffraction patterns and PDF data was obtained using synchrotron radiations at Diamond Light Source, Oxfordshire (chapter 5). The PXD data was refined using GSAS[5] and standard patterns were obtained from the inorganic crystal structure database (ICSD).[6] Most of the powder samples obtained at lower annealing temperature presented poor crystallinity. To obtain good resolution of the peaks the patterns were collected overnight using low scan speed of 0.2 and 0.02 step size to obtain maximum data points. The diffractometer peak shape was refined using α-quartz (SiO_2) as standard. This material was selected primarily because of its availability in pure form and also because its crystal structure is well characterized.

2.2 Pair distribution function (PDF)

X-ray atomic pair distribution function (PDF) is an X-ray scattering technique that can be used to study the local structure of materials at the atomic scale. The technique requires scattering data to be collected to very high scattering angles using high energy powder diffraction coupled with Fourier transform to produce the PDF data.

PDF data was collected at beam line I15 at ambient pressure and temperature at diamond light source Oxfordshire UK. The beamline provides monochromatic high-energy X-rays from 20 to 80 keV. These X-rays focussed and collimated down to <20 μm can penetrate into complex sample assemblies permitting detailed mapping of structural order or disorder, chemical fingerprinting, or single crystal structure determination. The sample environment for acquiring X-ray PDF data initially has to be compact but very versatile to be able to accommodate high-throughput including variable temperature experiments at ambient pressure. The flexibility of the sample station should facilitate the development and installation of more complex sample environments. Pair distribution function data was collected for the vanadium nitride material to find out the structural variations in the samples obtained at various temperatures. Sample preparation procedures are given in chapter 5. Schematic diagram of the beam line I15 section is given in the figure 2.3.

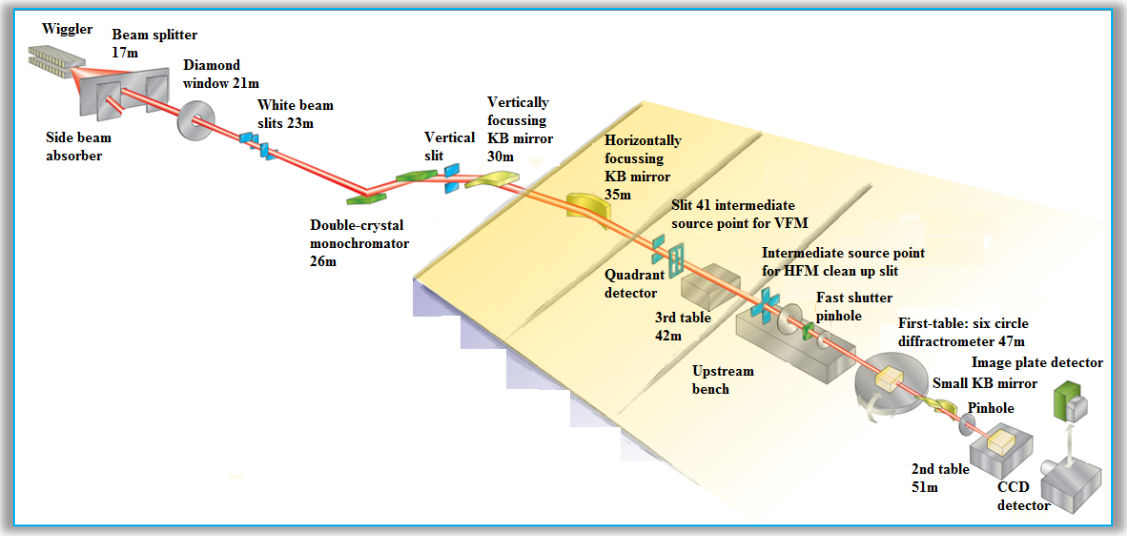

Figure 2.3: Schematic representation of the beam line I15; image obtained from www.diamond.ac.uk

The high resolution opens the possibility of novel studies of phase transitions in large macromolecules as a function of temperature, leading to improved methods for the preparation of large single crystals. The high intensity X-rays can probe more deeply into the sample than laboratory techniques, and the use of resonant diffraction allows complex structures with low "normal" electron contrasts to be studied.

PDF data is initially obtained in the form of an image which is integrated to the diffraction pattern using software Fit2D to obtain a .Chi file. The .Chi file is then processed with a software PDFgetX2 software to subtract the background and to obtain the Fourier transform G(r) of the total structure factor S(Q) obtain from the diffraction pattern as .Gr file. Final PDF data .Gr was refined using software PDFgui, a brief description is given below.

2.2.1 PDFgui

PDFgui is a graphical interface built on the PDFfit2 engine, which is a program as well as library for real-space refinement of crystal structures based on the atomic pair distribution function (PDF) method. PDFgui organizes fits and simplifies many data analysis tasks, such as configuring and plotting multiple fits. PDFfit2 is capable of fitting a theoretical three dimensional structure to atomic pair distribution function data and is ideal for nanoscale investigations. The fit system accounts for lattice constants, atomic positions and anisotropic atomic displacement parameters, correlated atomic motion, and experimental factors that may affect the data. The atomic positons and thermal coefficients can be constrained to follow symmetry requirements of an arbitrary space group.[7]

2.3 Thermogravimetric analysis

Thermogravimetric analysis (TGA) is a thermal analysis technique in which the change in sample mass can be followed over a period of time during heating under an inert or reactive gas. It was used herein to determine the thermal stability of the material and the fraction of the volatile components. TGA was carried out in Mettler Toledo TGA/SDTA85le instrument (Fig. 2.4) under flowing N_2 (chapter 4) or Ar (rest of the chapters) with flow rate of 65 ml/min and temperature ramp rate of 10 °C/min.
Due to the high air sensitivity of the amide precursors and nitride products, the equipment was mounted inside a glovebox filled with nitrogen. Hence the risk of partial oxidation of the sample during handling, which would result in inaccuracies during analysis, was minimised.

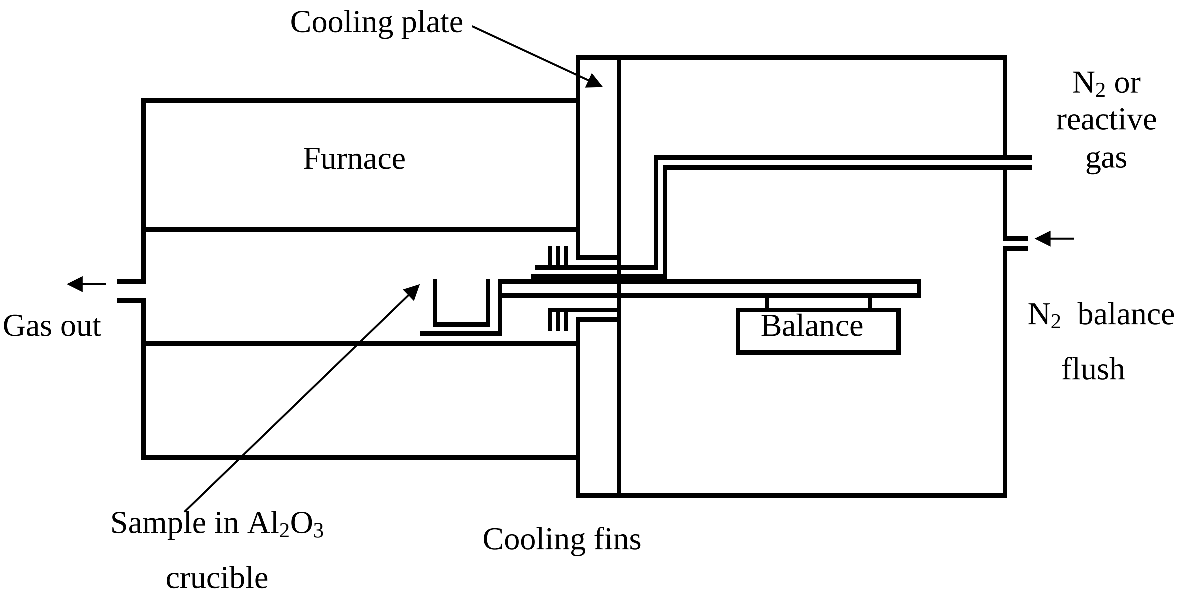

Figure 2.4: A schematic diagram of the Mettler Toledo TGA851e

Pre-programmed heating regimes were adopted for the TGA samples heated under a flow of very high purity nitrogen (Air Products BiP grade). The sample (between 10–30 mg) was loaded in a dry alumina crucible (vol: 150 μL) and then placed onto the balance arm within the analyser. It was held at 25 °C for 10 minutes before gradually heating to 800 °C at a heating rate of 10 °/min under a flow of gas (50 mL/min) for the whole procedure. At 800 °C the sample was then held for 20 or 60 minutes before allowing it to cool back to 25 °C. The balance assembly measures the initial sample mass and then continuously monitors any change in mass as a function of temperature and time throughout the procedure.

2.3 Microanalysis

Microanalysis was carried out on precursor materials and annealed nitrides. Information of the quantities of carbon, hydrogen, nitrogen and chlorine were collected. This information can be used as a guide to sample stoichiometry compared to calculated percentage composition based on ideal materials. Around 5–15 mg of sample was sealed inside the glovebox and sent to MEDAC Ltd., Egham, Surrey, who handled samples in the glovebox. Different precursors as well as the annealed products were analysed to compare the C, H and N concentration.

2.4 Infrared spectroscopy

Infrared spectroscopy is a straightforward method for identification of chemical bonds (functional groups) within molecules. It is concerned with changes in the dipole moment that are produced from vibration or rotation. The absorption of IR radiation depends on increasing the energy of vibration or rotation associated with a covalent bond. This increase results in a change in the dipole moment of the molecule or solid. Nearly all materials containing covalent bonds will show absorption in the IR. The only exceptions are homonuclear diatomic molecules because no mode of vibration or rotation produces a change in the electric dipole of the molecules. Generally, the absorption of IR photons may be due to either change in the bond length (stretching) or alteration of the bond angles (bending). The former one is usually denoted by the symbolism ν and the later as δ. Stretching can involve symmetric and asymmetric stretching modes.

IR experiments are typically based on passing IR radiation through a thin sample of compound and measuring which energies of the applied IR radiation are transmitted by the sample. IR spectra can be recorded for solids, liquids and gases using different sample arrangements. The absorption by a specific group occurs in a characteristic region of the spectrum. These absorptions appear as a series of peaks and are referenced by simply comparing them with tables of known compounds.[8] Similar frequencies occur in different molecules, therefore a vibration is considered as reflecting the atoms involved and the strength of bond holding them together.

Infrared spectroscopy was performed using a PerkinElmer spectrum One FT-IR spectrometer in conjunction with PerkinElmer's analytical software Spectrum v3.05. Solid samples were prepared by incorporating them into a pressed pellet of cesium iodide or potassium bromide for analysis. Due to the sensitivity of the precursor, the samples had to be prepared inside a nitrogen filled glovebox. A weighed portion of sample, approximately 0.2 mg, was mixed with 20 mg, of highly purified CsI or KBr using a pestle and mortar. The sample and CsI or KBr were ground well to reduce the particle size; otherwise the large particles would scatter the infrared beam causing a sloping profile in the baseline of the spectrum. CsI or KBr does not absorb in the region studied so will not interfere with the spectrum. The mixture was placed in an evacuable die and subjected to a pressure of 10 MPa for two minutes. The amide precursor samples, due to higher air sensitivity, were sealed between two CsI plates using a sample holder for air sensitive materials, while the nitride samples obtained at higher temperature were run quickly after taking out of the glove box, using a standard holder.

2.5 Raman spectroscopy

Raman spectroscopy involves the inelastic scattering of monochromatic radiations after contact with the molecular media. A spectrum is obtained due to exchange of energy between the photon and the molecule, where scattered photon can be higher or lower in energy than the incident photon. It gives information about the difference in energy by measuring the change in rotational or vibrational energy of the molecule and gives information of its energy levels. Raman was carried out for the manganese nitride samples (chapter 3) with the aim to test for the presence of graphitic carbon. Raman spectra were collected on Renishaw 2000 microscope in the frequency range of 2000 to 400 cm^{-1}, using He-Ne laser beam, 2.7 mW (power) with a wave length of 632.8 nm.

2.6 Electron microscopy

Electron microscopy (EM) uses electrons to create an image of the sample. Smaller objects and details can be detected than with a light microscope since the wavelength of the electrons is much shorter than that of visible light photons. Furthermore it has much higher magnification that reaches up to two million times which can be used to examine metals and crystalline structures and the characteristic morphologies of the various surfaces.

Transmission electron microscopy (TEM) has been utilised throughout the study for this thesis. TEM employs a beam of electrons which are directed to the specimen. The working of an electron microscope is discussed below.

The thermoionic gun, as shown in figure 2.4, is the most widespread system for generating electrons. The filament, acts as a cathode; it is heated and the electrons emitted from it are accelerated by a positive potential applied down the gun column toward the anode and a beam of electrons is generated. A negative potential is applied to the ‘Wehnelt Cap’ so that any emitted electron from the filament is repelled by that cap toward the horizontal centre. The electrons are collected in the space between filament tip and Wehnelt Cap, called a space charge. Those electrons at the bottom of the space charge nearest to the anode can exit the gun area through a small hole moving down the column be used in imaging.

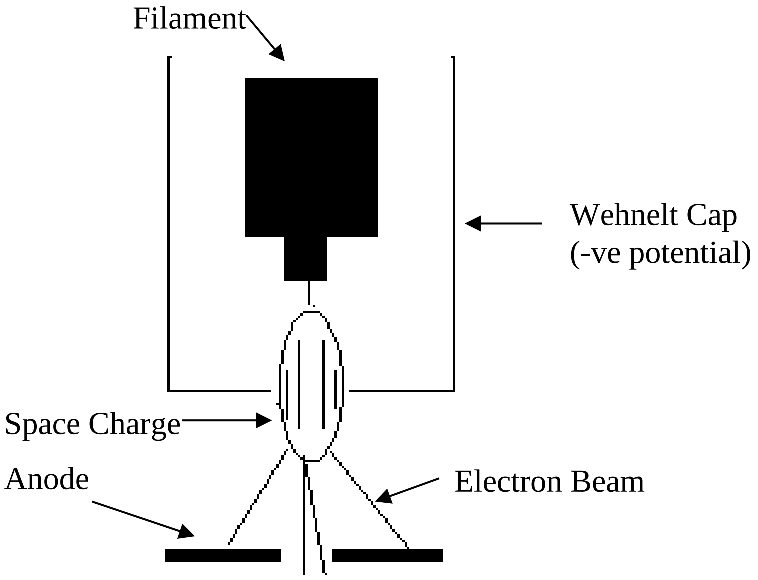

Figure 2.5: The electron gun in electron microscope

Once the stream of electrons departs the gun, it is passed through the first condenser lens that is used to form the beam and limit the amount of current in the beam. The beam is constricted by a condenser aperture which is used to eliminate the high-angle electrons from the beam. The second condenser lens forms the electrons into a thin, coherent beam and the objective lens focuses the scanning beam onto the desired part of specimen to be analysed, Fig. 2.5.

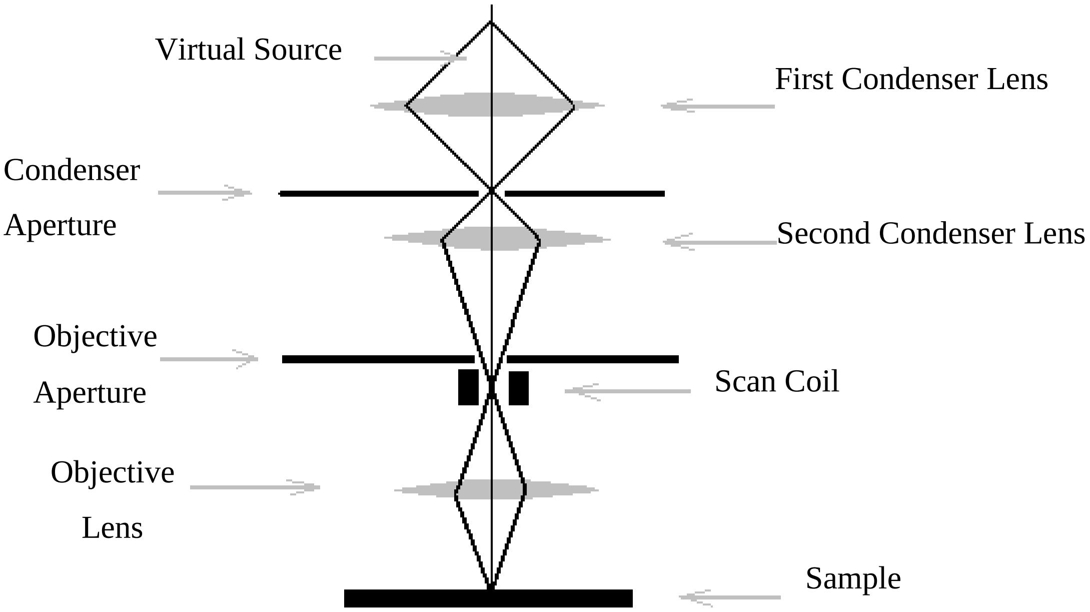

Figure 2.6: A schematic representation of the SEM focussing process

2.5.1 Transmission Electron Microscopy

In transmission electron microscopy TEM, a thin specimen is irradiated with an electron beam of uniform current density. Electrons are emitted from the electron gun and illuminate the specimen through a two or three stage condenser lens system. The objective lens provides the formation of either an image or a diffraction pattern of the specimen. The electron intensity distribution behind the specimen is magnified with a three or four stage lens system and viewed on a fluorescent screen. The image can be recorded digitally by a CCD camera.

TEM was carried out on a Hitachi H7000 with accelerating voltage of 75 kV at Biomedical Imaging Unit, Southampton General Hospital. High resolution transmission electron microscopy and electron diffraction was performed with JEOL JEM-3010 with accelerating voltage of 300 kV (chapter 3). Samples were prepared by ultrasound dispersal using dry toluene as the solvent and were deposited on carbon coated Cu grids. The technique was used to obtain images of the morphology of the nanostructured particles and nanotubes, and approximate particle sizes.

2.7 N_2 physiosorption analysis

The adsorption of N_2 gas is widely used for determining the surface area and pore size distribution of a variety of different solid materials. As a result specific surface area and pore size distribution can be estimated.

2.6.1 Adsorption isotherms

When the adsorption of N_2 gas is applied to a solid (degassed under vacuum or in flow of inert gas at ~ 150-200 °C) at 77 K, the amount of N_2 gas is physically adsorbed and increases with the pressure. As a result, plots of adsorbed gas as a function of relative pressure are gained with different shapes. These plots are called adsorption isotherms. There are six types of adsorption isotherms (Fig. 2.7) according to IUPAC classification[9]. The relationship between the adsorbed gas volume V and the relative pressure P/P_o can be represented as:

$$V = f\left(\frac{P}{P_o}\right)T \qquad (2.3)$$

where V is the volume of adsorbed gas with a pressure P, P_o is the saturation pressure and T is the absolute temperature.

Type I isotherms are characteristic of microporous solids. Type II and III represents macroporous solids with strong or weak adsorbate and adsorbent interaction respectively. Type IV and V are the characteristic isotherms with hysteresis loop. These types represent the mesoporous materials where capillary condensation takes place in the adsorbate pores.

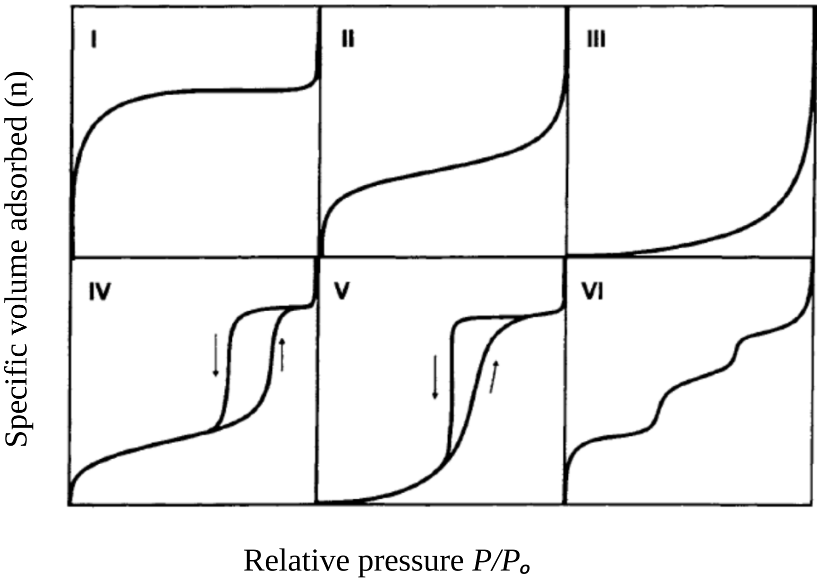

Figure 2.7 Types of adsorption/desorption isotherms

2.6.2 Pore size distribution (PSD)

Porous solids are materials having pores, cavities and channels and may vary from one solid to another in their shapes and sizes. Porous materials on the basis of pore size are classified in to three different pore-size regimes according to their average width i.e. microporous < 20 nm, mesoporous < 50 nm and macroporous < 50 nm.

The pore size is expressed either in terms of diameter (or radius), or with width of the slits. This distribution of the pores can be homogeneous, bimodal or heterogeneous according to the number of distinct pore maxima of the solid being analysed.

2.6.3 BET method

The Brunauer, Emmett and Teller method is widely used with N_2 physisorption analysis for measuring surface area of a given solid S_{BET}.[10] This method is based on the following equation:

$$\frac{P/P_o}{V\left(1-\frac{P}{P_o}\right)} = \frac{1}{V_m c}\left(\frac{P}{P_o}\right) \qquad (2.3)$$

where P and P_o are the equilibrium saturation pressure of the adsorbate, V is the volume of the adsorbed gas, V_m is the unimolecular volume of the adsorbed gas (i.e volume of the gas, covering the solid surface, with the thickness of one molecule) and c is a constant depending on the nature of the adsorbate and adsorbent material.

The BET surface area is determined by using the following equation,

$$S_{BET} = \frac{V_m \times N_A \times a_m}{m_v} \qquad (2.4)$$

where N_A is the Avogadro's number, a_m is the cross sectional area of an adsorbed N_2 molecule (16.2 Å) and m_v is the molar volume of N_2 at 77 K. is the cross sectional area of N_2. BET surface area measurement and pore size distribution measurements were carried out using micrometrics gemini 2375 V5.01.

2.8 Cyclic voltammetry

Cyclic voltammetry (CV) is an electroanalytical technique used to characterise the electrochemical behaviour of material surfaces, through different interfacial mechanisms occurring between the electrode and the electrolyte at the contact surfaces.

CV applies a cycled potential to an electrochemical cell and measures the current flow through the cell that results.[11] The potential is measured against a known reference electrode. The electrochemical curve represents Faradaic or/and non-Faradaic processes that occurred during the potential sweeping.[7] CV can provide quantitative observations of surface behaviours such as adsorption/desorption, reduction/oxidation of an electrode surface or dissolved electrolyte, and electro catalytic changes such as oxygen reduction or hydrogen evolution.[11] A rectangular box shaped curve is observed if capacitance is the main process occurring at the electrode, sometimes with extra peaks in the case of pseudocapacitors. A typical CV profile of a rectangular shape is shown in figure 2.8.

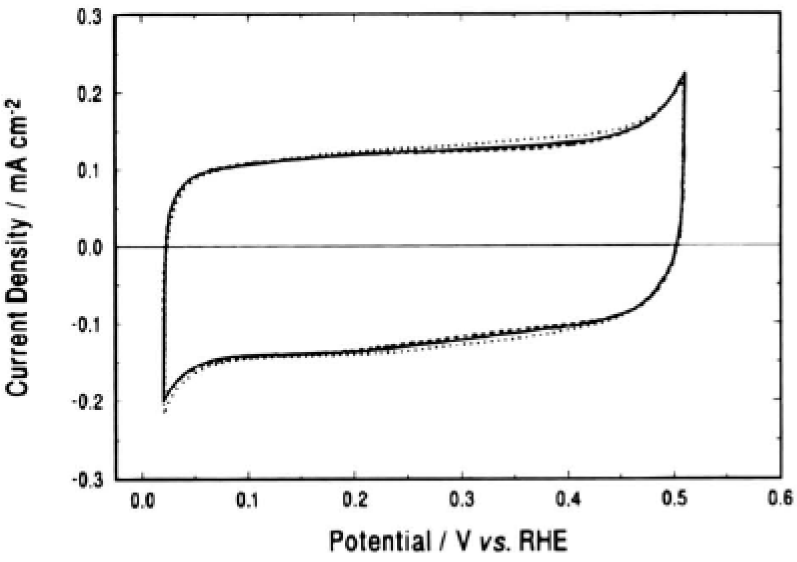

Figure 2.8 Cyclic voltammograms i vs. E profiles for a MoN_x film electrode[10]

The capacitance for synthesized materials (MoN_x, Mn_3N_2 or TiN) was measured by carrying out CVs on composite electrodes. Electrochemical cells were assembled with three electrodes: (i) a working electrode in which the active materials were the synthesised binary and ternary nickel nitrides, (ii) the counter electrode was a high surface area Pt mesh, (iii) a reference electrode which was Hg/HgO containing 1M KOH, $Hg/HgSO_4$ containing 0.5 M K_2SO_4 or Hg/HgSO4 containing 0.5 M H_2SO_4. Reference electrodes were chosen depending on the electrolyte, either acidic (H_2SO_4), basic (KOH) or neutral (K_2SO_4) solutions. The Potentiostat controlled the potential between the reference electrode and working electrode, and measured the current between the working electrode and counter electrode. During the CV experiment the potential was scanned through the cell and then the current flow through the working electrode was measured by the potentiostat.

For electrochemical capacitor devices, cyclic voltammetry gives a useful overall basis for the characterization of the performance of the system in terms of (a) the reversibility of the charge and discharge processes, (b) the distinction between any distinguishable stages in the charging and/or discharging processes, (c) the accumulated charge as a function of potential through the integration of the voltammograms, (d) the range of potentials between which the electrodes can be operated for charge acceptance and disposal, and (f) the dynamical behaviour of the electrode for charge acceptance and disposal derived from the dependence of the current-response regime. Electrochemical charge/ discharge measurements were carried out using Bio-logic SP-150 Potentiostat.

2.9 References

1. International Centre for Diffraction Data, 12 Campus Boulevard, Newton Square, Pennsylvania 19073-3273, U.S.A.
2. A. C. Larson and R. B. Von-Dreele, GSAS manual, LANSCE MS-H805, Los Alamos National Laboratory, Los Alamos NM, NM 87545, 2000.
3. H. M. Rietveld, *Acta Cryst.*, 1967, **22**, 151.
4. H. M. Rietveld, *J. Appl. Cryst.*, 1969, **2**, 65.
5. R. B. Von Dreele and A. C. Larson, Generallized structure analysis system, Los Alamos National Laboratory, NM87545, USA, December 2002 release.
6. D.A. Fletcher, R. F. McMeeking and D. Parkin, *J. Chem. Inf. Comput. Sci.*, ICSD accessed via The United Kingdom Chemical Database Service, 1996,, **36**, 746.
7. C. L. Farrow, P. Juhas, J. W. Liu, D. Bryndin, E. S. Bozin, J. Bloch, T. Proffen and S. J. L. Billinge, *J. Phys.: Condens. Matter*, 2007, **19**, 335219.
8. K. Nakamoto, *Infrared and Raman Spectra of Inorganic Compounds, Theory and Applications in Inorganic Chemistry*, Wiley-Interscience, 1997.
9. G. S. Karlberg, T. F. Jaramillo, E. Skúlason, J. Rossmeisl, T. Bligaard and J. K. Nørskov, *Phys. Rev. Lett.*, 2007, **99**, 126101.
10. T. C. Liu, W. G. Pell and B. E. Conway, *J. Electrochem. Soc.*, 1998, **145**, 1881.
11. T. C. Liu, W. G. Pell, B. E. Conway and S. L. Roberson, *J. Electrochem. Soc.*, 1998, **145**, 1882.

3 Solvothermal synthesis of manganese nitride and charge storage

3.1 Introduction

Four stable intermediate phases (ε,η,ζ,θ) in the Mn-N binary system exist. The ε phase (Mn_4N)[1] has a face-centred (f.c.c) structure, and the ζ phase ($Mn_5N_{2,}$[1, 2] Mn_2N,[3] and $Mn_2N_{0.85}$)[4] a hexagonal closed packed (h.c.p) one, while η (Mn_3N_2)[1, 2] and θ phase (MnN, Mn_6N_5)[5, 6] exhibit the face centred tetragonal structure with NaCl-type. Manganese nitrides have previously been studied as magnetic materials with unique magnetic properties. MnN, Mn_3N_2 and Mn_2N are antiferromagnetic, while Mn_4N is ferromagnetic. [5, 7] Antiferromagnetic Mn_2N has a magnetic structure with four sublattices with the same orthorhombic unit cell as the chemical one.[3] Eddine et al.[8] studied the crystallographic and magnetic structures of $Mn_2N_{0.85}$ by means of powder neutron diffraction.[9]

Manganese powder was nitrided in flowing ammonia gas and the specimen heated with manganese metal at 600 °C for one week to obtain Mn_2N.[3] The Mn_2N crystals grown were hexagonal platelet or pyramidal. MnN was prepared as a single phase by dielectric (DC) reactive sputtering in a mixture of gas Ar-N_2.[5] Deposited film of MnN of 130 μm was stripped off and powdered. The powder sample was stress relieved by annealing in vacuum at 510 K for 4 hrs. Nanocrystalline Mn_4N and Mn_2N were prepared by homogenization and nitrogenation of as-milled Mn powders under different conditions through mechanical alloying of the powders.[10] η-Mn_3N_2 has been reported[6] by heating a mixture of manganese powder and NaN_3 in an autoclave at 750 °C for 6 days. In an autoclave nitriding of Mn-In and Mn-Sn alloys or heating the mixture of Mn_4N and substituent metal produced Mn_4N.[11]

To prepare MnN_x manganese powder was mixed with sodium azide and heated in an autoclave for 3 days at 750 °C under inert atmosphere.[12] Neutron diffraction showed one or two manganese nitride phases and in some cases MnO is found as well. Manganese nitrides have been reported via a Solvothermal method.[13] $MnCl_2$ and NaN_3 is grounded to fine powder inside the glove box and loaded in to a high pressure, high temperature stainless steel reactor partially filled with toluene. The temperature was raised to 70 °C (4 h hold) and then raised to 220 °C (20 °C/h, 1 day hold) and then gradually increased to 280 °C (20 °C/ day) and finally to 290 °C (1 day hold). Total reaction time was about 6 days. The reaction was carried out in two different ways yielding different products. A stirred loose powder reaction of metal halide and metal azide yielded MnN while a pellet-based reaction yielded a mixture of tetragonal Mn_3N_2 (75 %) and cubic Mn_4N (25 %). Crude product was washed with degased methanol to remove sodium salt. Crystals of ϑ-Mn_6N_5 and η-Mn_3N_2 have been prepared in high pressure autoclaves by reaction of MnI_2 with $NaNH_2$ (I:2) in ammonia at 6 kbar and temperatures from 400 to 450 °C and 450 to 600 °C, respectively.[14] Another solvothermal route reporting tetragonal MnN as a reaction was sodium azide and $MnCl_2$.[13] Reactants were ground separately and loaded into a high-pressure high-temperature stainless steel reactor. Slow heating ramps were chosen to avoid rapid exothermic degradation of metal azide intermediates, which could lead to product decomposition. A maximum temperature of 290 °C is achieved to obtain the final product. Reactions required several days and the product was aggregated nanoparticulates, with lower nitrogen contents. Mn_4N has been reported[15] through solid state metathesis reaction of MnI_2 and LiN_3. The reaction was carried out by heating the mixture at 400 °C in a conventional oven.

Electrochemical supercapacitors of manganese nitrides have not yet been reported elsewhere, however a rich literature of manganese oxide has been published in the recent past. The charge storage mechanism in manganese oxide is mainly due to pseudocapacitive reactions occurring on the surface and in the bulk of the electrode. It involves the surface adsorption of electrolyte cations on the manganese oxide:[16-18]

$$(MnO_2)_{surface} + C^+ + e^- \leftrightarrow (MnOOC)_{surface}$$

The redox reaction relies on the intercalation or de-intercalation of electrolyte cations in the bulk of the manganese oxide:

$$(MnO_2) + C^+ + e^- \leftrightarrow (MnOOC)$$

Where C^+ is the electrolyte cation (H^+, Na^+, and K^+). In the above mechanism the redox reaction occurs between the III and IV oxidation state of Mn ions.
Hydrated manganese oxides exhibit specific capacitance within the 100-200 F g^{-1} range in alkali salt solutions, which are much lower than those for RuO_2 ECs. Current MnO_2 based supercapacitors have limited use due to low specific capacitance, lack of structural stability, long cyclability, and low rate capacity.[18] An oxide layer can develop during cycling of metal nitride electrodes[19] in aqueous electrolytes and that created our interest in making nanoparticulate manganese nitrides.

In our current study we report Mn_3N_2 through a solvothermal reaction of $MnCl_2$ and $LiNH_2$. Standard solid state metathetical (SSM) synthesis of metal nitrides involves reaction between metal halides and nitrogen sources including Li_3N, $LiNH_2$, NaN_3, or Ca_3N_2.[15, 20-24] SSM are extremely exothermic reactions, and fast heating leads to product decomposition. Solvothermal conditions are desirable for metathesis reactions because the heat produced can be absorbed by the solvent, resulting in more controlled growth of small-scale crystallites.[25]

In our current study we report Mn_3N_2 through a solvothermal reaction of $MnCl_2$ and $LiNH_2$. Efforts are made to synthesise the product using different precursors and methods. The purpose of this study is to obtain a phase pure manganese nitride of various compositions and morphologies of the material, and use the material to analyse its electrochemical properties. Capacitance is measured using cyclic voltammetry.

3.2 Synthesis of manganese nitride

Synthesis of manganese nitride was initially attempted by solution phase ammonolysis of manganese acetate $Mn(CH_3COO)_2$ and annealing the polymer under NH_3. PXD patterns showed green colour manganese oxide (MnO).[26] Solvothermal reaction between $MnCl_2$ and NaN_3 yielded nitrogen deficient (> 4%) Mn_3N_2 with a high level of carbon (9 to 44 %) contamination. Carbon contents increased with increase of reaction temperature. This could be due to the high temperature and fast heating ramps which may have caused rapid exothermic degradation of metal azide intermediates, and solvent decomposition. Reaction between $MnCl_2$ and $LiNH_2$ yielded phase pure tetragonal Mn_3N_2. The sample preparation and characterization using the $LiNH_2$ reaction is discussed in this chapter.

3.2.1 Solvothermal reaction of $MnCl_2$ with $LiNH_2$

Solvothermal synthesis whether using NaN_3 (mentioned above) or $LiNH_2$ as nitrogen sources was carried out in a 75 cm^3 stainless steel autoclave (Parr 4740CH) provided with a pressure gauge arm. Typically $MnCl_2$ (0.5g, 0.004 M) and $LiNH_2$ (0.19 g, 0.008 M) were weighed and ground together and transferred into a silica bomb liner. 20 ml of dry benzene was added to the mixture and stirred with a spatula. The liner was transferred to the bomb and this was sealed. The bomb was heated at 350, 400, 450, 500 or 550 °C for 15 hrs and then left to cool to room temperature. The black sample and the solvent were transferred to a Schlenk tube inside the glove box. It was washed and filtered three times using 20 ml of dry methanol to remove lithium salts and finally the black solid product was dried under vacuum and collected inside the glove box under nitrogen. Yield of the products after washing and drying the powders is ~ 200 mg at each temperature. No pressure in the autoclave was observed at any temperature during the reaction. Reaction scheme for the process can be written as below:

$$MnCl_2 + 2Li\mathrm{NH_2} \rightarrow \text{"}\mathrm{Mn(NH_2)_2}\text{"} + 2LiCl$$

$$3\text{"}\mathrm{Mn(NH_2)_2}\text{"} \rightarrow Mn_3N_2 + 4NH_3$$

3.3 Analysis of manganese nitride samples obtained from the reaction of $MnCl_2$ with $LiNH_2$

PXD data (Fig. 3.1) for the samples obtained from the reaction of $MnCl_2$ and $LiNH_2$ has shown phase pure tetragonal Mn_3N_2 up to 500 °C, while at 550 °C low intensity peaks for Mn_2N were observed at 40 and 42° 2θ with the d-spacing of 2.2 or 2.15 Å, respectively. Mn_2N peaks at 550 °C can be indexed using the Fe_2N lattice with the phase group *Pbna*[3] (Fig. 3.3). PXD patterns were refined using GSAS.[27] Standard patterns were obtained from the inorganic crystal structure database (ICSD).[28] All the patterns were refined with the reported tetragonal phase *I*4/*mmm* for η-Mn_3N_2.[29] The fit to the crystalline Mn_3N_2 obtained at 350 °C is shown in figure 3.2. The average of refined lattice parameters for all the η-Mn_3N_2 are a = 2.975 Å slightly higher than the standard value of a = 2.966 Å. Similar lattice parameters a = 2.975 Å are reported with some MnO impurities.[30] Crystallite size was refined using Scherrer equation given in the GSAS manual.[31] Refined lattice parameters and crystallite sizes of the manganese nitride samples obtained under solvothermal conditions are given in table 3.1. Refined lattice parameters were obtained by refining the background for the patterns, scale factor, atomic occupancies, thermal parameters and the peak shapes for each sample.

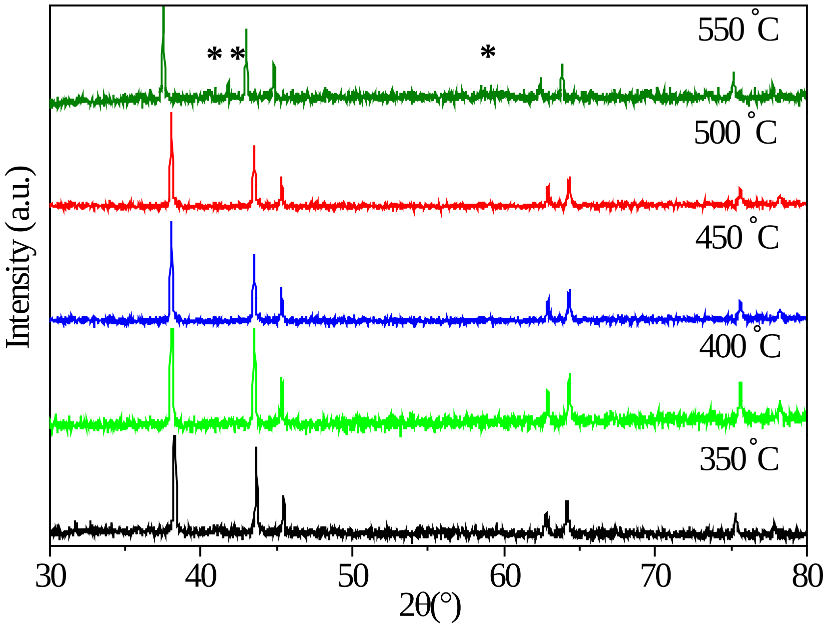

Figure 3.1: PXD patterns for Mn_3N_2 samples prepared under various conditions at various temperatures. Reflections due Mn_2N at 550 °C labelled with asterisks.

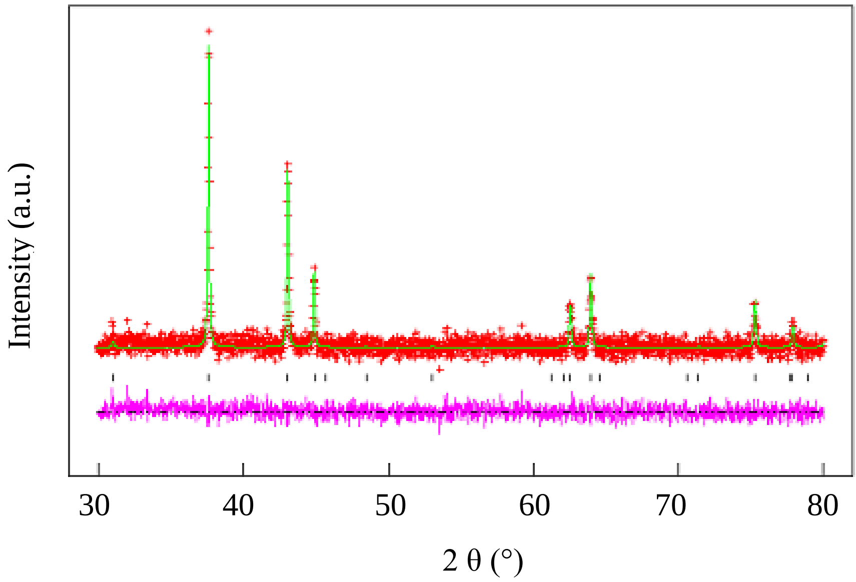

Figure 3.2: Fit to the crystalline Mn_3N_2 obtained at 350 °C. Crosses mark the data points, upper continuous line the calculated profile and lower continuous line the difference; tick marks are the positions of allowed reflection positions for Mn_3N_2.

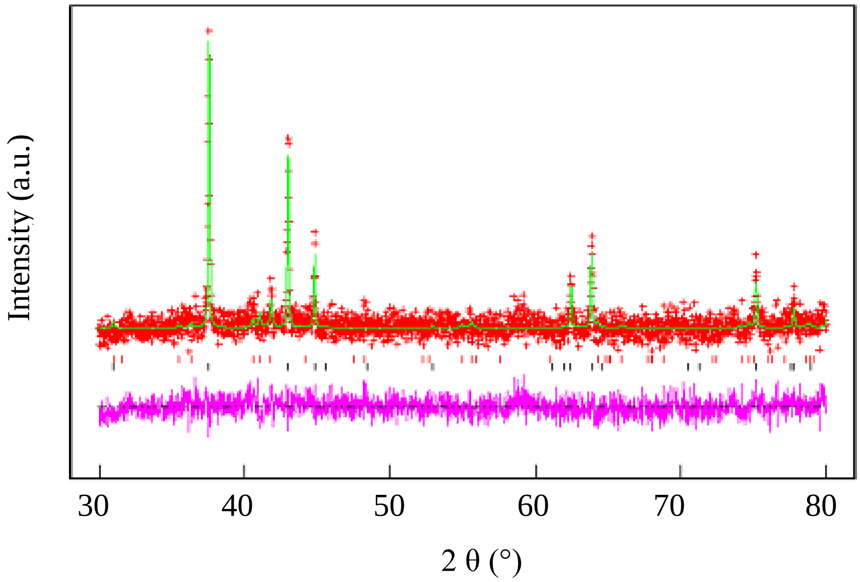

Figure 3.3: Fit to the crystalline Mn_3N_2 obtained at 550 °C. Crosses mark the data points, upper continuous line the calculated profile and lower continuous line the difference; tick marks are the positions of allowed reflection positions for Mn_3N_2.

Table 3.1: Refined lattice parameters for Mn_3N_2 obtained from solvothermal reaction of $MnCl_2$ and $LiNH_2$ at given temperatures.

Sample temp. °C	Phase	a (Å)	b(Å)	c(Å)	Rwp/Rp (%)	Crystallite size nm
350	Mn_3N_2	2.9733(3)		12.1258(12)	4.6/3.6	71
400	Mn_3N_2	2.9774(3)		12.1422(14)	7.2/5.7	53
450	Mn_3N_2	2.9771(2)		12.1417(10)	5.4/4.7	80
500	Mn_3N_2	2.9754(14)		12.1341(7)	4.8/3.8	75
550	Mn_3N_2	2.9728(4)		12.1238(6)	6.6/5.2	87
550	Mn_2N	5.6609(2)	5.0574(4)	4.4449(7)		68

η-Mn_3N_2 model in *I*4/*mmm* from Hasegawa Yagi,[29] who reported a = 2.994(1) and c = 12.499(5) Å. ζ-Mn_2N in *pbna* from Mekata et al,[3] who reported a = 5.668(3), b = 4.909(5) and c = 4.537(2) Å.

Elemental analysis (Table 3.2) for the samples obtained through $LiNH_2$ nitrogen source showed small amounts of carbon. Hydrogen was found in all the samples in the range of 1.34 to 1.73%. Nitrogen was found in the range of 7.93-10.80 % in the samples obtained through the $LiNH_2$ route. The theoretical percentage of nitrogen in Mn_3N_2 is 14.5%. So the observed compositions were all nitrogen deficient.

Table 3.2: Elemental analysis for the samples obtained through $LiNH_2$

Temperature (°C)	%C	%H	%N	Composition
350	<0.10	1.46	10.33	$Mn_3N_{1.45}C_{0.05}H_{2.7}$
400	0.32	1.34	10.80	$Mn_3N_{1.45}C_{0.05}H_{2.51}$
450	0.31	1.31	10.68	$Mn_3N_{1.43}C_{0.05}H_{2.5}$
500	0.79	1.41	9.78	$Mn_3N_{1.3}C_{0.12}H_{2.6}$
550	2.02	1.73	7.93	$Mn_3N_1C_{0.95}H_{3.24}$

Thermogravimeteric analysis (Fig. 3.4) shows two step mass losses. During the first step at temperature below 400 °C the mass loss could correspond to residual amide group elimination. Mass loss above 700 °C corresponds to nitrogen loss from nitride samples.[32] The mass loss in the first step is greater in the samples obtained at 350 °C due to the presence of amide groups in the samples; the samples heated at higher temperature showed less mass loss at this temperature. As the sample anneals and crystallises the NH_x groups are lost. A rapid mass loss above 700 °C in the sample obtained at 550 °C could be attributed to carbon loss that is higher in the sample.

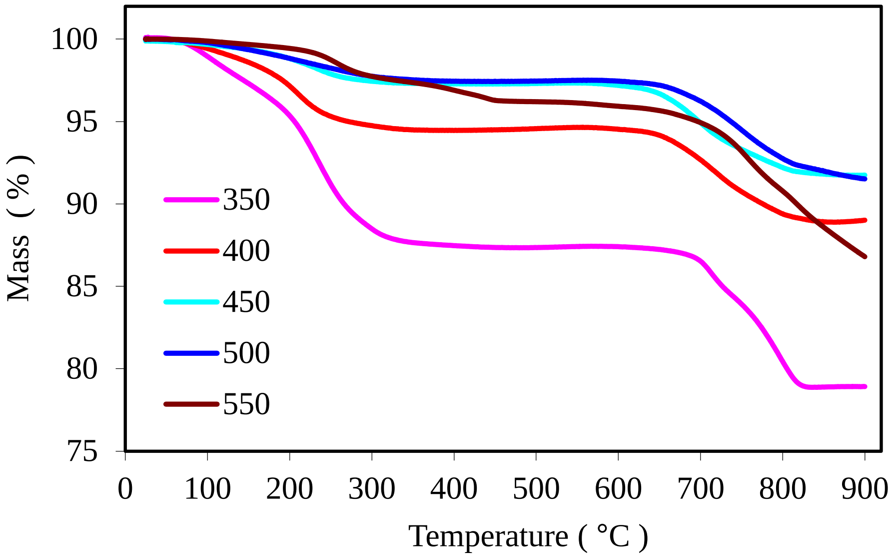

Figure 3.4: TGA curves for the samples of Mn_3N_2 produced at given temperatures.

IR spectra (Fig. 3.5) show absorption peaks at 3480-3490 cm^{-1} that correspond to residual ν-(NH).[32] and 1650-1700 cm^{-1} δ-(NH_2).[32, 33] Stretching for ν-(C-H) is found at 2890 to 2980 cm^{-1}, 1440 to 1270 cm^{-1} ν-(C-N). Ammonia is clearly evident in such reactions; hence solvent/nitride surface reaction may occur at higher temperature. Metal nitrogen peak is observed at ~ 650 cm^{-1}. C-H stretching is more prominent as the solvent decomposition increases at higher temperature that is consistent with higher C content seen in analytical data.

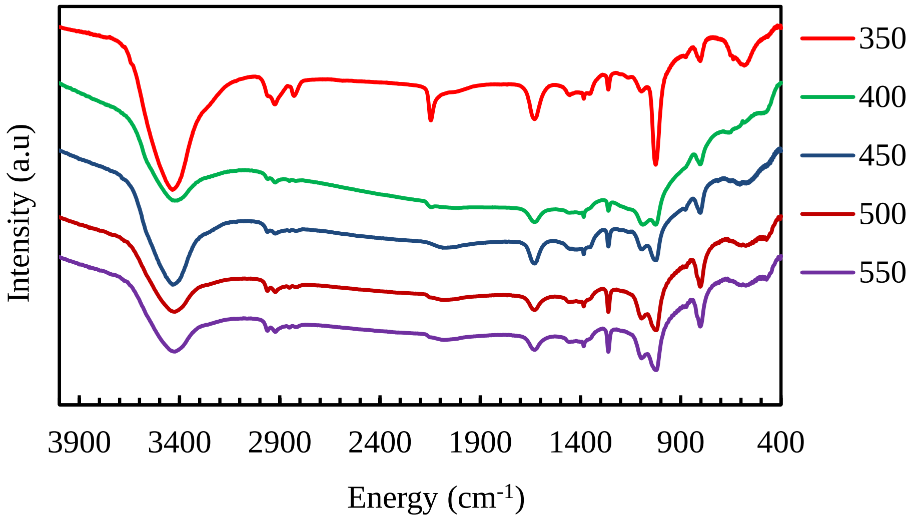

Figure 3.5: IR spectra for Mn_3N_2 samples obtained at the given temperatures (°C)

Samples for TEM (Fig. 3.6) were made by 4 hours ultrasonic dispersion in dry methanol in a sample vial and deposition on a carbon coated Cu grid. Two grids for each sample were prepared in a way that two drops from the top region on the first or two drops from the bottom region of sample suspension were poured on the 2nd grid with the help of a pipette to ensure the random sampling. Further the images were taken from various parts of the grid for each sample. Nanotube structures 20 to 120 nm in length and ~20 nm in diameter were found in the sample synthesised at 350 °C, while spherical particles of ~ 30-40 nm size were observed at 400 °C and above. Images show the particle agglomeration at higher temperature. Increasing the surface area and electrical conductivity of the desired material (e.g. nanotubes or nanorod morphology) may increase the specific capacitance of the material.[34] Calculated crystallite size from the Rietveld refinements (Table 1) are higher than the particle sizes seen in the TEM images. That could be due to the change in the peak shape from uniform strains in the manganese nitride grains.

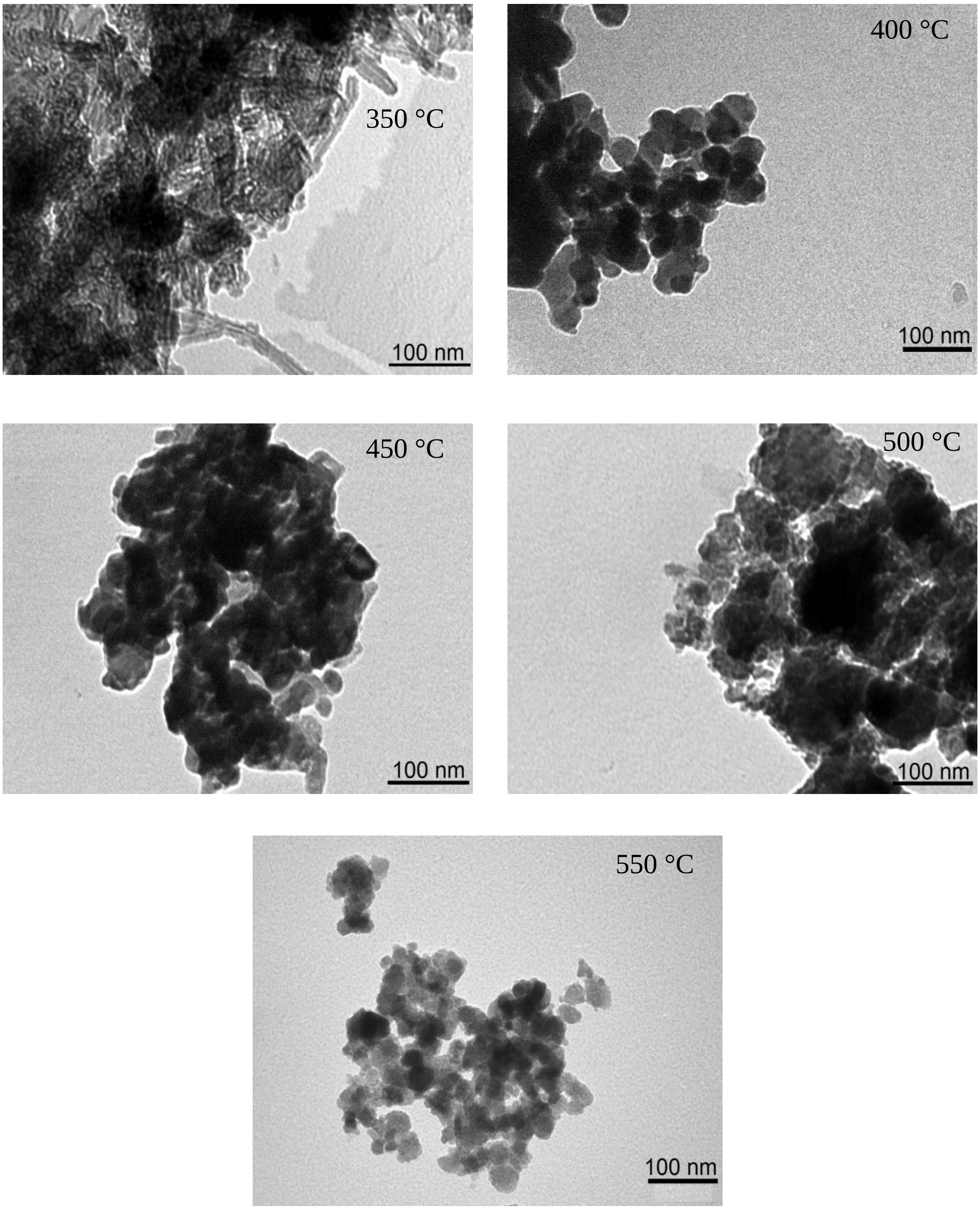

Figure 3.6: TEM images for Mn_3N_2 samples at the given temperatures

High resolution images and electron diffraction (Fig. 3.7) were also carried out to analyse the detail morphology of one of the Mn_3N_2 samples obtained at 350 °C. The image taken for the tube like Mn_3N_2 structures on 20 nm scale (Fig. 3.7 A) shows the network of interconnected of manganese nitride tubes. The selected area electron diffraction pattern of a region containing only this type of structure showed rings corresponding to the major diffraction peaks of Mn_3N_2. These are broad due to overlap between more than one reflection and not all the reflections are observed, presumably reflecting the partial alignment of the particles that are lying flat on the TEM grid. A single crystal of manganese nitride (Fig. 3.7 B) of ~ 3 μm in size is also found to exist in the sample; no such a crystal was found in any other TEM grid after multiple repeats in the sample or looking the at the other parts of the grid. Carbon nanoparticles were also observed (Fig. 3.7 C) in some parts of the TEM grid; the HRTEM shows the d-spacing is consistent with graphite fringes.[35]

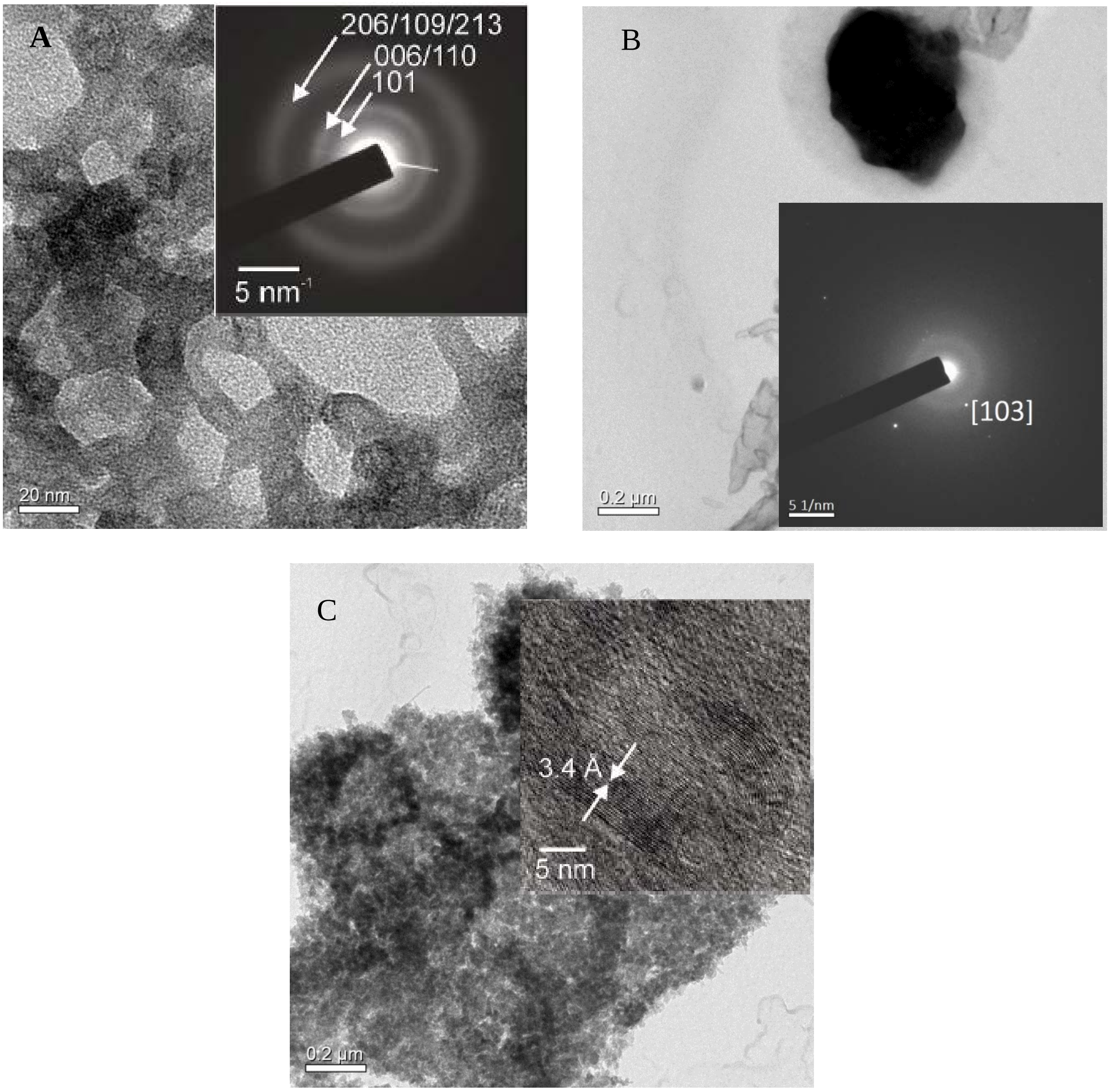

Figure 3.7: TEM image of Mn_3N_2 obtained at 350 °C; tube like structure and electron diffraction (A); manganese nitride single crystal and its electron diffraction (B); carbon nanoparticles and (C); HRTEM.

Surface area analysis shows the surface area (table 3.3) of the material decreasing with increasing reaction temperature, as the agglomeration of the particles occurs due to fast reaction of $LiNH_2$ and $MnCl_2$ at high temperature. The hysteresis loops (Fig. 3.8) show type IV isotherm, typical of the existence of randomly connected spherical pores. The loop is narrow in the samples with less surface area. At higher pressures the slope shows increased uptake of adsorbate as pores become filled. Pore diameter of all the samples lies in the mesoporous range. Samples obtained at 500 °C and below have an ordered mesoporous texture, while multiple pore sizes are observed at 550 °C (Fig. 3.9). Studies of activated carbons with different pore sizes in various electrolytes, show the capacitance increase was limited even for the most porous samples with no linear relationship between the SSA and the capacitance.[36, 37] It was identified that the pore size distribution larger than the size of two solvated ions could be a way to improve the energy density and power capability. Error estimation for the surface area values was found to be ± 1 $m^2\ g^{-1}$ and PSD was ±1 Å.

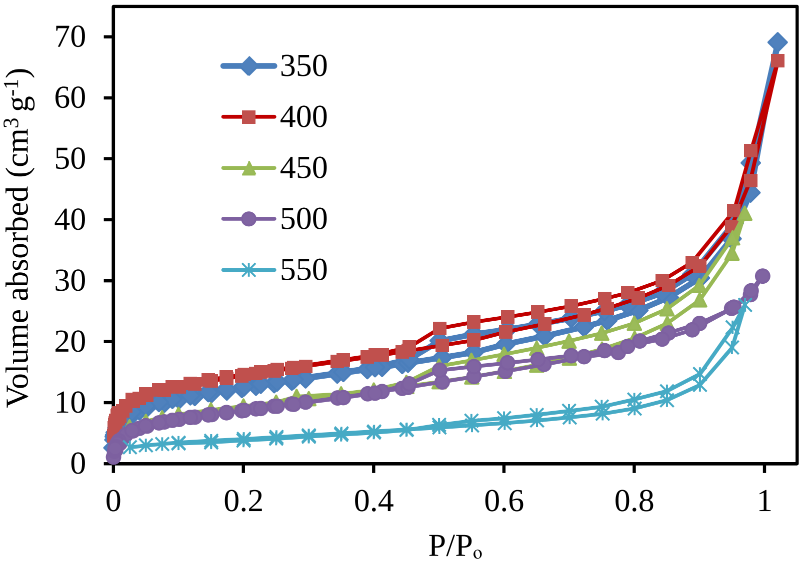

Figure 3.8: N_2 adsorption/desorption isotherms for the Mn_3N_2 samples obtained at the given temperatures (°C)

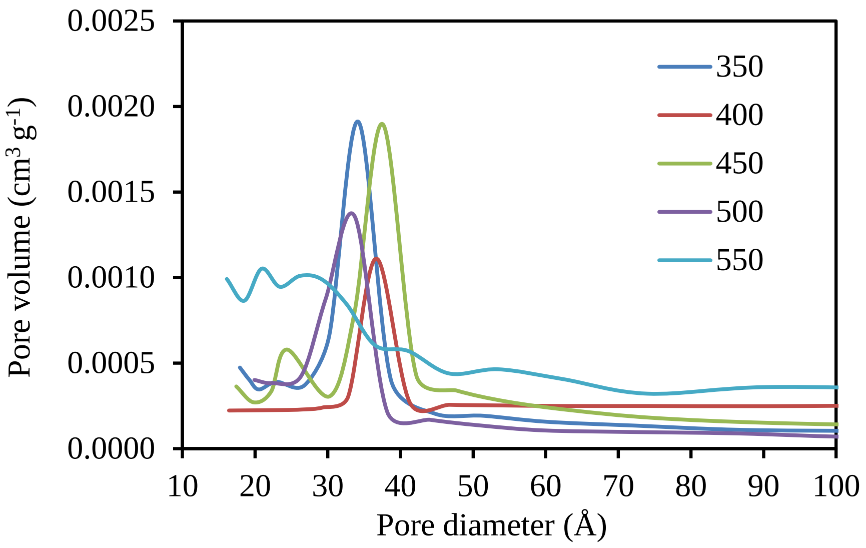

Figure: 3.9: N$_2$ BJH pore size distribution for the Mn$_3$N$_2$ samples obtained at the given temperatures (°C)

Table: 3.3: Surface area S_{BET} measurement and pore diameter (PD) of Mn$_3$N$_2$ samples.

Temperature (°C)	S_{BET} (m^{2}g^{-1})	PD (Å)
350	44	34
400	46	36
450	32	37
500	31	33
550	13	20 to 54

Raman spectra (Fig. 3.10) were collected in the frequency range of 2000 to 400 cm^{-1}, using an He-Ne laser with a wavelength of 632.8 nm. Raman was carried out to look for the presence of graphitic carbon that is seen in the TEM studies. Raman spectra for graphitic carbon show peaks for D or G band at 1350 or 1580 cm^{-1}, respectively.[38, 39] The single peak at ~ 650 cm^{-1} can be referred to Mn-N stretching as has been observed in high pressure studies of TiN, MoN and VN.[40] The peak is more broad and intense as the temperature increased suggesting the increasing structural stability. The optical intensity of the spectrum increased with decreasing of nitrogen content while could be due to less vibration of the lighter N atom in the nitrogen deficient samples, as observed in case of TiN.[41] A He-Ne laser with a wavelength of 632.8 nm was used for species excitation.

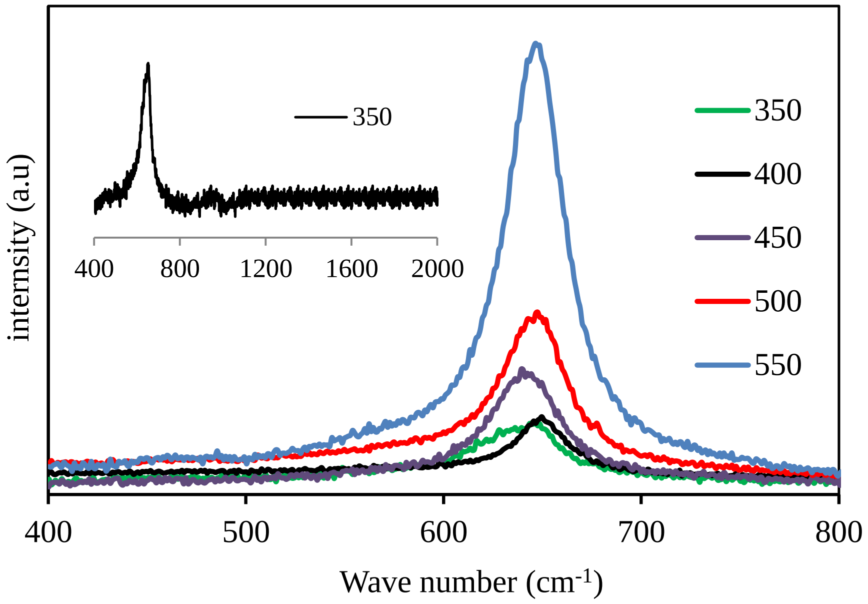

Figure 3.10: Raman spectra obtained for the Mn_3N_2 samples obtained at the temperatures (˚C) given in the figure legend, the inside graph show the whole range data for a sample obtained at 350 °C.

3.4 Capacitance measurement

The capacitance of the material was measured through cyclic voltammetry using a three electrode cell. A Hg/HgO electrode was used as a reference electrode, while a thin platinum gauze of 0.005 mm thickness was used as a counter electrode. A high surface area counter electrode is used to ensure it has a higher capacitance than the working electrode capacitance that limits the current passed. The working electrode was made by disc or ink electrode method. The procedures of making electrodes are discussed in their respective section. The cell used for electrochemical analysis is given in figure 3.11. The electrolyte was degassed to remove excess oxygen by bubbling nitrogen for 30 minutes through the solution. A blanket of nitrogen was maintained over the electrolyte surface while acquiring the voltammograms.

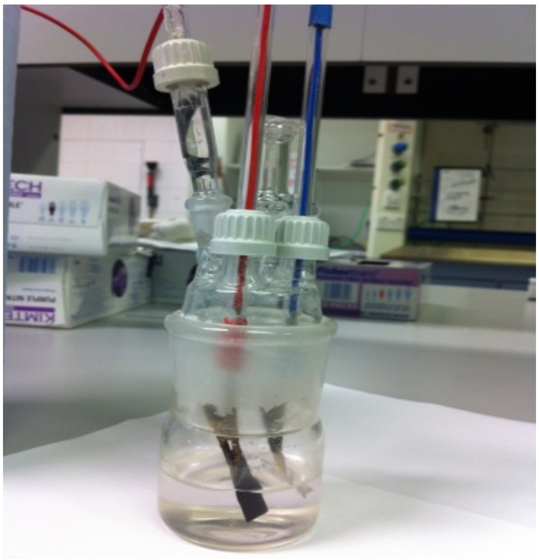

Figure 3.11: Three-electrode cell used for electrochemical processing

A number of different working electrode assembly methods were tried with Mn_3N_2 active material, both as composite discs with carbon and a binder, and inks coated onto various current collectors. The understanding developed here was then carried out through to other active materials.

3.4.1 Disc electrode method

Disc electrodes were prepared by grinding the electrode material (75%) with carbon black (20%) and Teflon (5%), and rolled under a high pressure steel roller to a thickness of 10 µm sheets. Sheets were then cut into round electrodes with 1 cm diameter, and dried overnight at 120°C under vacuum. Electrodes were constructed by pressing them into platinum gauze for electronic conduction. An average of ~ 18 mg of the active material was incorporated into the discs. The shape of the voltammograms (Fig. 3.12) largely deviated from the standard rectangular shape expected for a double layer capacitor, where could be due to the poor ionic conduction of electrolyte ions through the electrode surface with the electrode surface covered with the Teflon binder in the rolling process of making electrode sheets under high pressure. The performance of electrodes as compared to the mass loaded is very low, though a large stability window of 1.6 V is observed except for the sample obtained at 550°C. An average capacitance of 3 F g^{-1} was measured for all the samples at 100 mV s^{-1} using disc-electrodes. As it was believed that most of the electrode surface in not exposed to the proton adsorption process and that is one of the reasons for low electrochemical activity of the active material, the idea of disc electrodes was not investigated further.

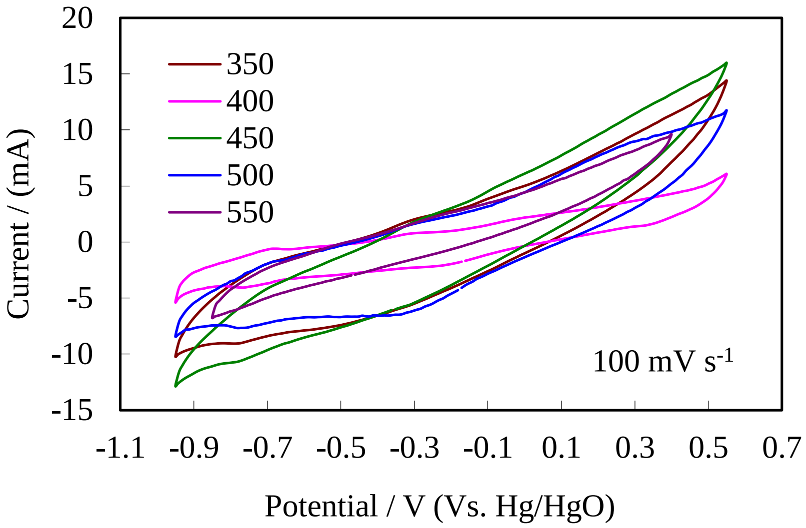

Figure 3.12: Cyclic voltammograms obtained for disc electrodes of Mn_3N_2 samples at the given temperatures (°C) in 1 M KOH.

3.4.2 *Ink electrode method*

Electrode ink was prepared by grinding together Mn_3N_2 (75 wt %) and acetylene black (20 wt %). Polyvinylidene fluoride (PVDF) (5 wt %) was fully dissolved into the desired volume of cyclopentanone, (CP) by stirring the solution for 2 hours, (1.5 ml per 100 mg of electrode material). The mixture of Mn_3N_2 and carbon black was added to PVDF solution and stirred overnight to obtain the electrode ink. CP is one of the few low-toxicity solvents capable of dissolving PVDF. Potential stability of various current collectors Carbon rod, nickel or titanium foil were examined for their use as the substrate for casting electrode ink. The procedure adopted for electrode preparation is discussed below.

3.4.3 Choice of current collector for ink electrodes

The current collector is responsible for the transfer of electric charge to and from the electrode material and consequently should have high electrical conductivity and low interfacial electrical resistance to the active electrode material. Additionally, the current collector must be passive in contact with the electrolyte; provide structural robustness for the electrode; be thin enough to minimize current collector mass; and be flexible to allow handling and assembly into different device topologies.[42]

3.4.4 Ink cast carbon rod electrode

A carbon rod of 4 cm length (Fig. 3.13) was used as the working electrode. 1.5 cm of the rod was coated with electrode material by dipping the rod for a duration of 2 minutes into electrode ink prepared by the above procedure. The coated carbon rod was left to dry overnight at 120 °C under vacuum in a Schlenk tube to remove all traces of the solvent. Cyclic voltammograms for the blank carbon rod were collected first to establish its potential window (Fig. 3.14). A Mn_3N_2 sample obtained at 350 °C was used for this purpose. 2.5 mg of the electrode material was found to be deposited onto the carbon rod.

Figure 3.13: Carbon rod coated with Mn_3N_2 electrode ink.

The carbon rod was observed to be oxidised above 0.4 V or reduced below - 0.6 V (Fig. 3.14). Oxidation peaks can be seen at – 0.1 and – 0.45 V and a reduction peak at – 0.45 V.

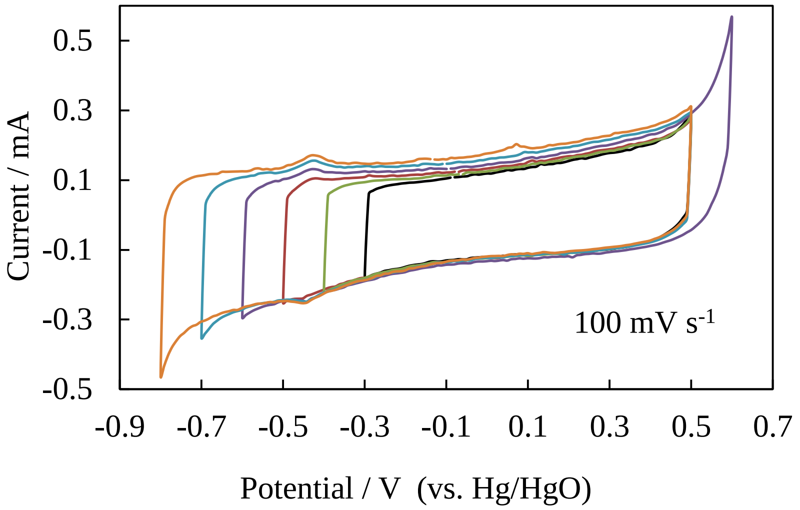

Figure 3.14: Stability windows for blank carbon rod as a current collector in 1M KOH

Cyclic voltammograms (Fig. 3.15) for ink cast carbon rod electrodes were obtained in 1 M KOH against a Hg/HgO reference electrode at the scan rates of 100, 25 and 2 mV s^{-1}. A potential window of – 0.9 to 0 was chosen after observing the oxidation and reduction behaviour of electrode material at the scan rate of 100 mV s^{-1}. No oxidation or reduction peaks for the electrode material are observed in the voltammograms at any potential. Comparing the amount of current passed through the ink cast (Fig. 3.15) and blank carbon rod (Fig. 3.14) no further attempt is made to study the efficacy of active material coated over carbon rod. The low capacitance value of 1.5 F g^{-1} at 100 mV s^{-1} is also a reason for no interest in carbon substrate.

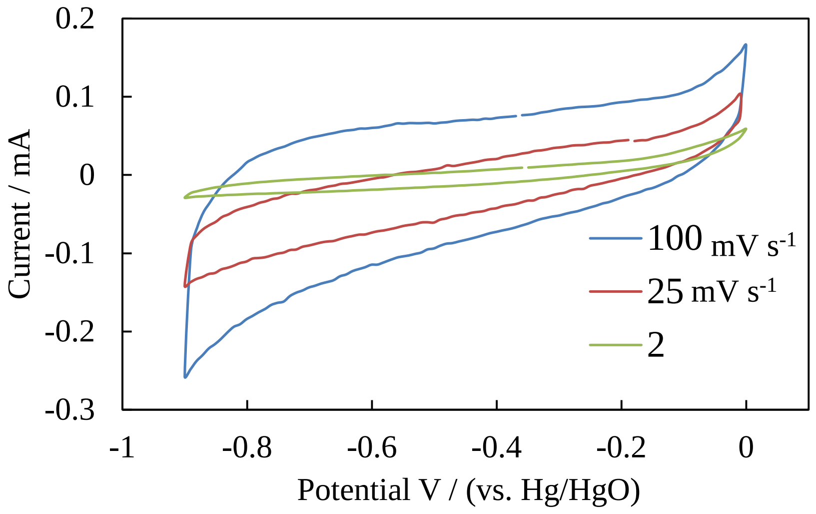

Figure 3.15: Voltammograms for coated carbon rod electrode in 1M KOH at the given scan rates

3.4.5 Ink cast nickel foil electrodes

Nickel foil of 0.05 mm thickness was used for making ink film working electrodes (Fig. 3.16). The surface of the metal foils was cleaned with sandpaper and the surface dust was removed with ethanol-wettened tissue. The foil was left to dry in open air at room temperature. Electrode inks were made through the procedure given above. The foil was cut in to small pieces of size 1.5 × 2.5 cm. Electrode ink was poured over the nickel foil covering 1.5 × 1.5 cm of area using a pipette. Electrodes were left to dry in air for a few hours and finally overnight under vacuum at 120 °C. The foil was weighed before film deposition and after drying the film. ~1.6 mg of the electrode material was weighed on the substrates after drying.

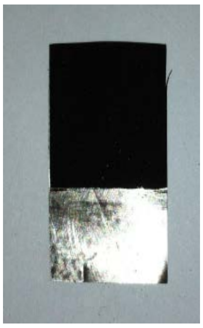

Figure: 3.16: Mn_3N_2 ink film over titanium current collector

A reference for the current collectors, blank Ni foils were obtained by running in 1M KOH vs Hg/HgO reference electrode at 100 mV/s (Fig. 3.17). Blank Nickel foil was observed to be stable between - 0.55 to 0.6 V of potential window. Nickel foil showed oxidation peaks at -0.3 and – 0.6 V, and a reduction peak at -0.15 V, while covering larger charge area than any other substrate studied here.

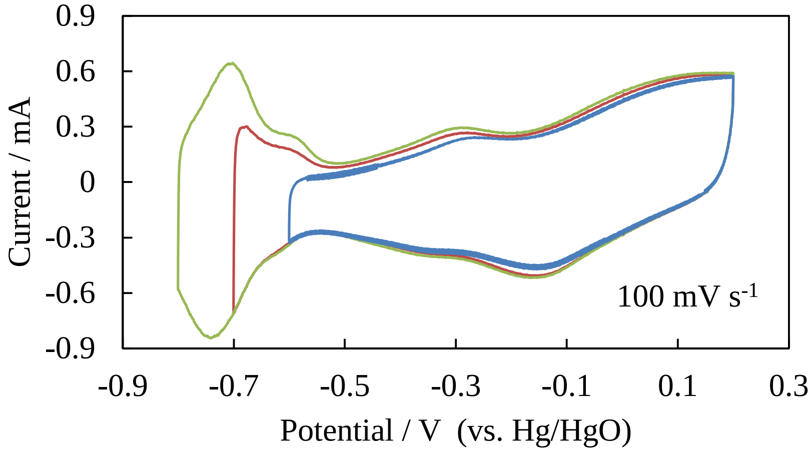

Figure 3.17: Potential windows for blank Ni foil as a current collector in 1 M KOH.

Ink cast nickel foil electrodes were run at 100 and 25 mVs^{-1} in a potential window of – 0.65 and 0.55 V (Fig. 3.18). Prominent oxidation peaks at 0, 0.2 and 0.45 V and reduction troughs are seen at 0.4 V. Redox behaviour at – 0.2 V is supposed to come from nickel foil as observed in voltammograms obtained for blank foil, which is reduced after multiple cycling. The capacitance of Mn_3N_2 was observed to fall as the number of cycles increased, demonstrating the instability of the active material in electrochemical processing. The maximum capacitance of 91 F g^{-1} was calculated at scan rate of 25 mV s^{-1} in 10th cycle while the lowest of 36 F g^{-1} in 100th cycle at a 100 mV s^{-1}. Capacitance is reduced from cycle 10 to 100 by 42 and 28 % at 100 and 25 mV s^{-1} scan rates, respectively. Nickel substrate was not used for further Mn_3N_2 samples due to appearance of redox features of nickel foil itself. Capacitances measured for the nickel foil ink deposited electrode are given in table 3.4.

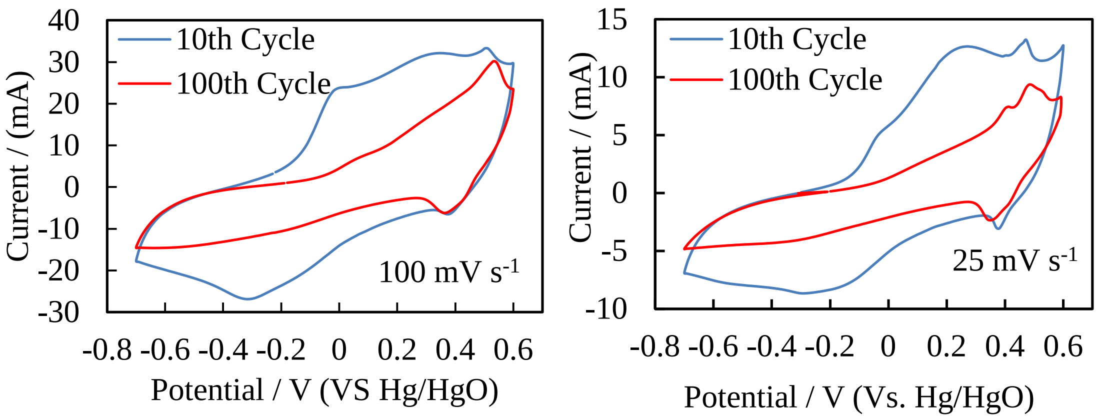

Figure: 3.18: Voltammograms for Mn_3N_2 at 350 °C deposited over nickel foil, in 1 M KOH.

Capacitance of Mn_3N_2 samples on nickel foil (Table 3.4) substrate at 100 and 25 mV s^{-1}. Capacitance has been decreased by 42 and 32 % at 100 and 25 mV s^{-1} from 1^{st} to 100^{th} cycle number.

Table 3.4: Capacitance of Mn_3N_2 sample obtained at 350 °C on nickel foil substrate.

Scan rate mV s^{-1}	Cycle number	Capacitance F g^{-1}
100	10	62
100	100	36
25	10	91
25	100	65

3.4.6 *Ink cast titanium foils electrodes*

Titanium foils with a similar thickness were used as the current collector. Ink film deposition and drying of electrode procedures were also the same as for nickel electrodes. Titanium foil was chosen as the current collector for the casting over electrode ink, as no redox features are observed in voltammograms (Figure 3.19) for titanium foil, and it is stable in a large voltage range of 0.4 to -0.6 V, with a negligible amount of charge area.

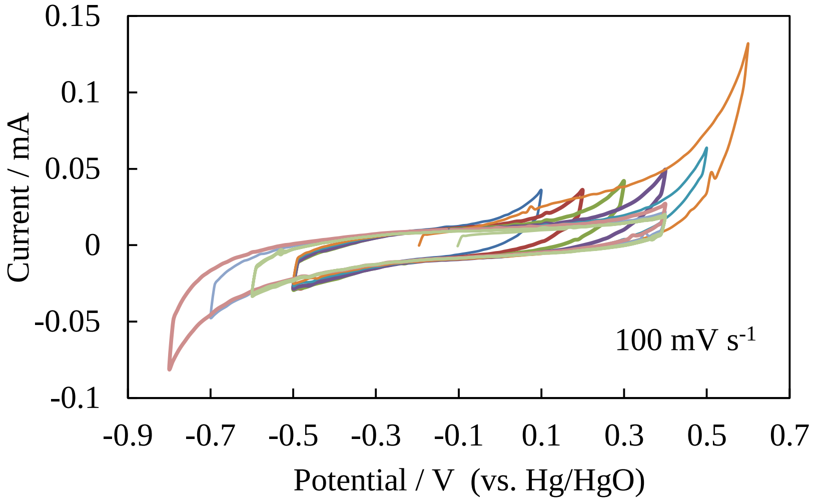

Figure 3.19: Potential windows for blank Ti foil as a current collector in 1M KOH.

Electrochemical test was carried out for all the Mn_3N_2 samples in a potential window range of – 0.6 to 0.3 V. Capacitances measured for manganese nitride samples in 1 M KOH against Hg/HgO reference electrode are given in table 3.5. Sample obtained at 350 °C show the highest capacitance of 299 F g^{-1} at 2 mV s^{-1}. Sample obtained at 550 °C has been found relatively more stable than the other samples in electrochemical processing. Samples obtained at lower temperature seems to possess unstable structure due to which the surface deterioration in electrochemical reaction is relatively high at lower scan rates. An electrode of Mn_3N_2 sample obtained at 550 °C was also tested in 0.5 M of H_2SO_4. The electrode material was found highly unstable in the potential window of 0.9 as for basic electrolyte. Capacitance with acidic electrolyte for this sample was measured as 1.23 Fg^{-1} at 100 mV s^{-1}. Acidic electrolyte was not used for further electrochemical testing due to instable behaviour of Mn_3N_2 voltammograms and low capacitance value.

Cyclic voltammograms for the Mn_3N_2 samples obtained at 350 - 550 ºC shown in figures 3.20 – 3.24 respectively, were obtained in 1 M KOH with 1.6 mg of active material loading over 1.5 × 1.5 cm area of current collector.

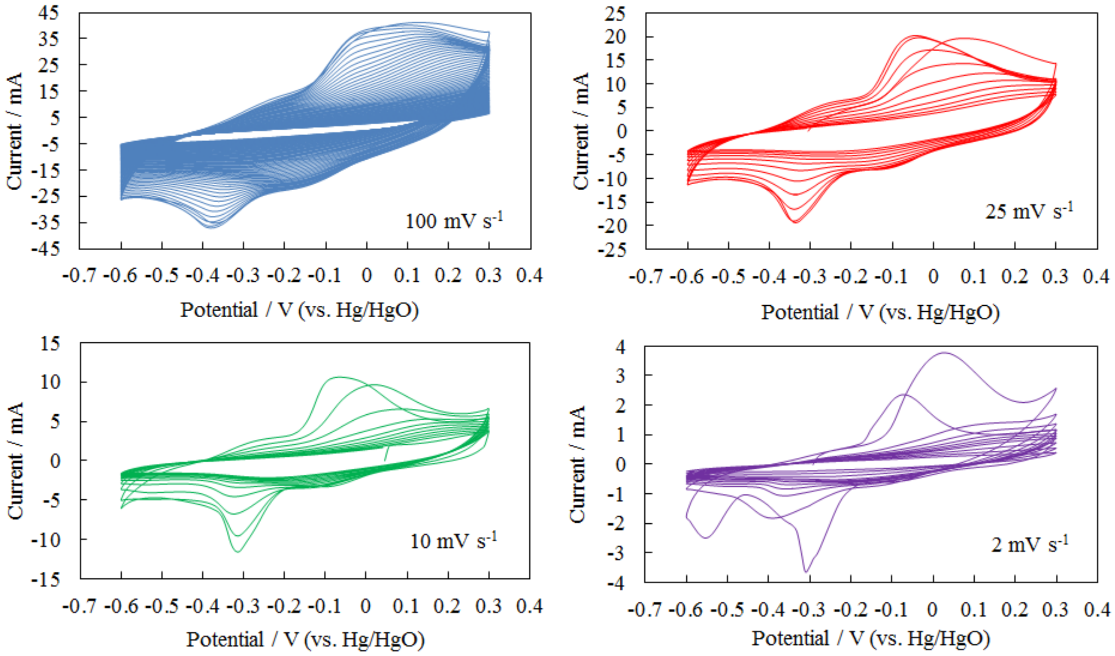

Figure 3.20: Voltammograms for Mn_3N_2 sample obtained at 350 °C

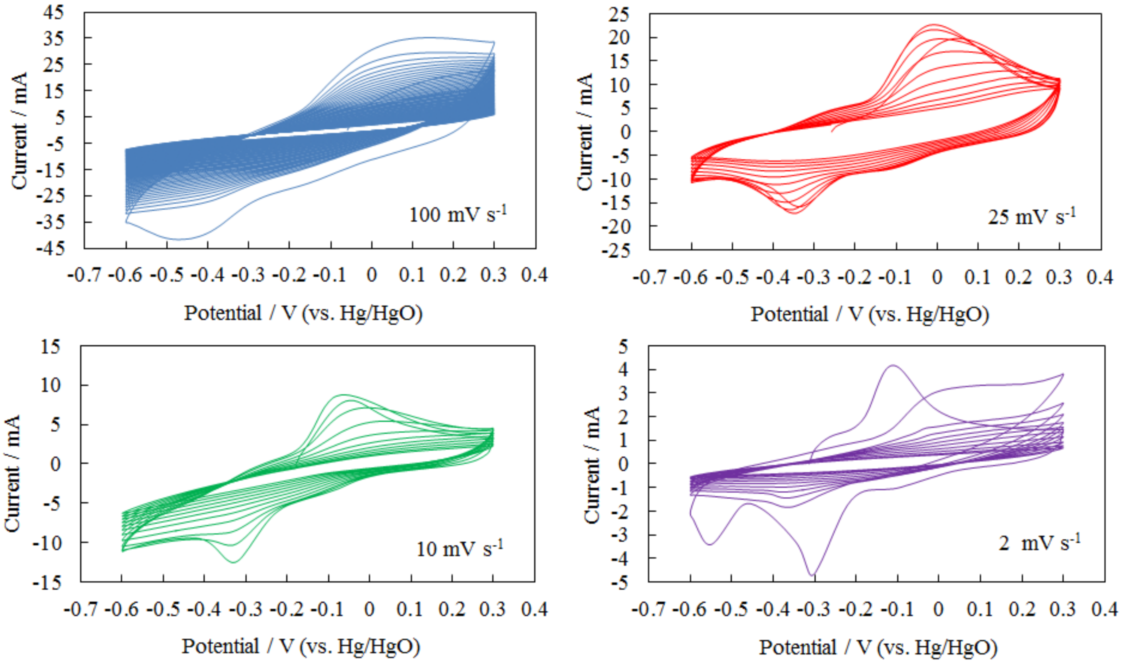

Figure 3.21: Voltammograms for Mn_3N_2 sample obtained at 400 °C

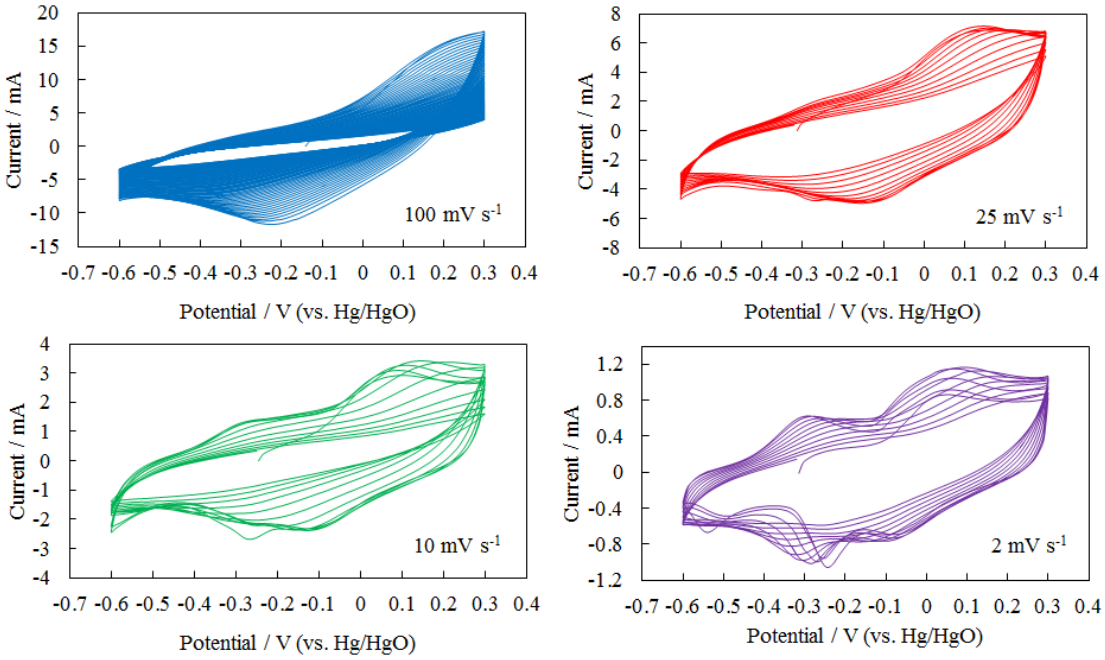

Figure 3.22: Voltammograms for Mn_3N_2 sample obtained at 450 °C

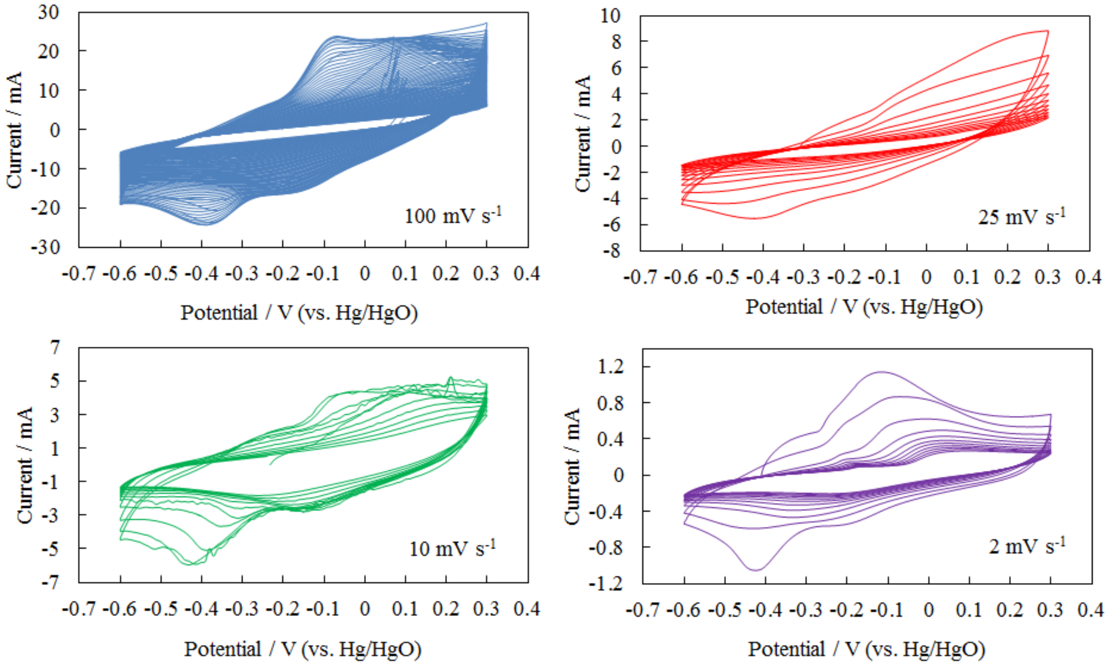

Figure 3.23: Voltammograms for Mn_3N_2 sample obtained at 500 °C

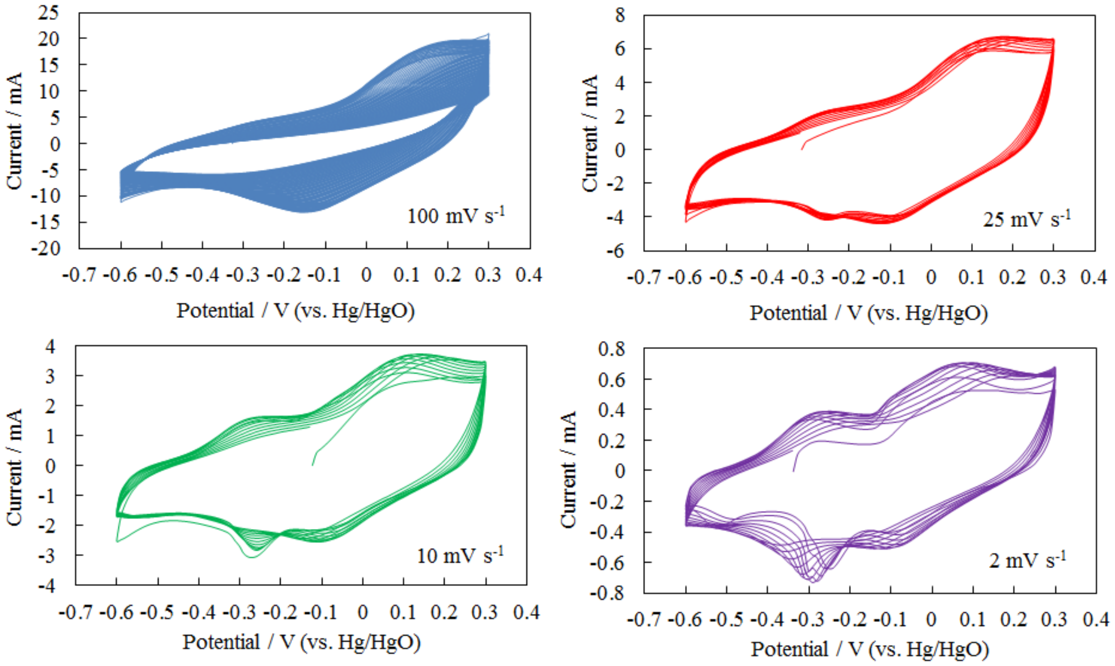

Figure 3.24: Voltammograms for Mn_3N_2 sample obtained at 550 °C

Table 3.5: Specific capacitance F g^{-1} of Mn_3N_2 samples obtained from the solvothermal reaction of $MnCl_2$ and $LiNH_2$ at the given temperatures.

Scan rate (mV s^{-1})	**100**			**25**		**10**		**2**	
Scan number	**1**	**10**	**100**	**1**	**10**	**1**	**10**	**1**	**10**
350 °C	130	98	17	205	74	229	54	299	91
400 °C	121	82	21	191	89	215	94	261	64
450 °C	70	57	16	115	70	140	57	180	116
500 °C	87	80	17	96	25	121	51	132	51
550 °C	66	64	30	79	77	111	107	123	118

A graph between capacitance and scan number (Fig. 3.25) shows the process of surface degradation of Mn_3N_2 at 100 mV s^{-1} (100 cycles, data from table 3.5). The rate of capacitance drop becomes slower after 30th cycle in all the samples and steady after 40 cycles. The capacitance drop with cycling is less in the sample obtained at 550 °C than rest of the samples at any temperature, where Mn_2N crystallises out as the second phase. We may assume that, producing high surface area, phase pure Mn_2N could be of interest for the supercapacitor applications.

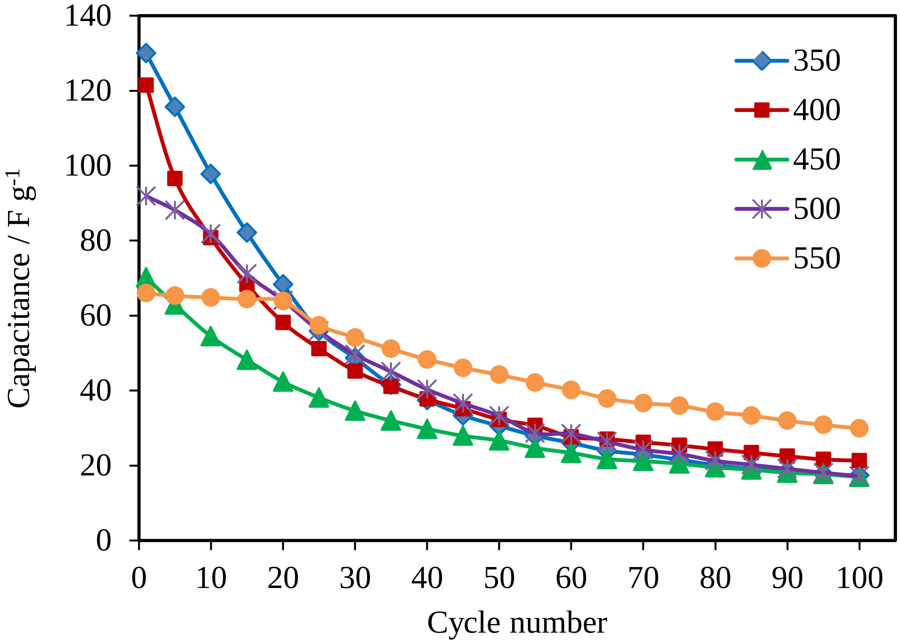

Figure 3.25: Plot show capacitance drop with cycle number of Mn_3N_2 electrodes at scan rate of 100 mV s^{-1} in 1 M KOH vs Hg/HgO reference electrodes. Figure legend shows the temperature (°C) at which the samples were obtained.

Plot between capacitance and scan rate shows the capacitance was higher at slower scan rates in all the samples (Fig. 3.26). Capacitance values were calculated at first scan at each scan rate, which are given in the table 3.5.

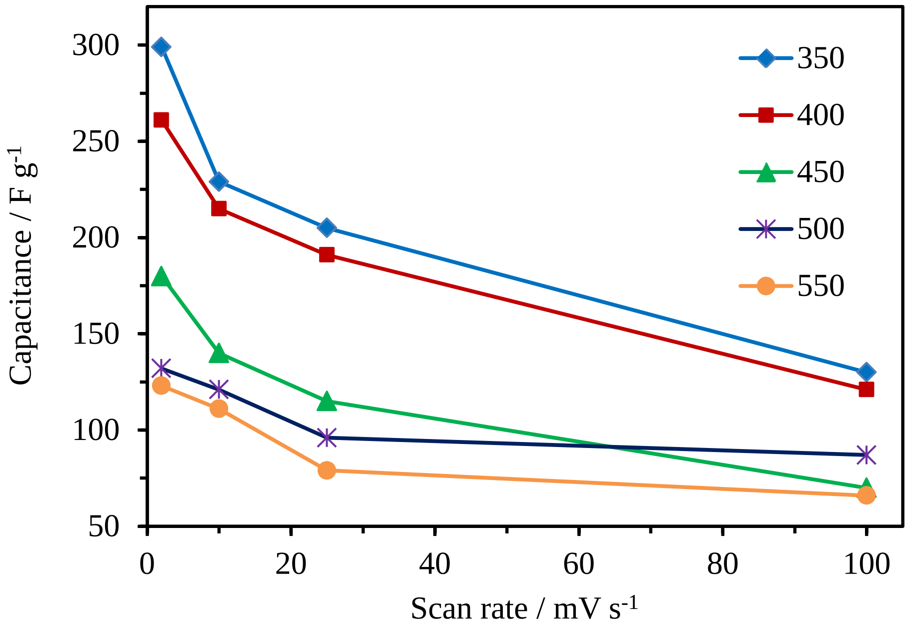

Figure 3.26: Variation of specific capacitance with scan rate for the Mn_3N_2 electrodes at the given temperatures (°C).

Cyclic voltammograms for the Mn_3N_2 samples are found electrochemically unstable as the scan rate decreases. Redox peaks (Table 3.6) become more intense at slower sweep rate, the intensity reduces with cycle number. Most of the redox features at slower scan rate eventually becomes flatter after10th cycle, show no more ion absorption taking place. The oxidation peak at – 0.1 V moves towards the cathodic end by the factor of 0.2 V at all the scan rates. 1st and 2nd redox potentials are mostly consistent in all the samples and scan rates.

Table 3.6: Redox potentials of Mn_3N_2 samples at various scan rates (--) no features

	Redox potentials (V), at given scan rate (mV s^{-1})							
Scan rate (mV s^{-1})	**100**		**25**		**10**		**2**	
	Ox.	*Red.*	*Ox.*	*Red.*	*Ox.*	*Red.*	*Ox.*	*Red.*
350 °C	0.1	- 0.15	- 0.3	- 0.1	-0.3	- 0.1	- 0.1	- 0.35
	- 0.2	- 0.35	- 0.1	- 0.32	-0.1	- 0.32		
400 °C	0.1	- 0.19	--	0.3	--	- 0.29	--	--
450 °C	0.15	- 0.18	0.15	- 0.18	0.1	- 0.1	0.1	- 0.1
					- 0.28	- 0.28	- 0.28	- 0.28
500 °C	0.1	- 0.38	- 0.1	- 0.35	- 0.1	- 0.35	- 0.1	- 0.35
550 °C	0	- 0.38	0.1	- 0.1	0.1	- 0.1	0.1	- 0.1
			- 0.28	- 0.25	- 0.28	- 0.25	- 0.28	- 0.25

3.5 Conclusions

Reaction of $LiNH_2$ and $MnCl_2$ yields phase pure tetragonal Mn_3N_2 up to 500 °C, while small Mn_2N phase impurity is observed at 550 °C. Samples are found to be contaminated with small amount of carbon and hydrogen. Carbon contamination increase at high temperature as the solvent decomposition increases. Samples are more nitrogen deficient at higher temperature. TGA shows two step mass losses, amide below 400 °C and N above 650 °C and some of the carbon. IR spectra are consistent with product composition. TEM images show nanotubes of manganese nitrides at 350 °C that is confirmed with electron diffraction data. Manganese nitride single crystal on micro scale is also observed. Fringes with d-spacing of 3.4 Å confirmed the presence of carbon nano-particles in this sample, however raman spectra didn't show any peak for graphitic carbon. Nano-particles in the size range of 30-40 nm were observed at all the other temperature. Capacitances of the material were tested using cyclic voltammetry in a basic electrolyte. Disc electrodes were found with poor efficiency due to the binder covering the electrode surface. Electrochemical behaviour of various current collectors in 1 M KOH was examined. Poor electronic conduction of carbon electrode and chemical interaction of nickel foil with electrolyte makes these current collectors unsuitable for our material. Cyclic voltammograms for the electrode ink deposited over titanium show the redox nature of the manganese nitride in aqueous electrolyte. The redox process is largely irreversible as the redox features gets flatter with the cycle number, with decrease of capacitance. Highest capacitance of 225 F g^{-1} is observed in the sample obtained at 350 °C at 2 mV s^{-1}. Capacitance drop up to 10th cycle is more prominent at lower scan rates. Running electrodes at 100 mV s^{-1} for 100 cycle show the capacitance drop becomes very slower over 30 cycles and most of capacity is lost, whereas the sample obtained at 550 °C shows a stable capacitance than rest of the samples at any scan rate.

3.6 References

1. F. Lihl, P. Ettmayer, A. Kutzelnigg and Z. Metallk, 1962, **53**, 715.
2. O. Prelinger, *Montash. Chem.*, 1894, **15**, 391.
3. M. Mekata, J. Haruna and H. Takaki, *J. Phys. Soc. Jpn.*, 1968, **25**, 234.
4. M. Eddine, *Acta Cryst.*, 1911, **33**, 2696.
5. K. Suzuki, T. Kaneko, H. Yoshida, Y. Obi, H. Fujimori and H. Morita, *J. Alloys. Cmpds.*, 2000, **306**, 66.
6. A. Leineweber, R. Niewa, H. Jacobs and W. Kochelmann, *J. Mater. Chem.*, 2000, **10**, 2827.
7. W. J. Takei, R. R. Heikes and G. Shirane, *Phys. Rev.*, 1962, **125**, 1893.
8. M.N. Eddine and E.F. Bertaut, *Solid State Commun.*, 1977, **23**, 147.
9. M.N. Eddine and E.F. Bertaut, *Acta Cryst.*, 1977, **B 33**, 2696.
10. W.J. Feng, N.K. Sun, J. Du, Q. Zhang, X.G. Liu, Y.F. Deng and Z.D. Zhang, *Solid State Commun.*, 2008, **148**, 199.
11. M. Mekata, *Phys. Soc. Jpn.*, 1962, **17**, 796.
12. A. Leineweber, H. Jacobs and W. Kochelmann, *J. Alloys Cmpds.*, 2004, **368**, 229.
13. J. Choi and E. G. Gillan, *Inorg. Chem*, 2009, **48**, 4470.
14. G. Kreiner and H. Jacobs, *J. Alloys Cmpds.*, 1992, **183**, 345.
15. J. C. Fitzmaurice, A. L. Hector and I. P. Parkin, *J. Chem. Soc., Dalton Trans.* , 1993, 2435.
16. M. Toupin, T. Brousse and D. Belanger, *Chem. Mater.*, 2004, **16**, 3184.
17. S. C. Pang, M. A. Anderson and T. W. Chamman, *J. Electrochem. Soc.*, 2000, **147**, 444.
18. W. Wei, X. Cui, W. Chen and D. G. Lvey, *Chem. Soc. Rev.*, 2011, **40**, 1697.
19. D. Choi, G. E. Blomgren and P. N. Kumta, *Adv. Mater.*, 2006, **18**, 1178.
20. E. G. Gillan and R. B. Kaner, *Inorg. Chem.*, 1994, **33**, 5693.
21. A. L. Hector and I. P. Parkin, *Polyhedron*, 1995, **14**, 333.
22. I. P. Parkin and A. T. Rowley, *J. Mater. Chem.*, 1995, **5**, 909.
23. A. L. Hector and I. P. Parkin, *J. Mater. Chem.*, 1995, **7**, 1728.
24. R. A. Janes, M. Aldissi and R. B. Kaner, *Chem. Mater.*, 2003, **15**, 4431.
25. B. Mazumder, Pietro Chirco and A. L. Hector, *Inorg. Chem.*, 2008, **47**, 9684.

26. M. J. Radler, J. B. Cohen, G. P. Sykora, T. Mason, D. E. Ellis and J. J. Faber, *J. Phys. Chem. Sol.*, 1992, **53**, 141.

27. R. B. Von-Dreele and A. C. Larson, Generallized structure analysis system, Los Alamos National Laboratory, NM87545, USA, December 2002 release.

28. D.A. Fletcher, R. F. McMeeking and D. Parkin, *J. Chem. Inf. Comput. Sci.*, ICSD accessed via The United Kingdom Chemical Database Service, 1996,, **36**, 746.

29. M. Hasegawa and T. Yagi, *J. Alloys and Cmpds.*, 2005, **131**, 403.

30. S.I. Ping-Zhan, J. Wei, W. Hai-Xia, Z. Min, G.E. Hong-Liang, C. Chul-Jin and L.E.E. Jung-Goo, *Chin. Phys. Lett.*, 2012, **29**, 128101.

31. R. B. Von-Dreele and A. C. Larson, GSAS Manual, LANSCE MS-H805, Los Alamos National Laboratory, Los Alamos NM, NM 87545, 2000.

32. M. H. Chisholm, V. Baxter, J. Gama, F. Distasi, A. L. Hector and I. P. Parkin, *Chem. Mater.*, 1996, **8**, 1222.

33. K. Nakamoto, Infrared and Raman Spectra of Inorganic and Organic Coumpunds 3rd ed.; J. Wiley: New York, 1978.

34. W. Y. Gang and Z. X. Gang, *Electrochem. Acta*, 2004, **49**, 1957.

35. T. E. Saraswati, S. Tsumura and M. Nagatsu., *Jpn. J. Appl. Phys.*, 2014, **53**.

36. J. Gamby, P. L. Taberna, P. Simon, J. F. Fauvarque and M. Chesneau., *J. Power Sources*, 2011, **101**, 116.

37. H. Shi, *Electrochem. Acta*, 1995, **41**.

38. M. Fang, K. Wang, H. Lu, Y. Yang and S. Nutt, *J. Mater. Chem.*, 2009, **19**, 7098.

39. D. Yuan, X. Yuan, W. Zou, F. Zeng, X. Huang and X. Zhou, *J. Mater. Chem.*, 2012, **22**.

40. O. Shebanova, E. Soignard and P. F. Mcmillan, *High Pressure Research*, 2006, **26**, 87.

41. C. C. Chen, N. T. Liang, W. S. Tse, I. Y. Chen and J. G. Duh, *Chinese J. Phys.*, 1993, **32**, 205.

42. X. Zhao, B. M. Sanchez, P. J. Dobson and P. S. Grant, *Nanoscale*, 2011, **3**, 839.

4 Synthesis of molybdenum nitrides and charge storage behaviour

4.1 Introduction

Interest in molybdenum nitride stems from applications in catalysis,[1] its magnetic behaviour,[2] superconductivity[3, 4], potential use as diffusion barrier films in microelectronic devices,[5] and its excellent corrosion resistance including to boiling sulfuric acid.[6] Hard wear resistance coatings,[7, 8] potentially useful on machine tools, have been formed from molybdenum nitride. The major interest has been its heterogeneous catalytic activities (similar to group VIII metals) in many hydrogen involving reactions. Molybdenum nitrides exhibit good catalytic activities for hydrodesulfurization (HDS)[9-13] and hydrodenitrogenation (HDN)[14-17]reactions, carbon monoxide hydrogenation, ammonia synthesis, and ethane hydrogenolysis[18] and hence it might offer a cost-effective alternative to existing catalysts.[17]

Molybdenum forms a variety of nitrogen-containing compounds MoN_x. Within the Mo-N system, known phases include the stoichiometric hexagonal compound δ-MoN and non-stoichiometric cubic γ-Mo_2N.[19-22] Phase diagram studies of the Mo-N system show only the hexagonal δ-MoN exists at the stoichiometric composition.[23] A cubic high-temperature modification γ-MoN_x of NaCl-type structure is present at lower N concentration ($x = 0.61$ to 0.75).[24,25] Figure 4.1 shows the structures of some molybdenum nitride phases.

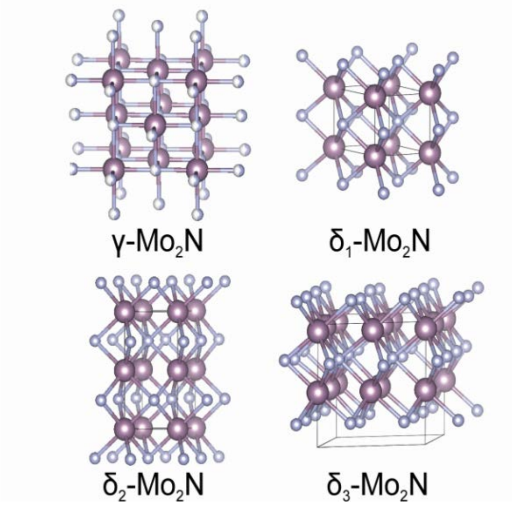

Figure 4.1: The structure of some molybdenum nitride phases.

MoN was first synthesised in 1930 by nitridation of molybdenum powder in an ammonia atmosphere at 700-1000 K.[26] Molybdenum nitride samples of hexagonal and cubic structure were prepared at pressures up to 7 GPa and temperatures up to 2300 K using molybdenum powder and 25 μm thick molybdenum foil.[27] The starting material was put into a hexagonal BN container with a graphite heater, and the reaction was carried out in a pyrophylite cylinder with tantalum AC contacts on the top and bottom of the cylinder. Surface analysis of the samples showed boron and carbon from the reaction container. These impurities could influence the electrical properties of the sample.

Thin films of molybdenum nitride have been reported via CVD by ammonia nitridation of $MoCl_5$ and $Mo(CO)_6$ diluted in N_2 or Ar using a cold-wall, vertical pancake-style reactor. NH_3 nitridation of $MoCl_5$ produced thin films of mixed phase δ-MoN and γ-Mo_2N, with δ-MoN more favoured at high temperature and high flow of NH_3.[28] The MoN films were only obtained using $Mo(CO)_6$ below 500 and above 700 °C, while mixtures of Mo_2N and MoN were obtained from both the precursors at all other temperatures except Mo_2N at 400-450 °C through $MoCl_5$. The MoN obtained through $Mo(CO)_6$ contained a high level of carbon. Plasma-assisted CVD of molybdenum nitride at high temperature from $MoCl_5$ and NH_3 has also been reported.[29] Other molybdenum nitride film preparation methods include the direct nitridation of molybdenum layers with NH_3[30] and techniques such as molecular beam epitaxy,[31, 32] ALD[33, 34] and reactive sputter deposition.[35]

Recently Hector and co-workers[36] reported nanoparticles of molybdenum nitrides via solvothermal synthesis using $MoCl_5$ with $LiNH_2$ or NH_3 as the nitriding source. Amorphous molybdenum nitride was obtained after 24 hours heating at 450 °C, while rock salt cubic MoN was obtained after 24 hours heating at 550 °C. Benzene was used as the solvent. Lattice parameters were a = 4.106(4) Å using $LiNH_2$ or a = 4.095(8) Å with NH_3. The products so obtained have significant carbon content due to solvent decomposition.

Wang[29] and co-workers used a flow of NH_3/N_2 mixture over $MoCl_5$ powder in an alumina boat with a silica tube to produce molybdenum nitrides. With pure NH_3 as the nitriding source, an amorphous MoN_{1-x} and NH_4Cl mixture was obtained at 400 °C with poorly crystallized product up to 500 °C. Hexagonal δ-MoN was obtained up to 600 °C. A mixture of δ-MoN and γ-Mo_2N was obtained up to 700 °C and cubic γ-Mo_2N at 800 °C. Low concentrations of ammonia favoured the formation of γ-Mo_2N at low temperature. The product obtained at 600 °C contained 2-7 wt % oxygen. The same authors used a solvothermal route with ammonia or hydrazine as solvent with $MoCl_5$ to obtain γ-Mo_2N.[29] The $MoCl_5$ was contained in a gold tube placed in the reaction vessel of nickel-based alloy which was able to withstand 500 MPa. The solvent was introduced and the vessel was heated in the furnace. Since the reaction was carried out in a closed reaction vessel, the NH_4Cl by-product was systematically found mixed with the nitride phases.

Lengauer[37] used the same precursor in a related study. $MoCl_5$ was heated under flow of ammonia in a mullite tube at temperatures of 770-1060 K. WC-type δ-MoN with lattice parameters of a = 2.851 (2) Å and c = 2.782(3) Å was obtained. At 950 K, a mixture of δ-MoN and γ-Mo_2N_{1-x} was obtained, with the γ-phase content increasing with temperature. Lattice parameters of γ-Mo_2N_{1-x} were to be found temperature dependent and decreased from a = 4.188(1) Å at 970 K to a = 4.170(1) Å at 1060 K, whereas the δ-MoN were not changed. At 1060 K δ-Mo_2N was observed with lattice parameters of a = 5.740(2) Å and c = 5.624(3) Å, which are significantly larger than the doubled cell parameters of the WC-type MoN. Spherical particles were observed due to melting of $MoCl_5$ before the reaction to δ-MoN was complete, which also causes agglomeration of the product particles and enlarges the particle size.

Molybdenum nitride was used in low temperature fuel cells as a cathodic electrocatalyst. Mo_xN (x = 1 or 2) on Ti substrate displayed electrochemical stability in acidic 4.4 M H_2SO_4 electrolyte at anodic potential +0.67 V (vs SHE) during 50 cycles.[38] However, this electrocatalyst showed surface damage such as cracking and crumbling in the high cathodic (below –0.1 V vs SHE) and anodic (above +0.67 V vs SHE) potential regions due to cathodic and anodic corrosion, respectively. Cyclic voltammograms (CV) of a δ-Mo_2N electrode were obtained 1 mol/L H_2SO_4, 1 mol/L KCl, 1 mol/L H_2SO_4 and 3 mol/L H_2SO_4 aqueous solution, respectively.[39] δ-Mo_2N showed good electrochemical performance with specific capacitance of 172 F/g and in a broad potential window of – 0.6 to 0.5 V in 1 M H_2SO_4 electrolyte. Recently single crystal mesoporous molybdenum nitride (Mo_3N_2) nanowires have been studied for its improved electrochemical properties.[40] The specific capacitance of meso-Mo_3N_2-NWs (~ 220 F g^{-1}) is much higher than that of common- Mo_3N_2 (66 F g^{-1}) at a scan rate of 50 mVs^{-1}.

Molybdenum nitrides were prepared from two different precursor sources, $MoCl_5$ and $Mo(NMe_2)_4$. Chloride or amide precursors were subjected to solution phase ammonolysis to produce chloroimide or amide precursors. Precursors were annealed at various temperatures to produce molybdenum nitrides. Molybdenum nitrides from $MoCl_5$ were synthesised during my MPhil studies and hence were reported in a previous thesis. Surface areas of the samples and their electrochemistry were studied during the PhD project. The work was further extended to produce molybdenum nitrides from $Mo(NMe_2)_4$ using the same reaction conditions as used for the chloride precursor source and to use these materials in supercapacitor applications to compare the materials obtained from two different precursor sources. The synthesis and characterisation of molybdenum nitrides from the chloroimide precursor source will be discussed in brief to allow an understanding of structural, compositional and electrochemical behaviour of both the materials.

4.2 Synthesis of MoN_x from solution phase ammonolysis of $MoCl_5$

All procedures were carried out under oxygen free conditions. $MoCl_5$ (2g) was dissolved in dry n-hexane (20 ml) and was stirred for 2 h to ensure dissolution. 20 ml liquid NH_3 (dried over sodium) was condensed into the $MoCl_5$ solution at -78 °C with continuous stirring. A bright yellow precipitate appeared as ammonia started condensing into the solution. The mixture was left to warm to room temperature under N_2 as the excess ammonia evaporated. The yellow precipitate turned dark brown and finally to a fluffy black powder while evaporating the NH_3. The black precipitate of molybdenum amide polymer ~2.5 g was then filtered, dried under vacuum and transferred to the glove box.

The likely reaction is given below:

$$MoCl_5 + a\,NH_3 \rightarrow {}^{1}\!/_{n}\,[MoCl_x\,(NH_2)_y(NH)_z]_n + b\,NH_4Cl$$

4.2.1 Pyrolysis of the molybdenum chloroimide precursor

1 g of the black molybdenum chloroimide polymer was transferred to a ceramic boat inside a silica tube, which was loaded inside the glove box. The silica tube was provided with an arrangement of taps to allow flushing of the hoses before the samples were exposed to the gas flow (Fig. 4.2). Samples were then heated under flowing ammonia to 500, 600, 700, 800, 900 or 1000 °C for 2 h. Polymer samples were also heated at 500 °C for longer durations of 12, 24 or 48 h. A column of molecular sieve was used to dry the ammonia. An average of 0.35 g of molybdenum nitride was obtained after annealing 1g of the polymer. The ammonium chloride formed during ammonolysis sublimed out at 340 to 360 °C during annealing and collects on the inner cold walls of the furnace tube. Contamination of the MoN_x product with ammonium chloride was prevented by placing a roll of aluminium foil inside the furnace tube such that the ammonium chloride condensation occurred on it. It was then removed before taking out the boat containing the nitride sample.

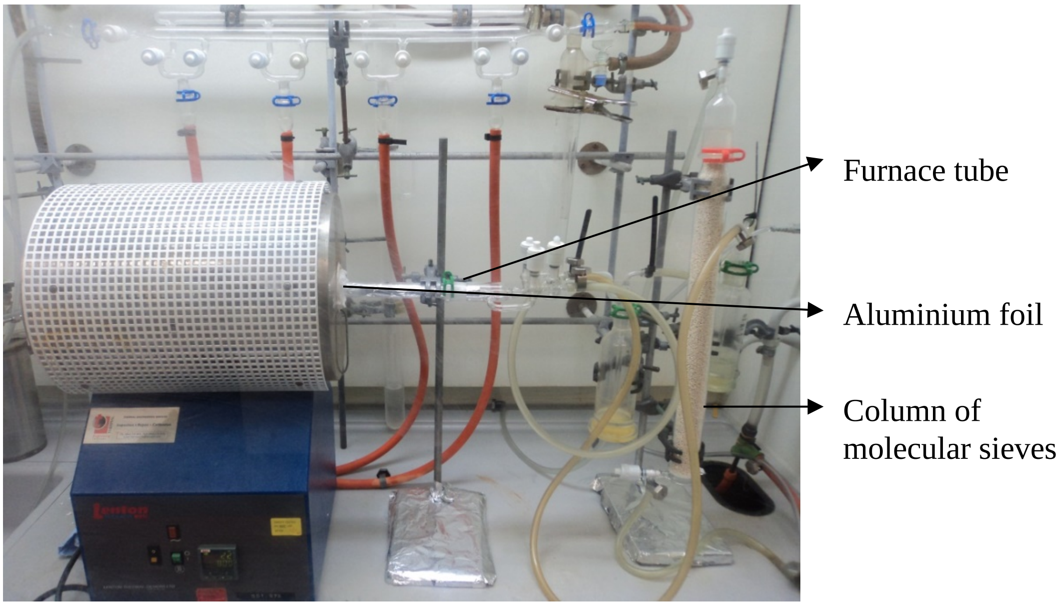

Figure 4.2: Annealing arrangement of the apparatus used for the pyrolysis of the polymeric molybdenum chloroimide precursors.

4.3 Synthesis of MoN_x from solution phase ammonolysis of $Mo(NMe_2)_4$

Synthesis of $Mo(NMe_2)_4$ was carried out by following the procedure given by Chisholm and Bradley.[41] All procedures were carried out under nitrogen. ~10 ml of liquid ammonia (distilled from sodium/ammonia) was added to a solution of 0.5 g $Mo(NMe_2)_4$ in THF under nitrogen with continuous stirring. The reaction mixture was left to come to room temperature until the excess ammonia was evaporated. The black precipitate of molybdenum amide polymer ~ 0.280 g was then filtered and dried under vacuum. The likely reaction is given below:

$$[Mo(NMe_2)_4] + a\,NH_3 \;\rightarrow\; {}^{1}\!/_{n}\,[Mo(NMe_2)_x(NH_2)_y(NH)_z]_n \;+ b\,HNMe_2$$

4.3.1 Pyrolysis of the imide polymer precursor

The polymer was transferred to a ceramic boat and loaded into a silica tube inside the glove box. The silica tube was provided with an arrangement of taps to allow flushing of the hoses before the sample was exposed to the gas flow. The sample was then heated under flowing ammonia to 500, 600, 700, 800, 900 or 1000 °C for a period of 2 h, or at 500 °C for 48 hr. A column of molecular sieves (synthetic zeolite, pore size 3 Å) was used to dry the ammonia.

4.4 Analysis of the chloroimide polymeric precursor

The chloroimide polymer precursor obtained from the reaction of $MoCl_5$ and ammonia contains significant amounts of NH_4Cl and some solvent with an overall composition $MoC_{0.2}H_{15.5}N_{4.8}Cl_{1.2}$. The IR spectrum (Fig. 4.3) shows a broad strong band at 3150 cm^{-1} (ν_{NH}), a strong sharp band at 1599 cm^{-1} (δ_{NH2}) and weak bands at 3048 and 2826 (ν_{CH}), and 2000-800 cm^{-1}.

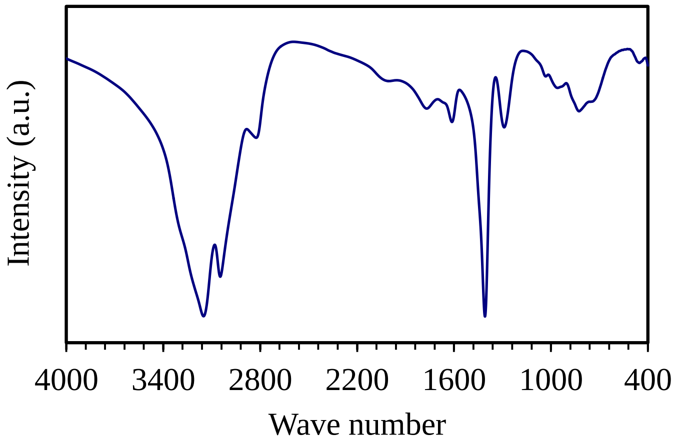

Figure 4.3: IR spectrum for chloroimide polymer precursor.

The TGA profile (Fig. 4.4) shows ~20% mass loss below 300 °C due to sublimation of NH_4Cl then steady loss to a plateau around 600 °C and a further steady mass lost to 800 °C. In total it loses 74% of mass over this temperature range. Similarly to our $[Mo(NMe_2)_4]$-derived imide polymer results, the $[Mo_2(NMe_2)_6]$-derived polymers had a barely discernible plateau[42], and this can be attributed to the lower initial oxidation state and the wide stoichiometry ranges exhibited by the molybdenum nitrides.

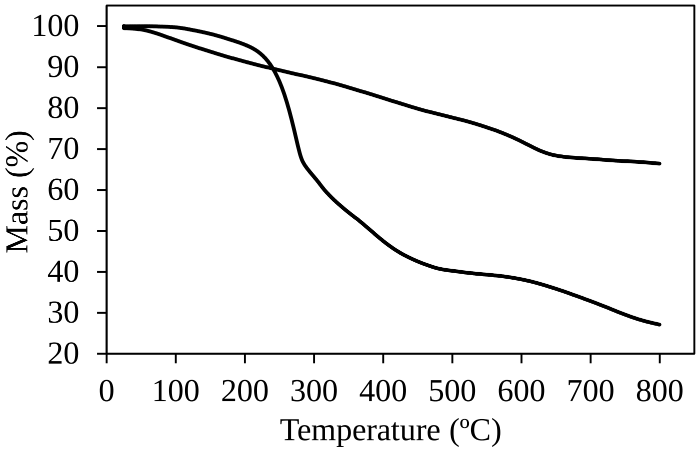

.

Figure 4.4: TGA profiles for the thermal decomposition of the chloroimide (bottom) and imide (top) polymer precursors under flowing nitrogen.

4.4.1 Analysis of the chloroimide derived MoN_x

Annealing the chloroimide polymer in flowing ammonia resulted in phase pure δ_1-MoN at 500 °C, mixture of δ_1-MoN/γ-Mo_2N at 600 °C and γ-Mo_2N at 700-1000 °C (Fig. 4.5). Diffraction peaks for δ_1-MoN became sharper with increasing the annealing time at 500 °C as the particle size increased. Choi and Kumta found γ-Mo_2N from a similar polymer between 600 and 800 °C.[43] No NH_4Cl reflections were observed in PXD data, suggesting the NH_4Cl by-product was removed effectively by sublimation onto aluminium foil placed inside the colder part of the furnace tube (Fig 4.2). Rietveld refinements were carried out using GSAS[44] to fit the PXD data to obtain the lattice parameters. Standard patterns were obtained from the inorganic crystal structure database (ICSD).[45] Lattice parameters for γ-Mo_2N are in the range of 4.16 to 4.22 Å and all our values (Table 4.1) fit within this range, with the variation consistent with the known compositional variations that can occur in this phase.[45, 46] Literature lattice parameters for δ_1-MoN are in the more tightly defined range of a = 2.86(1) and c = 2.79(2) Å[37, 47], again our values fall in this range. Crystallite sizes (Table 4.1) were obtained from the Lorentzian broadening using the adaptation of the Scherrer equation given in the GSAS manual.[48]

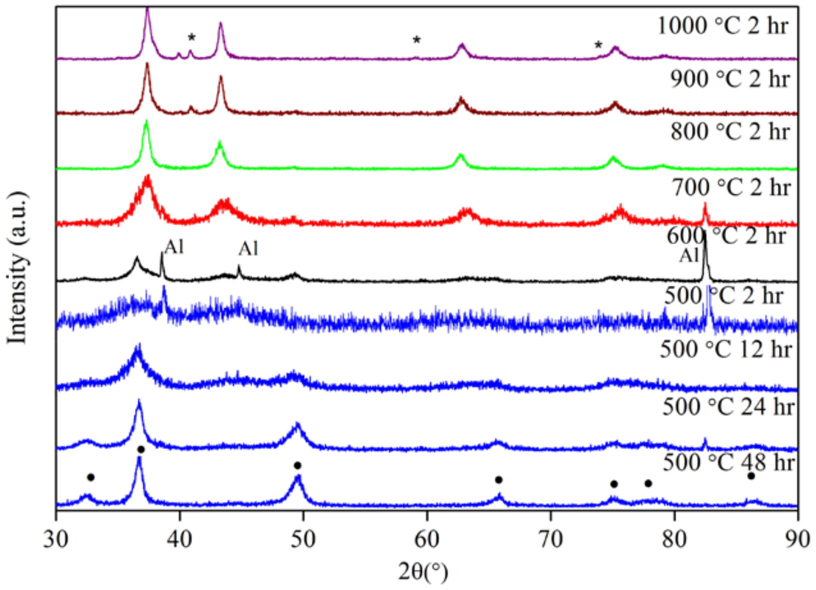

Figure 4.5: PXD patterns of chloroimide-derived molybdenum nitride samples heated in ammonia under the labelled conditions. Closed circles show the positions of reflections due to δ_1, MoN_x and asterisks the reflections of Mo metal. Peaks from the Al sample holder are labelled as Al.

Combustion analyses of the samples obtained at 500 °C show the samples close to stoichiometric δ_1-MoN, with a small amount of chloride impurity (Table 4.1). No chloride contamination was found in the sample obtained at 600 °C, and it remained stoichiometric in composition. Samples obtained at higher temperatures were found to be lower in nitrogen content, but nonetheless nitrogen-rich compared with the γ-Mo_2N formulation. This rocksalt-type phase varies widely in stoichiometry but our measured compositions are richer in nitrogen that the phases listed in ICSD.[45]

Table 4.1: Refined parameters and analytical data for molybdenum nitride samples produced by pyrolysis of the chloroimide precursor.

Temperature /°C	Heating time /h	*a* /Å	*c* /Å	Crystallite size /nm	Composition
1000	2	4.1967(7)	-	22	$MoN_{0.62}$
900	2	4.2017(10)	-	16	$MoN_{0.62}$
800	2	4.2044(8)	-	20	$MoN_{0.64}$
700	2	4.155(3)	-	22	$MoN_{0.71}$
600	2	4.176(3)	-	24	$MoN_{1.00}$
		2.866(3)	2.815(3)	27	
500	2	-[a]	-	-	$MoN_{1.13}Cl_{0.08}$
500	12	4.170(7)		21	$MoN_{1.02}Cl_{0.08}$
		2.870(6)	2.810(6)	23	
500	24	2.8536(14)	2.7974(16)	20	$MoN_{1.06}Cl_{0.03}$
500	48	2.8530(9)	2.7955(11)	32	$MoN_{1.08}Cl_{0.05}$

Cubic (γ-Mo_2N) patterns refined in *Fm*-3*m*, hexagonal (δ_1-MoN) in *P*-6*m*2 using atom positions from ICSD and nitrogen occupancies calculated from the combustion analysis data. C and H contents were <0.10 % throughout; stoichiometric MoN contains 12.73% N. [a] Pattern too broad for Rietveld refinement.

4.5 Analysis of imide derived polymeric precursor

The IR spectrum of the imide polymer precursor (Fig. 4.6) shows a strong, broad band at 3245 cm^{-1} (ν_{NH}), a sharper strong band at 850 cm^{-1} ν-(MoN) and weaker features at 2930-2760 ν-(C-H) and 1605 cm^{-1} δ-(NH_2). Combustion analysis yielded a composition of $MoC_{0.92}H_{4.61}N_{2.15}$. The TGA trace (Fig. 4.4) shows a gradual mass loss up to 800 °C, with the mass loss accelerating above 700 °C, probably due to thermal decomposition of the nitride products. Baxter *et al.* used mass spectrometry to examine exhaust gases from TGA of imide derived materials, and found dual weight loss profiles for many metals corresponding mainly to condensation reactions before the plateau (amine and ammonia loss) and reduction of the metal (nitrogen loss) after the plateau.[42] This is similar to the profile obtained with the chloroimide polymer if the ammonium chloride loss feature is discounted.

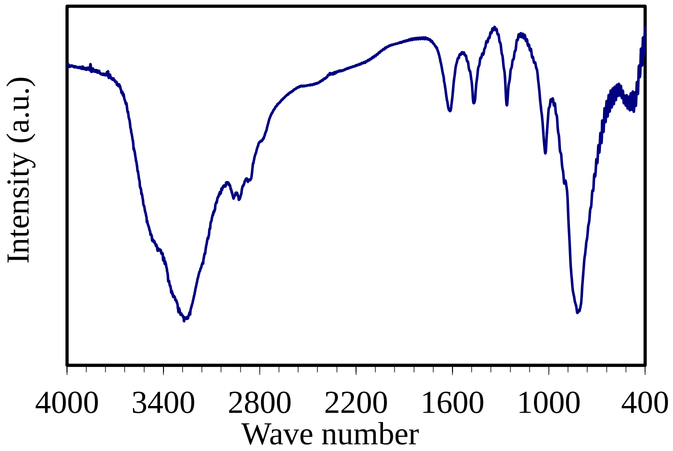

Figure 4.6: IR spectrum for imide polymer precursor.

4.5.1 Analysis of the imide derived MoN$_x$

Pyrolysis in ammonia of the imide polymer (that was derived from reaction of $Mo(NMe_2)_4$ and ammonia) at temperatures up to 900 °C resulted in samples that gave broad, rocksalt-like reflections (Fig. 4.7). Hexagonal MoN$_x$ was observed only at high temperature, a direct reversal of the phase behaviour that was observed in chloroimide derived samples (Fig. 4.5). At 900 °C all of the rocksalt peaks can be indexed using the cubic unit cell of γ-Mo_2N. PXD data show that the reflections due to δ_1-MoN phase were observed to grow between 800 and 1000 °C. At lower temperature the structure tends to distort from the standard cubic geometry; where enlargement of the angle between 111 and 200 reflections can be seen. This type of distortion has been previously observed in Hf_3N_4, where it was initially described in terms of a rhombohedrally distorted defect rocksalt lattice[49] and later found to be due to a tetragonally distorted defect fluorite lattice.[50] No specific distortion was found that modelled these molybdenum nitride samples well. The sample produced by annealing at 500 °C for 48 h is especially interesting as it is stoichiometric in nitrogen content (Table 4.1) but has a large structural distortion – this suggests the structure type is not a standard rocksalt arrangement and that could be the reason for the very different phase behaviour relative to the chloroimide-derived samples. Ammonolysis of a polymer derived from [$Mo_2(NMe_2)_6$] resulted in γ-Mo_2N at 450 °C and no mention of a structure distortion was made in the paper.[42] At 1000 °C some decomposition to Mo metal was also observed.

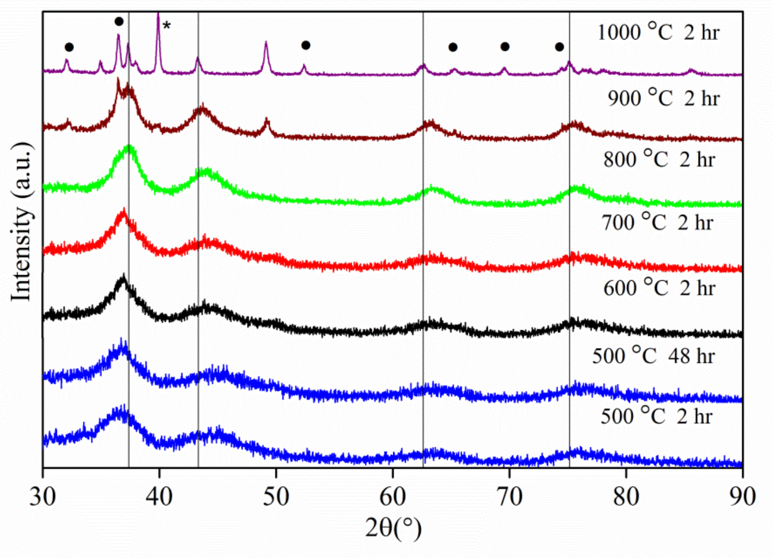

Figure 4.7: PXD patterns of molybdenum nitride samples produced by heating the imide polymer precursor in ammonia under the conditions shown. The vertical lines show the reflection positions of cubic MoN at 900 °C, closed circles are the positions of δ_1-MoN reflections and the asterisk shows a peak due to molybdenum metal.

PXD patterns for MoN_x samples were refined using GSAS.[48] PXD patterns for the samples at 800 °C and below this temperature were fitted using cubic (γ-Mo_2N) patterns refined in *Fm*-3*m*. PXD patterns for the samples obtained at 900 and above 1000 °C were refined cubic and hexagonal (γ-Mo_2N/δ_1-MoN) in *P*-6*m*2 using atom positions from ICSD.[45] Refined patterns for molybdenum nitride samples obtained at 800 °C (cubic γ-Mo_2N) and at 900 °C (γ-Mo_2N/δ_1-MoN) are shown in figures 4.8 and 4.9. Refined lattice parameters and the crystallite sizes are given in table 4.2. Refined lattice parameters were obtained by refining the background for the patterns, scale factor, thermal parameters and the peak shapes for each sample.

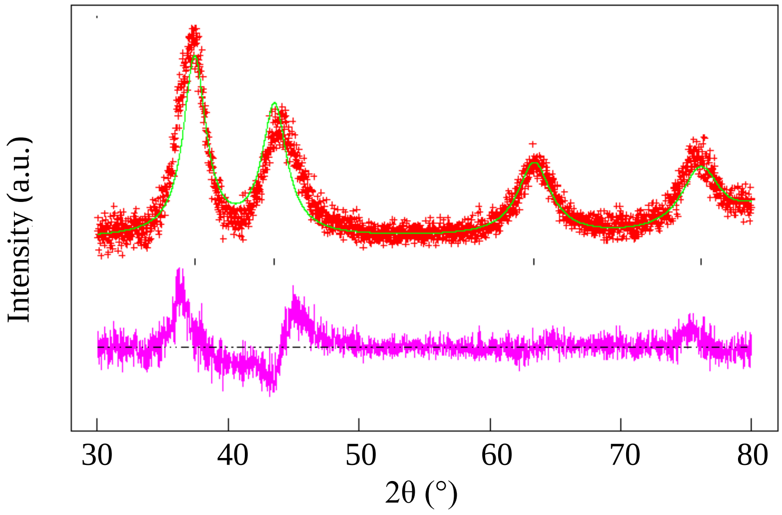

Figure 4.8: Fit to the crystalline molybdenum nitride sample obtained at 800 °C. Crosses mark the data points, upper continuous line the calculated profile and lower continuous line the difference; tick marks are the positions of allowed reflections positions for rock salt γ -Mo_2N.

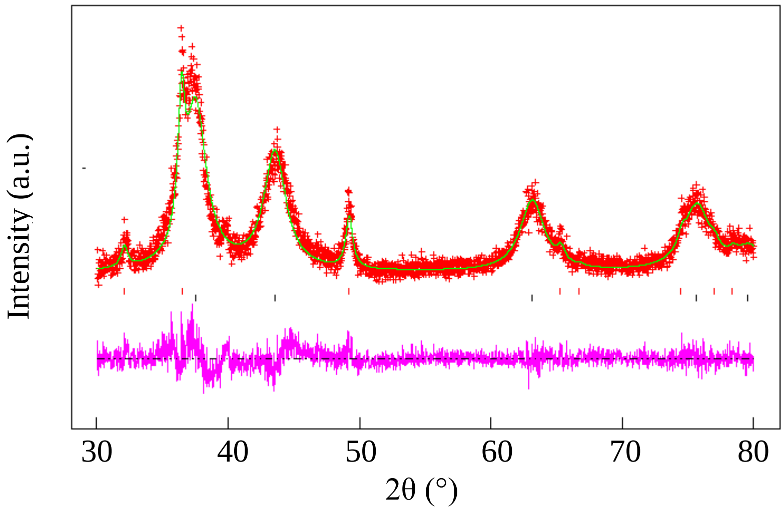

Figure 4.9: Fit to the crystalline molybdenum nitride sample obtained at 900 °C. Crosses marks the data points, upper continuous line the calculated profile and lower continuous line the difference, upper tick marks are the positions of allowed reflection positions for rock salt γ -Mo_2N and lower tick marks for the hexagonal δ_1-MoN.

Table 4.2: Refined lattice parameters and crystallite size of MoN samples obtained through pyrolysis of chloroimide polymer under various conditions.

Temperature /°C	Heating time /h	*a* /Å	*c* /Å	Crystallite size /nm
1000	2	4.2118(8)	-	14
		2.8627(6)	2.8266(7)	28
900	2	4.175(5)	-	4
		2.863(8)	2.807(8)	14
800	2	4.14[a]	-	9
700	2	4.06[a]	-	6
600	2	4.07[a]	-	4
500	2	4.04[a]	-	4
500	48	4.08[a]	-	4

X-ray diffraction patterns for the samples at 1000 and 900 °C refined using cubic (γ-Mo_2N, *Fm*-3*m*) and hexagonal (δ_1-MoN, *P*-6*m*2) structure models with atom positions from ICSD and nitrogen occupancies calculated from the combustion analysis data.

[a] Pattern not subjected to Rietveld refinement due to the structure distortion described in the text; the given lattice parameter is an average cubic value for the observed reflections.

Combustion micro analysis (Table 4.3) shows all the cubic molybdenum nitride samples to be nitrogen-rich relative to the γ-Mo_2N phase and that the nitrogen content decreased with increasing annealing temperature. Samples produced at 800 °C and below contained trace amounts of carbon due to incomplete removal during decomposition of dimethylamide groups, but interestingly none was detected in the sample heated for 48 h at 500 °C. This longer heating period also increased the nitrogen content, which can only mean it was oxidised by the ammonia during this process with hydrogen the likely by-product.

Table 4.3: Elemental analysis for Mo_xN samples obtained at the given annealing temperature and time (h).

Sample temp. (°C)	Annealing time (h)	% C	% H	% N	Composition
500	48	<0.1	<0.1	12.9	MoN
500	2	0.80	0.92	9.4	$MoN_{0.7}C_{0.08}H_{0.6}$
600	2	0.57	<0.1	10.9	$MoN_{0.83}C_{0.05}$
700	2	0.28	<0.1	10.6	$MoN_{0.81}C_{0.3}$
800	2	0.34	<0.1	10.9	$MoN_{0.84}C_{0.03}$
900	2	<0.1	<0.1	12.9	$MoN_{0.8}$
1000	2	<0.1	<0.1	7.9	$MoN_{0.58}$

C and H contents were <0.10% where not stated otherwise; stoichiometric MoN contains 12.73% N

TGA analysis showed two step mass losses (Fig. 4.10). During the first step at lower temperature (0-400 °C) the mass loss corresponds to amide group elimination as ammonia and amine leave the system. Above 700 °C nitrogen is lost.[42] The mass loss at lower temperature was greater in the samples obtained at 500 °C due to the presence of amide groups in the samples; however the samples heated at the same temperature for longer duration showed reduced loss of amide groups. As the sample annealed and crystallised the NH_2 and NH groups were lost.

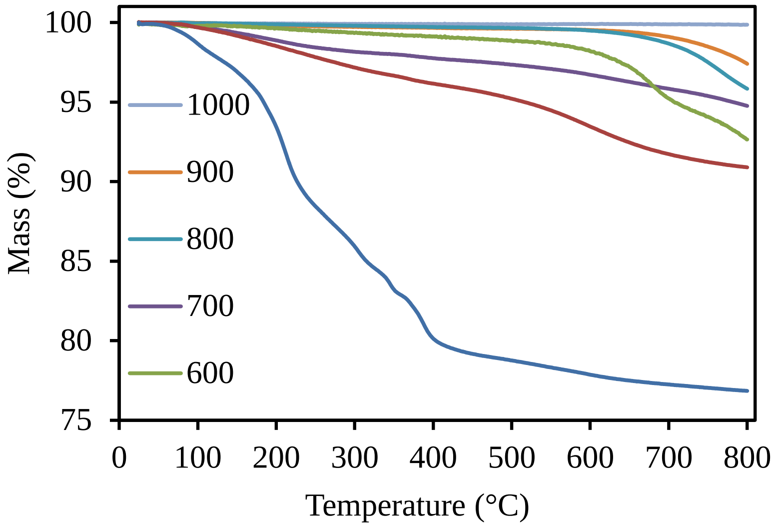

Figure 4.10: TGA curves for amide derived MoN_x samples obtained at the given temperatures (°C) annealed under ammonia for 2 h, and curve 500 (b) for 48 h.

Infrared spectra (Fig. 4.11) show the low intensity absorption peaks at 3430-3450 cm^{-1} which corresponds to residual ν_{NH}.[42] Weak peaks at 1580-1610 cm^{-1} in the samples annealed at 800 °C and below for shorter time, could be attributed to (ν_{NH2}).[42, 51] No such peak was observed in the samples obtained at 500 °C for 48 h or at temperatures above 800 °C. The broad absorption band observed in all samples at ~ 1000 cm^{-1} is attributed to ν_{M-N}. A series of sharp peaks is also observed in the samples heated at lower temperature for the shorter time periods, showing the structure development is incomplete.

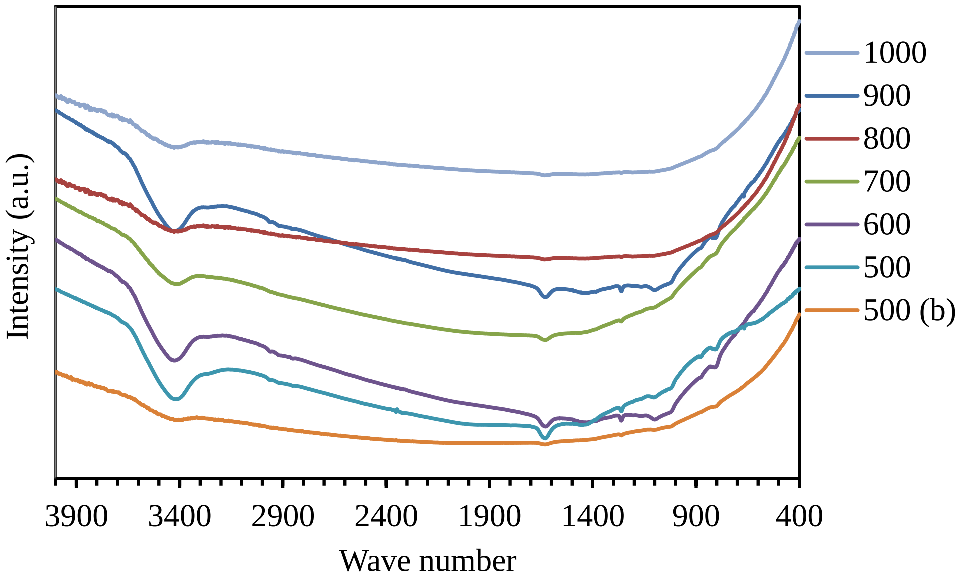

Figure 4.11: IR spectra for amide-derived MoN$_x$ samples obtained at the given temperatures (°C) annealed under ammonia for 2 h, series 500 (b) annealed for 48 h.

Transmission electron microscopy (TEM) was performed on a Hitachi H7000 with an accelerating voltage of 75 kV. Samples were made by ultrasound dispersal using dry toluene as the solvent. The samples in toluene were left in the ultrasonic bath for 4 hours and were deposited on carbon-coated Cu grids by depositing a drop of the solvent containing the powders. The grids were left overnight for drying inside the fume hood at room temperature. TEM images of imide-derived MoN$_x$ samples (Fig. 4.12) obtained even at higher temperatures showed nanotubes with some particles which were also asymmetric in shape. Only spherical particles were seen at 1000 °C. Increasing the surface area of the desired material (e.g. nanotubes or nano rod morphology) often increases the specific capacitance of the material.[52]

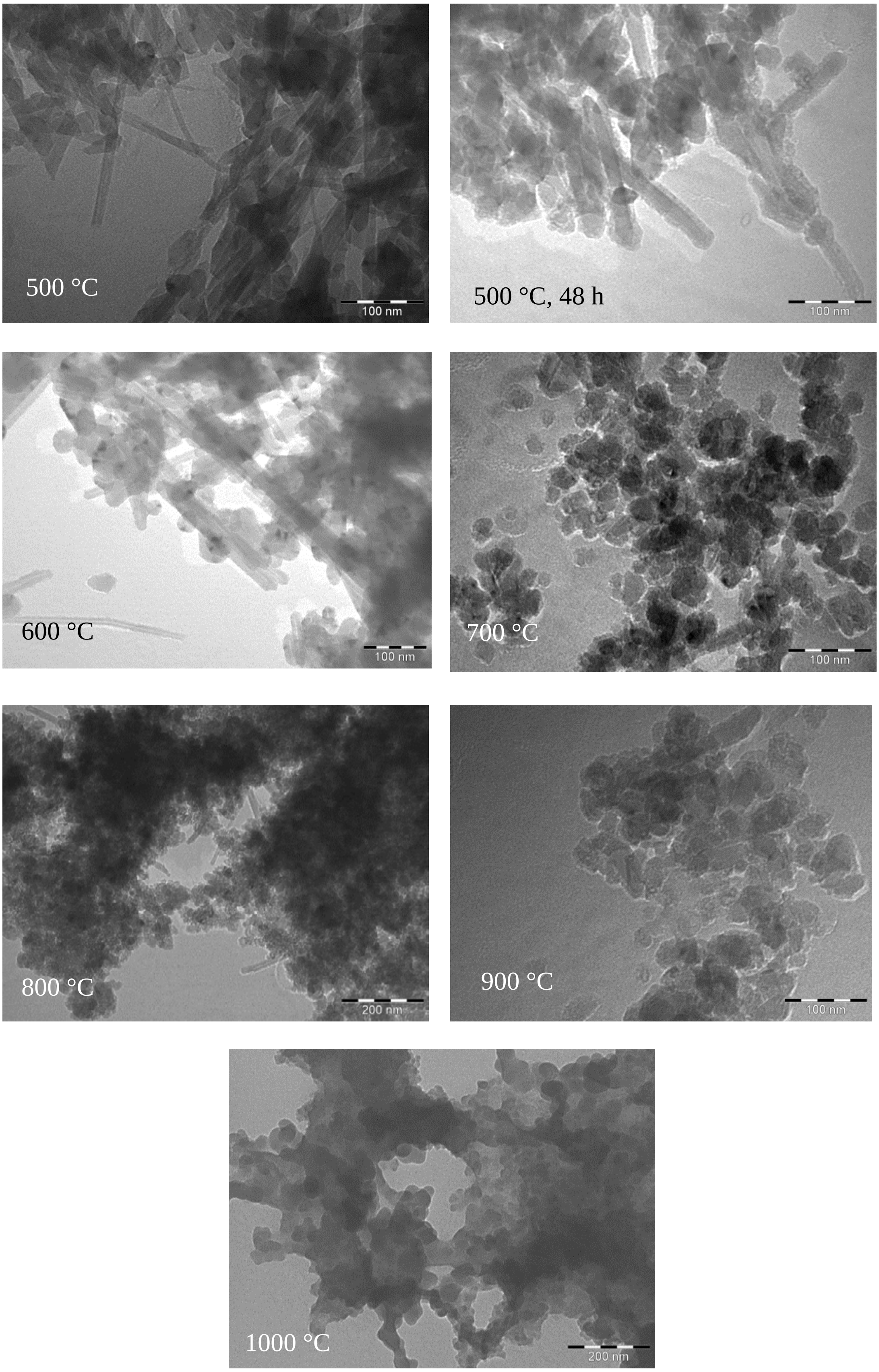

Figure 4.12: TEM images obtained for the amide-derived MoN_x samples at the given temperatures.

BET surface area analysis shows type IV isotherms (Figs. 4.13 and Figs. 4.14) for both the chloride and amide-derived materials. The shape of the hysteresis loops is determined by the mesoporous nature of the material; a clear capillary condensation step at relative pressure of 0.45 can be seen in the isotherms for the chloride-derived samples obtained at lower temperature, which moves to lower pressure in the high temperature samples. Isotherms are more elongated for the amide-derived samples, which showing the occurrence of micro and mesoporous structures together. The surface area of chloride- derived samples decreases with increase in temperature or annealing time (Table 4.4). A chloroimide-derived sample annealed at 500 °C for 2 hr showed the highest surface area of 70 m^2 g^{-1}. While the highest surface area of 10 m^2 g^{-1} was seen in the sample obtained at 600 °C for amide derivatives. Pore distribution data (Table 4.4) for both types of materials was found to be in the mesoporous range. The error estimation of BET surface area values was found to be ± 1 m^2 g^{-1} and of PSD ± 1 Å.

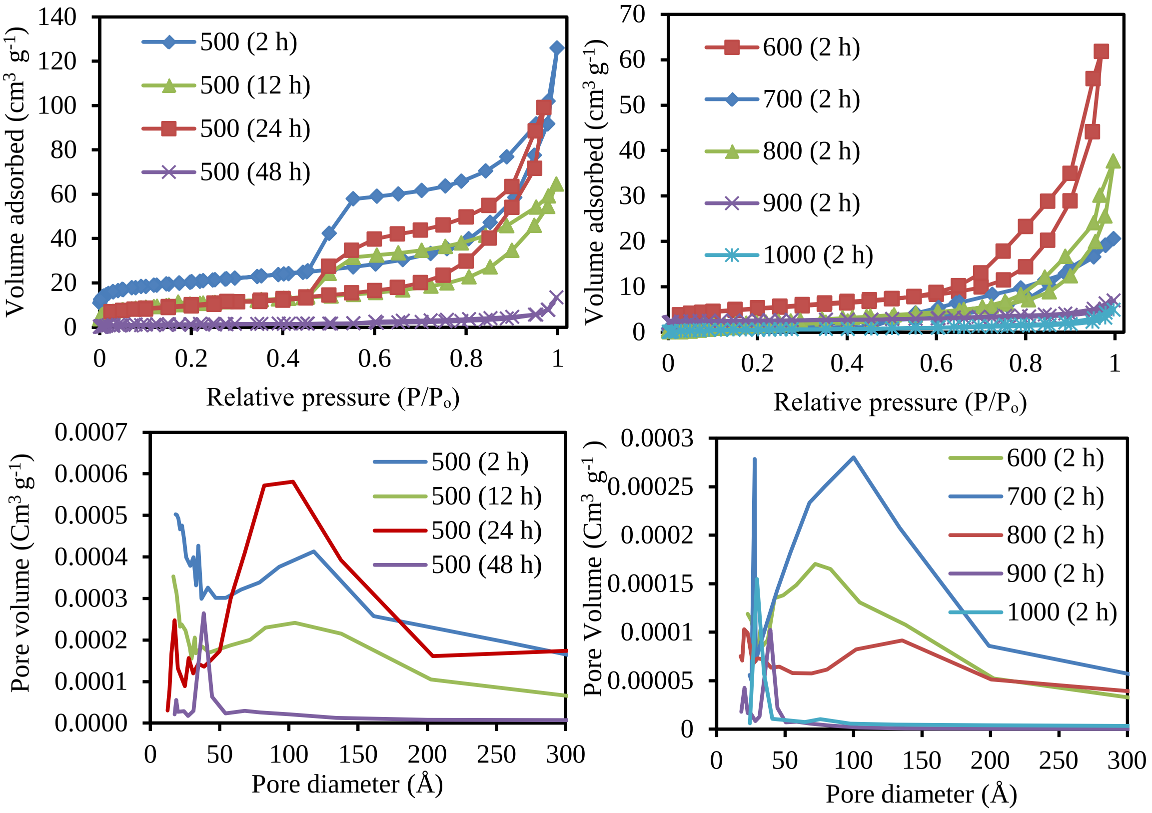

Figure 4.13: N_2 adsorption/desorption isotherms (top) and pore size distribution plots (bottom) for the chloroimide-derived MoN_x samples obtained at the given conditions (°C).

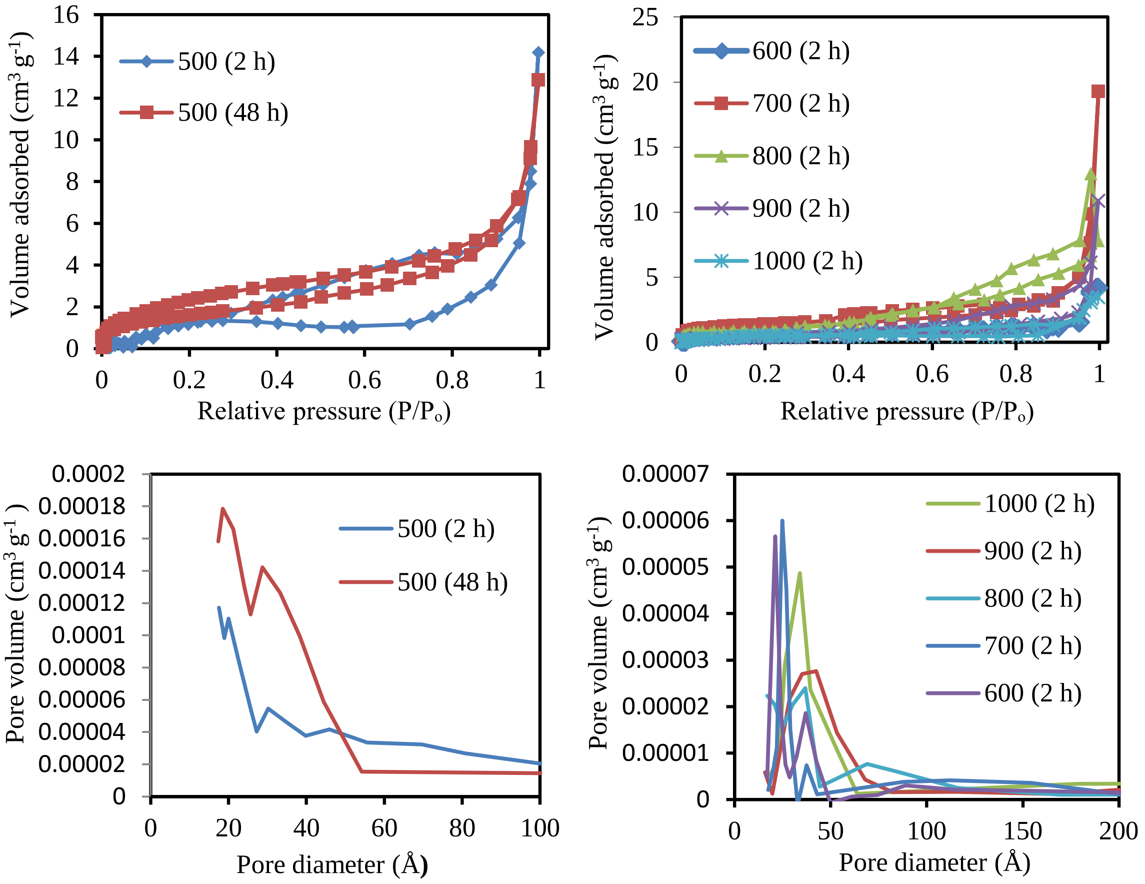

Figure 4.14: N_2 adsorption /desorption isotherms (top) and pore size distribution plots (bottom) for the amide-derived MoN_x samples obtained at the given conditions (°C).

Table 4.4: S_{BET} surface area and pore size distribution values for chloride- or amide-derived samples. (--) samples not synthesised under these conditions.

Temperature °C/ annealing time (h)		Chloride derived MoN_x		Amide derived MoN_x	
		Surface area (m^2 g^{-1})	PSD (Å)	Surface area (m^2 g^{-1})	PSD (Å)
500	2h	70	100	8	30
500	12h	37	110	--	--
500	24h	35	100	--	--
500	48h	4	40	8	30
600	2h	17	70	10	25
700	2h	10	100	5	30
800	2h	8	130	3	30
900	2h	3	40	3	40
1000	2h	2	30	2	35

4.6 Capacitance measurements

Capacitance of the material was measured through cyclic voltammetry using three electrode cells. A Hg/$HgSO_4$ electrode was used as a reference electrode, with a thin platinum gauze of 0.005 mm thickness as a counter electrode. Working electrodes were made by depositing an ink of active material onto a titanium foil current collector (procedure as given in chapter 3, page 60). ~ 2 mg of active material was weighed to be deposited after drying the electrode. The electrolyte was degassed to remove by bubbling nitrogen for 1 h through the solution. A blanket of nitrogen was maintained over the electrolyte surface while acquiring the voltammograms. Three electrode cell assemblies can be seen in chapter 3 (Fig. 3.11).

Conway et al.[53] explains the behaviour of Mo_xN electrodes in a way that the proton and an electron are involved on the same side of the redox process e.g.

$$Mo^{3+} + N^{3-} + H^{+} + e^{-} \leftrightarrow Mo^{2+} + NH^{2-}$$

in the surface region of the nitride film. However, there is a possibility that the surface of the nitride film may already be hydrolysed in aqueous acid, giving rise to interfacial OH^- and O^{2-} groups so that an oxy/hydroxide redox couple could be potential determining at the hydrolysed interface, e.g.

$$Mo^{3+} \cdot O^{2-} \cdot OH^{-} + H^{+} + e^{-} \leftrightarrow Mo^{2+}(OH^{-})_2$$

or some similar nonstoichiometric species.

Cyclic voltammetry for MoN_x samples was carried out in aqueous 0.5 M K_2SO_4 or 0.5 M H_2SO_4. Previous studies of electrochemical behaviours of MoN_x were carried out in H_2SO_4[38, 39, 53-55] or KOH[43] electrolytes. The reference electrode was Hg/$HgSO_4$ filled with $K_2SO_{4(aq)}$ or $H_2SO_{4(aq)}$ of the same molarity as used in the cell. The potential window was set after testing the electrode material for its anodic and cathodic red-ox stability factor. A potential window of 0.6 or 0.7 V was used for H_2SO_4 or K_2SO_4 electrolyte, respectively; strong oxidation or reduction tails were observed outside of this window. Electrodes of each sample were cycled sequentially at a series of scan rates starting at 100, 25, 10 and 2 mV s^{-1} for 10 cycles and finally at 100 mV s^{-1} for 100 cycles to analyse the charge storage capacity and variation in the capacity with charge/discharge stability in electrolytic reactions.

Cyclic voltammograms of the chloroimide-derived samples in H_2SO_4 (Fig. 4.15) showed fairly rectangular shape in a 0.6 V potential window with a broad reduction feature at ca. – 0.35 V, that is more prominent at slower scan rates. After sequential runs at a series of scan rates, both the capacitance and the shape of the CVs were similar to those observed at the start of the process with 140 cycles in between.

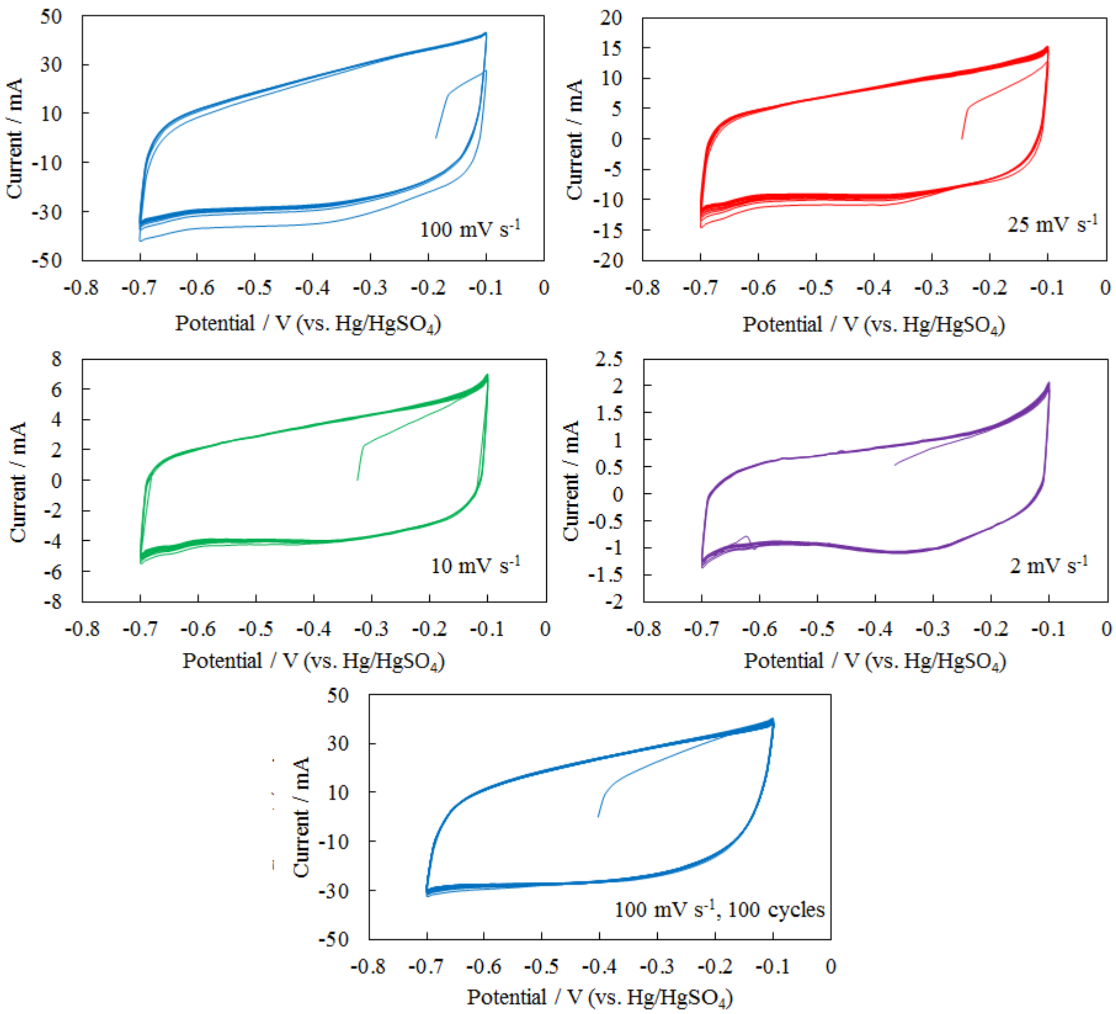

Figure 4.15: Cyclic voltammograms of chloroimide-derived molybdenum nitride (heating conditions: 2 h at 500 °C) at the given scan rates (showing 10, or 100 cycles) in 0.5 M $H_2SO_{4(aq)}$, loading 2 mg over 1.5 × 1.5 cm electrode area.

CVs in $K_2SO_{4(aq)}$ were observed to be more tilted than those in $H_2SO_{4(aq)}$ at higher scan rates indicating higher resistance (Fig. 4.16). Other authors have suggested that the conductivity and the radius of the hydrated electrolyte cation is a limitation on the high rate performance of electrolytes containing $K^+_{(aq)}$.[39, 56] The shape of the CVs becomes closer to a normal rectangular profile at slower scan rates. Redox features are more visible in the CVs in K_2SO_4 electrolyte at slower scan rates. Samples show slight oxidation at slower scan rate in this potential range; however, the CVs regain their initial shape at higher scan rate and maintain this shape over further 100 cycles.

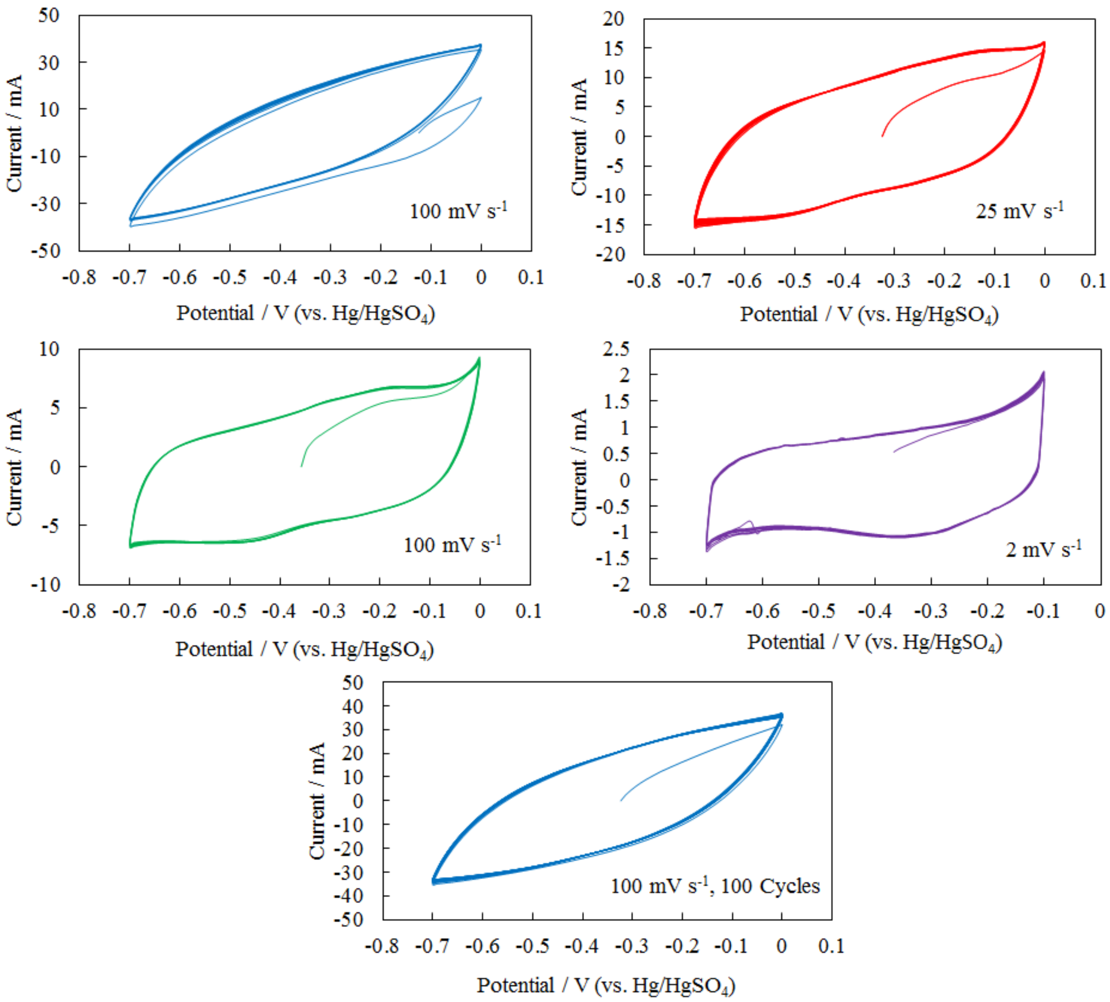

Figure 4.16: Cyclic voltammograms of chloroimide-derived molybdenum nitride (heating conditions: 2 h at 500 °C) at the given scan rates (showing 10, or 100 cycle) in 0.5 M $K_2SO_{4(aq)}$, loading 2 mg over 1.5 × 1.5 cm electrode area.

CVs of imide-derived samples (Fig. 4.17) in $H_2SO_{4(aq)}$ showed a potential window of 0.6 V as observed in the chloroimide-derived materials, but shifted to a slightly higher potential (0 to -0.6 V vs $Hg/HgSO_4$). The CV shows three clear distinct redox features at any scan rate contrary to the chloroimide-derived samples, where these peaks are not prominent in sulphuric acid electrolyte. A short reduction tail was seen in the cyclic voltammograms obtained a lower scan rates, though the material tend to kept its original composition as the shape of the CV at 100 mV s^{-1} shows its initial charge/discharge profile.

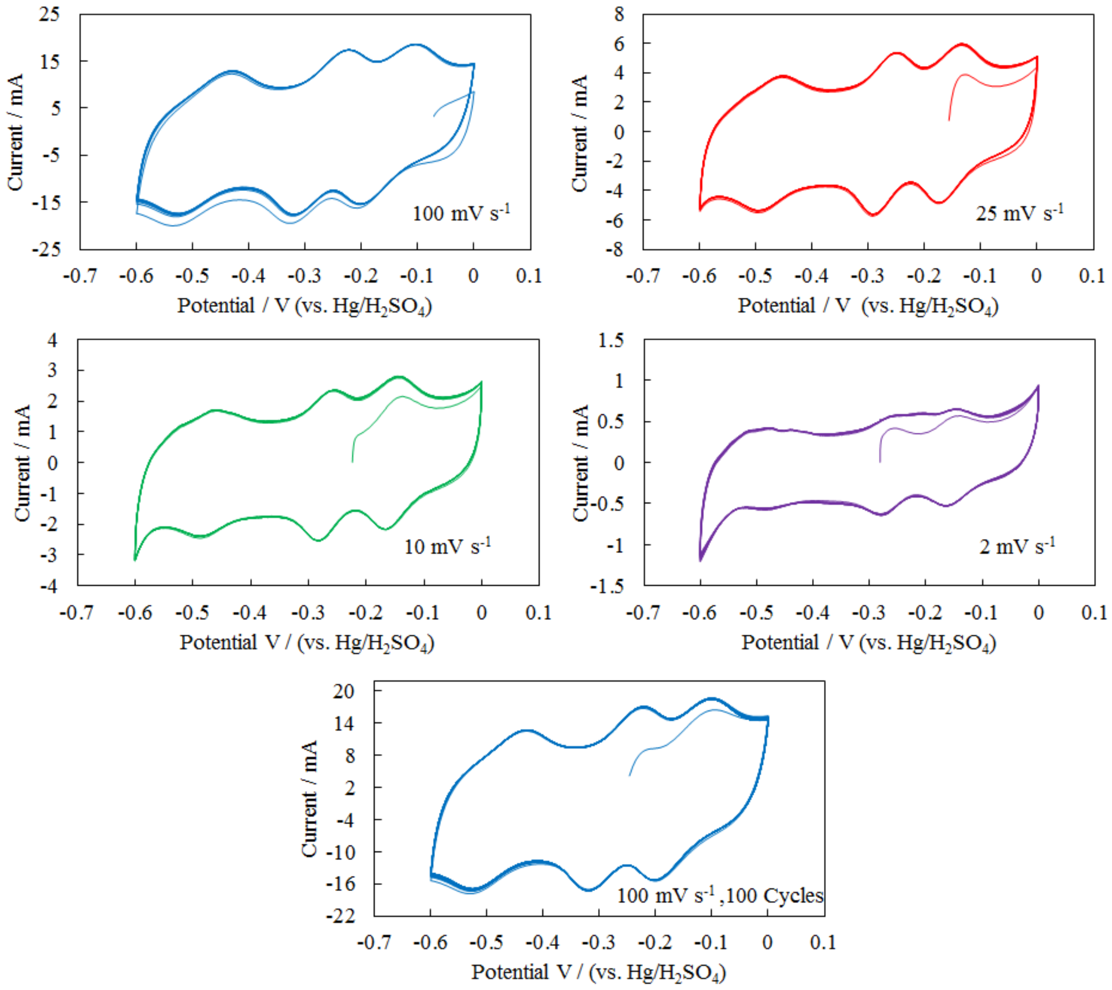

Figure 4.17: Cyclic voltammograms of imide-derived molybdenum nitride (heating conditions: 2 h at 600 °C) at the given scan rates (showing 10 or 100 cycles) in $H_2SO_{4(aq)}$, loading 2 mg over 1.5 × 1.5 cm electrode area.

CVs of imide-derived samples in $K_2SO_{4(aq)}$ (Fig. 4.18) showed a potential window of 0.7 V as observed for the chloroimide-derived materials (0 to -0.7 V vs $Hg/HgSO_4$). Cyclic voltammograms obtained at fast sweep rate shows the shape of the CVs are tilted, reflecting the lower K^+ transport rate relative to H^+, and not all the three redox peaks are prominent as seen as on lower sweep rate. Redox peaks in K_2SO_4 are slightly moved to a lower potential.

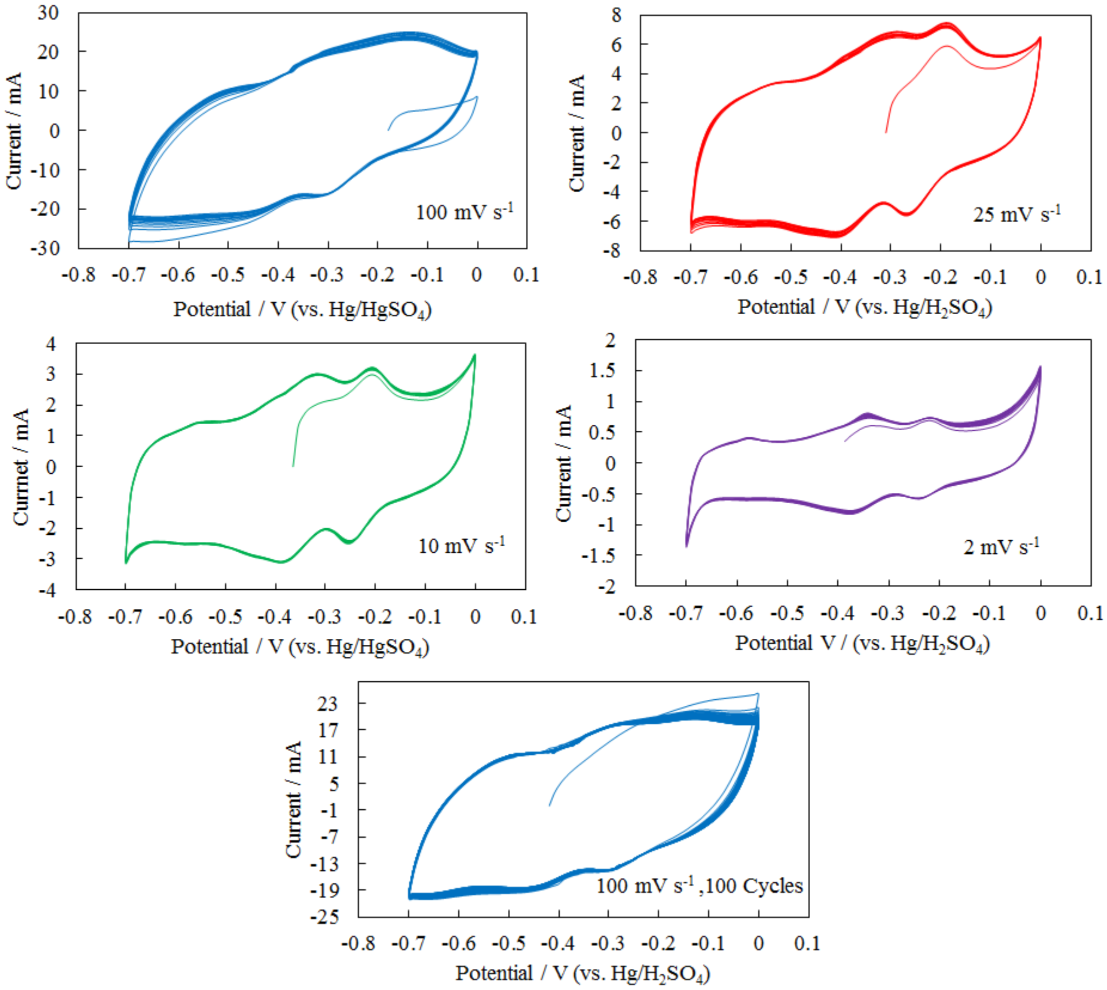

Figure 4.18: Cyclic voltammograms of imide-derived molybdenum nitride (heating conditions: 2 h at 600 °C) at the given scan rates (showing 10 or 100 cycles) in $K_2SO_{4(aq)}$, loading 2 mg over 1.5 × 1.5 cm electrode area.

Specific capacitances for all the MoN_x samples obtained through pyrolysis of chloroimide precursor under various conditions are given in table 4.5 (in H_2SO_4 electrolyte) and table 4.6 (in K_2SO_4 electrolyte). The sample obtained at 500 °C annealed for 2 h showed a specific capacitance of 200 F g^{-1} in H_2SO_4, comparable with the highest values reported for molybdenum nitrides in the literature, and 275 F g^{-1} in $K_2SO_{4(aq)}$ exceeding the previous reports.[38-40, 43, 53-55] Capacitance of the samples obtained at lower temperatures fell by around 50% at faster sweep rate, while the capacitance difference with sweep rate was low in the samples obtained at higher temperature. Capacitances were found to decrease with increasing annealing temperature, as expected for a double layer process as the surface area of the sample decreases.

Table 4.5: Specific capacitance (F g^{-1}) in 0.5 M H_2SO_4 of molybdenum nitride samples obtained by pyrolysis of the chloroimide precursor under the conditions shown.

Scan rate (mV s^{-1})	**100**		**25**		**10**		**2**		**100**	
Scan number	**1**	**10**	**1**	**10**	**1**	**10**	**1**	**10**	**1**	**100**
500 °C, 2 h	113	109	158	146	167	160	202	202	106	102
500 °C, 12 h	85	85	113	106	156	162	193	189	86	81
500 °C, 24 h	87	87	126	120	141	138	163	163	90	90
500 °C, 48 h	37	36	44	41	46	41	50	48	31	25
600 °C, 2 h	58	56	71	69	76	63	85	81	48	41
700 °C, 2 h	47	46	49	48	51	49	58	51	31	30
800 °C, 2 h	22	20	23	23	25	23	31	30	17	15
900 °C, 2 h	16	15	17	14	18	18	24	24	12	12
1000 °C, 2 h	15	12	17	17	17	18	26	26	14	15

Table 4.6: Specific capacitance (F g^{-1}) in 0.5 M K_2SO_4 of molybdenum nitride samples obtained by pyrolysis of the chloroimide precursor under the conditions shown.

Scan rate (mV s^{-1})	**100**		**25**		**10**		**2**		**100**	
Scan number	**1**	**10**	**1**	**10**	**1**	**10**	**1**	**10**	**1**	**100**
500 °C, 2 h	85	85	158	158	214	214	275	275	82	82
500 °C, 12 h	83	83	114	107	156	161	241	245	86	84
500 °C, 24 h	84	84	151	146	188	181	250	241	78	76
500 °C, 48 h	26	26	37	37	49	49	67	67	25	24
600 °C, 2 h	64	62	87	82	93	89	112	110	59	57
700 °C, 2 h	59	52	72	68	92	83	97	93	52	48
800 °C, 2 h	35	32	39	39	41	37	53	50	31	30
900 °C, 2 h	34	32	38	38	42	40	49	49	26	26
1000 °C, 2 h	29	27	37	33	42	40	48	48	24	24

Specific capacitances for molybdenum nitride samples obtained through annealing the amide polymer precursor under ammonia are given in table 4.7 ($H_2SO_{4(aq)}$) and table 4.8 ($K_2SO_{4(aq)}$). The highest capacitance (161 F g^{-1} in $K_2SO_{4(aq)}$ or 148 F g^{-1} in $H_2SO_{4(aq)}$) was measured for a sample annealed at 600 °C for 2 h in ammonia, assuming all the imide and organic groups had been decomposed (H 0%). It is noteworthy that these samples stored significant amount of charge even though they were lower in surface area than the chloroimide derived samples. Overall these results, combined with the more prominent redox features in the CVs, suggest that pseudocapacitance (redox activity) takes a much more prominent role in the distorted rocksalt structure imide-derived molybdenum samples and that the effect of double layer capacitance is more significant in the chloroimide-derived materials. Charge storage capacity decreased in molybdenum nitride samples obtained at high temperature, as particle size increased, and in the lower temperature sample annealed for short time (due to undecomposed precursor residues).

Table 4.7: Specific capacitance (F g^{-1}) in 0.5 M H_2SO_4 of molybdenum nitride samples obtained by pyrolysis of the imide precursor under the conditions shown.

Scan rate (mV s^{-1})	**100**		**25**		**10**		**2**		**100**	
Scan number	**1**	**10**	**1**	**10**	**1**	**10**	**1**	**10**	**1**	**100**
500 °C, 2 h	37	37	53	51	58	58	70	63	32	31
500 °C, 48 h	64	63	71	69	86	85	107	107	61	60
600 °C, 2 h	74	69	92	92	109	109	148	148	69	67
700 °C, 2 h	23	21	25	23	30	27	32	31	19	18
800 °C, 2 h	22	22	25	24	24	24	30	30	17	16
900 °C, 2 h	18	18	22	22	26	26	34	34	17	17
1000 °C, 2 h	12	11	14	11	16	16	18	18	10	9

Table 4.8: Specific capacitance (F g^{-1}) in 0.5 M K_2SO_4 of molybdenum nitride samples obtained by pyrolysis of the imide precursor under the conditions shown.

Scan rate (mV s^{-1})	**100**		**25**		**10**		**2**		**100**	
Scan number	**1**	**10**	**1**	**10**	**1**	**10**	**1**	**10**	**1**	**100**
500 °C, 2 h	50	50	55	54	60	60	72	72	39	39
500 °C, 48 h	62	60	65	63	72	72	91	91	57	55
600 °C, 2 h	74	67	96	93	119	119	161	161	65	61
700 °C, 2 h	25	23	26	25	31	31	47	47	23	23
800 °C, 2 h	19	18	21	20	23	23	35	33	20	20
900 °C, 2 h	16	14	26	26	28	28	33	33	14	14
1000 °C, 2 h	16	14	18	18	21	21	25	25	12	10

Plotting the graph for capacitance vs. number of cycles (Fig. 4.19) shows capacitance is maintained up to 100 cycles for all the samples obtained through annealing chloride or amide precursors under ammonia. The plots below are for the final 100 cycles of the data given in the last columns of the capacitance tables 4.5 to 4.8.

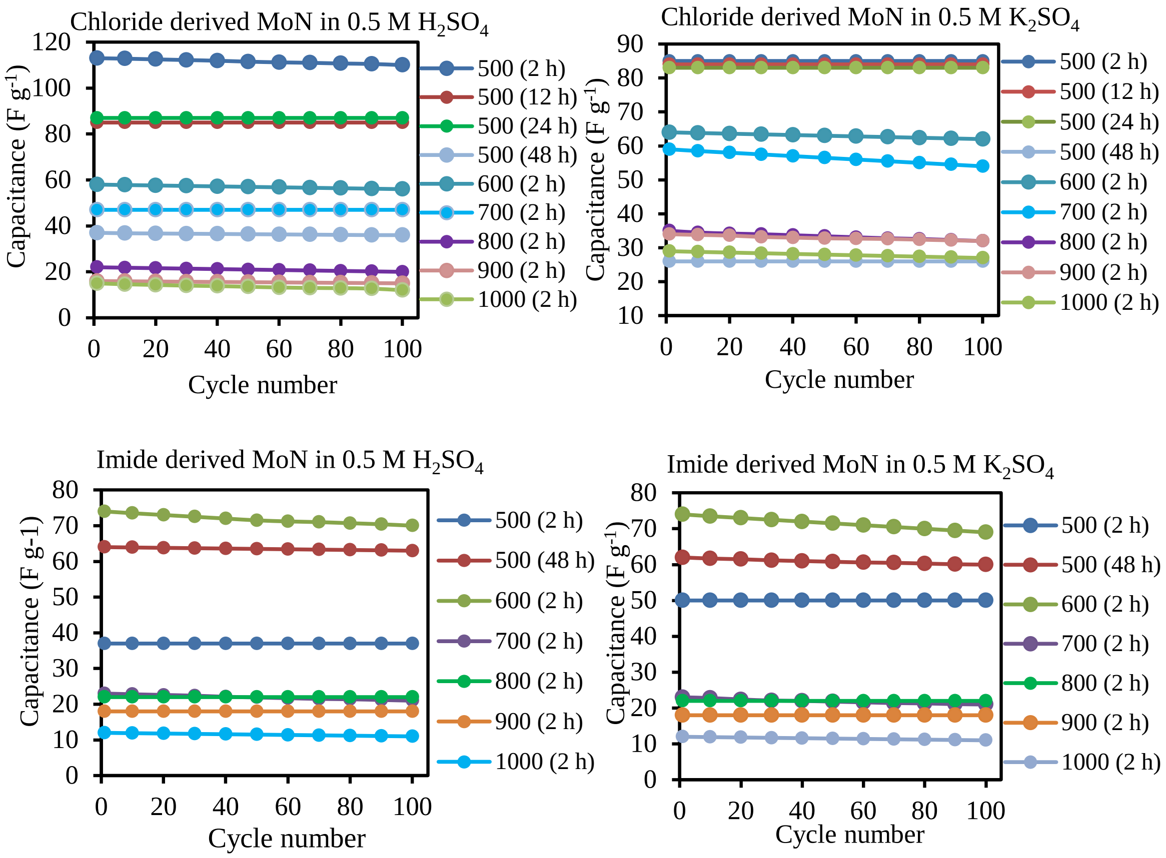
Chloride derived MoN in 0.5 M H_2SO_4

Chloride derived MoN in 0.5 M K_2SO_4

Imide derived MoN in 0.5 M H_2SO_4

Imide derived MoN in 0.5 M K_2SO_4

Figure 4.19: Plots showing the charge stability of chloride or amide derived MoN_x in the given conditions (temperature °C and time h) at 100 mV s^{-1} up to 100 cycles in $H_2SO_{4(aq)}$ or $K_2SO_{4(aq)}$ (as given in the chart titles).

Plotting the capacitance data vs sweep rate (Fig. 4.20) shows the capacitance drop from slow to high scan rate in all the imide or chloride derived samples. Capacitance drop from slow to high sweep rates is less in the samples obtained at higher temperature; suggest the ion absorption rate through the active material surface becomes similar at any scan rate.

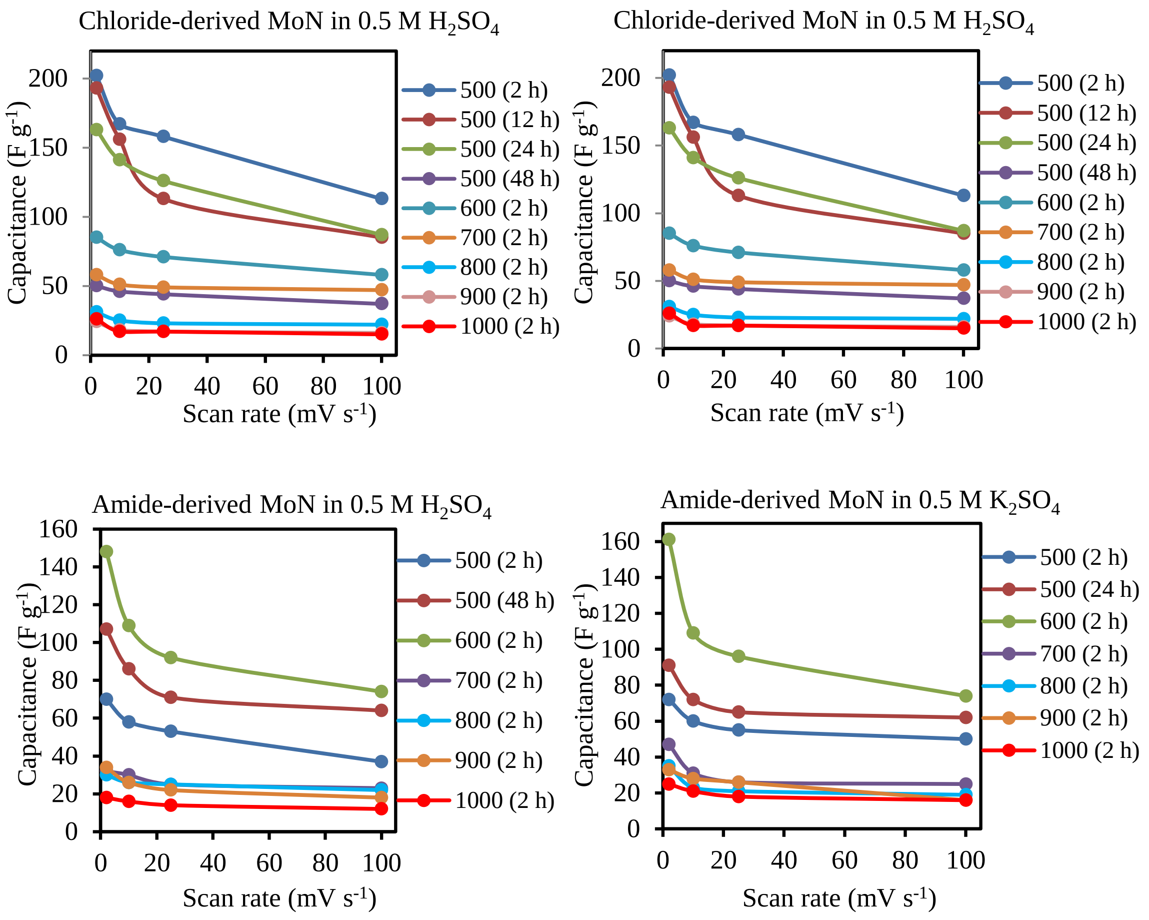

Figure 4.20: Plots showing the capacitance vs the scan rate of chloride or amide derived MoN_x in the given conditions (temperature °C and time h), in $H_2SO_{4(aq)}$ or $K_2SO_{4(aq)}$ (as given in the chart titles)

4.6.1 *Redox potentials of chloride derived MoN_x electrodes*

Redox potentials for MoN samples obtained through pyrolysis of chloroimide precursor are given in (Table 4.9) $H_2SO_{4(aq)}$ and (Table 4.10) $K_2SO_{4(aq)}$. In $H_2SO_{4(aq)}$ a common broad reduction peak is observed at *ca.* - 0.35 V at any scan rate. An oxidation peak at - 0.36 V is seen only in the sample obtained at 600 °C. An extra reduction peak at - 0.24 V at high scan rate is shifted to high potential of - 0.21 V with another reduction at *ca.* - 0.54 V found at lower scan rates for the sample obtained at 700 °C. The sample obtained at 700 °C did show oxidation peaks at - 0.53, - 0.34, and 0.24 V; those were also observed in the sample at 1000 °C. The oxidation tail was found to slightly increased in length at lower scan rate when the electrodes were made of the samples obtained at 600 °C or above. In $K_2SO_{4(aq)}$ no redox peaks were observed at high scan rates in the samples obtained at 500 °C annealed from 2 to 24 h, while oxidation peaks at *ca.* - 0.18 or reduction at - 0.44 were found in these samples at lower scan rates of 10 or 2 mV s^{-1}. Oxidation peaks at - 0.19 or reduction at - 0.28 V were found common in the rest of the samples at 100 mV s^{-1}. Two oxidation peaks ca. - 0.23 and - 0.3 V and two reduction peaks at - 0.25 and - 0.38 V were consistently found at 25, 10 or 2 mV s^{-1} in all the samples. Redox features were mostly broad for chloroimide-derived samples in both the electrolytes.

Table 4.9: Redox potentials (V) vs Hg/$HgSO_4$ in 0.5 M H_2SO_4 of molybdenum nitride samples obtained by pyrolysis of the chloride precursor under the conditions shown. No features (--).

Redox potentials (V), at given scan rate (mV s^{-1})								
Scan rate	**100**		**25**		**10**		**2**	
	Ox.	Red.	Ox.	Red.	Ox.	Red.	Ox.	Red.
500 °C, 2 h	--	- 0.35	--	- 0.35	--	- 0.35	--	- 0.35
500 °C, 12 h	--	- 0.35	--	- 0.35	--	- 0.35	--	- 0.35
500 °C, 24 h	--	- 0.35	--	- 0.35	--	- 0.35	--	- 0.35
500 °C, 48 h	--	- 0.35	--	- 0.37	--	- 0.37	--	- 0.35
600 °C, 2 h	- 0.32	- 0.3	- 0.32	- 0.36	- 0.32	- 0.36	--	- 0.32
700 °C, 2 h	- 0.24	- 0.53	- 0.2	- 0.21	- 0.2	- 0.21	- 0.2	- 0.21
	- 0.34		- 0.46	- 0.32	- 0.46	- 0.32	- 0.26	- 0.32
			- 0.56	- 0.52	- 0.56	- 0.52	- 0.46	- 0.64
800 °C, 2 h	--	- 0.35	--	--	- 0.35	--	--	- 0.35
900 °C, 2 h	--	- 0.35	--	--	- 0.35	--	--	- 0.35
1000 °C, 2 h	- 0.32	- 0.37	- 0.46	- 0.29	- 0.44	- 0.32	- 0.54	--
			- 0.52		- 0.52			

Table 4.10: Redox potentials (V) vs Hg/$HgSO_4$ in 0.5 M K_2SO_4 of molybdenum nitride samples obtained by pyrolysis of the chloride precursor under the conditions shown. No features (--).

Redox potentials (V), at given scan rate (mV s^{-1})								
Scan rate	**100**		**25**		**10**		**2**	
	Ox.	Red.	Ox.	Red.	Ox.	Red.	Ox.	Red.
500 °C, (2 h)	--	--	--	--	- 0.18	- 0.44	- 0.34	- 0.4
500 °C, (12 h)	--	--	--	--	- 0.18	- 0.44	- 0.34	- 0.4
500 °C, (24 h)	--	--	--	--	- 0.18	- 0.47	- 0.34	- 0.42
500 °C, (48 h)	--	--	- 0.21	- 0.48	- 0.22	- 0.44	- 0.34	- 0.4
600 °C, (2 h)	- 0.34	- 0.4	- 0.38	- 0.27	- 0.24	- 0.27	- 0.22	- 0.23
						- 0.36	- 0.36	- 0.38
700 °C, (2 h)	- 0.19	- 0.29	- 0.23	- 0.25	- 0.23	- 0.25	- 0.22	- 0.23
			- 0.3	- 0.38	- 0.3	- 0.40	- 0.37	- 0.38
800 °C, (2 h)	- 0.19	- 0.29	- 0.23	- 0.25	- 0.23	- 0.25	- 0.22	- 0.23
			- 0.3	- 0.38	- 0.3	- 0.38	- 0.36	- 0.36
900 °C, (2 h)	- 0.18	- 0.28	- 0.23	- 0.25	- 0.23	- 0.25	- 0.23	- 0.25
			- 0.34	- 0.38	- 0.34	- 0.38	- 0.34	- 0.38
1000 °C, (2 h)	- 0.19	- 0.26	- 0.21	- 0.25	- 0.21	- 0.25	- 0.21	- 0.25
	- 0.32	- 0.37	- 0.32	- 0.38	- 0.32	- 0.38	- 0.32	- 0.38

4.6.2 Redox potentials of amide-derived MoN_x electrodes

Redox features for the samples obtained through pyrolysis of imide precursor source were visible in almost all the samples and at all scan rates. Redox features were at constant potentials for a specific scan rate in $H_2SO_{4(aq)}$ for various samples (Table 4.11). Three reduction peaks at - 0.12, - 0.23 and - 0.42 V and three oxidation peaks at - 0.19, - 0.3 and - 0.5 V were found consistently in all the samples at various scan rates. Redox features were observed to be weaker in the samples obtained at high temperatures. Redox features in $K_2SO_{4(aq)}$ (Table 4.12) were observed to be less prominent for the samples obtained at lower temperatures, though any peaks observed were at similar potentials to those observed in H_2SO_4. The sample obtained at 1000 °C showed very small redox peaks at any scan rates. The capacitance exhibited by these materials is mainly from redox processes in the surface region of the deposited active material; and there was always an interfacial double layer component of the capacitance, in parallel. Equal amounts of oxidation and reduction charge were passed in all curves indicating that reversible surface redox processes were occurring in the electrolytic cells.

Table 4.11: Redox potentials (V) vs Hg/$HgSO_4$ in 0.5 M H_2SO_4 of molybdenum nitride samples obtained by pyrolysis of the imide precursor under the conditions shown. No features (--).

	Redox potentials (V), at given scan rate (mV s^{-1})							
Scan rate	**100**		**25**		**10**		**2**	
	Ox.	Red.	Ox.	Red.	Ox.	Red.	Ox.	Red.
500 °C, 2 h	- 0.12	- 0.19	- 0.13	- 0.16	- 0.14	- 0.16	- 0.14	- 0.24
	- 0.23	- 0.3	- 0.24	- 0.29	- 0.25	- 0.24	- 0.23	- 0.3
	- 0.42	- 0.51	- 0.44	- 0.46	- 0.43	- 0.48	- 0.51	
500 °C, 48 h	- 0.13	- 0.18	- 0.14	- 0.17	- 0.15	- 0.16	- 0.15	- 0.16
	- 0.25	- 0.3	- 0.26	- 0.28	- 0.27	- 0.28	- 0.23	- 0.27
	- 0.43		- 0.54		- 0.45			
600 °C, 2 h	- 0.12	- 0.18	- 0.14	- 0.16	- 0.14	- 0.16	- 0.14	- 0.16
	- 0.23	- 0.3	- 0.26	- 0.27	- 0.25	- 0.27	- 0.27	- 0.27
	- 0.43	- 0.4	- 0.48	- 0.48	- 0.44	- 0.48		
700 °C, 2 h	- 0.15	- 0.17	- 0.15	- 0.17	- 0.15	- 0.16	- 0.15	- 0.16
	- 0.26	- 0.29	- 0.26	- 0.27	- 0.27	- 0.27	- 0.23	- 0.27
	- 0.46	- 0.47	- 0.46	- 0.47	- 0.44	- 0.48		
800 °C, 2 h	- 0.15	- 0.18	- 0.15	- 0.16	- 0.15	- 0.16	- 0.15	- 0.16
	- 0.26	- 0.29	- 0.26	- 0.26	- 0.26	- 0.26	- 0.24	- 0.27
	- 0.46	- 0.48	- 0.46	- 0.46	- 0.46	- 0.46	- 0.49	
900 °C, 2 h	- 0.15	- 0.18	- 0.16	- 0.18	- 0.26	- 0.19	- 0.22	- 0.25
	- 0.26	- 0.29	- 0.27	- 0.29	- 0.46	- 0.29	- 0.38	- 0.37
	- 0.46	- 0.48	- 0.46	- 0.49				
1000 °C, 2 h	- 0.26	- 0.27	- 0.26	- 0.27	--	- 0.27	--	--

Table 4.12: Redox potentials (V) vs Hg/HgSO$_4$ in 0.5 M K$_2$SO$_4$ of molybdenum nitride samples obtained by pyrolysis of the imide precursor under the conditions shown. (--) no features.

	Redox potentials (V), at given scan rate (mV s^{-1})							
Scan rate	**100**		**25**		**10**		**2**	
	Ox.	Red.	Ox.	Red.	Ox.	Red.	Ox.	Red.
500 °C, (2 h)	- 0.13	- 0.28	- 0.18	- 0.25	- 0.2	- 0.23	- 0.2	- 0.23
			- 0.29	- 0.41	- 0.29	- 0.37	- 0.35	- 0.37
					- 0.53		- 0.57	
500 °C, (48 h)	- 0.2	- 0.28	- 0.22	- 0.27	- 0.32	- 0.37	- 0.35	- 0.37
	- 0.32	- 0.41	- 0.33	- 0.37				
	- 0.53							
600 °C, (2 h)	- 0.18	- 0.30	- 0.2	- 0.27	- 0.2	- 0.24	- 0.22	- 0.24
	- 0.37	- 0.41	- 0.31	- 0.4	- 0.32	- 0.38	- 0.34	- 0.36
					- 0.54		- 0.57	
700 °C, (2 h)	- 0.18	- 0.28	- 0.21	- 0.22	- 0.24	- 0.24	- 0.34	- 0.24
	- 0.32	- 0.41	- 0.33	- 0.33	- 0.37	- 0.36		- 0.36
	- 0.52	- 0.59	- 0.52	- 0.53	- 0.57			
800 °C, (2 h)	- 0.18	- 0.28	- 0.21	- 0.26	- 0.24	- 0.25	- 0.22	- 0.24
	- 0.31	- 0.41	- 0.32	- 0.41	- 0.34	- 0.37	- 0.34	- 0.36
	- 0.52	- 0.59	- 0.53	- 0.57	- 0.55	- 0.57	- 0.57	
900 °C, (2 h)	- 0.2	- 0.27	- 0.32	- 0.25	- 0.33	- 0.37	- 0.35	- 0.36
	- 0.32	- 0.39	- 0.57	- 0.40			- 0.56	
	- 0.53							
1000 °C, (2 h)	- 0.25	- 0.28	--	--	--	--	--	--

The stability of the molybdenum nitride samples, which showed the highest capacitances (chloroimide-derived annealed at 500 °C for 2 h and amide-derived annealed at 600 °C for 2 h) were also tested for 1000 cycles (Fig. 4.21). Capacitance was maintained well through 1000 cycles, with only the amide derivative showing an initial drop of ~ 10 % in H$_2$SO$_4$, and even this system then stabilizing.

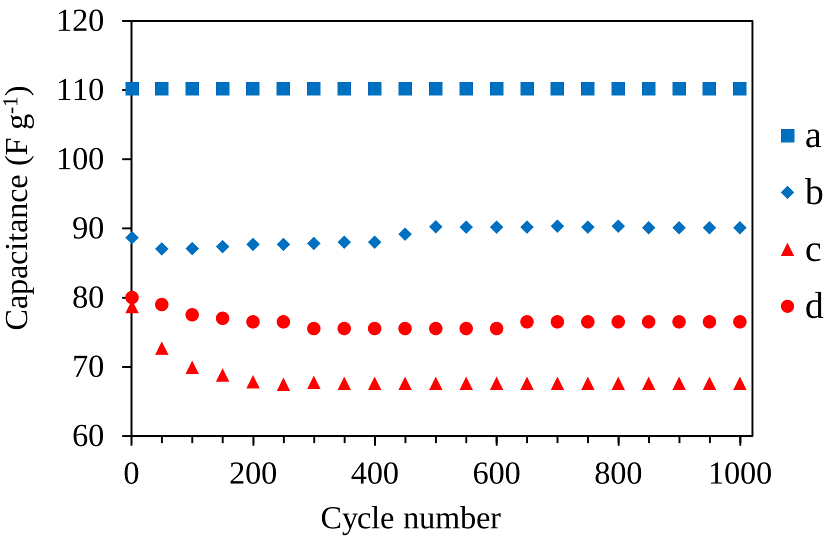

Figure 4.21: Variation in specific capacitance of chloroimide-derived molybdenum nitride (heating conditions 500 °C for 2 h) over 1000 charge/discharge cycles at 100 mV s^{-1} in $H_2SO_{4(aq)}$ (a) and $K_2SO_{4(aq)}$ (b) electrolyte, and imide-derived molybdenum nitride (heating conditions 600 °C for 2 h in $H_2SO_{4(aq)}$ (c) and $K_2SO_{4(aq)}$ (d).

4.7 Conclusions

Pyrolysis of chloroimide or imide polymer precursors under ammonia under various conditions yielded γ-Mo_2N or δ_1-MoN. Combustion microanalysis showed the chloroimide derivatives contained a small amount of chloride contamination at 500 °C, with some carbon at low temperature. The amide-derived material showed imide residues at 500 °C with short annealing times, while a small amount of contamination due to carbon was found at all other temperatures. TEM images showed spherical particles for chloroimide derivatives, while nano-tubes were observed up to 900 °C in imide derivatives. The highest surface area of 70 m^2 g^{-1} was observed for a chloroimide derivative at 500 °C annealed for 2 h. Surface area decreased with increasing annealing temperature or time at lower temperature. Imide derivatives were found to have surface areas below 10 m^2 g^{-1}. Specific capacitances were found to be higher for chloroimide derivatives in both the electrolytes. The highest capacitance of 275 F g^{-1} in $K_2SO_{4(aq)}$ or 202 F g^{-1} in $H_2SO_{4(aq)}$ was calculated for a chloroimide derived sample annealed at 500 °C for 2 h. Imide derivatives showed the highest capacitance of 166 F g^{-1} in K_2SO_4 at 2 mV s^{-1} for a sample obtained at 600 °C. Capacitance was found to be stable for chloroimide- or imide-derived MoN_x through 1000 cycles, only imide derivatives showed small initial drop in capacitance in sulphuric acid, which then stabilized.

4.8 References

1. A. G. Cairns, J. G. Gallagher, J. S. J. Hargreaves, D. Mckay, E. Morrison, J. L. Rico and K. Wilson, *J. Alloys Cmpds.*, 2009, **479**, 851.
2. H. Wang, W. Li and M. Zhang, *Chem. Mater.*, 2005, **17**, 3262.
3. W. E. Pickett, B. M. Klen and D. A. Papaconstantopoulos, *Physica*, 1981, **B 107**, 667.
4. Z. You-Xiang and H. Shou-An., *Solid State Commun.*, 1983, **45**, 281.
5. R. Fix, R. G. Gordon and D. M. Hoffman, *Thin Solid Films*, 1996, **288**, 116.
6. M. Nagae, T. Yoshio, Y. Takemoto and J. Takada, *J. Amer. Ceram. Soc.*, 2001, **84**, 1175.
7. P. Hones, R. Sanjines and F. Levy, *Surf. Coat. Technol.*, 1997, **94-95**, 398.
8. C. Wiemer, R. Sanjines and F. Levy, *Surf. Coat. Technol.*, 1996, **86-87**, 372.
9. S. Gong, H. Chen, W. Li and B. Li, *Catal. Comm.*, 2004, **5**, 621.
10. M. Nagai, T. Miyao and T. Tsuboi, *Catal. lett.*, 1993, **18**, 9.
11. J. Trawczy´nski, *Catal. Today*, 2001, **65**, 343.
12. E. J. Markel, S. E. Burdick, M. E. Leaphart-II and K. L. Roberts, *Catalysis*, 1999, **182** 136.
13. T. Kadono, T. Kubota and Y. Okamoto, *Catal. Today*, 2003, **87**, 107.
14. S. Ramanathan and S. T. Oyama, *Phys. Chem.*, 1995, **99**, 16365.
15. M. Nagai and T. Miyao, *Catal. Lett.*, 1992, **15**, 105.
16. S. Z. LI, J. S. Lee, T. Hyeon and K. S. Suslick, *App. Catal.*, 1999, **184**, 1.
17. M. Nagai, Y. Goto, A. Miyata, M. Kiyoshi, K. Hada, K. Oshikawa and S. Omi, *Catalysis*, 1999, **182**, 292.
18. H. He, H. X. Dai, K. Y. Ngan and C. T. Au, *Catal. Lett.*, 2001, **71**, 147.
19. H. Jehn and P. Ettmayer, *J. Less Common Metals*, 1978, **58**, 85.
20. T. Kawashima, E. T. Muromachi and P. F. McMillan, *Physica C*, 2007, **460**, 651.
21. L. C. Bull, T. Kawashima, P. F. McMillan, D. Machon, O. Shebanova, D. Daisenberger, E. Soignard, E. T. Muromachi and L. C. Chapon, *J. Solid State Chem.*, 2006, **179**, 1762.
22. P. Ettmayer, *Monatcsh Chem.*, 1970, **101**, 127.
23. D. A. Evans and K. H. Jack, *Acta. Cryst.*, 1957, **10**, 833.

24. H. Hehn and P. Ettmayer, *J. Less Common Metals*, 1978, **58**, 85.
25. M. B. Kanoun, S. Goumri-Said and M. Jaouen, *Phys. Rev.* , 2007, **76**, 134109.
26. G. Hagg, *Z. Phys. Chem.*, 1930, **B 7**, 339.
27. B. Cendlewska, A. Morawski and A.Misiuk, *J. Phys. F: Met. Phys.*, 1987, **17**, L71.
28. S. L. Roberson, D. Finello and R. F. Davis, *Thin Solid Films*, 1998, **324**, 30.
29. A. Wang, F. Capitain, V. Monnier, S. Matar and G. Demazeau, *J. Mater. Synth. Proces.*, 1997, **3**, 235.
30. M. Maoujoud, M. J. Offergeld and F. Bouillon, *App. Surf. Sci.*, 1993, **64**, 81.
31. K. Inumaru, K. Baba and S. Yamanaka, *App. Surf. Sci.*, 2006, **253**, 2863.
32. L. Hiltunen, M. Leskelä, M. Mäkelä, L. Niinistö, E. Nykänen and P. Soininen, *Thin Solid Films*, 1988, **166**, 149.
33. V. Miikkulainen, M. Suvanto and T. A. Pakkanen, *Thin Solid Films*, 2008, **516**, 6041.
34. V. Miikkulainen, M. Suvanto and T. A. Pakkanen, *Chem. Mater.*, 2006, **19**, 263.
35. Y. Wang and R. Y. Lin, *J. Mater. Sci. Eng.*, 2004, **112**, 42.
36. P. Chirico, A. L. Hector and B. Mazumder, *Dalton Trans.*, 2010, **39**, 1.
37. W. Lengauer, *J. Crystal Growth*, 1988, **87**, 295.
38. S.L.Roberson, D. Finello and R. F. Davis, *J. App. Electrochem.*, 1999, **29**, 75.
39. Li. Xue-Liang, X. Yan, W. Hua, W. Hua-lin, W. Wei-dong and C. Xiang-ying, *Trans. Nonferous Met. Soc. China*, 2009, **19**, 620.
40. K-Hoon Lee, Y-Woo Lee, A-Re Ko, G. Cao and K.-W. Park, *Am. Ceram. Soc.*, 2013, **96**, 37.
41. D. C. Bradley and M. H. Chisholm, *J. Chem. Soc*, 1971, 2741.
42. M. H. Chisholm, D. V. Baxter, G. J. Gama, F. Distasi, A. L. Hector and I. P. Parkin, *Chem. Mater.*, 1996, **8**, 1222.
43. D. Choi and P. N. Kumta, *J. Am. Ceram. Soc.*, 2011, **94**, 2371.
44. R. B. Von-Dreele and A. C. Larson, Generallized structure analysis system, Los Alamos National Laboratory, NM87545, USA, December 2002 release.
45. D.A. Fletcher, R.F. McMeeking and D. Parkin, *J. Chem. Inf. Comput. Sci.*, ICSD accessed via The United Kingdom Chemical Database Service: 1996, **36**, 746.
46. C. L. Bull, P. F. McMillan, E. Soignard and K. Leinenweber, *J. Solid State Chem.* , 2004, **177**, 1488.

47. A.Y. Ganin, L. Kienle and G.V. Vajenine, *J. Solid State Chem.*, 2006, **179**, 2339.
48. R. B. Von-Dreele and A. C. Larson, GSAS Manual, LANSCE MS-H805, Los Alamos National Laboratory, Los Alamos NM, NM 87545, 2000.
49. J.W. Li, D. Dzivenko, C. A. Zerr, Y. P. Fasel and R. R. Zhou, *Z. Anorg. Allg. Chem.*, 2005, **631**, 1449.
50. A. Salamat, A.L. Hector, B.M. Gray, S.A.J. Kimber, P. Bouvier and P.F. McMillan, *J. Amer. Chem. Soc.* , 2013, **135**, 9503.
51. K. Nakamoto, Infrared and Raman Spectra of Inorganic and Organic Compounds, 3rd ed.; J. Wiley: New York, 1978.
52. W. Y. Gang and Z. X. Gang., *Electrochem. Acta*, 2004, **49**, 1957.
53. T.C. Liu, W.G. Pell, B.E. Conway and S.L. Roberson, *J. Electrochem. Soc.*, 1998, **145**, 1882.
54. D. Finello, New Developments in Ultracapacitor Technology, Report no. WL-TR-95-7024, Wright Laboratory, Eglin Air Force Base, Florida, USA, 1995.
55. C. Chen, D. Zhao and X. Wang, *J. Mater. Chem.*, 2006, **97**, 156.
56. R.N. Reddy and R.G. Reddy, *J. Power Sources*, 2006, **156**, 700.

5 Synthesis of vanadium nitrides and use in supercapacitors

5.1 Introduction

Vanadium nitride is suitable for many uses due to its unique properties, including extreme hardness, wear resistance, excellent oxidative stability and corrosion resistance, high-temperature stability, electrical conductivity and electrodes for supercapacitors.[1-3] Vanadium nitride has also been studied as an important industrial catalyst for its selectivity and stability in hydroprocessing,[4, 5] hydrotreating[6, 7] and ammonia synthesis and decomposition.[8]

Three nitride phases for vanadium hcp β-V_2N_{1-y} (ε- Fe_2N type), fcc δ-VN_{1-x} (NaCl type) and δ′-VN_{1-x} ($V_{32}N_{26}$) have been reported with their structures, decomposition temperature, and ranges of homogeneity. Vacancies on the nitrogen sublattice were identified to be a reason for composition variation in these phases.[9, 10] Other intermediate phases with the stoichiometry of $V_{16}N$, $V_{13}N$, V_9N, V_8N, V_9N_2, and V_4N have also been reported, but it is believed that these phases are metastable if indeed they do exist.[9] The Structure of δ′-VN_{1-x} has not been unambiguously determined, however Onozuka, identified δ′-VN_{1-x} to have an ordered arrangement of N atoms with doubling of the lattice parameter of the NaCl-type structure after prolonged annealing of δ-VN_1.[11] Cluster approach studies of nitrogen vacancies and chemical bonding in sub-stoichiometric vanadium nitride (V_6N_{18}) show the existence of N vacancies lead to local lattice relaxation and rearrangement of the interatomic bonds in their neighbourhood; the appearance of strong V–V bonds through the vacancy site are known to exist as well. Vacancies on non-metal sites lead to the lowering of the total energy of the cluster and stabilization of the defect phase.[12] Single crystal X-ray diffraction studies of stoichiometric vanadium nitride NaCl type (space group *Fm*3*m* at 298 K) shows its transformation into a tetragonal (space group *P*42*m*) phase at 205 K. The phase transition at 205 K is presumably due to an electronic instability which leads to a clustering of the metal atoms into tetrahedral V_4 units.[13]

Different techniques have been developed to prepare vanadium nitride (VN), including the traditional carbothermal, reduction and nitridation of metal oxides with graphite, heating metal powder under nitrogen.[14] Vanadium nitride and oxynitride coatings were achieved on glass substrates from the reaction of VCl_4 and NH_3 at 350-650 °C through chemical vapour deposition.[15] The films deposited over 450 °C, were found to be crystalline with NaCl type structure. Vanadium nitride films have also been grown by other techniques such as N_2/H_2 plasma processing,[16] ion beam assisted deposition,[17] magnetron sputtering,[18] metal organic CVD[19], pulsed laser deposition,[20] reactive magnetron sputter deposition,[21] rapid thermal program,[22] and laser molecule or beam epitaxy.[23]

Conventionally, vanadium nitride powder is prepared by direct nitridation of pure metal or by carbothermal reduction of an oxide under ammonia or nitrogen atmosphere. Calka and Williams reported vanadium nitride through ball milling of vanadium under nitrogen atmosphere with a milling time of 60 h,[24] whereas the similar synthesis was carried out recently with a milling time of 8 h under pressure of nitrogen gas.[25] Vanadium metal is the certain impurity in the synthesis of metal nitrides via a mechanical milling procedure. Phase pure vanadium nitride powders have been prepared by microwave-assisted combustion reaction of a porous metal powder mixed with NH_4Cl under N_2 gas.[26]

Tripathy *et al.* prepared VN through stepwise carbonitrothermal reduction of V_2O_5. A Mixture of vanadium oxide, carbon and a binder was made into pellets and heated over 1000 °C under flowing nitrogen. Chemical analysis shows the residual carbon and oxygen in the form of some oxynitride/carbonitride/carboxynitride phase(s) even at higher temperature of 1500 °C. Reaction was vigorous and pellets were found disintegrated at 1600 °C. Another carbothermal synthesis using a mixture of V_2O_3 and pine charcoal (1:3) yielded VN at 1200 °C under flowing nitrogen, with silica as an impurity.[27] Choi et.al. synthesised the vanadium nitride and carbides via the TPR (Temperature program reaction) of V_2O_5 with NH_3 and a mixture of CH_4 in H_2, respectively.[8] Materials so obtained contained VN or VN with small amount of V_2O_3 after the nitridation of vanadium oxide. Carburization of vanadium oxide yielded V_8C_7. Vanadium nitride was prepared through a guanidine-route in a low temperature solid state reaction of ammonium meta-vanadate (NH_3VO_3), and guanidine carbonate ($NH_2C(NH)NH_2 \cdot 1/2\ H_2CO_3$ Reaction produces an intermediate of ammonium m-vanadate (GmV). GmV is transformed to rock salt type VN below 800 °C.[28]

Nanocrystalline vanadium nitride was synthesised by the reaction of VCl_4 and $NaNH_2$ at room temperature. Morphology of the final product shows the nanocrystals with hollow structures.[29] Nano-structured VN synthesised by two-step ammonolysis reaction of metal halide have also been studied as the electrode material for supercapacitors. Reaction between VCl_4 and NH_3 yields amorphous $V(NH_2)_3Cl$ and NH_4Cl, that transform to rock salt VN at 400 °C. Composition of the VN sample at 400 °C is found to be $VN_{1.08}O_{0.36}Cl_{0.1}$. High specific capacitance of a VN sample obtained at 400 °C with a surface area of 38.8 $m^2\ g^{-1}$ was reported to be 1340 $F\ g^{-1}$ at scan rate of 2 $mV\ s^{-1}$, and 554 $F\ g^{-1}$at 100 $mV\ s^{-1}$. VN obtained at 1000 °C having low surface area of 2.4 $m^2\ g^{-1}$ showed capacitance of 58.3 $F\ g^{-1}$ at 2 $mV\ s^{-1}$.[1]

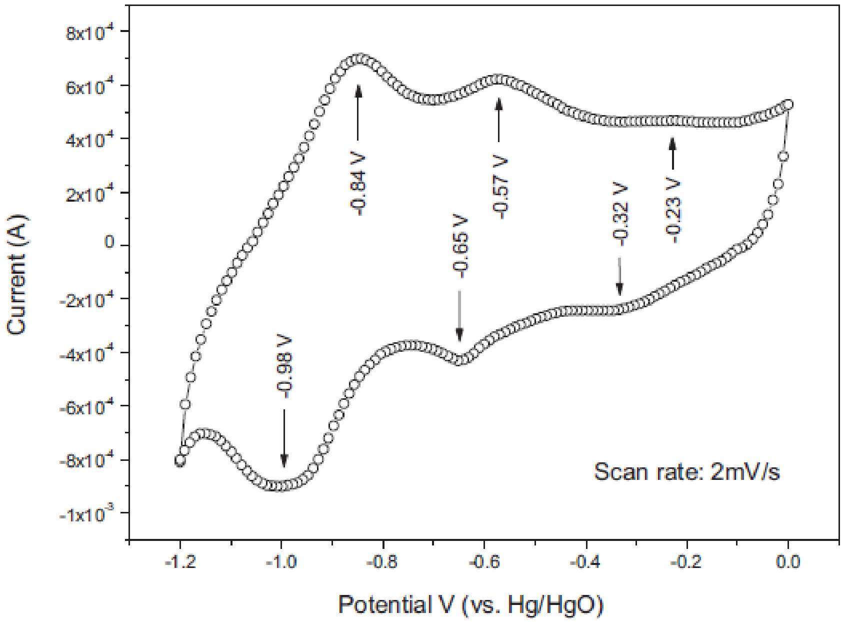

Figure 5.1: CV of VN nano-crystals synthesized at 600 °C scanned at 2 $mV\ s^{-1}$ in 1 M KOH.[1]

VN obtained by calcining V_2O_5 at xerogels under ammonia at 400 °C showed a specific capacitance of 161 $F\ g^{-1}$ at 30 $mV\ s^{-1}$ in a potential range of -0.95 to 0.15 V (1.1 V). The capacitance was found to decreased by 30 % of the original value when the scan rate was increased from 30 to 300 $mV\ s^{-1}$.[1] Vanadium nitride was synthesised by two step procedure involving mechano-chemical reaction of a V_2O_5 and Li_3N mixture induced by high energy mechanical milling followed by washing in water. Composition of the final vanadium nitride product is $VN_{0.8}O_{0.2}$. The crystalline VN thus synthesized has been analysed as a supercapacitor material in 1M KOH. It can be seen that the response changes from an almost square-like behaviour to more a distorted parallelogram as the scan rate increases. Both double layer and pseudocapacitor type response can be seen in the CV.[30]

In the current study two step ammonolysis of $V(NMe_2)_4$ was carried out to produce nano-crystalline vanadium nitrides. In the first step liquid ammonia was condensed over vanadium amide solution to form a polymeric precursor. The polymeric precursor was then heated under dry ammonia at different temperatures 300 - 1000 °C for 10 h at every temperature. Vanadium nitride powders were characterised and were used to test their charge/discharge behaviour and charge storage capacity using cyclic voltammetry.

5.2 Synthesis of vanadium nitride

Vanadium nitride samples were prepared from solution phase ammonolysis of $V(NMe_2)_4$. The procedure for $V(NMe_2)_4$ preparation is given below.

5.2.1 Synthesis of $V(NMe_2)_4$

$LiNMe_2$ (11.2 g) was taken in to a 1000 ml round bottom flask inside the glove box. The flask assembly was sealed, transferred to a fume hood and attached to a Schlenk line. 150 ml of dry EtO_2 and 100 ml of dry hexane were added to the $LiNMe_2$ and stirred until the amide was dissolved. 4.85 ml of VCl_4 was added to 50 ml of hexane in a 250 ml round bottom flask under nitrogen. The VCl_4 solution was slowly transferred to the ice cold $LiNMe_2$ solution using a cannula. The mixture was left stirring overnight at room temperature. LiCl was removed by filtration and the solvent was stripped off under vacuum until a dark green solid was obtained in the flask. The raw product was transferred to a sublimation tube fitted with a Young's tap for vacuum or nitrogen supply. The sublimation tube was then loaded into a tube furnace. The part of the sublimation tube that carries the raw material was placed in the centre of the tube furnace, while the 2nd half of the tube remained outside. The sublimation tube was cooled with dry ice, where the amide sublimes over the inner tube walls. ~ 8.5 g of $V(NMe_2)_4$, green colour, was sublimed out from the crude material at 80 °C, leaving behind ~ 1.5 g of the black chunky material un-sublimed. No efforts were made to identify the crude material left behind after the sublimation. The procedure was modified later on where hexane was used instead of benzene to overcome the solvent stripping off problem, the rest of the reaction conditions were kept the same. Using hexane increased the yield of $V(NMe_2)_4$ to 8.5 g due to enhancement in solvent removal step before sublimation. Vanadium amide obtained using hexane was used for materials discussed in chapter 7. Elemental analysis of the sample showed C 40.4 %, N 23.32 % and H 9.63 % which was close to theoretical composition of $V(NMe_2)_4$ with C 42 %, N 24.6 % and H 10.6 %.

5.2.2 Solution phase ammonolysis of $V(NMe_2)_4$

The reaction was carried out using a Schlenk line. ~20 ml of liquid ammonia was distilled into a solution of 2 g tetrakis(dimethylamido)vanadium in THF (20 ml) under nitrogen at -78 °C with continuous stirring. The reaction mixture was left to come to room temperature as the excess ammonia evaporated. The black precipitate of vanadium amide polymer ~ 0.8 g was then filtered and dried under vacuum.

5.*2.3 Pyrolysis of the polymeric vanadium amide precursor*

The polymer was then transferred to a ceramic crucible (boat shape) inside a silica tube, which was loaded inside the glove box. The silica tube was provided with an arrangement of taps to allow flushing of the hoses before the sample was exposed to the gas flow. The sample tube was then heated under flowing ammonia to 300 to 1000 °C at a step of 100 °C, separately for the duration of 10 h each. The heating ramp rate was set at 1 °C/min. A column of molecular sieves (synthetic zeolite) Ǻ, was used to trap the moisture of ammonia.

5.3 Analysis of polymeric precursor

Elemental analysis of the polymeric precursor showed, % C = 10.56 % H 3.02, N = 16.49, that give rise to the composition of $VN_{0.87}C_{0.65}H_{2.2}$.

The FTIR spectrum for the polymeric precursor (Fig. 5.2) shows a broad peak at 3215 cm^{-1} which demonstrates the presence of ν (NH).[31] Low intensity peaks in the range of

3000-2860 cm^{-1} are attributed to ν (CH). The absorption peak at ca. 1631 cm^{-1} is for δ (NH_2)[31, 32] and the peak at ca. 1263 cm^{-1} may be ν (CN). The strong band at 806 cm^{-1} is assigned to ν (M-N).[31]

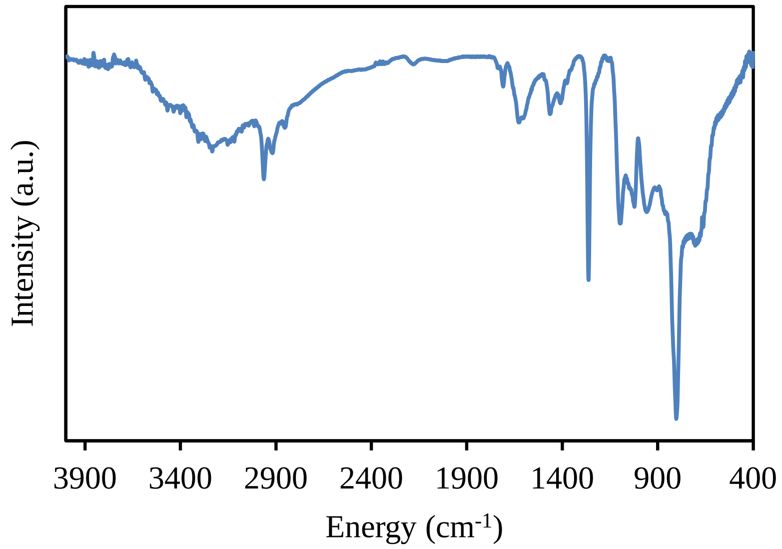

Figure 5.2: IR spectrum for the polymeric vanadium precursor.

Thermogravimetric analysis (TGA) (Fig. 5.3) for the polymeric precursor was obtained by annealing the polymer to 900 °C at a ramp rate of 10 °C/min under Ar flow of 50 ml min^{-1}. Previous studies using TGA-MS[31] showed that loss of amine and ammonia due to further condensation reactions is observed at lower temperatures. A total of ~ 28 % mass loss is observed in the analysis at this temperature profile. The TGA curve shows a two-step mass loss; the first step starting at lower temperature and ending at ~ 500 °C is due to amide and some NH_3 decomposition. The 2nd step which starts at ~ 550 °C is due to reduction of metal, where N_2 removal as well as ammonia loss due to further condensation takes place.[31]

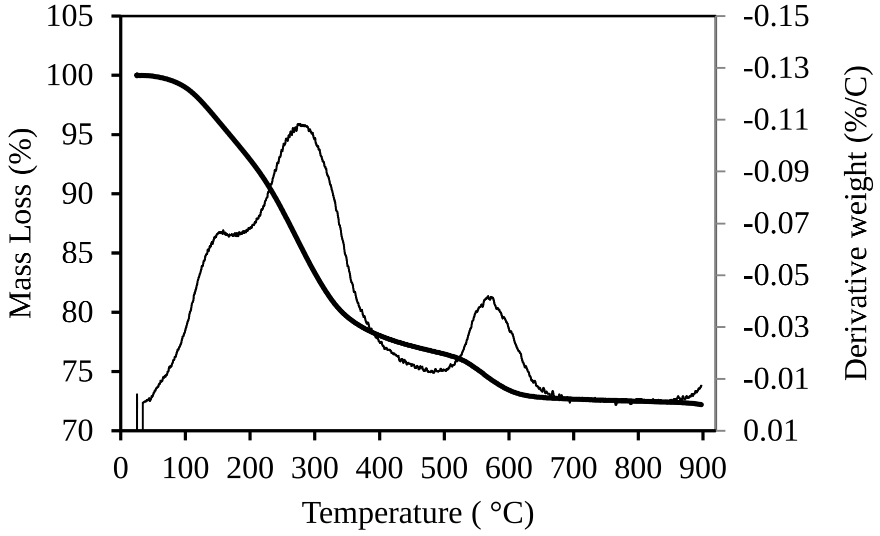

Figure 5.3: TGA curve for the polymeric vanadium precursor and the first derivative.

5.4 Analysis of VN_x samples

Thermogravimetric analysis (TGA) was carried out under 60 ml flow of Ar. Samples were heated to 900 °C at 10 °C/min ramp rate. TGA curves (Fig. 5.4) show two step mass losses. During the first step at lower temperature (100-500 °C) the mass loss corresponds to amide group elimination of the surface adsorbed ammonia. Mass loss over 600 °C corresponds to nitrogen loss from the nitride material.[31] The sample obtained at 300 °C showed 17 % , while sample obtained at 400 °C showed ~ 9 % mass loss that suggest the presence of organic groups in the final VN samples. The VN samples obtained at higher annealing temperature showed no mass losses at lower temperature in the TGA curves.

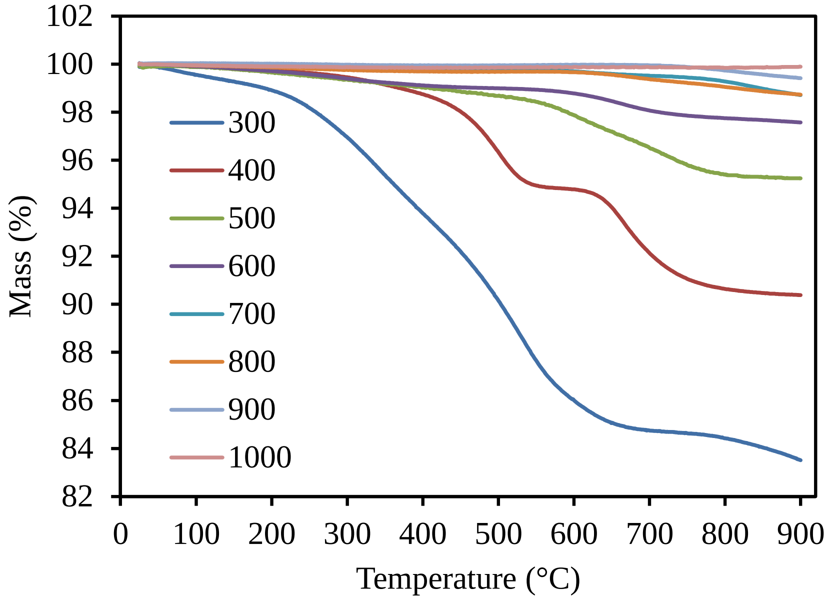

Figure 5.4: TGA curves for VN samples at the given temperature (°C).

IR spectra (Fig. 5.5) show low intensity absorption peaks at 3430-3450 cm^{-1} which corresponds to residual ν (NH).[31] These are not visible in the sample obtained at higher temperature. Weak peaks at 1580-1610 cm^{-1} in the samples annealed at 600 to 1000 °C, and in the samples annealed at 500 °C for shorter times, could be attributed to δ (NH_2).[31, 32] The absorption band observed in all samples at ~ 800 cm^{-1} is attributed to ν (M-N).[31]

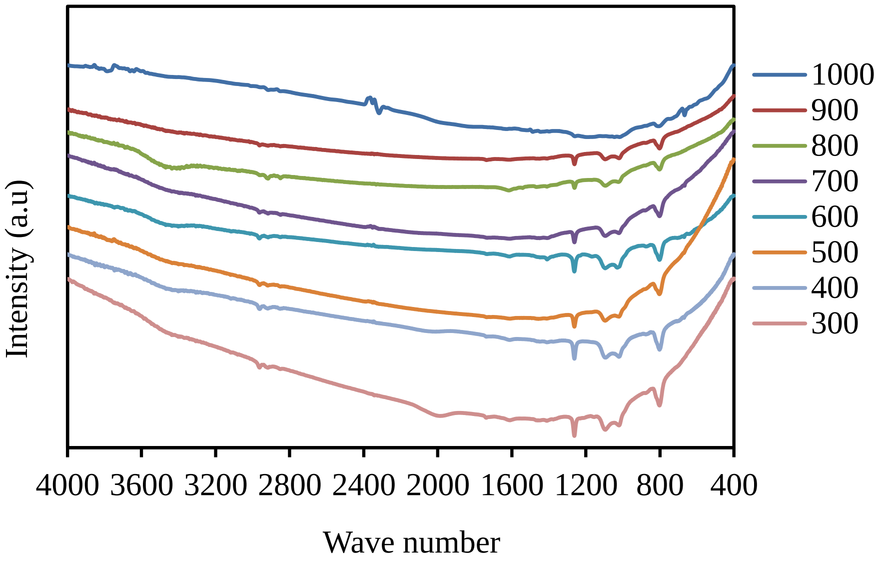

Figure 5.5: IR spectra for the VN samples obtained at given temperature (°C)

Carbon contamination in transition metal nitrides is an important consideration because it degrades electrical and optical properties and often causes adhesion problems.[33] However, carbon contents in transition metal nitrides increase the hardness of the material.[34] Carbon contents (Table 5.1) were found to be <0.64 %, and decreased with increasing annealing temperature of the metal nitrides. Small quantities of hydrogen were observed in the samples obtained at 500 °C and below this temperature. Samples obtained at 400 °C and below were found to be nitrogen rich. The presence of hydrocarbons in the samples at lower temperature suggests that not all the precursor is decomposed at lower temperature.

Table 5.1: Elemental analysis for the VN samples obtained at different temperature.

Temperature (°C)	%C	%H	%N	Composition
300	3	1.30	25.84	$VN_{1.4}C_{0.2}H_{0.96}$
400	2.68	0.89	23.88	$VN_{1.2}C_{0.14}H_{0.64}$
500	1.84	0.55	19.42	$VN_{0.9}C_{0.1}H_{0.35}$
600	0.71	<0.10	19.42	$VN_{0.9}C_{0.06}$
700	0.73	<0.10	19.76	$VN_{0.91}C_{0.034}$
800	0.42	<0.10	21.21	$VN_{0.99}C_{0.02}$
900	0.54	<0.10	20.20	$VN_{0.94}C_{0.03}$
1000	0.39	<0.10	20.87	$VN_{0.98}C_{0.02}$

PXD and PDF patterns were collected using the synchrotron radiation at Diamond light source Oxfordshire. Samples were sealed inside the glove box, in Kapton tubes of 2 cm long and 3 mm to collect the patterns.

PXD patterns (Fig. 5.6) for the vanadium nitride samples show crystalline rock salt structure at 500 °C and above this temperature. Peaks are broader in the patterns obtained for the samples at lower temperature, where an enlargement of the angle between 111 and 200 can be seen.

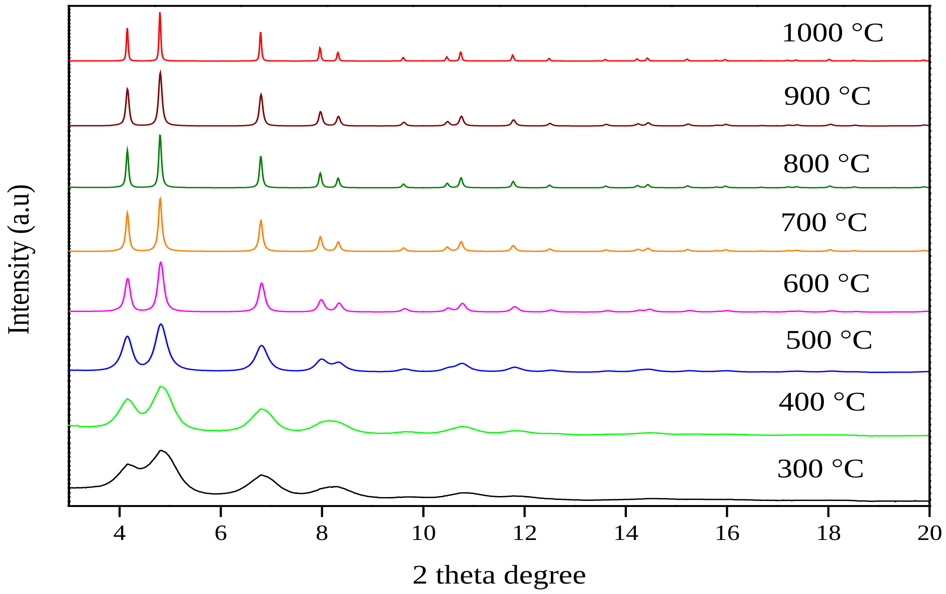

Figure 5.6: PXD patterns for the VN samples obtained at the temperatures given in the figure.

Rietveld refinement of PXD data (Fig. 5.7) for the phase pure vanadium nitride samples obtained at 1000 °C gives a good fit to the rock salt structure in space group *Fm*3*m*, with the a lattice parameter of a = 4.135 Å. A cif file[35] with the standard parameters was obtained from ICSD.[36] Patterns were refined using the GSAS.[37] Rietveld refinement of the samples obtained at 500 °C and above found lattice parameters in the range of 4.113 – 4.135 Å which are in good agreement with the bulk lattice parameter of cubic VN.[35, 38, 39] PXD patterns obtained at 300 °C were refined using the CW profile function 4 of GSAS[40] to allow modelling of microstrain broadening of the peaks. Local variation in the V occupancy due to defect structure affect directions parallel to the V-N bonds most strongly, hence $S_{400} > S_{220}$. These strains are averaged out along the 3-fold axis, as required to maintain cubic symmetry. Profile function 4 of the GSAS uses a successful description of the reflection asymmetry due to axial divergence described by Finger, as an implementation of the peak shape function.[41] This function also uses the microstrain broadening description as explained by Stephens.[42] Microstrain in the nanoparticles occurs due to imperfections within the crystalline lattice, including vacancies, dislocations and stacking faults. Crystallite sizes were in the range of 2-23 nm (Table 2), smaller at lower annealing temperature. Broadening of peaks at lower temperature suggests that some of the vanadium nitride sample remains uncrystallised which was confirmed through elemental analysis and thermogravimetric analysis.

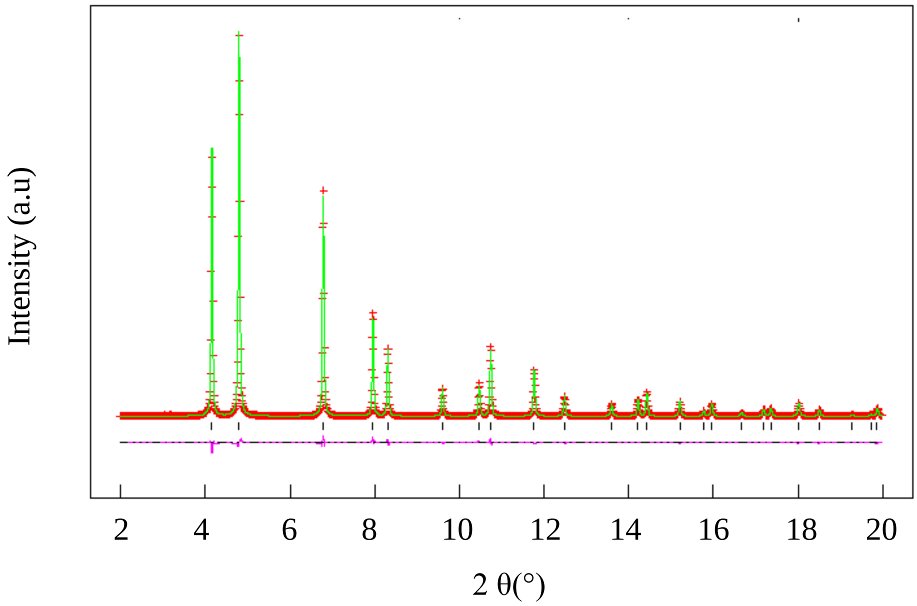

Figure 5.7: Rietveld fit to the PXD data for the phase pure VN obtained by pyrolysis of polymeric vanadium precursor at 1000 °C in ammonia for 10 h. Crosses mark the data points, upper continuous line the calculated profile and lower continuous line the difference; tick marks are the allowed reflection positions of NaCl type VN. Data was been collected using synchrotron radiation with a wave length of 0.17 Å.

Fitting the data for the samples obtained at 400 or 300 °C (Fig. 5.8) gave the rock salt lattice with lower values than the standard 4.13 Å (Table 5.2). Similar values for lattice parameters were reported by Choi et al.[1] for a sample obtained by ammonolysing VCl_4 at 400 °C, where the structure defects were claimed to be due to some oxygen atoms penetrating into the lattice, since cubic VO with a lattice parameter a = 4.08 Å can form a solid solution at the interface region between VN and the surface VO_x layer.[43] The structural defects in VN samples obtained at lower temperatures could be due to the partial substitution of nitrogen atoms with residual carbon atoms in the VN, or the occupancy of interstitial sites in the VN lattice by residual carbon atoms. Low values for a cubic VN nitride (a = 4.09 Å) have also been reported[25] for the samples obtained after nitridation of vanadium for short milling time under nitrogen, as the refinement of crystallite size, the formation of defects, and microstrain develops.[44] Previous studies for non-stoichiometric transition metal nitrides have reported that the *a* parameter is very sensitive to the nitridation level.[45-47]

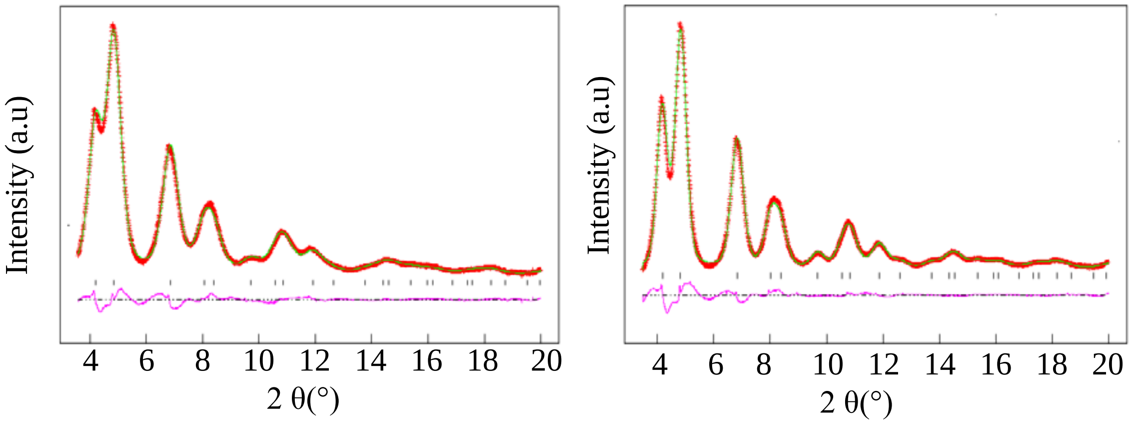

Figure 5.8: Rietveld fits to the PXD data for the phase pure VN obtained by pyrolysis of a polymeric vanadium precursor at 300 (left) and 400 °C (right) in ammonia for 10 hr. Crosses mark the data points, upper continuous line the calculated profile and lower continuous line the difference, tick marks are the allowed reflection positions of NaCl type VN. Data was been collected using synchrotron radiation with the wave length of λ 0.17.

Table 5.2: Refined lattice parameters for VN obtained at the given temperature.

Sample (°C)	a (Å)	R_w/R_p (%)	Crystallite size (nm)	V U_{iso} ($Å^2$)	N U_{iso} ($Å^2$)
300	4.077(3)	2.4/1.9	2	0.008	0.004
400	4.0968(16)	4.8/3.5	3	0.007	0.003
500	4.1132(9)	5.8/4.7	6	0.006	0.003
600	4.1197(4)	6.1/4.3	11	0.006	0.003
700	4.1311(2)	5 /3.4	14	0.006	0.003
800	4.1322(4)	4.8/3.9	16	0.006	0.005
900	4.1324(1)	4.3/3.2	19	0.006	0.005
1000	4.1356(0)	3.7/2.8	23	0.006	0.006

The crystal structure was also used to fit the PDF data of the vanadium nitride samples. Data was collected at room temperature to make a comparison with the Rietveld refinement of PXD data. PDF diffraction patterns were refined using the PDFgui[48] software. PDF fits for the vanadium nitride samples obtained at 300 - 1000 °C are shown in figures 5.9 and 5.10. All the samples have been refined using the same structure file for rock salt vanadium nitride that has been fitted to the PXD patterns. PDF patterns for the samples obtained at 600 °C and above were been refined to maximum r-range of 0-60, 500 °C to 0-40 while the range is reduced to 0-20 for the 300 and 400 °C samples, where no structure reflections were obtained above this range. Lattice parameters obtained from PDF (Table 5.3) had a similar pattern in vanadium nitride samples, with lower values for the samples obtained at lower temperature. Goodness of fit R_{wp} values of refined PDF data were slightly higher than the values obtained for refined Rietveld data. Numerical values of R_{wp} are normally higher for PDF data than the same quality Rietveld data. Crystallite size calculated through Rietveld refinement is similar to that from PDF analysis for the vanadium nitride samples obtained at lower temperature while slightly higher for high temperature samples.

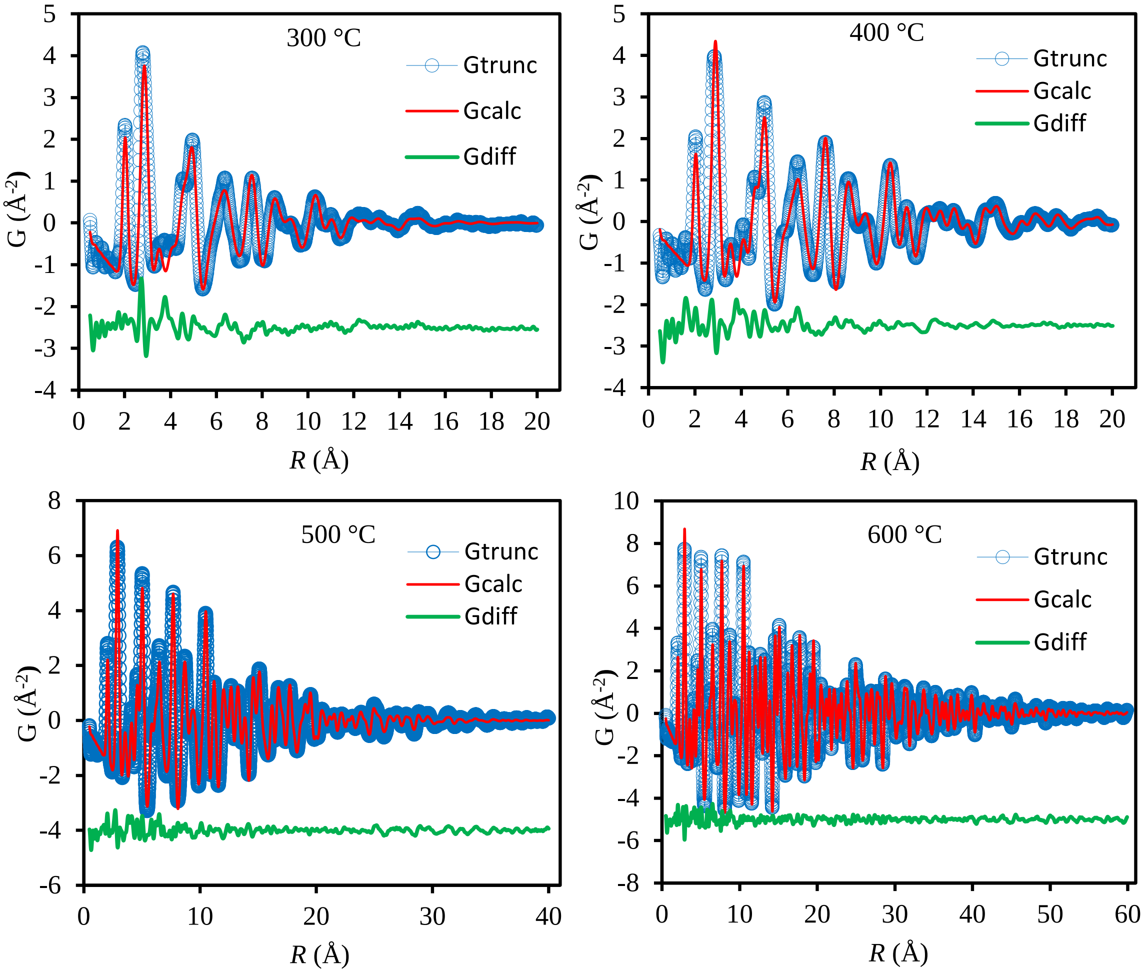

Figure 5.9: PDF fits to the diffraction data collected for vanadium nitride samples obtained at the given temperatures.

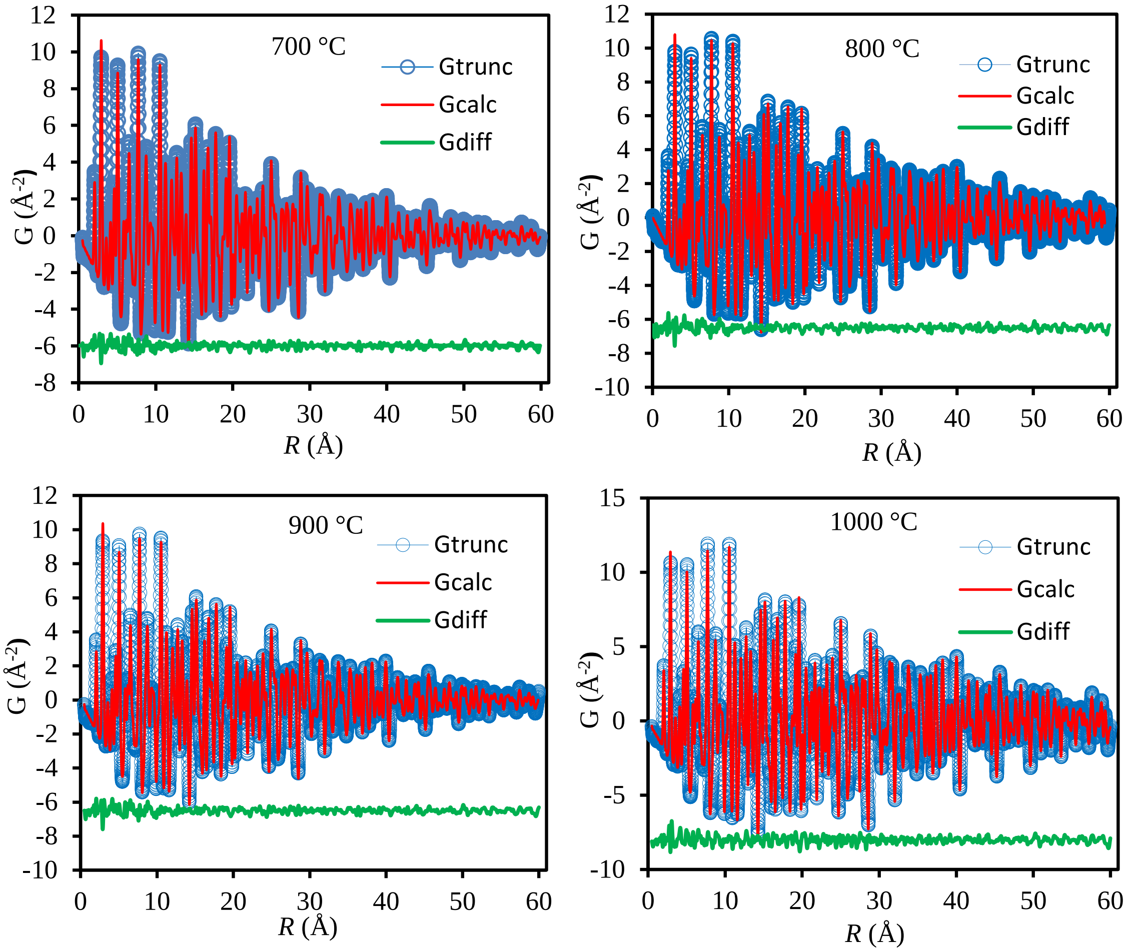

Figure 5.10: PDF fits to the diffraction data collected for vanadium nitride samples obtained at the given temperatures.

Table 5.3: Parameters from the refinement of PDF data of vanadium nitride samples at the given temperatures (°C).

Sample	a (Å)	R_{wp}	Sp-Diameter (nm)	V U_{iso} (Å^2)	N U_{iso} (Å^2)
300	4.0674	0.232	3.1	0.03	0.028
400	4.0984	0.210	3.7	0.022	0.017
500	4.1224	0.164	4.9	0.014	0.012
600	4.1237	0.098	8.1	0.011	0.010
700	4.1313	0.099	8.5	0.009	0.008
800	4.1318	0.09	9.1	0.008	0.007
900	4.1346	0.07	10.7	0.008	0.007
1000	4.1412	0.06	16.1	0.007	0.006

Comparison between the refined values of the lattice parameters through Rietveld or PDF data (Fig. 5.11, left) shows the values are similar for most of the vanadium nitride samples up to the first decimal. A graph making a comparison of refined crystallite size (Fig.5.11, right) reveals lower values obtained through Rietveld refinement than the PDF data refinement.

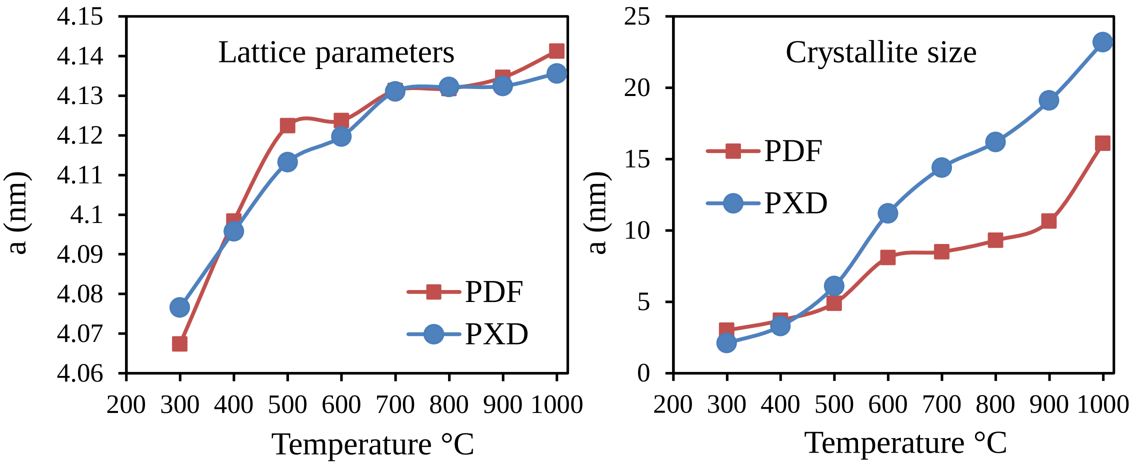

Figure 5.11: Graph showing the refined lattice parameter and crystallite size from PDF data or PXD data in vanadium nitride samples.

Thermal parameters (Fig. 5.12) for metal or non metal was higher when derived from PDF data, while lower through Rietveld refinement. Thermal vibration in Rietveld refinement for nitrogen atom or vanadium atoms for all the samples remained unchaged.

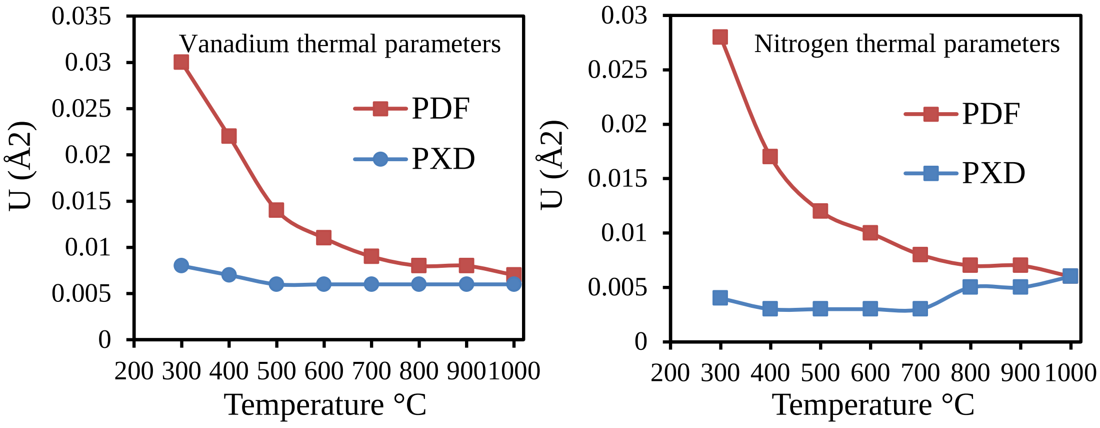

Figure 5.12: Graphs showing refined values of thermal parameters from PDF or PXD data for metal or nitrogen in vanadium nitride samples.

Surface areas (Table 5.4) for the samples lay in the range of 5-9 $m^2\ g^{-1}$, with the highest surface area of 9 at 600 °C. Pore diameter for all the samples was in the mesoporous range. The error estimation for surface area values was found to be ± 1 $m^2\ g^{-1}$ and for PSD ± 1 Å.

Table 5.4: Surface areas and pore diameters of the VN samples at the given temperature

Temperature (°C)	S_{BET} ($m^2\ g^{-1}$)	PSD (Å)
300	5	20-45
400	4	20-45
500	6	34
600	9	27
700	6	29
800	7	34
900	7	31
1000	7	31

Figure 5.13 shows the adsorption/desorption isotherms and figure 5.14 is the PSD of samples annealed at the given temperatures. Hysteresis loops show a type IV isotherm. At higher pressures the slope shows increased uptake of adsorbate as pores become filled. Isotherms for VN samples shows distinct capillary condensation step at ~ 0.5 P/P_o, which is attributed to well-developed mesoporous structure.

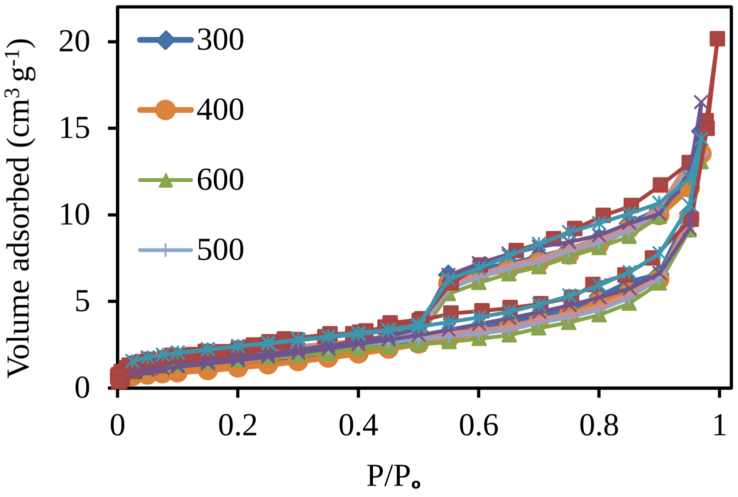

Figure 5.13: Nitrogen adsorption/desorption isotherm of VN_x samples at the given temperatures (°C).

Samples obtained at lower temperature showed multiple peaks in the measoporous and microporous range (Fig. 5.14).

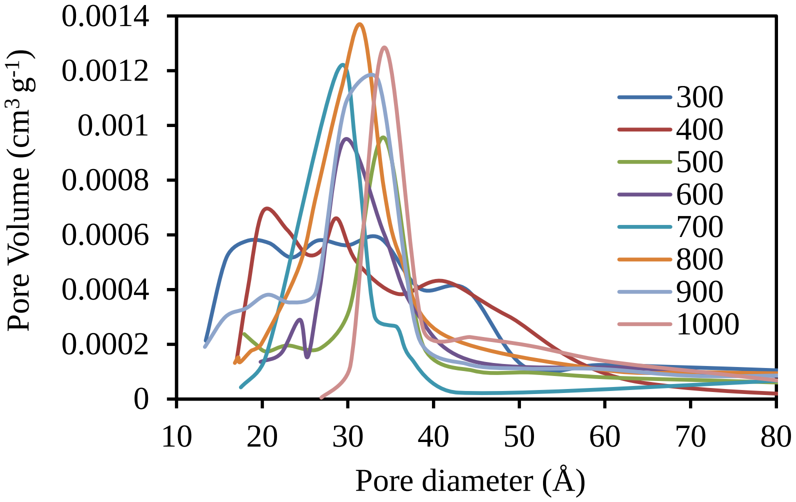

Figure 5.14: BJH pore size distribution of vanadium nitride samples at the given temperatures (°C).

Transmission electron microscopy (TEM) images (Fig. 5.15, 5.16) show the particles in the size range of 3 to 30 nm of spherical shape Particle sizes are similar as calculated through Rietveld or PDF refinement. Particles are spherical in shape and largely agglomerated due to long annealing time.

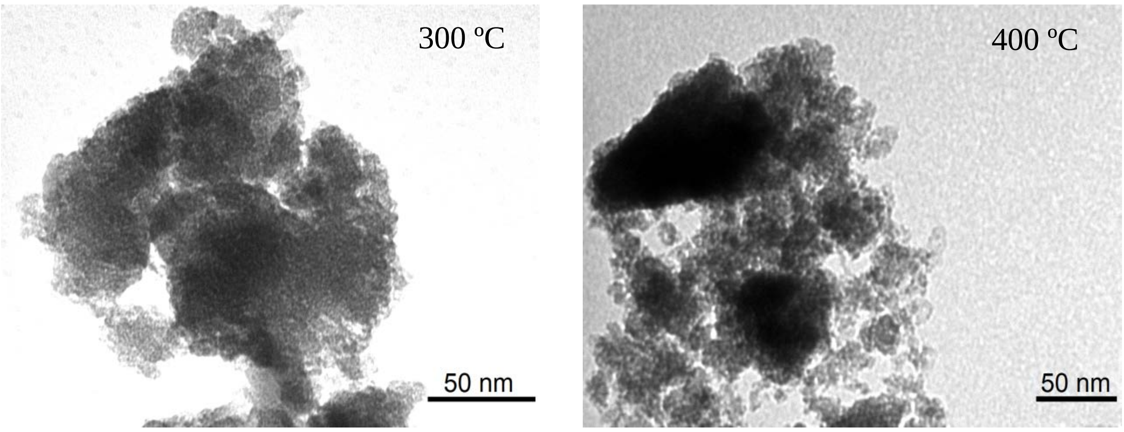

Figure 5.15: TEM images of VN samples obtained at the temperatures as labelled.

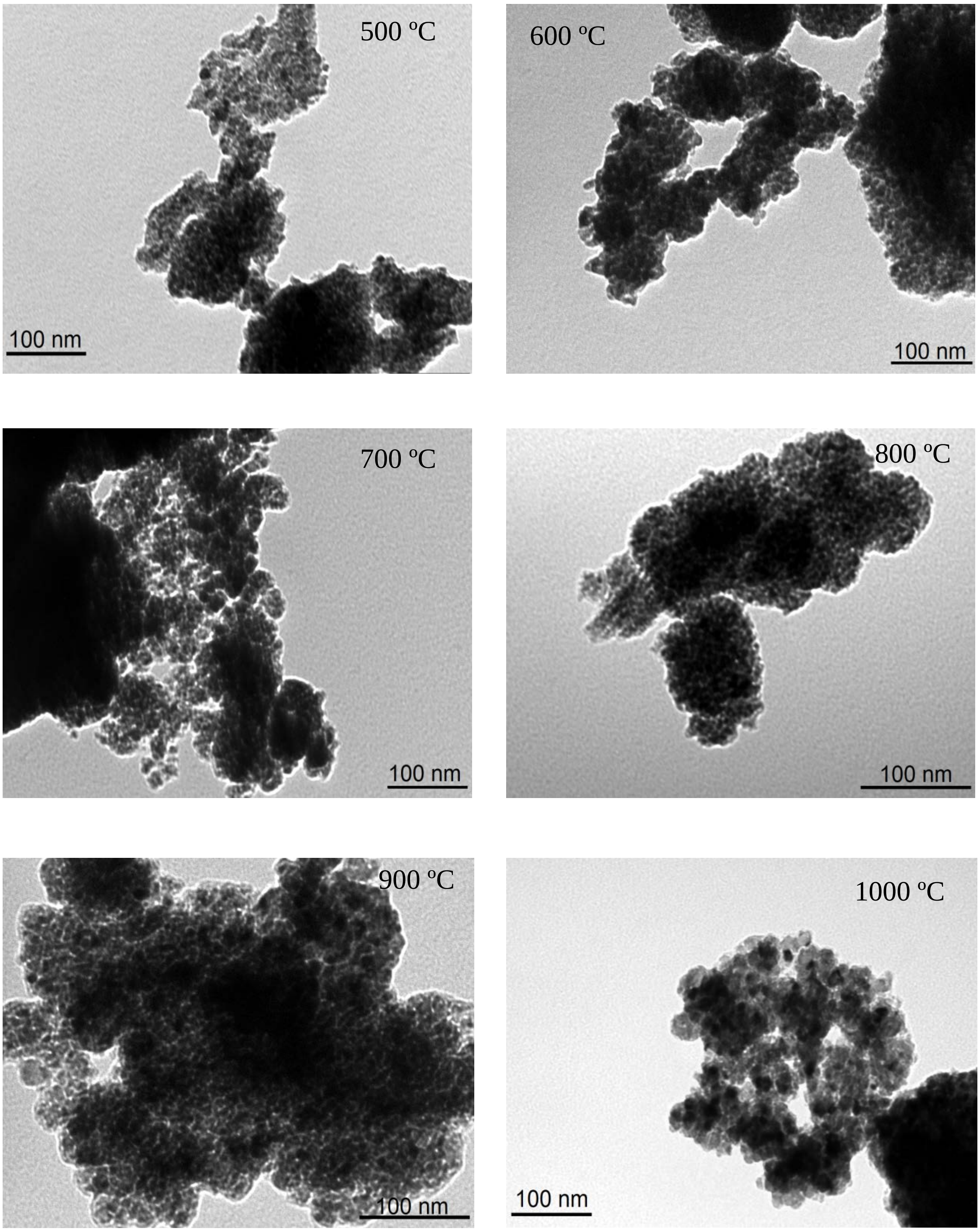

Figure 5.16: TEM images of VN samples obtained at the temperatures as labelled.

5.5 Capacitance measurements

Cyclic voltammetry is carried out to measure the capacitance of vanadium nitride samples. Electrodes are made using an ink-based method.

5.5.1 Preparation of electrode ink

Electrode inks were prepared by grinding together 75 wt.% of VN_x and 20 wt.% of acetylene black. PVDF wt. 5 % was fully dissolved in 1.5 ml of CP (Cyclopentanone) by stirring the solution for 4 hours. The mixture of VN_x and carbon black is added to PVDF solution and stirred overnight to obtain the electrode ink.

5.5.2 Ink deposition on the Ti substrate

Titanium foil was used as the substrate (1 × 2 cm pieces, 0.05 μm thickness, Advent research materials, Oxford, England). Any surface oxides were removed from the foil by rubbing the surface with abrasive paper. The substrate was cut into pieces, washed with ethanol and dried in air. Working electrodes were made by depositing electrode ink by pouring drops over the substrate of 1 × 1 cm area of the foil and leaving to dry at room temperature for at least 2 hours. The electrodes were finally dried over night at 120 °C under vacuum. ~ 0.6 mg of the electrode material was measured on each foil after drying.

5.5.3 Cyclic voltammetry

Cyclic voltammetry (CV) used three electrode cells with a 1M $KOH_{(aq)}$ filled Hg/HgO reference electrode and a high surface area platinum gauze counter electrode. A potential window for VN_x samples was set by running the electrode in various voltage ranges at the sweep rate of 100 mV s^{-1} (Fig. 5.17). Based on the redox behaviour (oxidation and reduction tail end) observed and with maximum columbic efficiency, a potential window of 0 to – 1.2 V was chosen for running the electrodes of all the samples to compare the charge storage ability.

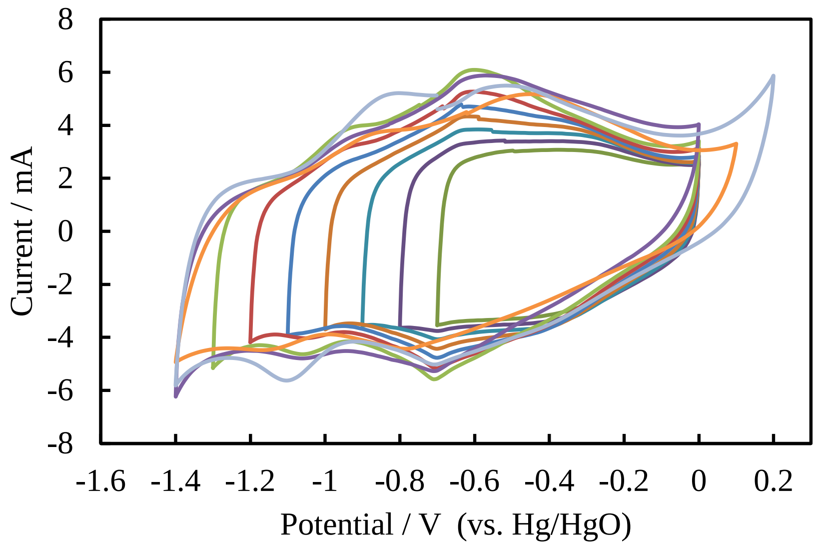

Figure 5.17: Cyclic voltammograms of VN samples obtained at 800 °C at different potential ranges, at the scan rate of 100 mV s^{-1}, in 1 M KOH.

Choi et al.[1] described the supercapacitive mechanism of nano-crystalline vanadium nitride as arising from a combination of an electrical double-layer formation and the Faradaic redox reaction reactions that occur on a partially oxidised nitride surface. In the presence of OH^- ions, an equilibrium reaction can occur on the nitride or oxy nitride surface as below:

$$VN_xO_y + OH^- \leftrightarrow VN_xO_y\|OH^- + VN_xO_y - OH$$

Where $VN_xO_y\|OH^-$ represents the electrical double layer formed by the hydroxyl ions absorbed on non-specific sites wherein a large increase in specific capacitance arises primarily due to successive oxidation by the hydroxyl species on the VN_xO_y surface due to electron transfer across the double layer.

Voltammograms of vanadium nitride samples obtained at 300 to 1000 °C are shown in figure 5.19 to 5.26. The electrodes were run for 100 scans at 100 mV s^{-1} and 10 scans each at 50, 20 and 2 mV s^{-1}. Capacitance measured for all the vanadium nitride samples are given in table 5.5.

Specific capacitance in F g^{-1} is measured using the following equation:

$$C = \frac{\int IdV}{\mathrm{S} \times 2 \ \times \mathrm{V} \ \times \mathrm{m}}$$

Capacitance was increased in most of the vanadium nitride samples at all the scan rates with the number of scans as the oxide surface developed (Table 5.5). The samples prepared at lower temperature showed a decrease in capacitance with scan number that could be due to lack of stability that we know may be present from the TGA and elemental analysis, or could be due to small particles fully converted to oxides and hence the conductivity is lost. The decrease in capacitance with scan number was less in the 400 °C sample than 300 °C as the carbon contents were reduced and the sample retained structure stability. Both the samples at lower temperatures have strong oxidation peaks in the CV (Fig. 5.19 and 5.20) at 2 mV s^{-1} contrary to rest of the samples. The capacity increased by an average of 40 % up to 100 scans in the samples obtained at 500 and 600 °C, while this increase was reduced to 25 % in the sample obtained at 1000 °C at 100 mV s^{-1} as the crystallite size of vanadium nitrides increased. The average capacitance increase was 7 % at the lower scan rates up to the 10th scan in all the vanadium nitride samples, except the samples obtained at lower temperature showed drop in capacitance (Table 5.5). The sample obtained at 600 °C showed a higher capacity than any other sample at any scan rate, and where this sample showed a 43% increase of capacity from 100 to 2 mV s^{-1} measured at 2nd scan at each scan rate. Choi et al.[1] reported the highest capacity of 1340 F g^{-1} for a VN sample at 2 mV s^{-1} that is 73 % higher than our material when measured at the same scan rate, where our sample is 23 % lower in surface area. Lower capacity in our VN samples could be due to the presence of carbonaceous contaminants into the crystal lattice. Percent reduction of capacitance between the scan rates can be illustrated in the following order 2 > 20 > 50 > 100.

Table 5.5: Capacitance measurements in F g^{-1} in 1 M KOH vs Hg/HgO reference electrode, for the VN samples obtained at the given temperatures.

Scan rate (mV s^{-1})	**100**			**50**		**20**		**2**	
Scan number	**1**	**10**	**100**	**1**	**10**	**1**	**10**	**1**	**10**
300 °C	35	30	2	42	28	47	20	51	26
400 °C	26	22	11	34	30	38	34	28	21
500 °C	39	42	70	34	34	36	39	31	35
600 °C	52	53	88	60	65	71	86	91	98
700 °C	42	43	55	58	63	67	71	84	90
800 °C	36	39	51	42	47	45	49	67	71
900 °C	17	18	21	24	29	26	31	35	39
1000 °C	18	19	24	20	21	22	23	29	36

Plotting a graph (Fig. 5.18) between charge capacities against the scan number of the vanadium nitrides samples obtained at different temperatures reveals that only the samples obtained at lower temperatures show drop in capacitance through 100 cycles.

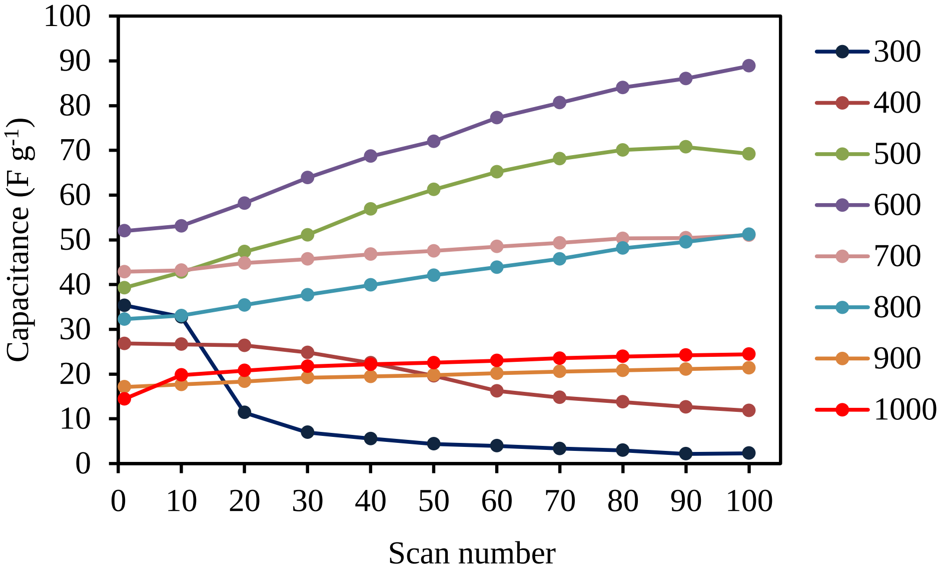

Figure 5.18: Variation of specific capacitance of vanadium nitrides (obtained at temperatures given in, (°C) over 100 charge and discharge scans at 100 mV s^{-1} in 1 M KOH vs Hg/HgO reference electrode.

Voltammograms for the samples obtained at 300 °C (Fig. 5.19 – 5.26) show weak redox features at higher scan rate, while the redox features seem to disappear at lower scan rates. Oxidation or reduction tails can be seen for this sample, i.e. the electrode material is not stable in the given potential range, resulting in large capacitance reduction with scan number. Weak redox features can be seen in the CVs for the vanadium nitride sample obtained at 400 °C up to 20 mV s^{-1}. All the samples above 400 °C showed similar shape of the CVs at any scan rate with prominent redox features at similar potentials. Some of the redox features seems to be flattened or less prominent at lower scan rates. Percent columbic efficiencies are measured from the voltammograms by dividing the $Q_{discharge}$ by Q_{charge} and taking the percentage, where $Q_{discharge}$ and Q_{charge} are the integrated areas below or above the potential axis respectively. The charge efficiency of the vanadium nitride sample at 300 °C is ~ 40 % at 2 mV s^{-1} while ~ 70 % at higher scan rates, though the efficiency increased to 85 and 92 % at the respective scan rates after the first few cycles. Columbic efficiency for the vanadium nitride sample obtained at 500 and 400 °C was ~ 60 % at 2 mV s^{-1} while ~ 80% at higher scan rates measured for 2nd scan. Charge efficiencies increased with scan number as the voltammograms stabilized. Samples obtained at 800 °C and above showed < 90 % efficiency at higher scan rates, while inconsistent efficiency values are seen at 2 mV s^{-1} that went slightly higher than 100% for the 2nd scan and came down to ~ 80 % with increase in scan number. Higher efficiencies were because of asymmetric shape of the CVs due to increase in reduction potentials. Voltammograms for all the samples at each scan rate were run with 0.6 mg of active electrode material loading on to 1× 1 cm area of titanium foil. Voltammograms in figures 5.19 to 5.26 showing 100 scans at 100 mV s^{-1} and 10 scans at 50, 20 or 2 mV s^{-1}.

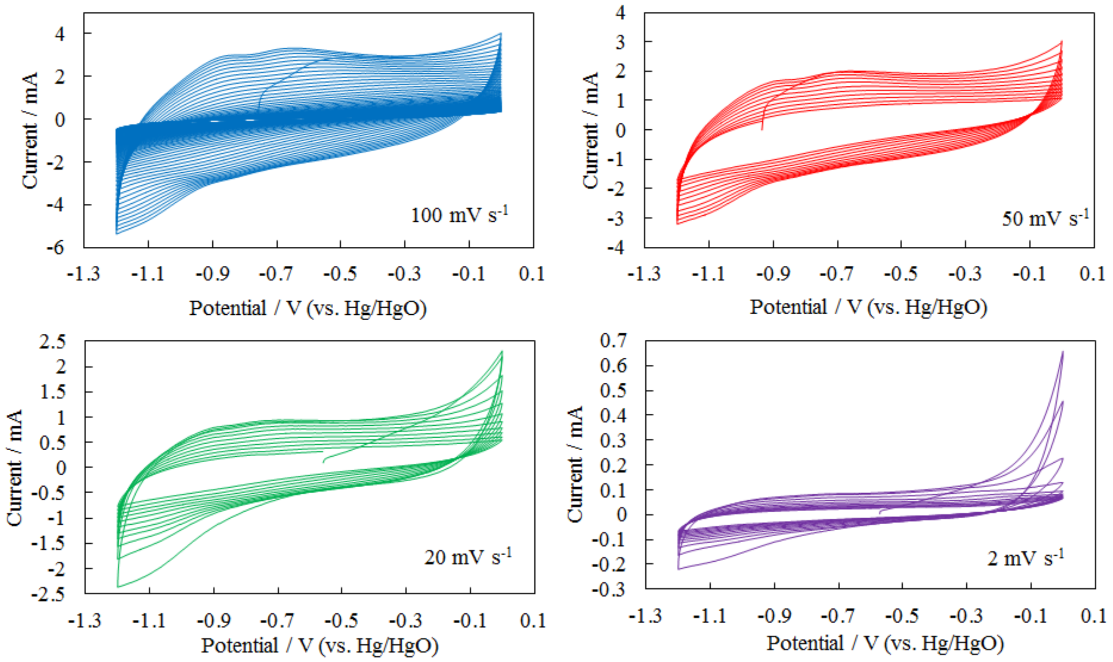

Figure 5.19: CVs for VN sample obtained at 300 °C in 1 M KOH

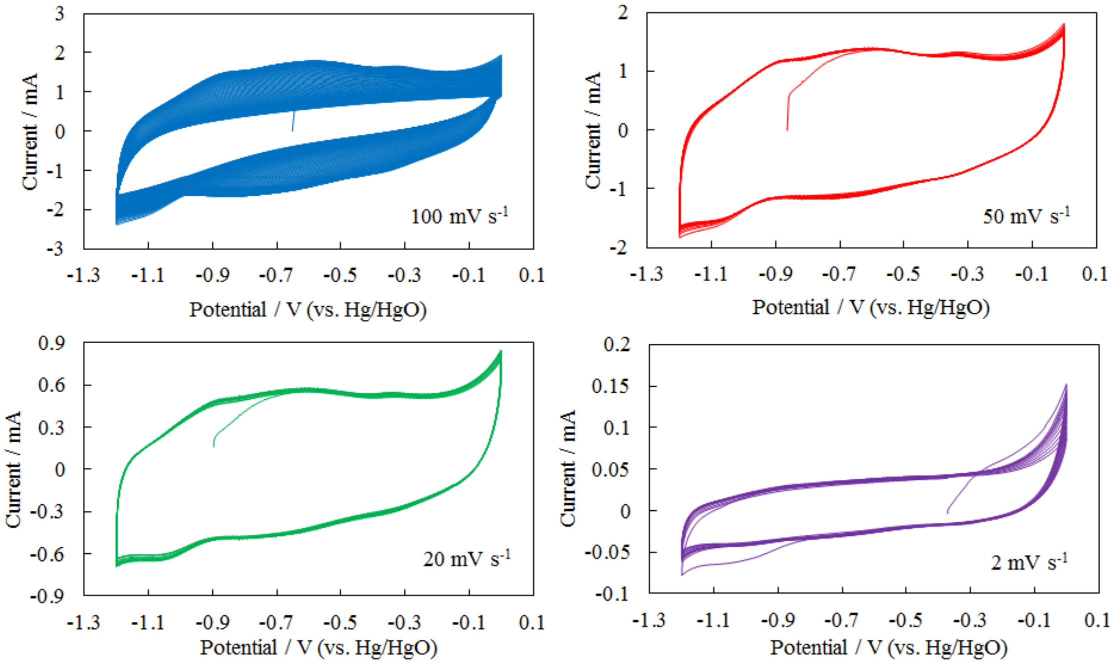

Figure 5.20: CVs for VN sample obtained at 400 °C in 1 M KOH

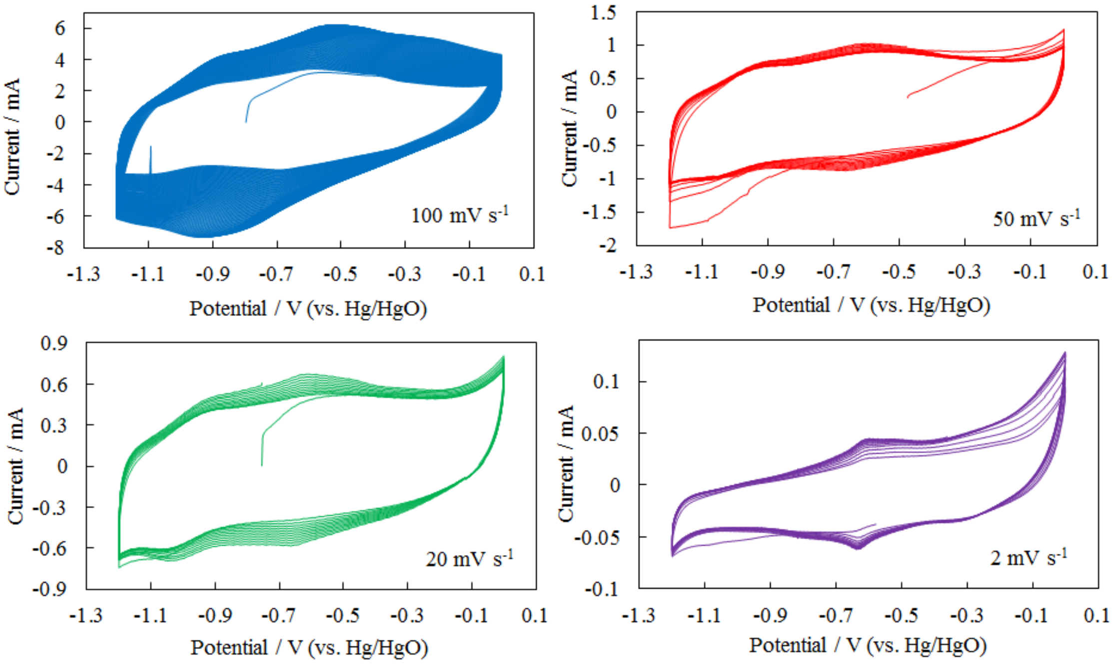

Figure 5.21: CVs for VN sample obtained at 500 °C in 1 M KOH

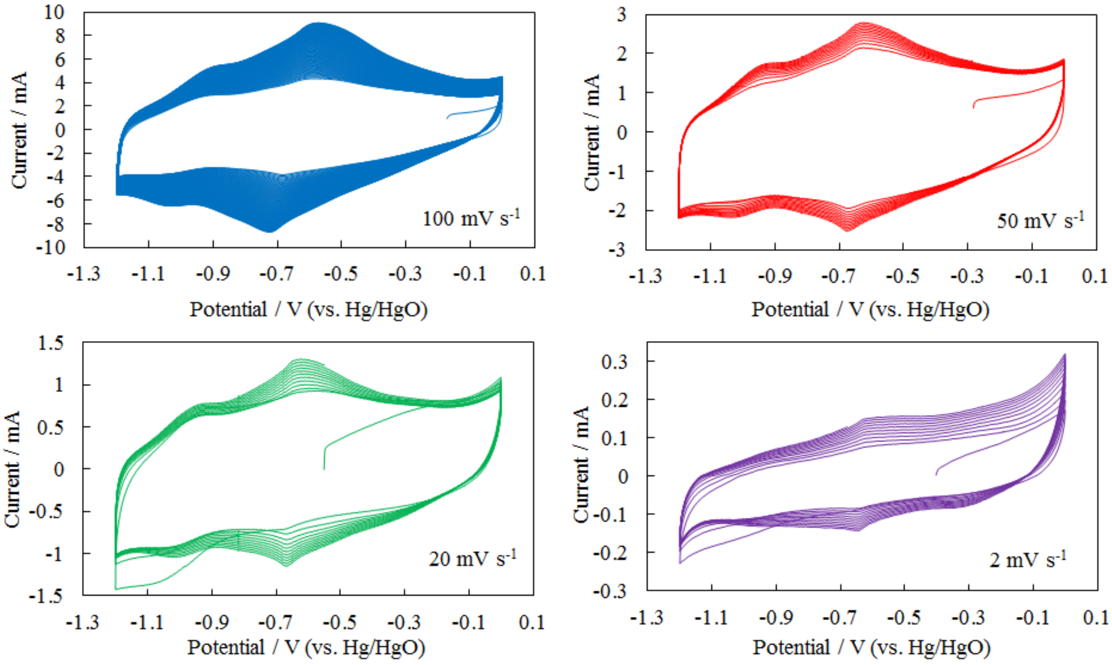

Figure 5.22: CVs for VN sample obtained at 600 °C in 1 M KOH

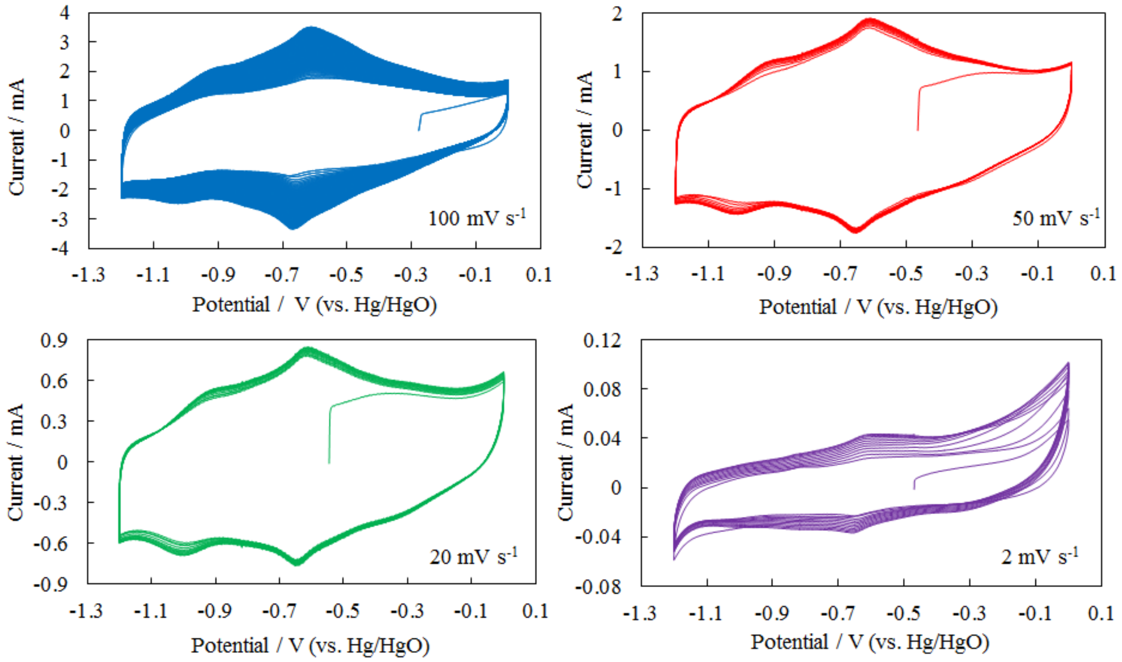

Figure 5.23: CVs for VN sample obtained at 700 °C in 1 M KOH

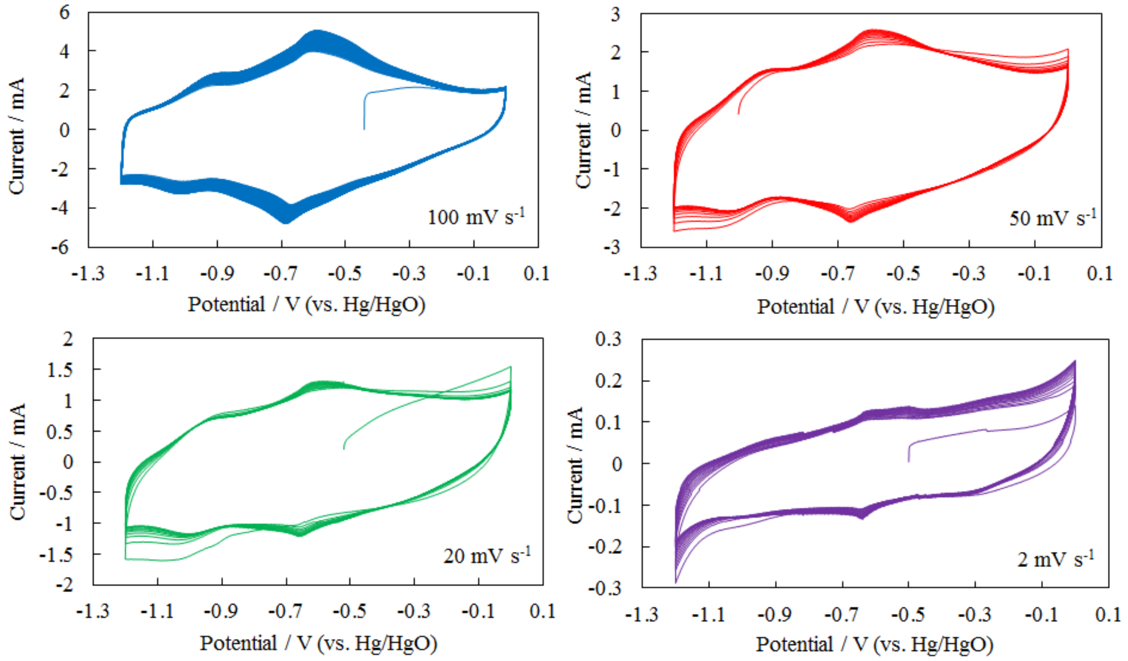

Figure 5.24: CVs for VN sample obtained at 800 °C in 1 M KOH

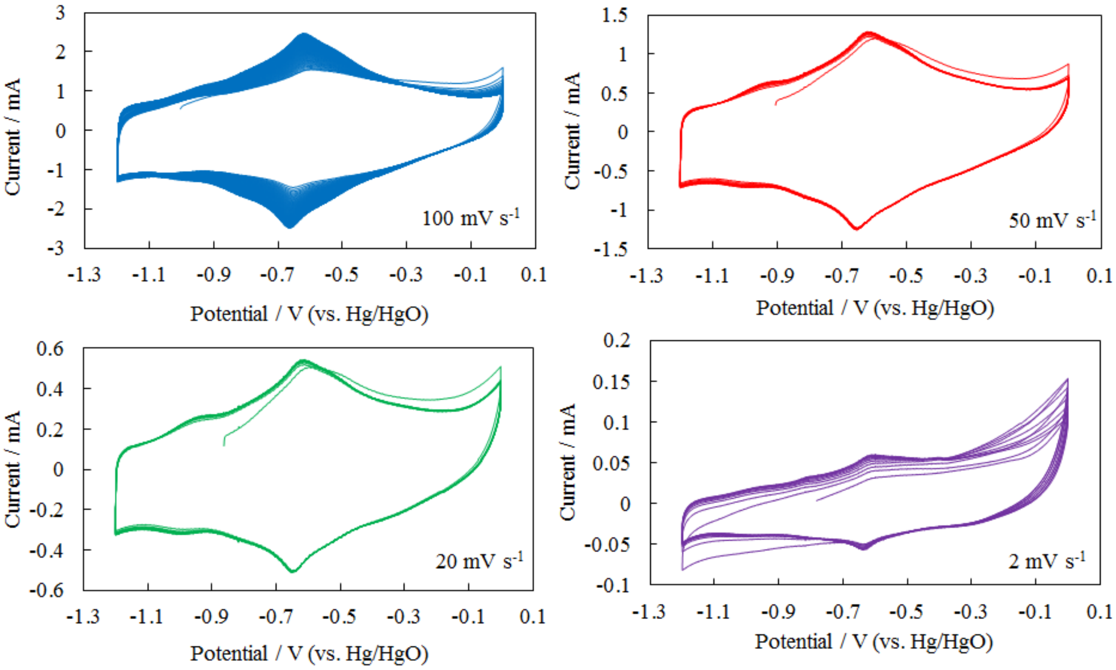

Figure 5.25: CVs for VN sample obtained at 900 °C in 1 M KOH

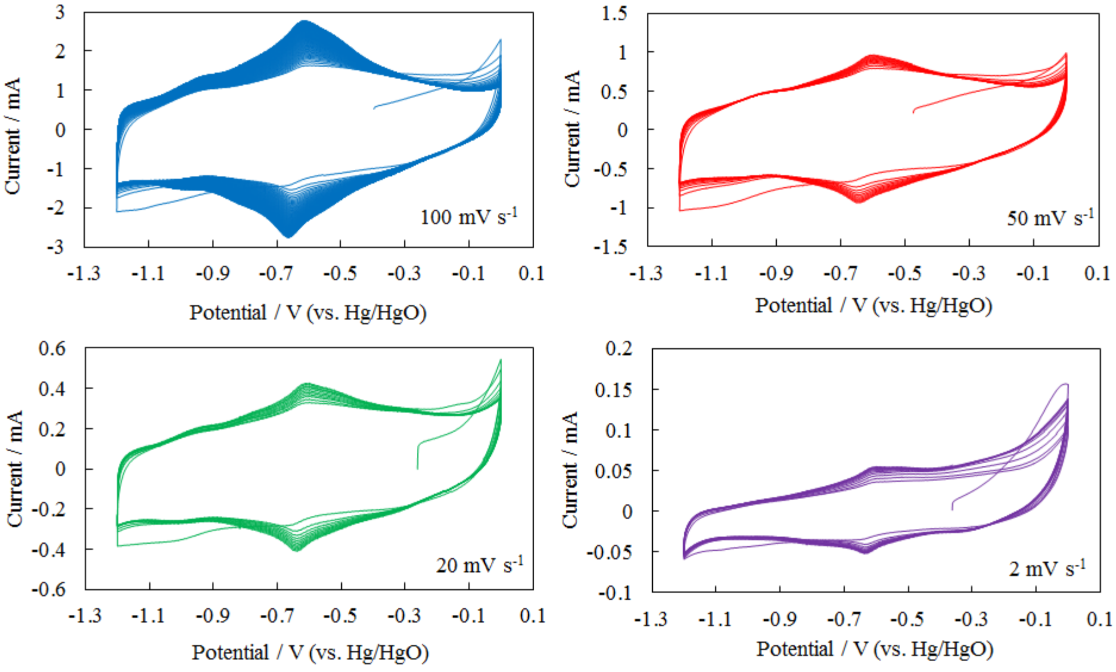

Figure 5.26: CVs for VN sample obtained at 1000 °C in 1 M KOH

The voltammogram in figure 5.27 is for a vanadium nitride sample obtained at 600 °C at 2 mV s^{-1} for 20 cycles, where an increase in capacitance was observed up to 20 cycles. The measured capacitance of 87 F g^{-1} at first, 99 F g^{-1} at 10th and 128 F g^{-1} at 20th scan, show an overall 32 % increase in capacitance until the 20th scan. Increase in capacitance was stabilized after 18th cycle.

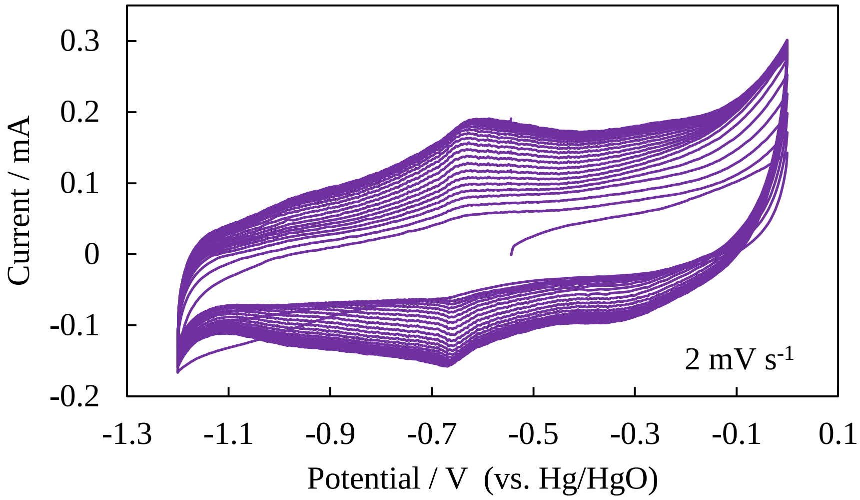

Figure 5.27: CV for VN sample obtained at 600 °C, in 1M KOH vs Hg/HgO reference electrode, at the 2mV s^{-1} (showing 20 scans).

Redox potentials observed in the voltammograms of vanadium nitride samples are listed in the table. Two main oxidation peaks near -0.9 V and -0.65 V and reduction peaks at – 0.7 and -1 V were observed in most of the samples at 20, 50 and 100 mV s^{-1}. A third oxidation peak at – 0.35 V at these scan rates was only visible in the vanadium nitride samples obtained at 300 and 400 °C, while only at 100 mVs^{-1} at 500 °C. The oxidation peak at – 0.35 V was absent in all the samples at 600 °C and above at any scan rate. An oxidation peak near – 0.6 V and a reduction peak near – 0.65 V was seen in all the samples at 2 mV s^{-1} except vanadium nitride obtained at 300 and 400 °C, where no redox features can be seen. A reduction peak at -0.37 V was observed at 2 mV s^{-1} in the samples obtained at 500 to 800 °C, which was absent in the samples above this temperature. H. J. Prashanth et al.[30] have also reported redox behaviour of nano-structured vanadium nitride in 1 M KOH in the potential window -1.2 to 0, 1.2 V. They observed redox peaks at -0.91 V and -0.61 V on the anodic scan and at -0.68 and -1.03 V on the cathodic scan. Both anodic and cathodic peaks are in close argument with to our current peaks at various scan rates listed in the table 5.6. Choi. et al.[1] reported oxidation peaks near -0.84, -0.57 and -0.23 V and reduction peaks at -0.98, -0.64 and -0.32 V in a voltammograms obtained at 2 mV s^{-1} for a vanadium nitride sample. It is reported that these potentials indicate that V undergoes redox reactions that span the II, III and IV oxidation states in the potential applied.[49]

Table 5.6: Redox potentials for vanadium nitride electrodes scanned at various scan rates in 1 M KOH vs Hg/HgO reference electrode.

	Redox potentials (V), at given scan rate (mV s^{-1})							
Scan rate mVs^{-1})	**100**		**50**		**20**		**2**	
	Ox.	***Red.***	***Ox.***	***Red.***	***Ox.***	***Red.***	***Ox.***	***Red.***
300	-0.83	-0.55	-0.9	-0.63	-0.8	-0.88		
	-0.63	-0.88	-0.72	-0.88				
400	-0.88	-0.5	-0.88	-0.65	-0.9	-0.71		
	-0.6	-0.8	-0.6	-1.05	-0.6	-1.12		
	-0.35		-0.35		-0.35			
500	-0.9	-0.73	-0.9	-0.65	-0.9	-0.65	-0.61	-0.35
	-0.6	-1.05	-0.63	-1.05	-0.62	-1.05		-0.62
	-0.37							
600	-0.88	-0.72	-0.9	-0.68	-0.9	-0.65	-0.62	-0.37
	-0.58	-1.05	-0.63	-1.03	-0.6	-1.05		-0.67
700	-0.92	-0.67	-0.93	-0.67	-0.93	-1.02	-0.63	-0.35
	-0.63	-1.03	-0.63	01.03	-0.63	-0.65		-0.65
800	-0.92	-0.67	-0.92	-0.67	-0.94	-1.02	-0.61	-0.63
	-0.62	-1.02	-0.63	-1.02	-0.62	-0.65		
900	-0.95	-0.65	-0.95	-0.65	-0.95	-1.01	-0.61	-0.63
	-0.62	-1.02	-0.62	-1.02	-0.62	-0.65		
1000	-0.95	-0.67	-0.95	-0.65	-0.95	-1.01	-0.61	-0.63
	-0.62	-1.03	-0.62	-1.03	0.62	-0.64		

The sample obtained at 600 °C was also run for 200 cycles in 1.2 V windows at 100 mV s^{-1}, that show an increase in capacitance up to 100 cycles, while the capacitance started decreasing after the 150th cycle with disappear of redox features (Fig. 5.28). It means the vanadium nitride sample is not stable in this potential range. The vanadium nitride anode is electrochemically unstable in aqueous solution due to the irreversibility of forming vanadium oxide (VO_x) on the surface.[2, 50, 51]

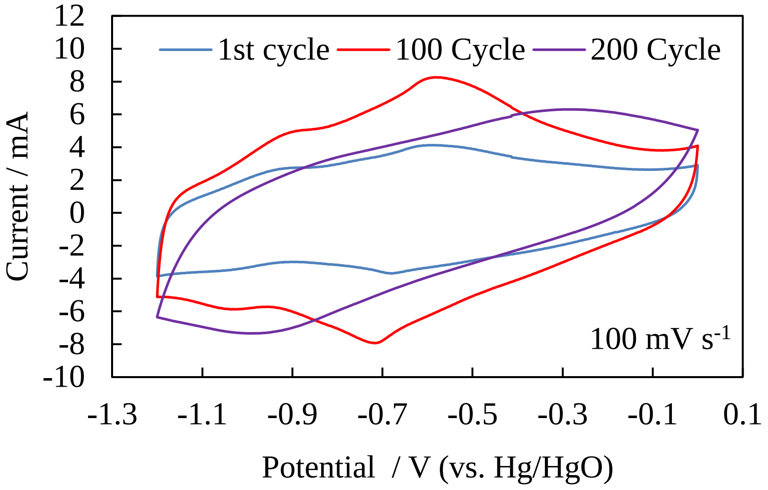

Figure 5.28: behaviour of a voltammograms through 200 cycles in 1 M KOH, of a vanadium nitride sample obtained at 600 °C.

Capacitance was observed to be stable up to 1000 scans in the smaller potential window of 0.7 V for a vanadium nitride sample obtained at 600 °C (Fig. 5.29). A fast increase in capacitance was observed up to 150 scans, levelling off by 1000 scans. A single oxidation peak was observed in the potential range at – 0.64 V that moved towards positive to – 0.58 V by the 1000th cycle. A reduction peak at – 0.68 could be seen during discharge, that moves towards negative potential with scan number. The movement of oxidation or reduction peaks towards positive or negative was 0.04 V. No change in the voltammogram shape was observed up to 1000 scans except movement of redox potentials across the potential axis.

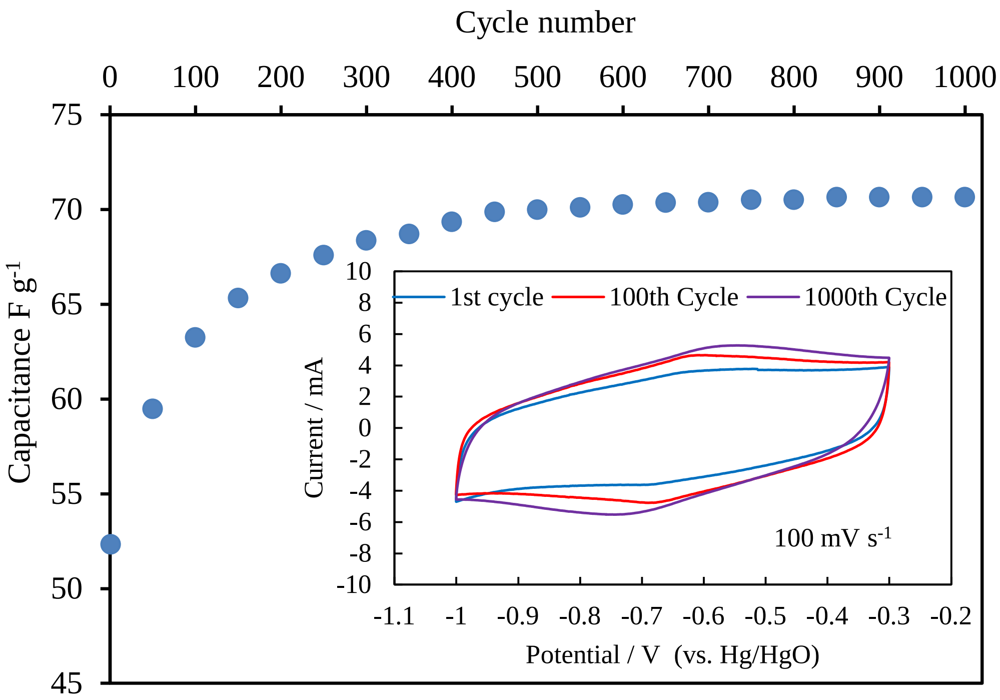

Figure 5.29: Plot showing capacitance vs cycle number and inside graph of voltammograms obtained in 1 M KOH for a vanadium nitride sample obtained at 600 °C.

Vanadium nitride samples were also run using different potential windows for 1000 scans to test the material stability for long runs. Cyclic voltammograms showing the 1st, 100th and 1000th scan in different potential windows are shown in Figure 5.30. Using a full range potential window of 1.2 V revealed a broad voltammogram at 100th scan, while it became narrow up to 1000th scan losing any redox features in the process, (Fig. 5.30 A). A potential window of 0.9 V (-0.1 to -1 V) showed a single redox feature and a narrow current profile at 1000th scan (Fig. 5.30 B). Moving towards more negative potential (-0.3 to -1.2 V) the 0.9 V window showed a reduction tail that disappeared in the initial scans, however two prominent redox features (reduction – 1.08 V, oxidation - 0.92 V) had nearly flattened at 100th the scan, and were not seen at the 1000th scan (Fig. 5.30 C) Capacitance in this range of potential is slightly higher at 1000th scan than in the potential windows discussed before. Using a window of 0.8 V (-0.2 to -1 V) showed stable capacitance up to 1000th cycle (Fig. 5.30 D). The voltammogram shows a small reduction initially that stabilised up to the 100th scan. Redox features get broader up to the 1000th scan, with no prominent peak.

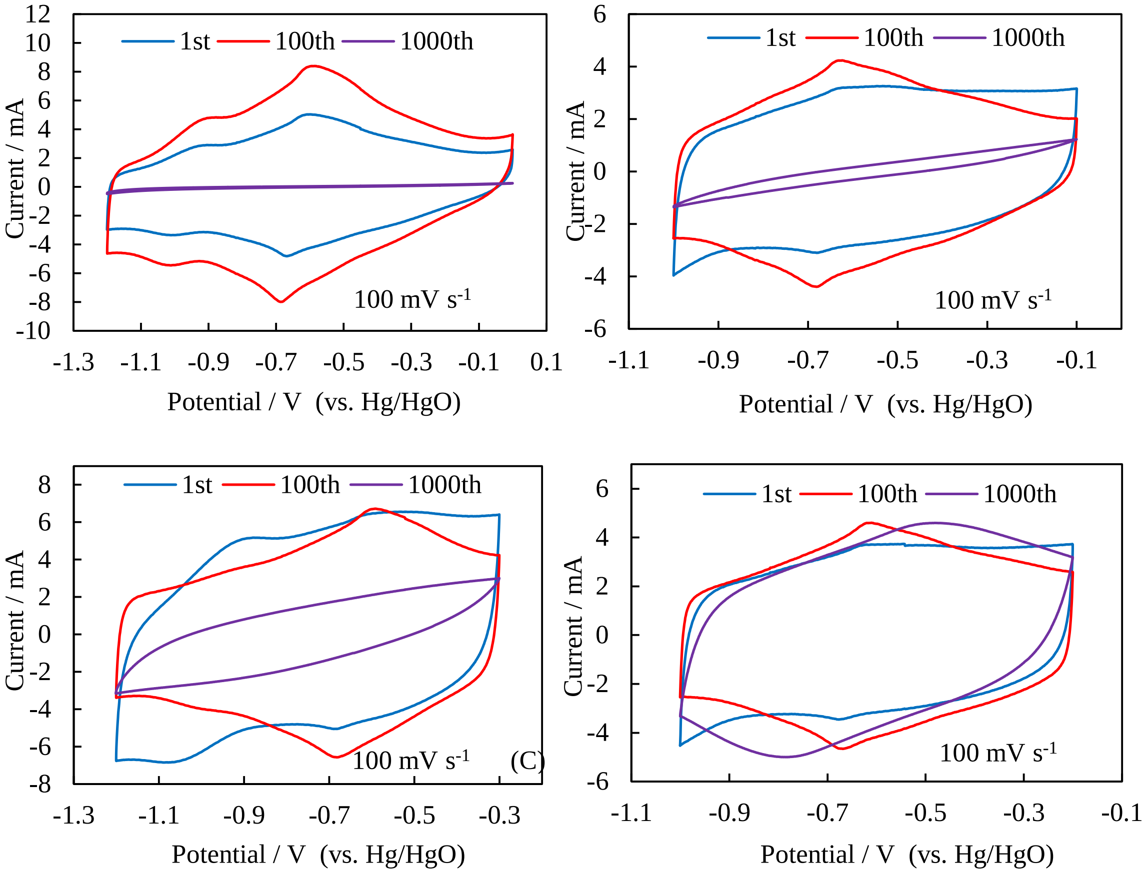

Figure 5.30: Cyclic voltammograms of vanadium nitride sample obtained at 600 °C over 1000 scans in 1 M KOH in various potential windows.

A graph of capacitance were cycle number (Fig. 5.31) shows that the capacitance started dropping after the 150th scan and about 87 % of the original capacitance was lost by the 500th scan when a potential window of 1.2 V was used. Using a 0.9 V window showed 87.5 % of the original capacitance up to the 500th cycle where it started dropping until it reached 24 % at the 1000th scan. Another 0.9 V towards more negative axes than the previous window showed the same percentage of remaining capacitance of 85.5 % up to the 500th, however, the capacitance drop by the 1000th scan was less i.e 44 % of the original capacitance. Potential windows of 0.8 V or 0.7 V showed a rapid increase in capacitance up to the 150th cycle, which became steady until the 1000th cycle. Broadening of redox peaks in the voltammogram obtained with 0.8 V occurred around the 800th scan, where a slight decrease in capacitance was observed at this point, however, the final capacitance remained higher than the initial.

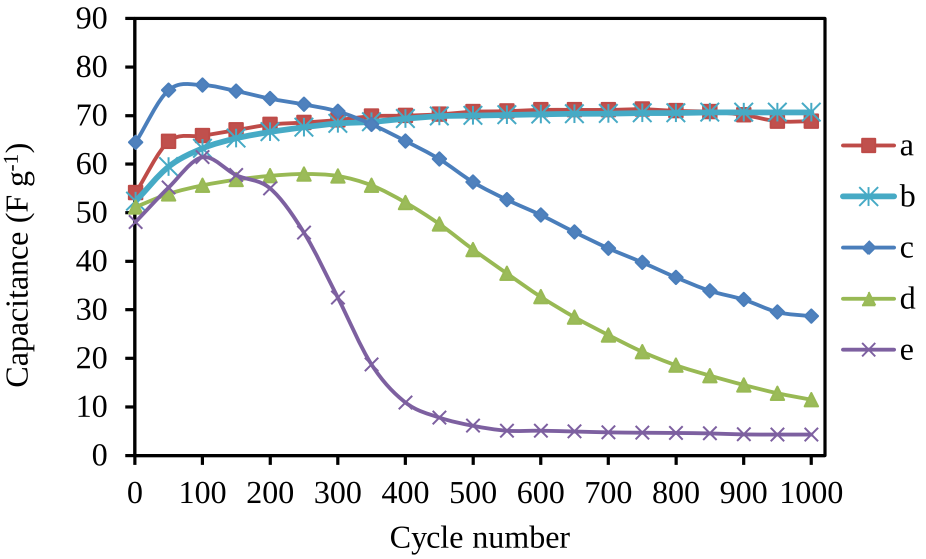

Figure 5.31: Graph showing capacitance vs cycle number for 1000 scans of a vanadium nitride sample obtained at 600 °C in different potential windows at scan rate of 100 mV s^{-1} in 1 M KOH, (a) – 0.2 to – 1.0, 0.8 V, (b) – 0.3 to – 1.0, 0.7 V, (c) – 0.3 to –1.2, 0.9 V, (d) – 0.1 to –1.0, 0.9 V and (e) 0 to – 1.2 V, 1.2 V.

5.6. Conclusions

Annealing the polymeric precursor obtained through solution phase ammonolysis of tetrakis dimethyl vanadium amide yielded standard rock salt vanadium nitride samples at higher temperature and distorted cubic vanadium nitride at lower temperature. Vanadium nitride obtained at 500 °C and below was found contaminated with organic matter due to un-annealed precursor that was visible in TGA curves as the major mass loss. No hydrogen contents found in the samples at 600 °C and above this temperature, while carbon contents were found to be decreased at higher temperature. A PXD pattern of vanadium nitride samples revealed the broadening of the 111 and 200 peaks at lower temperature due to small crystallite size. Rietveld refinement suggests the standard rock salt profile was observed in the vanadium nitride samples obtained at 600 °C and above this temperature, while the a parameter was found to be smaller as we go down to lower temperature samples. Profile fitting of vanadium nitride obtained at 300 °C was done by refining the parameters for microstrain broadening. PDF data of all the vanadium nitride samples revealed similar trend of lattice parameter values as seen in the Rietveld refinement with slightly higher R_{wp} values. Crystallite size calculated through PXD or PDF data was found in the range of 2 and 30 nm, increasing in the samples obtained at higher temperature. BET surface area suggests that all the vanadium nitride samples have a surface areas below 10 m^2 g^{-1}, with the highest surface area of 9 m^2 g^{-1} for the sample obtained at 600 °C. Nitrogen adsorption and desorption graphs suggest isotherm type IV, while pore size distribution suggests microporous and mesoporous material at 500 °C and below, and only mesoporous at 600 °C and above this temperature. TEM images suggests agglomeration of the particles in all the vanadium nitride samples; particles are mostly spherical in the size range of 2 to 35 nm, increasing for higher temperature samples. Electrochemical processing of vanadium nitride samples in 1M KOH against a Hg/HgO reference electrode suggest that the electrode material was stable in a 1.2 V potential window at a scan rate of 100 mV s^{-1}. Highest capacitance was observed in the sample obtained at 600 °C at the scan rate of 2 mV s^{-1}. An increase in capacitance with scan number was observed until the 150th scan at 100 mV s^{-1} in the potential range of 0 to – 1.2 V. Samples obtained at lower temperatures 300 and 400 °C tended to lose the capacity in the initial scans, because of the presence of organic matter in the samples. Voltammograms obtained after 1000 scans showed the stable capacitance in the potential window of 0.7 V (-0.3 to -1) and 0.8 V (-0.2 to -1).

7. References

1. D. Choi, G. E. Bloomgren and P. N. Kumta, *Adv. Mater.*, 2006, **18**, 1178.
2. A. M. Glushenkov, D. Hulicova-Jurcakova, D. Llewellyn, G. D. Lu and Q. Chen, *Chem. Mater.*, 2010, **22**, 914.
3. S. T. Oyama, *The chemistry of transition metal nitrides and carbides and nitrides*, Springer, 1996.
4. S. Ramanathan and S. T. Oyama, *J. Phys. Chem.*, 1995, **99**, 16365.
5. I. K. Milad, K. J. Smith and P. C. Mitchell, *Catal. Lett.*, 1998, **52**, 236.
6. H. Kwon, S. Choi and L. T. Thompson, *J. Catal.*, 1999, **184**, 236.
7. RP. Rodriguez, J. L. Brito, A. Albonronz, M. Labadi, C. Pfaff and S. Marrero, *Catal. Commun.*, 2004, **5**, 79.
8. J. G. Choi, J. Ha and J.-W. Hong., *Appl. Catal.*, 1998, **168**, 47.
9. O. N. Carlson, J. F. Smith and R. H. Nafziger, *Metall. Trans.* , 1986, **17 A**, 1647.
10. A. N. Christensen and B. Lebech, *Acta Cryst.*, 1979, **B35**, 2677.
11. T. Onozuka, *J. Appl. Crystallogr.*, 1978, **11**, 132.
12. L. Skala and P. Capkova, *J. Phys.: Condens. Matter.*, 1990, **2**, 8293.
13. F. Kubel, W. Lengauer, K. Yvon, K. Knorr and A. Junod, *Phys. Rev.: B*, 1988, **38**, 908.
14. P. T. Shaffer, *Plenum press handbooks of high-temperature materials*, **vol. 1**, Plenum press, New york, 1964.
15. I. P. Parkin and G. S. Elwin, *J. Mater. Chem.*, 2001, **11**, 3120.
16. A. M. Chaplanov and E. N. Shcherbakova, *Inorg. Chem.*, 2001, **37**, 233.
17. C. H. Ma, J. H. Huang and H. Chen, *Surf. Coat. Tech.*, 2000, **133**, 289.
18. R. Sanjines, P. Hones and P. Levy, *Thin Solid Films*, 1998, **332**, 225.
19. S. Abisset and F. Maury, *Surf. Coat. Tech.*, 1998, **200**, 109.
20. Z. N. Dai, A. Miyashita, S. Yamamoto, K. Narumi and H. Naramoto, *Thin solid film*, 1999, **347**, 117.
21. X. Chu and S. A. Barnett, *Vac. Sci.Technol.*, 1996, **14**, 3124.
22. I. Galesic and B. O. Kolbesen, *Thin solid film*, 1999, **349**, 14.
23. X. Liu, H. Lu, M. He, K. Jin, G. Yang, H. Ni and K. Zhao, *Mater. Lett.*, 2014, **123**, 38.
24. A. Calka and J. S. Williams, *Sci. Forum*, 1992, **88-90**, 787.

25. M. A. Roldan, V. L. Flores, M. D. Alcala, A. Ortega and C. Real, *J. Europ. Ceram. Soc.*, 2009, **30**, 2009.
26. B. Vaidhyanathan, D.K. Agrawal and R. Roy, *Mater. Res. Soc.*, 2000, **15**, 974.
27. E. Friederich and L. Sitting, *Z. Anorg. Allg. Chem.*, 1925, **144**, 169.
28. E. F. de Souza, C. A. Chagas, T. C. Ramalho and R. B. de Alencastro, *Dalton Trans.*, 2012, **41**, 14381.
29. L. Chen, Y. Gu, L. Shi, Z. Yang, J. Ma and Y. Qian, *Solid State Comm.*, 2004, **132**, 132.
30. P. J. Hanumantha, M. K. Datta, K. S. Kadakia, D. H. Hong, S. J. Chung, M. C. Tam, J. A. Poston, A. Manivannan and P. N. Kumta, *J. Electrochem. Soc.*, 2013, **160**, A2195.
31. M. H. Chisholm, V. Baxter, J. Gama, F. Distasi, A. L. Hector and I. P. Parkin, *Chem. Mater.*, 1996, **8**, 1222.
32. K. Nakamoto, *Infrared and Raman Spectra of Inorganic and Organic Compounds 3rd ed.;J. Wiley: New York,*, 1978.
33. D. M. Hoffman, *Polyhedron*, 1994, **13**, 1169.
34. H. J. Holleck, *J. Vac. Sci. Tech.*, 1986, **A 4**, 1384.
35. S. Hosoya, T. Yamagishi and M. Tokonami, *J. Phys. Soc. Jap.*, 1968, **24**, 363.
36. D.A. Fletcher, R. F. McMeeking and D. Parkin, *J. Chem. Inf. Comput. Sci.*, ICSD accessed via The United Kingdom Chemical Database Service, 1996,, **36**, 746.
37. R. B. Von Dreele and A. C. Larson, Generallized structure analysis system, Los Alamos National Laboratory, NM87545, USA, December 2002 release.
38. I. I. Timofeeva and L. K. Shvedova, *Neorganicheskie Materialy* 1972, **8**, 1169.
39. N. Kieda, K. Uematsu, N. Mizutani and M. Kato, *J. Less-Common Metals*, 1984, **99**, 131.
40. R. B. Von Dreele and A. C. Larson, GSAS Manual, LANSCE MS-H805, Los Alamos National Laboratory, Los Alamos NM, NM 87545, 2000.
41. V. Laar and Yelon, *J. Appl. Cryst.*, 1984, **17**, 47.
42. P. Stephens, *J. Appl. Cryst.*, 1999, **32**, 281.
43. C. Borgianni, V. D. Stefano and R. Grimaldi, *Less-Common Metals*, 1970, **20**, 299.
44. C. Dong and J. Langford, *Appl. Cryst.* , 2000, **33**, 1177-1179.

45. M. D. Aguas, A. M. Nartowski, I. P. Parkin, M. Mackenzie and A. J. Carven, *J. Mater. Chem.*, 1998, **8**, 1875.

46. Z. B. Zhao, Z. U. Rek, S. M. Yalisove and J. C. Bilello, *Thin Solid Film*, 2005, **472**, 96.

47. G. Kothleitner, M. Rogers, A. Berendes, W. Bock and B. O. Kolbesen, *Appl. Surf. Sci.*, 2005, **252**, 66.

48. C. L. Farrow, J. P. Juhas, W. Liu, D. Bryndin, E. S. Bozin, J. Bloch, Th. Proffen and S. J. L. Billinge, *J. Phys.: Condens. Matter.*, 2007, **19**, 335219.

49. H. Kelsall, I. Thompson and P. A. Francis, *J. Appl. Electrochem.*, 1993, **23**, 417.

50. D. W. Choi and P. N. Kumta, *Electrochem. Solid State Lett.*, 2005, **8**, A418.

51. L. Zhang, C. M. B. Holt, E. J. Luber, B. C. Olsen, T. H. Wang, M. Danaie, X. H. Tan, V. W. Lui, W. P. Kalisvaart and D. Mitlin, *Phys. Chem.*, 2011, **49**, 24381.

6 Template-based synthesis of high surface area titanium nitride for charge storage

6.1 Introduction:

Titanium nitride (TiN) is a useful material for some of its superior properties, such as wear resistance, hardness (2160 kg mm^{-2}), oxidative stability, corrosion resistance, and high conductivity (5×10^4 Ω^{-1} cm^{-1}). The last of these makes TiN an excellent candidate for electrodes in electrochemical capacitors.[1] TiN in combination with iron has also been studied as a catalyst for ammonia synthesis.[2]

TiN films were produced from $TiCl_4$ and N_2 through laser assisted CVD and light ion beam evaporation.[3, 4] TiN powders are generally produced through the reaction of the metal with nitrogen or ammonia at high temperatures.[5] Unreacted metal in the final product, long time scale and unsuitability for lower nitrides are the drawbacks of this method.[6, 7] Titanium was ground and heated under nitrogen for 48 h to produce TiN through mechanical milling.[8] TiN nanoparticles are often prepared from titanium oxide using ammonia as the nitrogen source at high temperature.[9-12] TiN is also produced by solid state metathesis reaction between $TiCl_3$ and Ca_3N_2.[1] However the metathesis reaction is a highly exothermic reaction (> 1400 °C) in < 1s and causes agglomeration of the particles with high yield of crystalline product.[13]

A dual templating synthesis of mesoporous TiN_x was reported by Bang et al. Hollow spheres of Zn_2TiO_4 were prepared as a precursor source from the reaction of zinc nitrate hexahydrate with a soluble Ti(IV) complex ($[NH_4]_2[Ti(O–H)_2(OCH(CH_3)CO_2)_2]$). Further nitridation of hollow zinc titanate under ammonia at 1000 °C produces hollow spheres of TiN_x with a surface area of 17 m^2 g^{-1}.[14] TiO_2 spheres were prepared by refluxing titanium glycolate with 20 ml of water at 80 °C for 3 h. The pore diameter of the glycolate was tuned by changing the amount of water. The highest surface area of 92 m^2 g^{-1} for a TiN sample was measured when more water was used in the TiO_2 synthesis. The presence of TiO_2 in the final product cannot be ruled out. A sample with surface area of 70 m^2 g^{-1} was tested for electrochemical behaviour, and showed the highest specific capacity of 144 F g^{-1} at

2 mV s^{-1}. A mixture of TiO_2 and cyanamide composite on heating to 800 °C under NH_3 for 1 h produced mesoporous TiN_x spheres.[15]

High surface area TiN has been reported by Kaskel et al. by ligand assisted precursor, where ligands are aliphatic amines, ethers and bipyridines. A $TiCl_4(THF)_2$-derived sample showed the highest surface area of 230 m^2 g^{-1} when the precursor was annealed at 873 K under ammonia for 1 h at 5 K min^{-1}. A TiN powders were found to be contaminated with Cl, C and H.[16] In a similar piece of work a ligand carrier $TiCl_4$ was ammonolysed under NH_3 to produce high surface area TiN_x, where a donor ligand has been used. The highest surface area of 200 m^2 g^{-1} for TiN_x was achieved by annealing the precursor at 973 K, which was used to test its catalytic activity in hydrogen transfer reactions. The particles catalyse the reduction of alkynes to alkenes with complex hydrides such as $NaAlH_4$ in solution. Samples were found contaminated with chlorine, and the residues of organic ligands.[17] Organic ligands may hinder sintering and produce higher surface areas in the synthesis of TiN_x nanoparticles due to the formation of a protective coke coating, but the latter can also lead to reduced activities due to passivation and shielding of the outer surface. Rock salt TiN_x was produced through ammonolysis of $Ti(NMe_e)_4$, where an amide precursor was prepared first by condensing ammonia over amide solution in pentane. The polymeric precursor is then annealed under flowing He.[18]

Nano-crystalline TiN has also been produced by two-step ammonolysis in argon atmosphere in which liquid $TiCl_4$ was reacted with condensed ammonia at room temperature, followed by heat treatment at ~ 400 °C. Solution phase ammonolysis of $Ti(NMe_2)_4$ and then pyrolysis of the precursor at different temperatures under NH_3 or N_2 yielded titanium nitride and carbonitrides. Stoichiometric TiN was obtained when the polymer precursor was heated above 700 °C under NH_3. Heating under N_2 leads to iso-structural titanium carbonitrides.[19] The highest capacitance of TiN is recorded as 238 F g^{-1} at 2 mV s^{-1} while 23.7 F g^{-1} at 100 mV s^{-1}.[20] A recent study of nanotubular TiN with surface area 31.4 m^2 g^{-1} showed 25, 28.7, 36.6, 51.0 and 74.2 F g^{-1} at current densities of 2.16, 1.28, 0.64, 0.32 and 0.16 A g^{-1} respectively.[21]

Our current study is focused on the synthesis of high surface area TiN powders through the infiltration of structure-directing agent (long chain amines). Long chain amines to template $Ti(NMe_2)_4$ were used to prepare the polymeric precursor. A non-templated precursor has also been prepared by solution phase ammonolysis of $Ti(NMe_2)_4$. The gels were obtained by drying the solvent from the reaction mixture under vacuum. All the polymeric precursors were annealed at 500 or 800 °C under ammonia for 10 hours at a ramp rate of 1 °C/min to obtain the TiN samples. Substantial research on TiN_x has been carried out for energy storage applications.[22-24] It is reasonably expected that high surface area TiN has potential for enhancing its electrochemical performance for supercapacitors and lithium ion batteries.[15]

6.2 Synthesis of TiN_x

Titanium nitride samples were prepared by annealing the polymer precursors obtained from ammonolysis of $Ti(NMe_2)_4$ or from a sol-gel route by adding various surfactants (long chain amines). All the procedures given below were carried out in oxygen-free conditions.

6.2.1 Solution phase ammonolysis of $Ti(NMe_2)_4$

2 ml $Ti(NMe_2)_4$ was dissolved in 20 ml of dry THF (tetrahydrofuran) in a Schlenk tube. The solution was stirred for at least 2 hours. Ammonia ~ 20 ml was condensed over sodium using dry ice and acetone to remove any moisture. The dry liquid ammonia was condensed over the tetrakis(dimethyleamido)titanium TDMAT solution using a cannula. A brown precipitate ~ 1.2 g was formed in the reaction tube. It was left to warm to room temperature. The excess of solvent was removed under vacuum, and the precipitate was transferred to the glove box. The chemical reaction to produce a polymer can be given as below.

$$[Ti(NMe_2\,)_4] + y + z\,NH_3 \;\rightarrow {}^1\!/_n\,[Ti(NMe_2)_x(NH_2)_y(NH)_z]_n + 4 - x\,NHMe_2$$

6.2.2 Template-based synthesis of TiN_x

$Ti(NMe_2)_4$ (2.67 ml, 0.0112 mol) was taken in a Schlenk tube and dissolved in 20 ml dry THF. Two additions of propyl amine $^nPrNH_2$ (0.92 ml, 0.0112 mol) were made to this solution 2 hours apart. The solution turned to dark red in about 5 minutes after the first addition of $^nPrNH_2$ (figure 6.1). $^nPrNH_2$ was dried by distilling it over BaO. The solution was left stirring overnight. A red sticky gel was obtained after removing the solvent under vacuum. A further two gels were prepared in the following way. 2.705 g of hexadecylamine (HDA) was dissolved in 20 ml of THF, or 4 g of cetyl trimethylammonium bromide (CTAB) was dissolved in 20 ml of hexane and stirred for 4 h (dissolution of CTAB was found to be poor in THF; hexane improved solubility to some extent). 2.67 ml of TDMAT was added to HDA or CTAB. Both the solutions were left stirring for 2 h and further two additions of $^nPrNH_2$ (0.92 ml, 0.0112 mol) were added to these solutions 2 h apart. The solutions were left stirring overnight and dried under vacuum to obtain the final gels. TDMAT and NH_3 yielded 1.2 g of the polymer and annealing the polymer under NH_3 at 500 or 800 °C yielded 76 or 66 % of TiN_x powders. TDMAT and $PrNH_2$ yielded 2.8 g of polymer and annealing the polymer at 500 or 800 °C under NH_3 yielded 46 or 54 % of the TiN_x powders respectively. A reaction between TDMAT, $^nPrNH_2$ and HDA yielded 4.6 g of polymer and annealing the polymer under NH_3 at 500 or 800 °C yielded 36.5 or 21 % of final TiN_x powders, respectively. A reaction between TDMAT, $^nPrNH_2$ and CTAB resulted in 5.65 g of polymer and annealing the polymer under NH_3 at 500 and 800 °C yielded 15 or 11 % of the final TiN_x products, respectively.

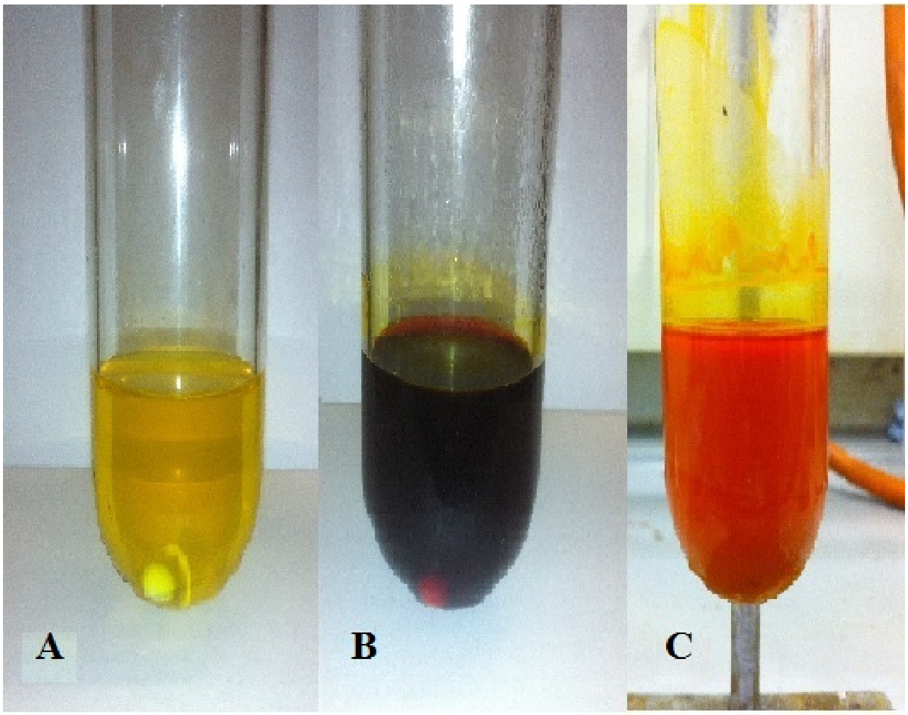

Figure 6.1: A TDMAT solution in THF, B after adding $^{n}PrNH_2$ and C after adding HDA.

6.2.3 Pyrolysis of the polymeric precursors (gels)

In the 2nd step the brown precipitate obtained from the solution phase ammonolysis of TDMAT or the template gels were transferred to an alumina boat and placed in the furnace tube with a specific arrangement of Young's taps to allow NH_3 flushing. The furnace tube was placed in the tube furnace and connected to an ammonia line. Ammonia gas was passed through the column of molecular sieves (3 Å pore size) to remove the moisture. All the samples were annealed at 500 or 1000 °C for 10 h at a ramp rate of 1 °C/min. The samples were stored inside the glove box for further analysis.

6.3 Analysis of polymeric precursors

Elemental analysis (Table 6.1) showed high contents of carbon due to the presence of the long chain amines of the templating agents. Polymer obtained from ammonolysis of TDMAT had lower C and H contents as no templating agent was added to the reaction.

Table 6.1: Elemental analysis of the polymers before annealing, polymers were obtained by reacting the reagents given in the table with TDMAT.

Polymer	% C	% H	% N
NH_3	17.42	4.96	6.22
$PrNH_2$	40.06	8.16	12.25
HDA/ $PrNH_2$	62.44	12.29	6.65
CTAB/$PrNH_2$	54.22	11.25	6.16

TGA curves for the polymeric precursors are shown in Figure 6.2. Polymer obtained from NH_3 as described above in the elemental analysis had less organic matter than the other 3 polymers obtained from template infiltration, hence showed less overall mass loss. Mass loss at temperatures lower than 500 °C is due to the amide groups NH_x and NR decomposition. Mass loss at 700 °C and above is due to N_2 and some NH_3.[18] Highest mass loss was observed for the polymer CTAB/$^2PrNH_2$. The sudden drop in the mass curve is seen from 250 to 290 °C, which largely belongs to the CTAB decomposition (CTAB decomposition temperature 237 – 247 °C) suggesting CTAB left the mixture before the pores were developed.

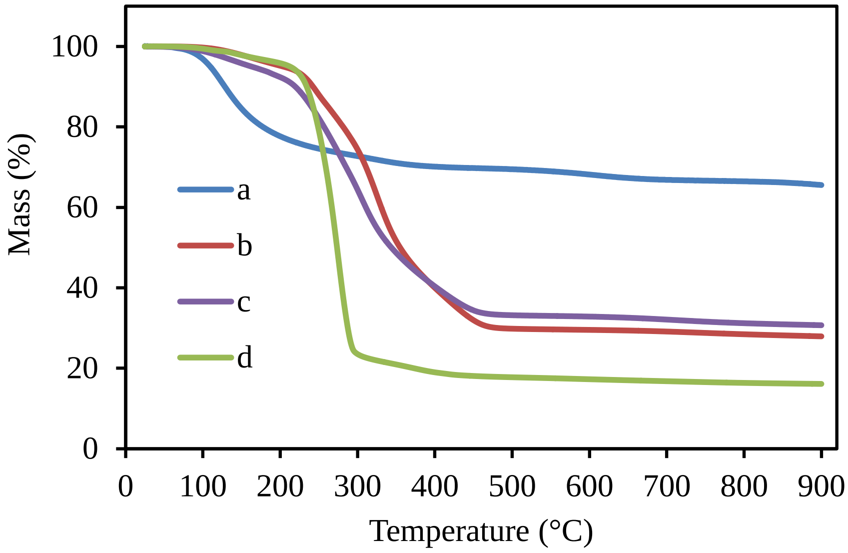

Figure 6.2: TGA plots for the polymers obtained from TDMAT reaction with, a NH_3, b $PrNH_2$, c HDA/$PrNH_2$ and d CTAB/$PrNH_2$ before annealing.

The FTIR spectra for the polymeric precursor (Fig. 6.3) shows a broad peak at 3350 cm^{-1} which demonstrates the presence of ν-(N–H).[19] Low intensity peaks in the range of 3000 - 2750 cm^{-1} are attributed to ν-(C–H). Intensity of C–H absorption bands increased as the length of amine chain was increased with changing the template to the reaction. Peaks at 1490 to 1390 cm^{-1} could be attributed to higher energy ν-(N–H) absorption.[18] The absorption peak at ca. 1655 cm^{-1} is consistent with δ-(NH_2), [18, 25] and the peak at ca. 1263 cm^{-1} may be ν-(CN). The IR data for all the amide polymers contained similar features, as to their relative composition, only the intensities of the peaks were lower for the NH_3 reaction.

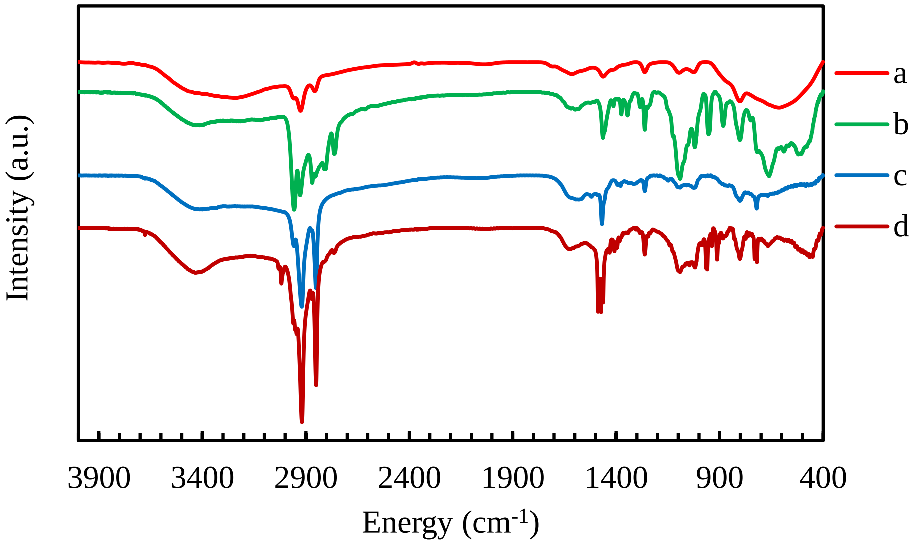

Figure 6.3: FT-IR spectra for the polymers obtained from TDMAT reaction with, a NH_3 , b $PrNH_2$, c HDA/$PrNH_2$ and d CTAB/$PrNH_2$ before annealing.

6.4 Analysis of annealed TiN_x samples

Annealing the polymers at 500 and 800 °C for 10 hours yielded TiN_x powders. The templated TiN_x samples at lower temperature were found black due to the presence of carbon contents resulting from polymer residues at lower temperature. TiN_x powders appeared to be different from various reactions. Annealing NH_3-based polymer yielded black ultra-fine powders at both temperatures, while $^{n}PrNH_2$- based powders were black at 500 °C and golden in colour at 800 °C. HDA-based polymer yielded a mix of golden and black powder at 500 °C while only golden at 800 °C, whereas CTAB-annealed powders were black at 500 °C and a mix of black and golden at 800 °C. Golden particles were highly agglomerated. Samples obtained at lower temperature were found more air sensitive than the samples at higher temperature. NH_3- or HDA-based samples at 500 °C burnt more vigorously after exposing to air. HDA/TDMAT-based powder at 800 °C showed decomposition occurred in few seconds after air contact, while NH_3 based sample at 800 °C was found stable in air. CTAB/$^nPrNH_2$ or $PrNH_2$ based samples at both the temperatures showed no effect of air exposure to the samples.

PXD patterns (Fig. 6.4 and 6.5) showed cubic phase titanium nitride.[26, 27] PXD for polymers annealed at 500 °C shows the broadening of peaks that suggest samples with very small particle sizes, while the peaks were sharp for the powders obtained at 800 °C. PXD data was refined using the cif file of the standard rock salt TiN lattice[28] obtained from ICSD.

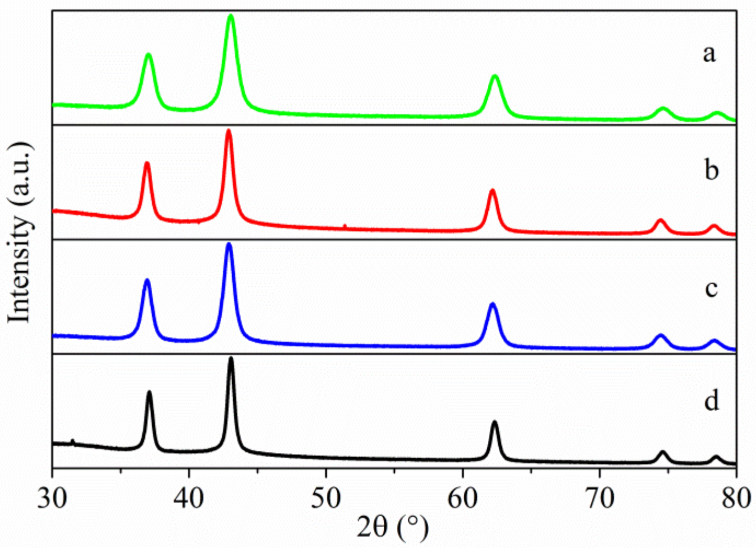

Figure 6.4: PXD patterns of the TiN_x samples after annealing the polymers obtained from TDMAT reaction with, a NH_3 , b $PrNH_2$, c HDA/$^nPrNH_2$ and d CTAB/$^nPrNH_2$ at 800 °C.

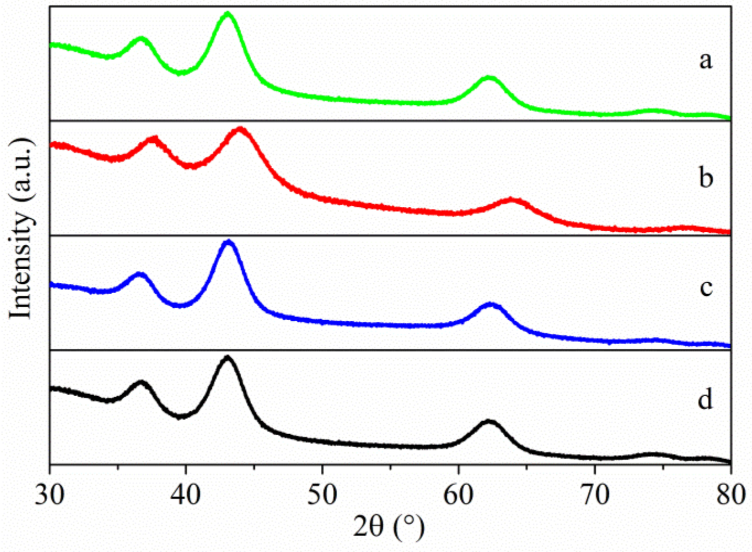

Figure 6.5: PXD patterns of the TiN_x samples after annealing the polymers obtained from TDMAT reaction with, a NH_3 , b $PrNH_2$, c HDA/$^nPrNH_2$ and d CTAB/$^nPrNH_2$ at 500 °C.

Diffraction patterns of TiN_x powders have been refined using GSAS[29] and the crystallite size calculated from the GSAS L_x parameter using the Scherrer equation.[30] Refined patterns for TiN_x samples obtained from NH_3-based polymer after annealing at 500 or 800 °C are shown in figure 6.6.

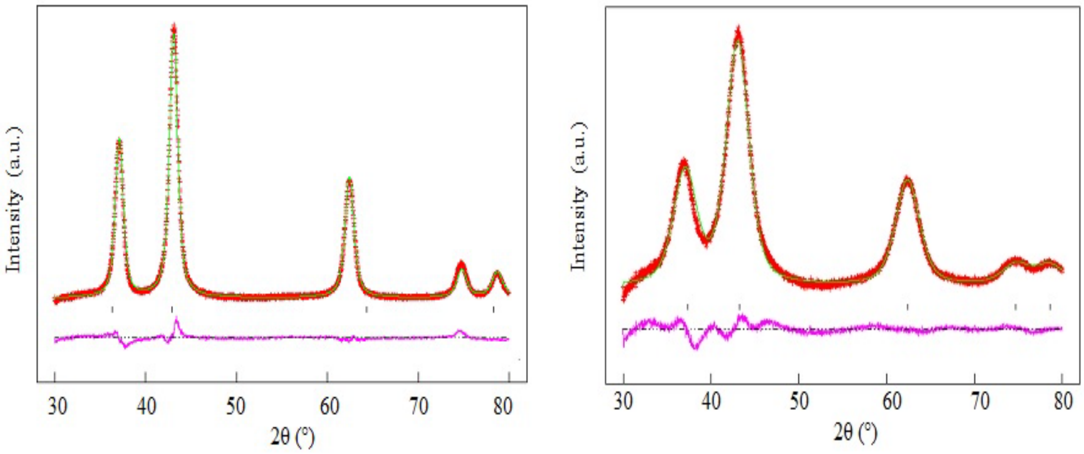

Figure 6.6: Fit to the PXD data for the phase-pure TiN_x obtained by pyrolysis of polymeric precursor obtained from solution phase ammonolysis of TDMAT and annealed under ammonia at 800 °C (left) and 500 °C (right) for 10 h. Crosses mark the data points, upper continuous line the calculated profile and lower continuous line the difference; tick marks are the allowed reflection positions of cubic TiN_x.

All the patterns were refined using cubic phase TiN lattice. Lattice parameters (Table 6.2) for all the TiN_x samples are similar with the value of a = 4.22 Å close to the literature values for TiN,[31]. The pattern obtain for the sample obtained for the polymer HDA/$PrNH_2$-based polymer annealed at 500 °C, showed smaller parameter value; a = 4.09 Å. Crystallite sizes of the TiN_x powders were smaller for the samples obtained at lower temperature. Useful nanocomposites of TiN_x require a crystallite size less than 10 nm to obtain maximum hardness.[32]

Table 6.2: Refined lattice parameters of TiN_x samples obtained from annealing the polymers obtained from TDMAT reaction with, a NH_3 , b $^nPrNH_2$, c HDA/$^nPrNH_2$ and d CTAB/$^nPrNH_2$ at 800 °C (left) and d at 500 or 800 °C.

	Sample temp. °C	a (Å)	R_{wp}/R_p%	Crystallite size nm
NH_3	800	4.218(14)	4.3/3.4	12.2
$PrNH_2$	800	4.227(18)	2.7/2.8	11.2
HDA/$PrNH_2$	800	4.226(17)	3.3/2.7	18.4
CTAB/$PrNH_2$	800	4.228(12)	3.1/2.3	19.2
NH_3	500	4.243(12)	2.3/1.8	8.1
$PrNH_2$	500	4.097(17)	1.4/1.0	4.2
HDA/$PrNH_2$	500	4.216(16)	2.4/1.9	3.1
CTAB/$PrNH_2$	500	4.226 (14)	3.1/2.4	5.3

Elemental analysis (Table 6.3) shows carbon and hydrogen contents were higher in the samples annealed at lower temperature along with the presence of H. Highest C and H contents were found in the TiN_x sample obtained from annealing the HDA/$^nPrNH_2$ polymer at 500 °C, that suggest the amide groups are not completely decomposed at this temperature. No H contents were found in the TiN_x samples obtained from CTAB/$^nPrNH_2$ based polymer due to poor condensation of CTAB with the amide mixture, and decomposition out below the annealing temperature as seen in the TGA (Fig. 6.4). The TiN_x samples were mostly nitrogen deficient. The theoretical percentage of nitrogen in TiN is 22.6 %.

Table 6.3: Elemental analysis of the TiN_x samples obtained after annealing the polymers (TDMAT + given reagents) under ammonia at the given temperatures.

Polymer	Temperature (°C)	% C	% H	% N	Composition
NH_3	500	1.03	1.59	18.22	$TiN_{0.77}H_{0.99}C_{0.004}$
NH_3	800	<0.1	0.58	20.01	$TiN_{0.86}H_{0.35}$
$^nPrNH_2$	500	1.47	1.13	19.11	$TiN_{0.83}H_{0.69}C_{0.008}$
$^nPrNH_2$	800	<0.1	<0.1	17.34	$TiN_{0.0.74}$
HDA/$^nPrNH_2$	500	2.32	1.56	16.18	$TiN_{0.71}H_{0.92}C_{0.03}$
HDA/$^nPrNH_2$	800	0.51	0.39	17.07	$TiN_{0.71}H_{0.23}C_{0.001}$
CTAB/$^nPrNH_2$	500	1.24	<0.1	19.23	$TiN_{0.83}C_{0.006}$
CTAB/$^nPrNH_2$	800	0.14	<0.1	21.59	$TiN_{0.94}$

The TGA trace of the polymeric precursor (Fig. 6.7) obtained through the ammonolysis of metal amides or templated metal amides showed two-step mass losses. Previous studies using TGA-MS[18] showed that loss of amine and ammonia due to further condensation reactions is observed at lower temperatures i.e. 100 to 400 °C, whereas above 700 °C loss of N_2 due to reduction of the metal often occurs as well as ammonia loss due to further condensation as the diffusion barrier is overcome. TiN_x samples obtained at higher temperature (800 °C) showed less mass loss (Fig. 6.7) as most of the amide groups were already pyrolysed under these conditions. The highest mass loss of ~ 24 % was observed in the TiN_x sample obtained from annealing the HDA/$^nPrNH_2$ polymer at 500 °C, where the presence of higher organic contents was confirmed from the elemental analysis data. Carbon contamination in transition metal nitrides is an important consideration because it degrades electrical and optical properties and often causes adhesion problems, however, the introduction of C to transition metal nitrides increases the hardness.[33, 34]

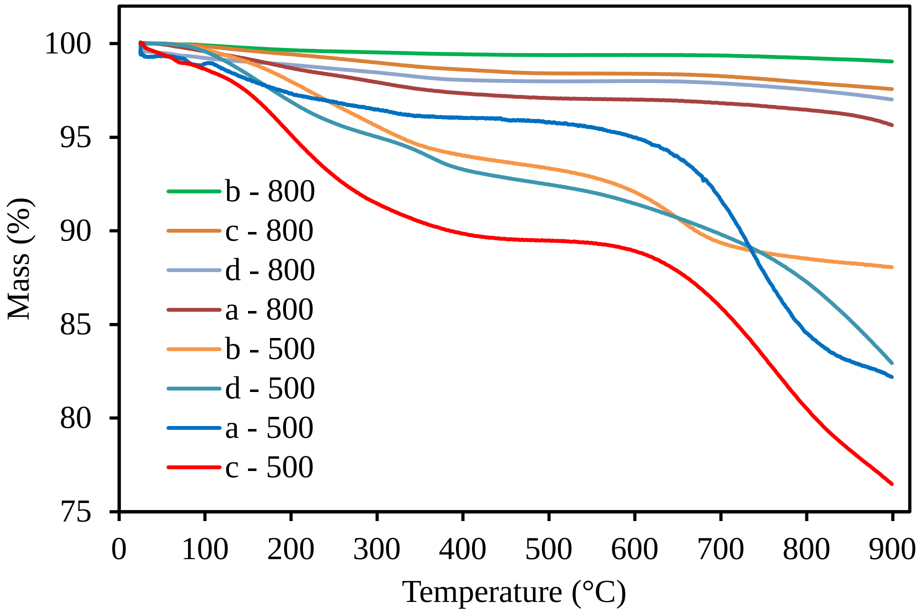

Figure 6.7: TGA plots for the TiN_x samples obtained from the reaction of TDMAT with, a NH_3 , b $^nPrNH_2$, c HDA/$^nPrNH_2$ and d CTAB/$^nPrNH_2$ after annealing at the given temperatures (°C).

FTIR spectra for the TiN_x samples after annealing the polymers at 500 or 800 °C was given in figure 6.8. The data confirms that the C–H or C–N peak intensities have become lower than in the spectra obtained for the polymers. The presence of organic matter is lower in the samples obtained at 800 °C than in the samples obtained at 500 °C. The M–N bond at higher wavelength was more visible in the samples obtained at 500 °C. Absorption peaks for amide groups were found less intense at higher temperatures as most of the amide groups were decomposed.

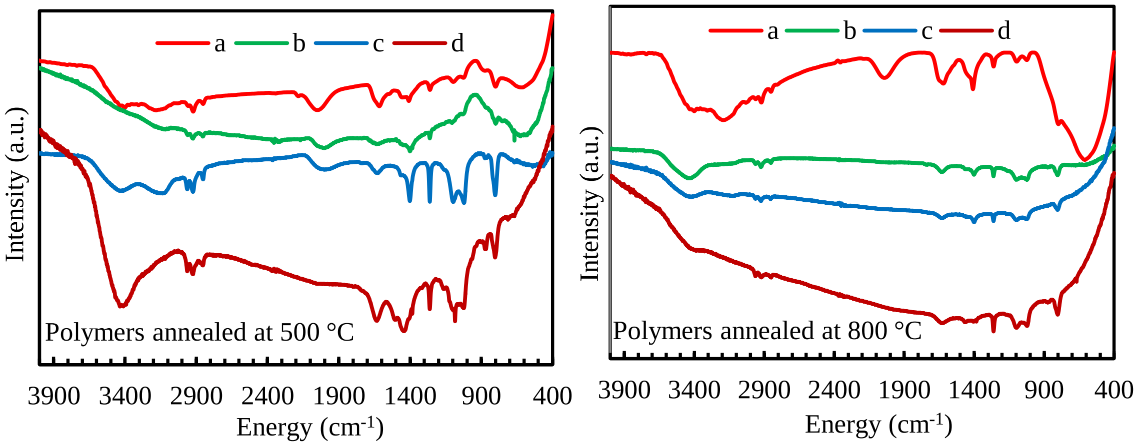

Figure 6.8: FT-IR spectra of the TiN_x samples obtained from annealing the polymers from TDMAT reaction with, a NH_3 , b $^nPrNH_2$, c HDA/$^nPrNH_2$ and d CTAB/$^nPrNH_2$.

BET N_2 adsorption/desorption isotherms for TiN_x samples (Fig. 6.9 and 6.10) obtained from polymers NH_3 and CTAB/$PrNH_2$ at 500 or 800 °C are type IV with a narrow hysteresis loop and the pore size distribution shows peak values in the mesoporous range i.e. 20 to 40 Å. Isotherms for the TiN_x sample from CTAB/$^nPrNH_2$-based polymer (Fig. 6.10, d) showed a distinct capillary condensation step at ~ 0.5 P/P_o, which is attributed to a well-developed uniform mesoporous material. Results of the nitrogen adsorption/ desorption analysis of TiN_x obtained from annealing $^nPrNH_2$- or HDA/$^nPrNH_2$-based-polymers at 500 or 800 °C exhibited a poorly defined type IV isotherm with a tendency to change to a type I isotherm (Fig. 6.9, b and 6.10 c). This behaviour is characteristic of materials with pore sizes on the borderline between the mesoporous and microporous ranges. TiN_x samples obtained from annealing HDA/$^nPrNH_2$-based polymer (Fig. 6.10, c) showed type I adsorption/ desorption isotherm for microporous materials, whereas BJH calculation from the adsorption branch showed no peak for TiN_x nanoparticles.

Multiple point surface area, total pore volume (TPV) and pore size distribution (PSD) data for TiN_x samples obtained from various polymers, annealed at 500 or 800 °C are given in table 6.4. Polymers annealed at lower temperature had higher surface area than the samples obtained at higher temperature. TiN_x powders obtained from annealing the HDA/$^nPrNH_2$-based polymer annealed at 500 °C showed the highest surface area of 319 m^2 g^{-1}, while a TiN_x obtained from NH_3-based polymer annealed at 500 °C had a surface area of 237 m^2 g^{-1} with the highest total pore volume (TPV) values. Pore diameter for most of the samples lay in the mesoporous range, while no peak values were obtained for the TiN_x samples obtained from annealing HDA/$^nPrNH_2$-based polymer at both the temperatures. Error estimation for surface area was found to be ± 1 m^2g^{-1} and for PSD ± 1 Å.

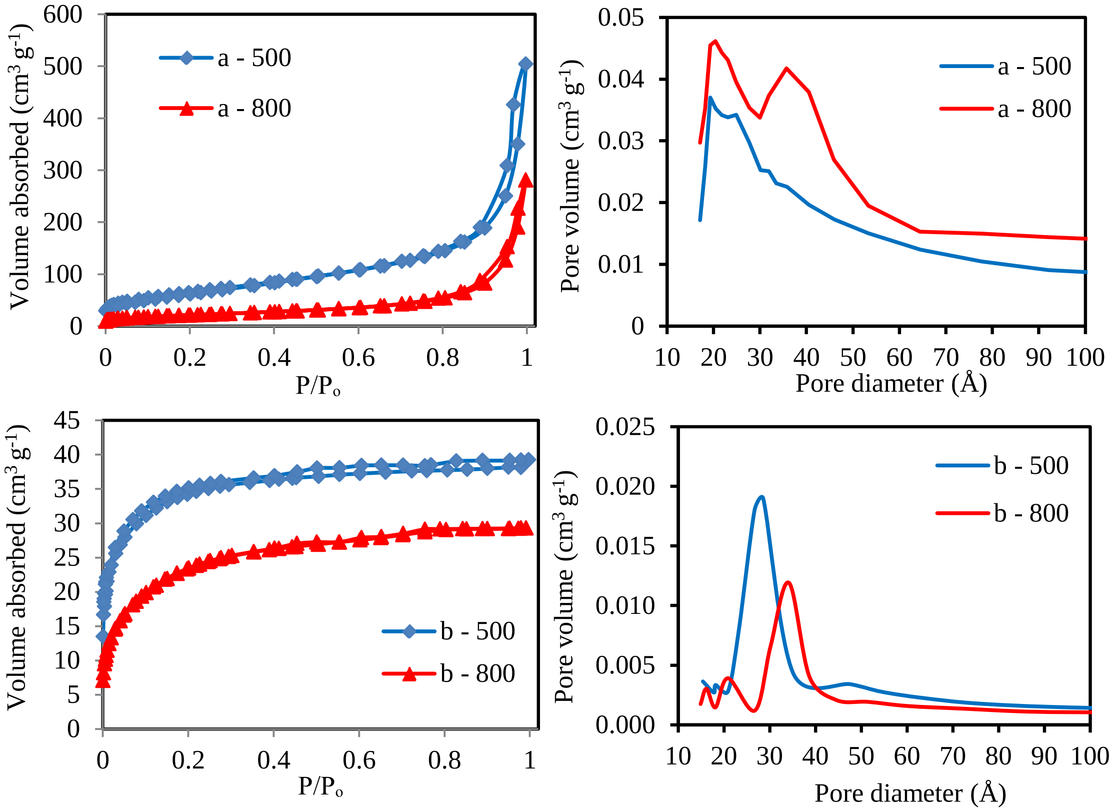

Figure 6.9: N_2 adsorption/desorption analysis data (left) and BJH pore size distribution (right) for the TiN_x samples obtained from TDMAT reaction with, a NH_3 and b $^nPrNH_2$, at the given temperatures (°C).

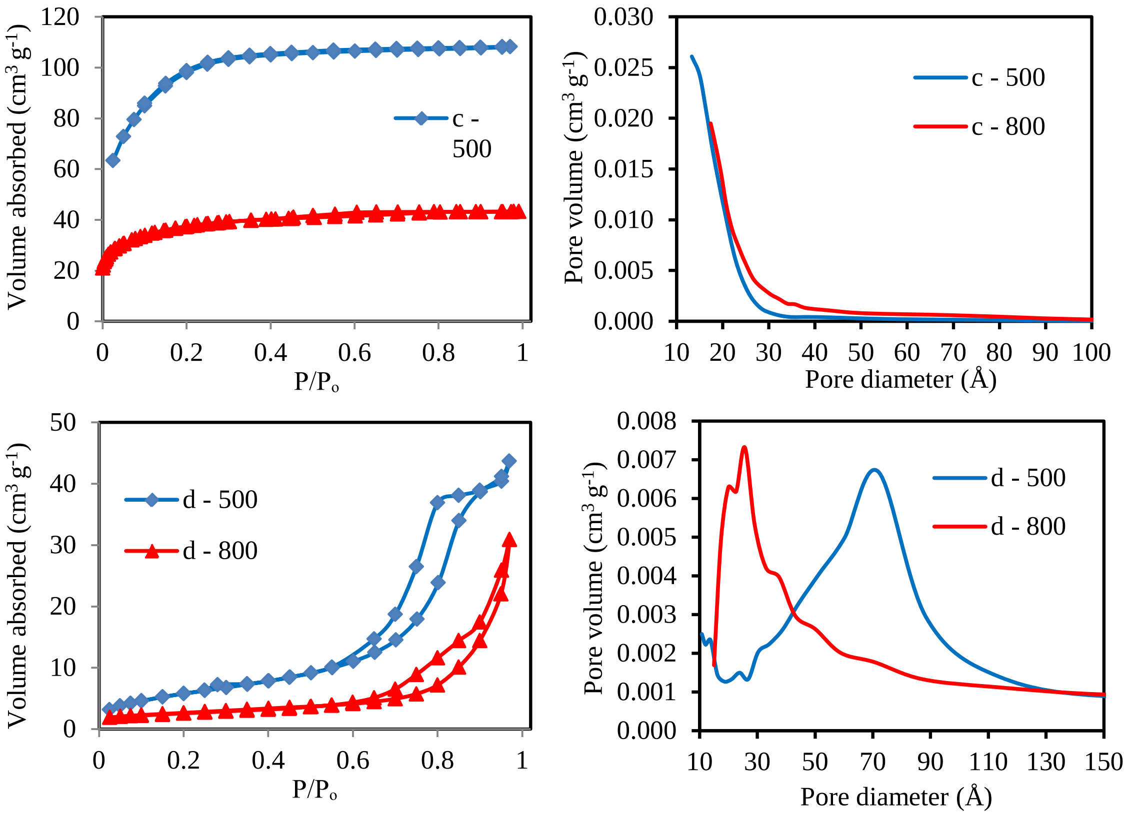

Figure 6.10: N_2 adsorption/desorption analysis data (left) and BJH pore size distribution (right) for the TiN_x samples obtained from TDMAT reaction with and c HDA/$^nPrNH_2$ and d CTAB/$^nPrNH_2$ at the given temperatures (°C).

Table 6.4: N_2 adsorption/desorption analysis data for the TiN_x samples obtained after annealing the polymers at the given temperatures.

Polymer	Annealing temperature (°C)	S_{BET} (m^2 g^{-1})	TPV (cm^3 g^{-1})	PSD (Å)
NH_3	500	237	0.78	20 – 40
NH_3	800	77	0.44	20 – 30
$PrNH_2$	500	116	0. 53	38
$PrNH_2$	800	38	0.12	34
HDA/$PrNH_2$	500	319	0.28	No peak
HDA/$PrNH_2$	800	110	0.17	No peak
CTAB/$PrNH_2$	500	48	0.02	70
CTAB/$PrNH_2$	800	23	0.05	23 – 60

Transmission electron microscopy images of TiN_x samples (Fig. 6.11 and 6.12) shows that the particles were spherical in shape, and particle sizes grew larger with increasing temperature. Particles sizes of TiN_x powders obtained at 500 °C were in the range of 5 to 10 nm, while the samples obtained at 800 °C showed the particle sizes in the range of 10 to 20 nm. The results were close to the particle sizes calculated through the Scherrer equation in table 4. Particles are mostly agglomerated.

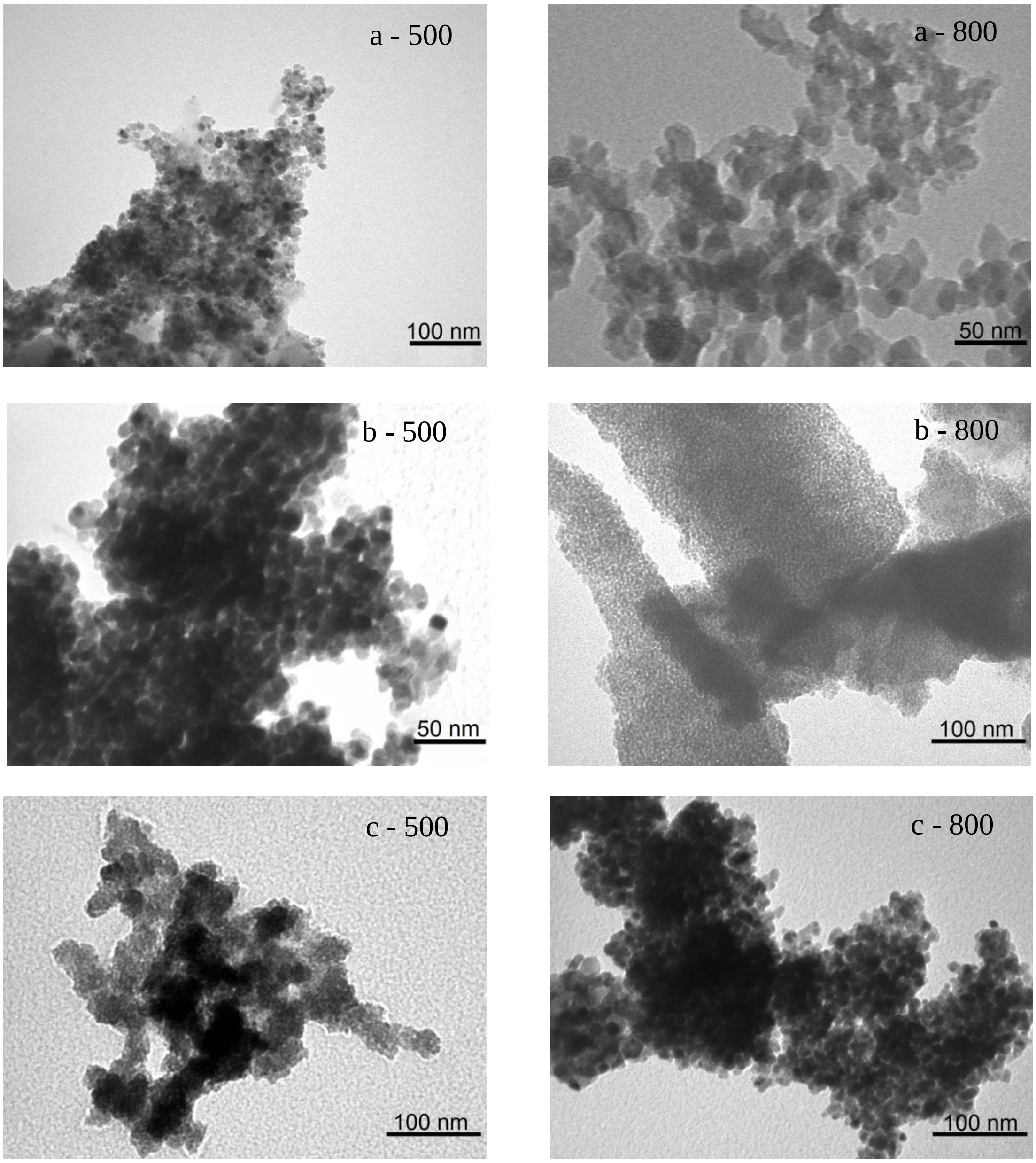

Figure 6.11: TEM images of TiN_x samples obtained from TDMAT reaction with, a NH_3, b $^nPrNH_2$, and c HDA/$^nPrNH_2$ at the 500 and 800 (°C).

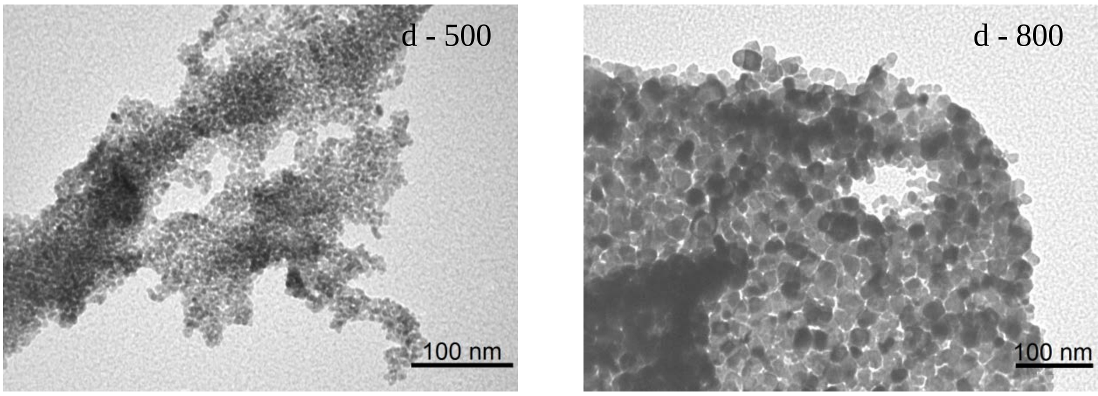

Figure 6.12: TEM images of TiN_x samples obtained from TDMAT reaction with, d CTAB/$^{n}PrNH_2$ at the 500 and 800 (°C).

6.5 Capacitance measurements

Capacitance of the materials is measured through cyclic voltammetry using a three electrode cell. A Hg/HgO electrode was used as a reference electrode, with a thin platinum gauze of 0.005 mm of thickness as a counter electrode. A high surface area counter electrode was used to ensure it had a higher capacitance than the working electrode capacitance that limits the current passed. A working electrode was made by the disc electrode method or depositing ink of active material over a metal foil substrate. The cell used for electrochemical analysis was given in chapter 3 figure 3.8. the electrolyte was degassed to remove excess oxygen by bubbling nitrogen for 30 minutes through the solution. A blanket of nitrogen was maintained over the electrolyte surface while acquiring the voltammograms.

6.5.1 Disc electrode method

Disc electrodes of TiN_x for analysis were prepared. Carbon black and Teflon were added to TiN_x nitride powder in the ratio of active material 75 %, carbon black 20 %, and Teflon 5%. Each electrode disc was 100 μm in thickness and of 1 cm diameter. Micro-discs were dried overnight under vacuum at 120 °C to remove the surface moisture. The mass of active material in each disc after drying was found to be ~ 16 mg. Active material was first passivated under flow of nitrogen with the help of a needle attached to a Schlenk line. Two small holes were made in the lid of the sample vial to be used as nitrogen inlet and an outlet needle. Samples were left for passivation procedure for 48 h. PXD was carried out for the sample after passivation to confirm any decomposition to the material.

Cyclic voltammograms of TiN_x electrodes were cycled in 1 M KOH (aq) using the scan rates of 100 and 25 mV s^{-1} (Figure 6.13 and 6.14). Electrode discs were prepared in four different ways to analyse the surface behaviour of TiN_x samples in electrochemical experiments i.e. using untreated sample, thermally oxidised, voltammeteric oxidised electrodes and potential step oxidised. The difference between various treatments is discussed in the next paragraph.

Untreated sample (no surface treatment) was used to make disc electrodes without any surface treatment. For thermal oxidation the TiN_x sample was heated at 300 °C in air for 2 h before making the electrodes. Voltameteric surface oxidation was carried out in 1 M KOH. The electrode disc was supported on a Pt gauze working electrode, with a Pt gauze counter electrode and Hg/HgO reference electrode and cycled between 0 and 1.2 V for 100 cycles. Potential step surface oxidation TiN_x electrode disc were individually oxidised by immersing the electrode into 1M KOH(aq) so that the meniscus of the electrolyte completely covered the disc area. The TiN_x disc was supported on to a coarse Pt gauze working electrode, with a fine Pt gauze counter electrode and Hg/HgO reference electrode and the cell potential was increased to 1.2 V for 100 s. Previous studies show that the TiN_x nanoparticles have a lower oxidation current than carbon black at operating potentials 1.0 and 1.2 V of a fuel cell, which indicates its corrosion resistance properties. Nitride components of TiN_x decrease and oxide/oxynitride layer components increase on the TiN_x surface during the potential cycling.[35] Disc electrodes were not found to be a good choice for manganese nitride samples (chapter 3), and did not show any better results for TiN_x samples. The results shown here for TiN_x disc electrodes were obtained in the initial stages of the project simultaneously with manganese nitride work.

A sample based on HDA/$PrNH_2$ at 800 °C with a surface area of 116 m^2 g^{-1} was used to make disc electrodes. Electrodes made from untreated sample showed the highest capacitance at all the scan rates. The electrodes that were potential step oxidised showed poor charge capacity compared to all the other types of electrodes at both scan rates. This decrease in capacity could be due to the fact, that potential scanning under highly basic conditions leads to chemical instability of the nano-sized TiN_x crystallites and some alterations to the surface composition. Disc electrodes were not tried anymore due to their low charge storage capacity (Table 6.5). The main reasons for poor capacity could be the binder that covers the electrode surface, and presence of organic matter in the TiN_x samples.

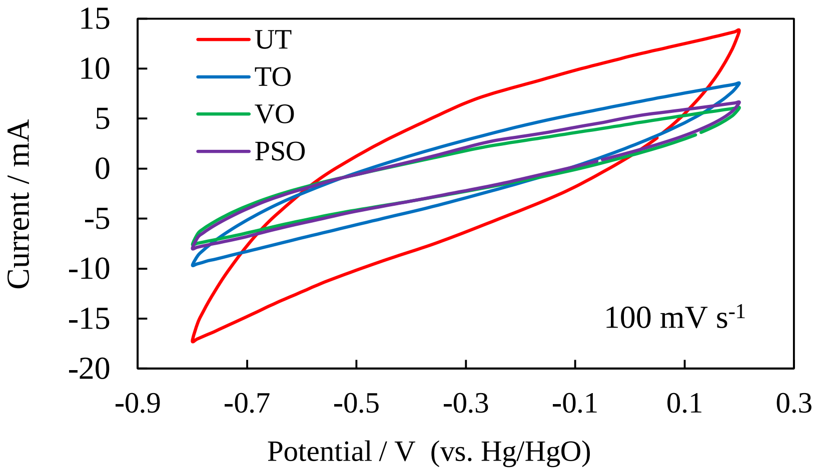

Figure 6.13: TiN_x aqueous cycling in 1 M KOH Vs Hg/HgO at 100 mV s^{-1}, where UT = untreated sample, TO = thermally oxidised, VO = voltametric oxidation and PSO is for potential step oxidation.

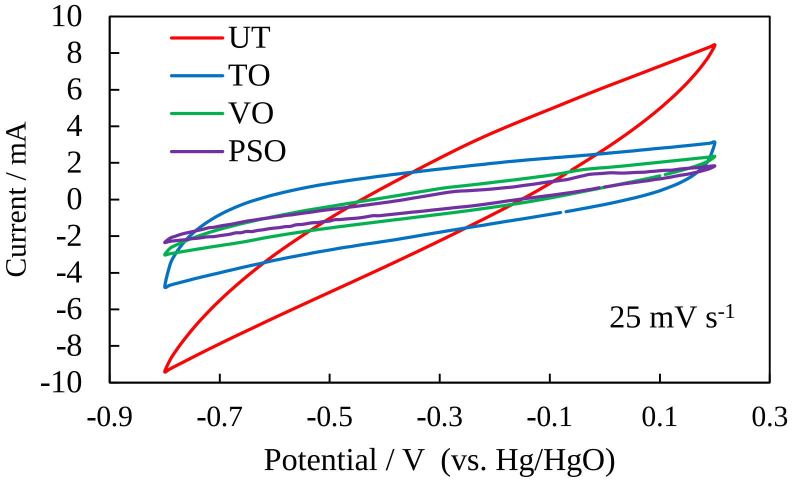

Figure 6.14: TiN_x aqueous cycling in 1 M KOH Vs Hg/HgO at 25 mV s^{-1}, where UT untreated sample, TO thermally oxidised, VO voltameteric oxidation and PSO = potential step oxidation.

Capacitance values (Table 6.5) at 100 or 25 mV s^{-1} did not show much difference. Electrode made of untreated sample still remained the highest of all the other electrodes tested after surface treatment.

Table 6.5: Capacitance for the CVs in figure 10 and 10.1

Scan rates	100 mV s^{-1}	25 mV s^{-1}
Surface treatment	Capacitance F g^{-1}	
Untreated	4	6
Thermal oxidation	4	4
Voltameteric oxidation	2	3
Potential step oxidation	1	3

6.5.2 *Ink electrode method*

Electrode inks were prepared by grinding together 75 wt. % of TiN_x and 20 wt. % of acetylene black. PVDF wt. 5 % was fully dissolved in 1.5 ml of CP (cyclopentanone) by stirring the solution for 4 hours. The mixture of TiN_x and carbon black was added to PVDF solution and stirred overnight to obtain the electrode ink. Titanium foil was used as the substrate (1 × 2 cm pieces, 0.05 μm thickness, Advent research materials, Oxford, England). Any surface oxides were removed from the foil by rubbing the surface with abrasive paper. The substrate was cut into pieces, washed with ethanol and dried in air. Working electrodes were made by depositing electrode ink by pouring drops over the substrate of 1 × 1 cm area of the foil and leaving to dry at room temperature for at least 2 hours. The electrodes were finally dried overnight at 120 °C under vacuum. ~ 0.6 mg of the electrode material was measured on each foil after drying. No surface treatment was carried out to the active materials in making ink electrodes.

Cyclic voltammograms were obtained by fixing the potential window of 1.0 V (- 0.6 to 0.4) vs Hg/HgO reference electrodes; electrodes were found to be oxidized or reduced when not in this range. The voltammograms shown in figure 6.15 were measured for the sample obtained from the HDA/$^{n}PrNH_2$-based polymer annealed at

800 °C, that was also tested through disc electrodes as discussed in section 6.5.1. Samples were run at 100 mV s^{-1} in 1 M or 6 M KOH to find out the effect on charge storage capacity. A specific capacitance of 15.2 F g^{-1} or 18 F g^{-1} was measured in 1 M or 6 M KOH respectively, observing no significant increase in capacitance in highly concentrated electrolyte. Some oxidation at the cathodic end was also observed when using 6 M KOH. An electrode was also run at a lower scan rate of 25 m V s^{-1}, the measured capacitance at lower scan rate showed a similar value of 14.3 F g^{-1} as obtained at higher scan rates.

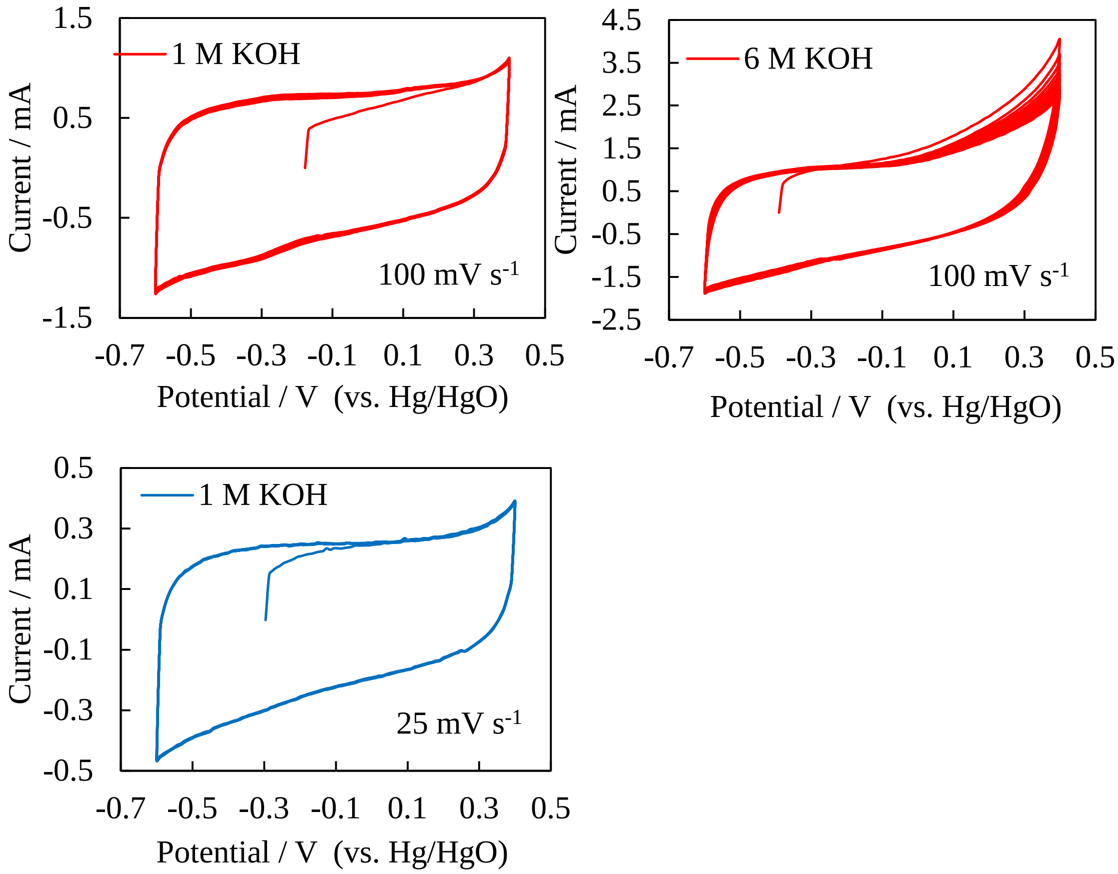

Figure 6.15: Cyclic voltammograms for a TiN_x sample obtained from annealing the HDA/^{n}PrNH_2-based polymer at 800 °C, at the given scan rates and electrolyte.

Voltammograms shown in figure 6.16 was obtained for TiN_x sample obtained from HDA/PrNH_2 based polymer annealed on 500 °C. The sample was found highly unstable at 100 mV s^{-1} in the given potential range. The sample was also tested by making electrode using Ni foil as the current collector, which showed similar results as were obtained with the Ti foil current collector. No further analysis was carried out for this sample.

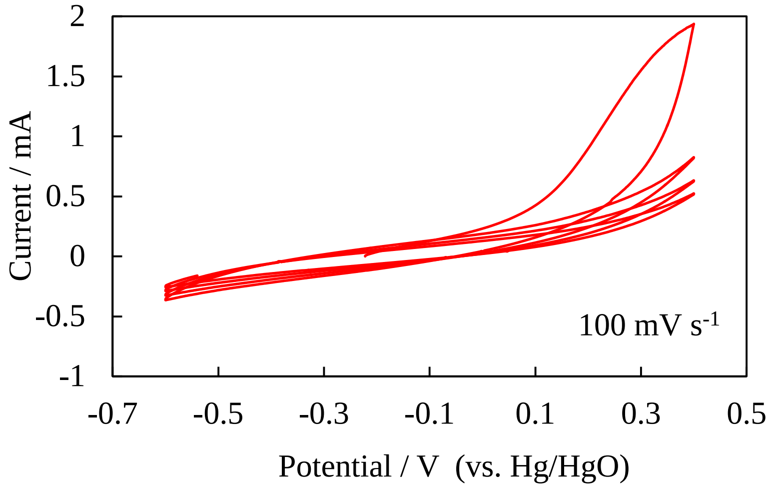

Figure 6.16: Cyclic voltammograms for a TiN sample obtained from annealing the HDA/^{n}PrNH$_2$-based polymer at 500 °C cast at Ni substrate, at the given scan rate in 1 M KOH electrolyte.

The cyclic voltammogram shown in figure 6.17 was obtained for a TiN$_x$ sample obtained from annealing a TDMAT/NH$_3$-polymer at 500 °C. The electrode was run in 1 M KOH at 100 mV s^{-1} in a 1.1 V potential window. Specific capacitance of 38 F g^{-1} was calculated on the 1st scan, which was then reduced to 33 F g^{-1} on the 10th and 5 F g^{-1} at 100th cycle.

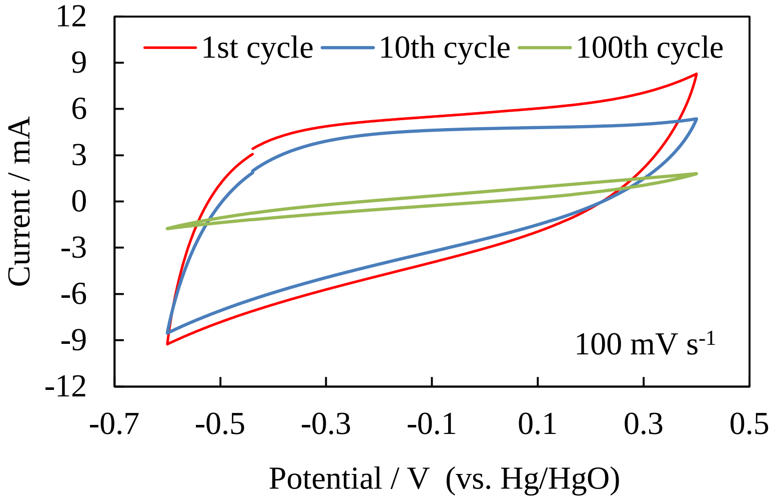

Figure 6.17: Cyclic voltammograms for a TiN sample obtained from annealing the NH_3-based polymer at 500 °C, at the given scan rate in 1 M KOH electrolyte.

The cyclic voltammogram shown in figure 6.18 was obtained for a TiN_x sample obtained from annealing a CTAB/^{n}PrNH$_2$-polymer at 500 °C. The electrode was run in 1 M KOH at 100 mv s^{-1} in 1.1 V of potential window. A specific capacitance of 17 F g^{-1} was calculated at 1st scan, which was then reduced to 15 F g^{-1} on the 10th and 3 F g^{-1} on the 100th cycle.

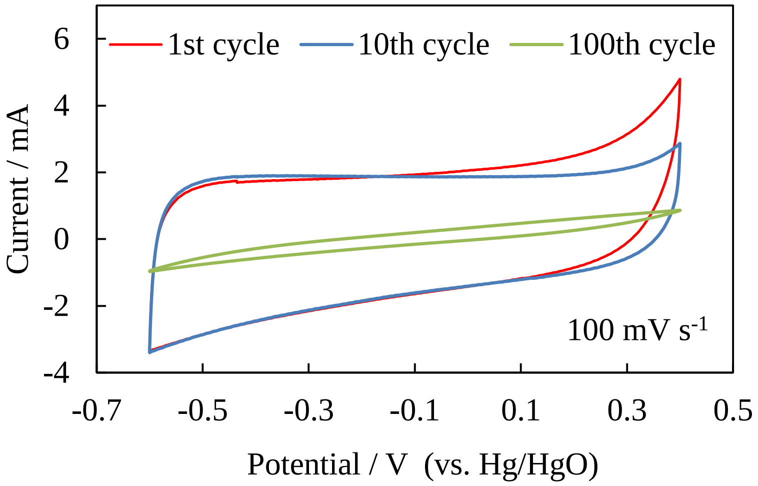

Figure 6.18: Cyclic voltammograms for a TiN_x sample obtained from annealing the CTAB/PrNH$_2$-based polymer at 500 °C, at the given scan rate in 1 M KOH electrolyte vs Hg/HgO reference electrode.

Transition between Ti^{4+} and Ti^{3+} occurs over -0.8 to 0.2 V vs Hg/HgO due to chemisorption of electrolyte (-OH) on to the TiN.[20] Since no Faradaic peak appears in the CV curve in our case, this suggests that most of the capacitance is due to the formation of electric double layer on electrode electrolyte interface.

No extensive studies of charge storage behaviour were carried out for TiN_x materials due to their poor charge capacities and fast capacitance drop with scan numbers. The main reasons for such behaviour could be the presence of organic matter in the samples which reduces the ionic activity on the electrode surface, and could also be their fast surface oxidation in the aqueous electrolytes.

6.6 Conclusions

The TiN_x samples were prepared with high surface area by forming the polymeric precursors through NH_3 condensation over TDMAT or adding structure directing agents i.e. long chain amines. Templating with various surfactants has been carried out to study the morphological variations of nano-sized TiN_x. Samples were obtained by annealing the polymers at 500 or 800 °C under ammonia at a slow temperature ramp rate of 1 °C/min to ensure the complete degradation of the long chain amine groups of the surfactants. All the annealed samples of TiN_x resulted in phase pure cubic TiN_x with small or no contamination by hydrocarbons. The highest carbon contents of 2.32 % were found in a sample annealed at 500 °C templated with HDA. All the samples annealed at 800 °C showed less than 0.5 % of carbon. TGA analysis showed higher mass loss in the samples annealed at 500 °C, suggesting the presence of imide groups at this temperature. A surface area of 319 $m^2 g^{-1}$ was measured for the TiN_x sample obtained from HDA/$^nPrNH_2$-based polymer pyrolysed at 500 °C. Transmission electron microscopy revealed particle sizes in the range of 3 to 20 nm. Cyclic voltammetry with the disc electrode showed no significance specific capacity when a TiN_x sample (untreated/surface treated) obtained from HDA/$^nPrNH_2$-based polymer pyrolysed at 800 °C was tested. As the binder material covers the surface of active material making an insulating shield, no appreciable capacitance was seen at any scan rate for TiN_x sample.

6.7 References

1. R. A. Janes, M. Aldissi and R. B. Kaner, *Chem. Mater*, 2003, **15**, 4431.
2. B. M. Biwer and S. L. Bernasek, *Appl. Surf. Sci.*, 1986, **25**, 41.
3. S. Ishihara and M. Hanabusa, *Appl. Phys.*, 1998, **84**, 596.
4. Y. Nakagawa, C. Grigoriu, K. Masugata, W.H. Jiang and K. Yatsui, *J. Mater. Sci.*, 1998, **33**, 529.
5. L. E. Toth, *Transition metal carbides and nitrides*, Acdemic Press: New York, 1971.
6. M. Eslamloograml and Z.A.Munir, *J. Am. Ceram. Soc.*, 1990, **73**, 2222.
7. S. Deevi and Z. A. Munir, *J. Mater. Res*, 1990, **5**, 2177.
8. R. M. Ren and Z.G. Yang, *Mater. Sci. Eng.*, 2000, **286**, 65.
9. B. Mazumder and A. L. Hector, *J. Mater. Chem.*, 2009, **19**, 4673.
10. J. Buha, I. Djerdj, M. Antonientti and M. Niederberger, *Chem. Mater.*, 2007, **19**, 3499.
11. W. Q. Jiang, G. R. Li and X. P. Gao, *Chem. Comm.*, 2009, 6720.
12. K.T. Jacob, R. Verman and R. M. Mallya, *J. Mater. Sci.*, 2002, **37**, 4465.
13. E.G. Gillan and R. B. Kaner, *Chem. Mater.*, 1996, **8**, 333.
14. J. H. Bang and K. S. Suslick, *Adv. Mater.*, 2009, **21**, 1.
15. S. Dong, X. Chen, L. Gu, X. Zhou, H. Xu, H. Wang, Z. Liu, P. Han, J. Yao, L. Wang, G. Cui and L. Chen, *J. Appl. Mater. Inter.*, 2010, **3**, 93.
16. S. Kaskel, K. Schilchte and M. Khanna, *J. Mater. Chem.*, 2003, **13**, 1496.
17. S. Kaskel, K. Schilchte and T. Kratzke, *Mol. Catal. A: Chem.*, 2004, **208**, 291.
18. M. H. Chisholm, V. Baxter, J. Gama, F. Distasi, A. L. Hector and I. P. Parkin, *Chem. Mater.*, 1996, **8**, 1222.
19. A. W. Jackson, O. Shebanova, A. L. Hector and P. F. McMillan, *J. Solid State Chem.*, 2006, **179**, 1383.
20. D. Choi and P. N. Kumta, *J. Electrochem. Soc.*, 2006, **12**, 2298.
21. X. Liu, Y. Zhang, T. Wu and J. Huang, *Chem. Comm.*, 2012, **48**, 9992.
22. Z. Y. Yuan and B. L. Su, *J. Mater. Chem.*, 2006, **16**, 663.
23. Y. Wan, Y. Shi and D. Zhao, *Chem. Comm.*, 2007, **1**, 897.
24. B.T. Holland, L. Abrams and A. Stein, *J. Am. Chem. Soc.*, 1999, **121**, 4308.
25. K. Nakamoto, *Infrared and Raman Spectra of Inorganic and Organic Compounds*, 3rd ed.; J. Wiley: New York, 1978.

26. M. Hasegawa and T. Yagi, *J. Alloys Compd.*, 2005, **403**, 131.
27. K. Aigner, W. Lengauer, D. Rafaja and P. Ettmayer, *J. Alloys Compd.*, 1994, **215**, 121.
28. A. N. Christensen, *Acta Chem. Scandi.*, 1974, **32**, 89.
29. R. B. Von Dreele and A. C. Larson, Generalized structure analysis system, Los Alamos National Laboratory, Los Alamos NM, NM 87545, USA, December 2002 release.
30. R. B. Von Dreele and A. C. Larson, GSAS Manuual, LANSCE MS-H805, Los Alamos National Laboratory, Los Alamos NM, NM 87545, 2000.
31. *PCPDFWIN Powder Diffraction File*, version 2.4; International Center for the Diffraction Data: Swarthmore, PA, 2003.
32. J. Patscheider, *Mater. Res. Soc. Bul.*, 2003, **28**, 180.
33. B. Mazumder and A. L. Hector, *Top. Catal.*, 2009, **52**, 1472.
34. H. J. Holleck, *Vac. Sci. Technol.*, 1986, **A 4**, 1384.
35. B. Avasarala and P. Haldar, *Electrochem. Acta*, 2010, **55**, 9024.

7 Solvothermal route to VN/C composites and use as supercapacitors

7.1 Introduction

Different techniques have been developed to prepare vanadium nitride (VN), including the traditional carbothermal, reduction and nitridation of metal oxides with graphite in N_2 atmosphere above 1000 °C, heating metal powder in N_2 flow at around 1350 °C,[1] reactive magnetron sputter deposition,[2] pulsed laser desorption (PLD),[3] ammonolysis of metal chlorides,[4] oxides[5] or sulphides[6] at 800-1400 °C, solid state metathesis (SSM),[7] and other methods. [8] Most of the relevant synthesis procedures have been discussed in chapter 5. A few of the examples of VN/C materials are discussed below.

Vanadium nitride/multiwalled carbon nanotube nanocomposites were produced using an inorganic or organic vanadium oxide precursor via a sol-gel route.[9] In these reactions the CNTs were introduced externally (30 wt %) to the organic ($VO(OC_3H_7)_3$) or inorganic (V_2O_5) precursors and heated under ammonia to obtain the VN/CNTs composites. Using hexadecyl trimethyl ammonium bromide (CTAB) as the template, mesoporous VN nanocrystalline was synthesized by NH_3 reduction of precursor V_2O_5. N_2 absorption results indicated that the surface area of the VN sample was 88 $m^2\ g^{-1}$ and most pores were distributed in the range of 2–6 nm. The supercapacitive behaviour of the VN electrode in 1 mol/L KOH electrolyte was studied by cyclic voltammetry (CV) and constant current charge-discharge measurements. The results showed that the mesoporous VN electrode had both electrical double-layer capacitive properties and redox pseudocapacitive properties. The specific capacitance of the VN electrode was 517 F g^{-1} at 1 mV s^{-1} and 275 F g^{-1} at a sweep rate of 10 mV s^{-1}.[10] An easy way to produce VN nanocomposites at relatively low temperature (800 °C) using simple precursors is presented. A self-catalytic growth approach has been developed for spontaneous preparation of superconducting VN/C nanocomposites composed of VN nanoparticles and well-defined carbon nanofibers. The carbon nanofibers were found to grow by a self-catalytic process through tiny VN nanocrystals. In this case, a homogeneous gel-like starting product has been formed that is converted by calcination into the corresponding metal nitride, without any preliminary treatments or further purification. The as-obtained nanocomposite showed an onset superconducting temperature at 9 K, which is similar to that reported for bulk VN.[11]

Nanostructured VN synthesised by a two-step ammonolysis reaction of metal halide was also studied as the electrode material for supercapacitors. Specific capacitance of 1340 F g^{-1} was obtained at a scan rate of 2 mV s^{-1}, with 554 F g^{-1} reported at a high scan rate of 100 mV s^{-1}.[12] VN obtained by calcining V_2O_5 at 400 °C showed a specific capacitance of 161 F g^{-1} at 30 mV s^{-1} and remained at 70 % of the original value when the scan rate was increased from 30 to 300 mV s^{-1}.[13]

In this chapter we have synthesised VN nanocomposites through a single precursor source via a solvothermal route. $V(NMe_2)_4$ has been reacted with dry ammonia in a hydrothermal bomb at various temperatures. The final product formed at any temperature contained a high amount of carbon. Carbon was found present as macro tubes surrounding the nanostructured VN particles. Detail of synthesis procedures and results are discussed below.

7.2 Synthesis

$V(NMe_2)_4$ was synthesised with the procedure given in chapter 5. $V(NMe_2)_4$ 0.5 g was placed in a hydrothermal bomb, with a silica liner inside. The bomb was sealed tightly inside the glove box, and then it was attached to a Schlenk line for nitrogen supply. Benzene 20 ml was added to the $V(NMe_2)_4$ inside the bomb through an opening on the top of the bomb under flowing nitrogen. NH_3 was condensed over sodium in a Schlenk tube by cooling it with a dry ice and acetone mixture. Dry ammonia ~ 6 ml was transferred and condensed over the $V(NMe_2)_4$ solution. The hydrothermal bomb was sealed again and left to warm to room temperature. The bomb was then heated overnight in a vertical tube furnace at 300, 400 or 500 ˚C. The pressure in the bomb was recorded as 25, 45 and 70 bar at 300, 400 or 500 °C after 16 hr heating. The furnace was turned off and the bomb was left to cool down to room temperature. The hydrothermal bomb was then attached to a Schlenk line in the fumehood to release the pressure inside. The sample with solvent from the bomb was transferred to a Schlenk tube inside the glove box. The solvent was removed using a filter and the final product was dried under vacuum. ~ 170 mg black powder VN/C was obtained at 300 °C, while ~ 145 mg was collected at 400 and 500 °C. All the samples were treated as air-sensitive for initial analysis, and were passivated by slow exposure to air for electrochemical investigation.

7.3 Analysis of VN/C samples

PXD patterns (Fig. 7.1) of VN/C samples show the peaks for cubic structure profile. The peaks were broad in the samples obtained at lower temperature. The data was checked against the JCPDS and ICSD data bases. Two unindexed peaks at 33 and 46, 2 θ(°) were also observed in the patterns.

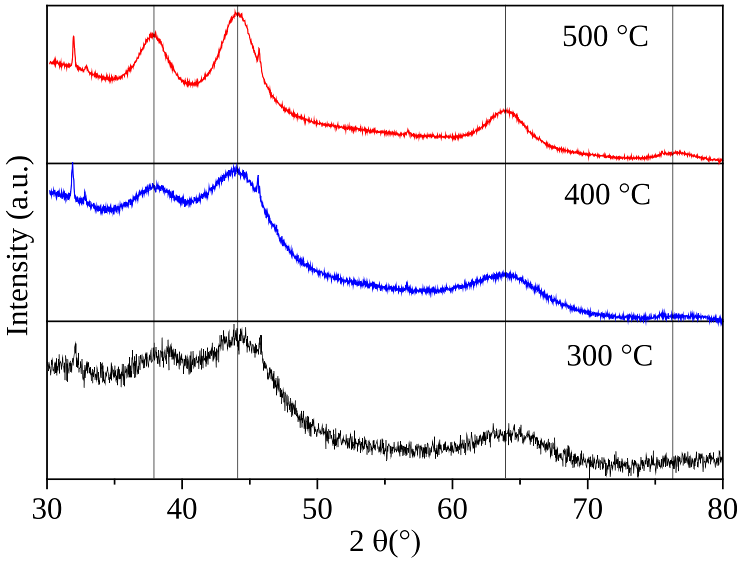

Figure 7.1: PXD patterns for VN/C obtained from solvothermal reaction of $V(NMe_2)_4$ and NH_3, at the given temperatures. Vertical lines are the reflection positions for rock salt vanadium nitride with the lattice parameter a = 4.13 Å. Peaks at 33 and 46, 2 θ(°) were not identified.

PXD data was refined using GSAS[14]. A fit to the PXD pattern of a VN/C sample obtained at 500 °C is shown in figure 7.2. The cif file with standard parameters for rock salt VN was obtained from ICSD and used for structure refinement.[15] Asymmetry of the reflections due to axial divergence at low angles was refined setting the "asym" option free to be refined, detail of which can be found as CW profile function 2 given in the GSAS manual.[16] Refined lattice parameters and the crystallite sizes are given in table 7.1. A sample obtained at 300 °C showed the low values of the lattice parameter similar to the VN sample obtained at 300 °C from ammonolysis of an amide polymer precursor (chapter 5).

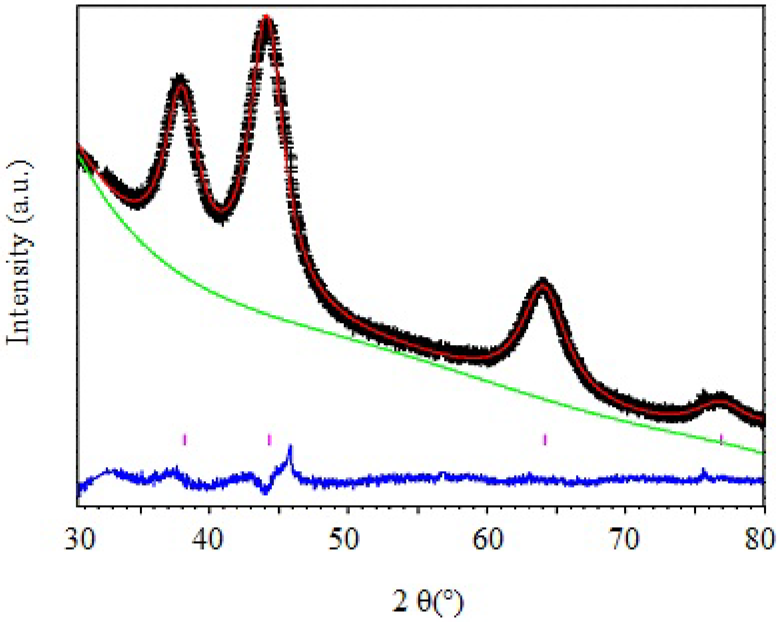

Figure 7.2: Rietveld fit to the VN/C sample obtained at 500 °C. Crosses marks the data points, upper continuous line the calculated profile and lower continuous line the difference; tick marks are the positions of allowed reflections for rock salt VN, and the continuous green line is the profile background.

Table 7.1: Refined lattice parameters, goodness of fit and crystallite size values for VN/C samples,

Sample temp. °C	a (Å)	R_{wp}/R_p %	Crystallite size nm
300	4.081(8)	3.7/3.1	3
400	4.164(4)	1.4/1.1	4
500	4.130(12)	1.3/1.1	6

Elemental analysis (Table 7.2) showed high carbon contents in all the samples. The reason could be low reactivity of NH_3 with $V(NMe_2)_4$, so incomplete amination reaction occured and some of the precursor decomposed without going to product, since ammonia has a poor cracking efficiency at lower temperature. Hydrogen contents decreased at higher temperature showing that most of the amide precursor had been converted into product with increase in temperature. Carbon in the final product was found to be 14.15, 12 and 11.5 weight % in the samples obtained at 300, 400 or 500 °C, respectively. Some of the carbon contamination could be due to the solvent decomposition as previously observed in the synthesis of metal nitrides through the solvothermal route.[17] The theoretical percentage of nitrogen in VN is 21.5 %.

Table 7.2: Elemental analysis of VN samples obtained by solvothermal reactions

Sample (°C)	% C	% H	% N	Composition
300	13.4	2.41	17.83	$VN_{0.95}C_{0.67}H_{1.8}$
400	10.74	1.23	20.02	$VN_{1.1}C_{0.59}H_{0.92}$
500	10.32	0.73	19.72	$VN_{1.03}C_{0.55}H_{0.39}$

A sample of VN/C was also prepared using 3 ml of NH_3 at 300 °C, which showed a very high carbon content of 19.5 % and no pressure in the bomb was observed with this amount of ammonia.

IR spectra (Fig. 7.3) show absorption peaks at 3400 cm^{-1} that correspond to residual ν-(NH)[18] and 1600-1700 cm^{-1} δ-(NH_2).[18, 19] Stretching for ν-(C-H) was found at 2890 to 2980 cm^{-1} and the peaks were more intense in the higher temperature sample and stretching between 1440 to 1270 cm^{-1} was attributed to ν-(C-N).

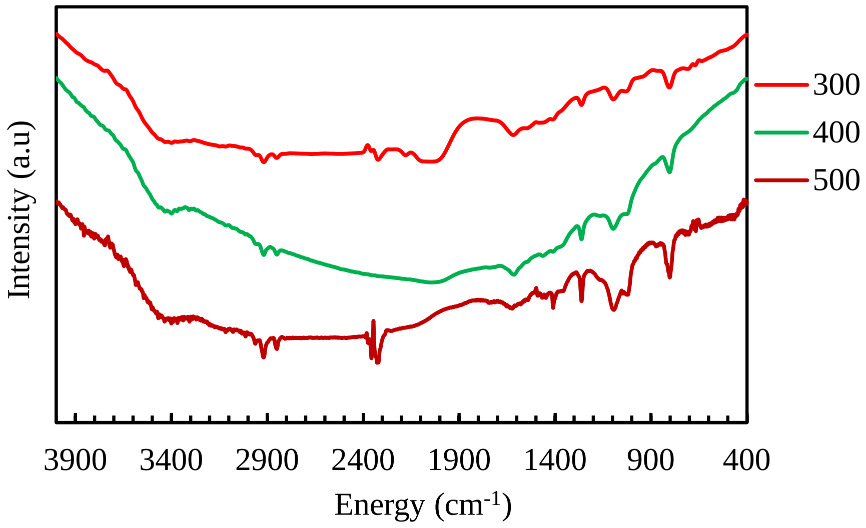

Figure 7.3: IR spectra for VN/C samples obtained at the given temperatures (°C)

The thermogravimetric analysis (TGA) curve (Fig. 7.4) for the polymeric precursor was obtained by annealing the samples at 900 °C. Previous studies using TGA-MS[18] showed that loss of amine and ammonia occurs at lower temperature. Samples obtained at 400 and 500 °C showed less mass loss in the first step below 500 °C. Mass loss above 600 °C corresponds to nitrogen and some of the ammonia. The sample obtained at 300 C showed a larger mass loss due to the presence of residual precursor. The low reactivity of NH_3 at lower temperature makes some of the precursor unreacted, as higher H_2 contents evidenced in the elemental analysis of the sample. Mass loss at lower temperature i.e. below 250 °C was not much even in the sample obtained at lower temperature as seen in the metal nitrides obtained through gas ammonolysis, where surface adsorbed NH_3 was evolved.

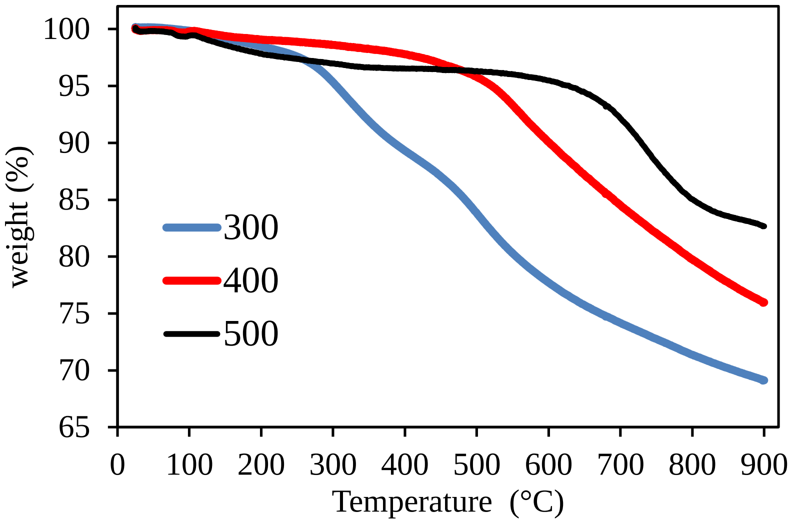

Figure 7.4: TGA curves under Ar flow for VN/C samples obtained at the given temperatures (°C)

TGA analyses on the synthesised samples under air flow were performed to analyse the composition of the material and to see its thermal stability in air (Figure 7.5). Samples were passivated first by slow exposure to air before exposing to the TGA air flow. Oxidation of carbonaceous residue is expected to decrease the weight, and oxidation of VN and VC species leads to an increase in weight. The sample obtained at lower temperature showed gradual mass loss throughout, which is consistent with the fact that a large amount of carbon residue from the precursor remained in the sample (Table 7.2) and was mostly present in the free form (Figure 4 B). The sharp decrease in mass at 400 to 450 °C corresponds to carbon decomposition.[20] Weight loss due to graphitic carbon was also observed in the similar temperature range in molybdenum carbide-carbon nanocomposite materials.[21] Weight gain in the samples obtained at 400 and 500 °C was 3.7 and 13 %, respectively.

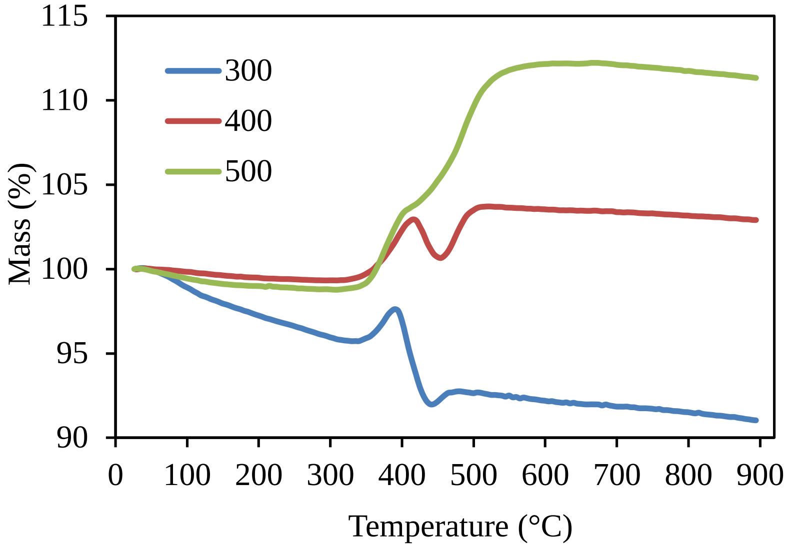

Figure 7.5: TGA curves under air flow for VN/C samples obtained at the given temperatures (°C).

TEM images show the carbon nanotubes encapsulating the nanostructured VN particles in every sample. A TEM image obtained for the VN/C sample at 300 °C shows some of the loose carbon particles dispersed with VN sample. Vanadium nitride particles were found in the size range of 2 to 10 nm, mostly in the form of an interconnected network. VN particles were also found with no carbon tube like structures, in the form of agglomerated clusters of small particles in the sample obtained at 500 °C (Figure 7.6 F). A TEM image for VN/C composite structures from a template route showed the tiny VN nanoparticles embedded in self-supported substrate microsheets, with carbon nanofibers arising from the body of the substrate.[11] Another study on the nanocomposite VN/CNTs showed the carbon nanotubes dispersed in small nanoparticles of VN.[9]

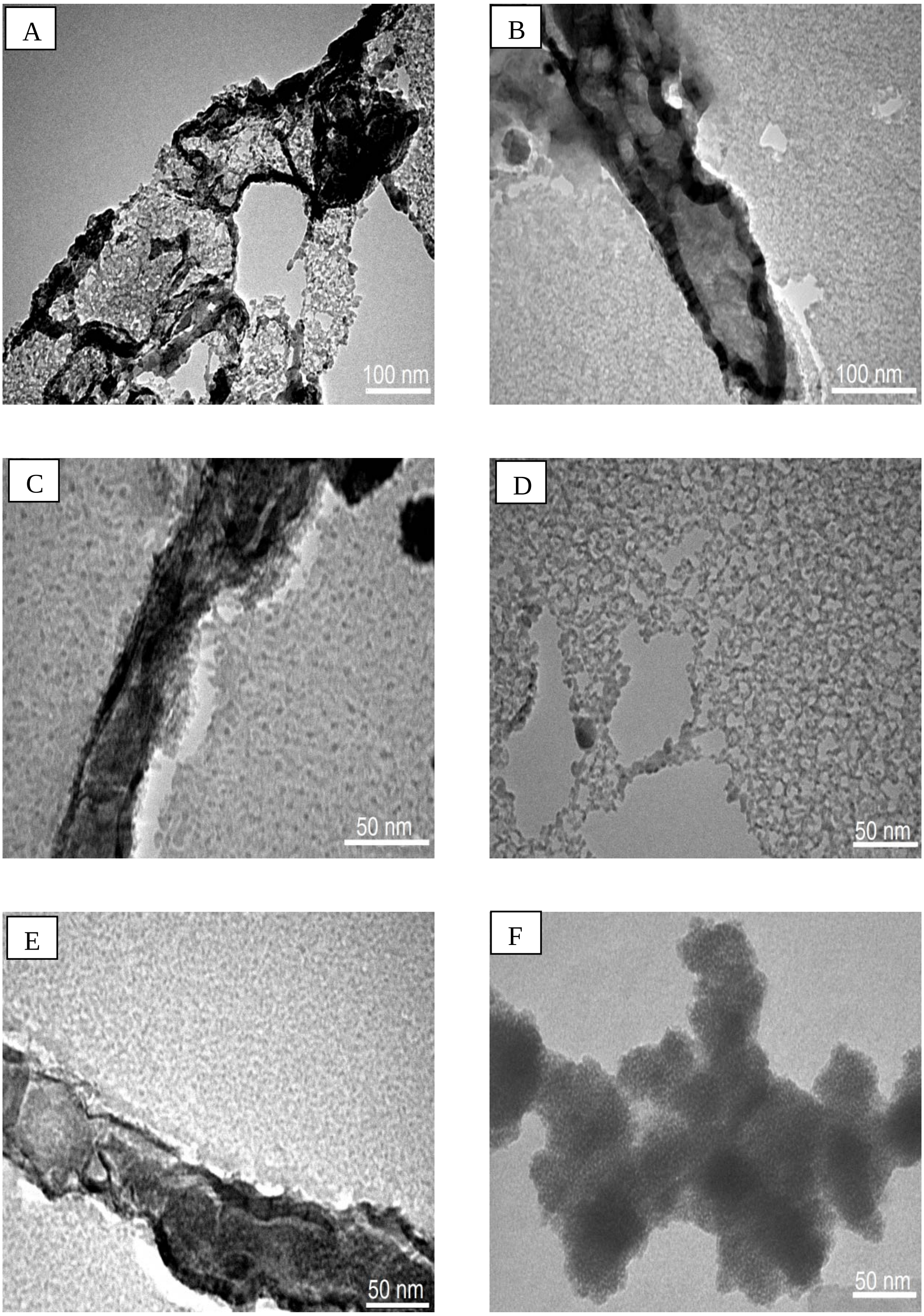

Figure 7.6: TEM images for VN/C structures obtained via solvothermal ammonolysis of $V(NMe_2)_4$ at 300 (A, B), 400 (C, D) and 500 °C (E, F).

The hysteresis loops show type IV isotherms, typical of the existence of randomly connected spherical pores (Fig. 7.7). Pore diameter of all the samples lay in the mesoporous range (Fig. 7.8). The highest surface area of 34 $m^2\ g^{-1}$ was measured for the sample obtained at 400 °C (Table 7.3). Error estimation for surface area values was found to be ±1 $m^2\ g^{-1}$ and for PSD was ±1 Å.

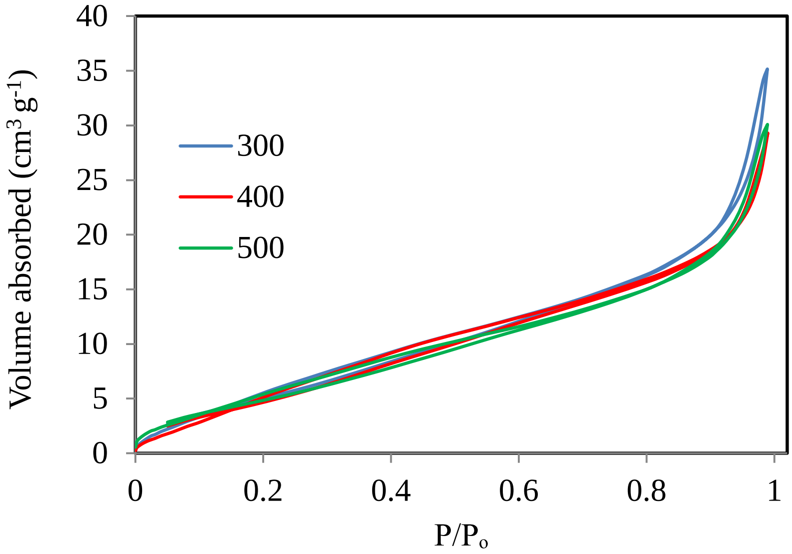

Figure 7.7: N_2 Adsorption/desorption isotherms for the Mn_3N_2 samples obtained at the given temperatures (°C).

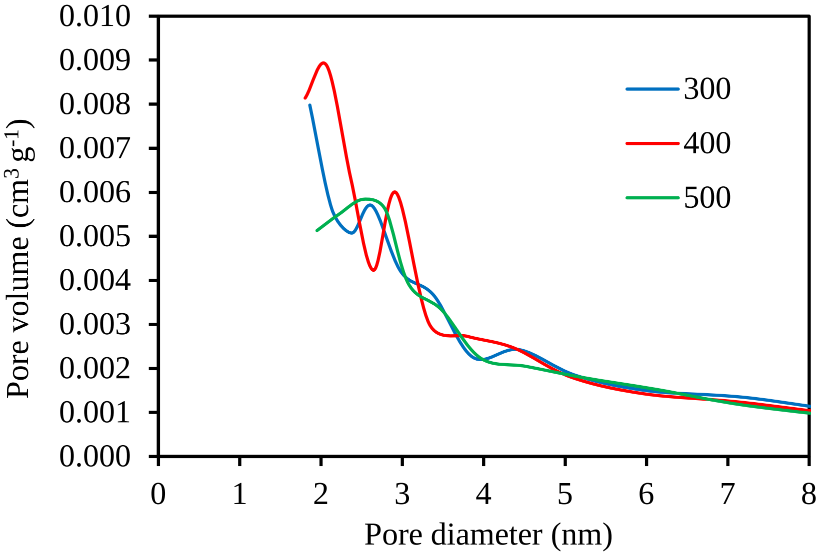

Figure 7.8: Pore size distribution for the VN/C samples obtained at the given temperatures (°C).

Table 7.3: S_{BET} surface area of VN/ C products obtained at the given temperature

Temperature (°C)	Surface area $m^2\ g^{-1}$	TPV ($cm^3\ g^{-1}$)	PSD (nm)
300	33	0.044	2-5
400	34	0.037	2-5
500	28	0.039	2-5

7.4 Capacitance measurements

The capacitance of the material was measured through cyclic voltammetry a using three electrode cell. A Hg/HgO electrode was used as a reference electrode, and a thin platinum gauze of 0.005 mm thickness as a counter electrode. The high surface area counter electrode was used to ensure it had a higher capacitance than the working electrode capacitance that limits the current passed. The Electrolyte was degassed to remove excess oxygen by bubbling nitrogen for 30 minutes through the solution. A blanket of nitrogen was maintained over the electrolyte surface while acquiring the voltammograms. Voltammograms were run with electrodes made by the ink method. Electrode ink was prepared by grinding together electrode material VN/C (80 wt %) and acetylene black (15 wt %). Polyvinylidene fluoride (PVDF) (5 wt %) was fully dissolved in the desired volume of cyclopentanone, (CP) by stirring the solution for 2 hours (1.5 ml per 100 mg of electrode material). The mixture of electrode material and carbon black is added to PVDF solution and stirred overnight to obtain the electrode ink. The working electrode was made by depositing ink of active material over a titanium foil substrate over the 1 × 1 cm area, drying in air for 2 h, and finally drying under vacuum overnight at 120 °C. 0.6 mg of the active material was found to be deposited after weighing the dried electrodes. All the voltammograms measured for these materials were based on the same area of electrode and material loading given in the description above.

An electrode made of a VN/C sample obtained at 500 °C was first run in different potential windows to choose the final potential stability window for the electrode (Fig. 7.9). No long oxidation or reduction tails were observed in a wide potential window of 1.3 V. However, a window of 1 V i.e. – 0.2 to –1.2 V on the basis of highest columbic efficiency of 98 %, with a reasonable rectangular shape, giving equal oxidation and reduction current profile was chosen.

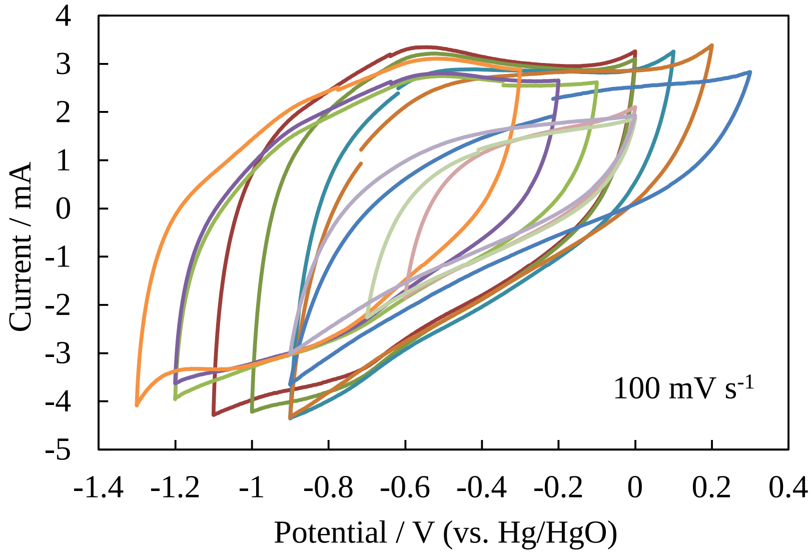

Figure 7.9: Potential window of VN/C in 1 M KOH against Hg/HgO at 100 mV s^{-1}.

Cyclic voltammograms obtained for VN/C samples are shown in figure 7.10 and 7.11. A capacitance drop was observed for the VN/C samples obtained at any scan rate. The sample obtained at 400 and 500 °C showed an increase in capacitance up to 50 cycles and then started dropping when run for 100 cycles at 100 mV s^{-1}. No capacitance drop was seen at other scan rates up to 10 cycles. No distinct redox features were seen in the sample observed at 300 °C. Oxidation peaks at – 1 and – 0.6 V, and a reduction peak - 0.75 V were observed in samples obtained at 400 and 500 °C.

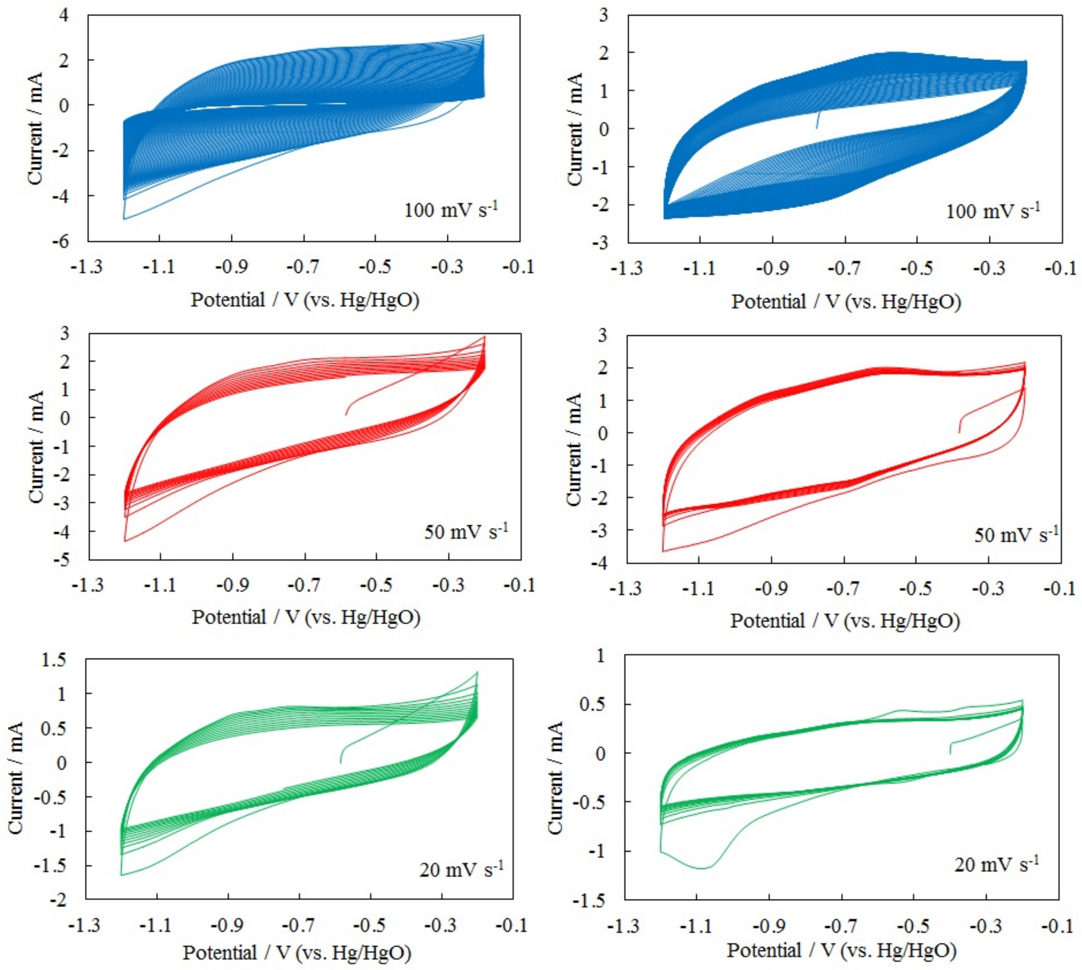

Figure 7.10: Cyclic voltammograms for VN/C samples obtained at 300 (right) and 400 °C (left) at the scan rates as labelled in 1 M KOH against Hg/HgO reference electrode.

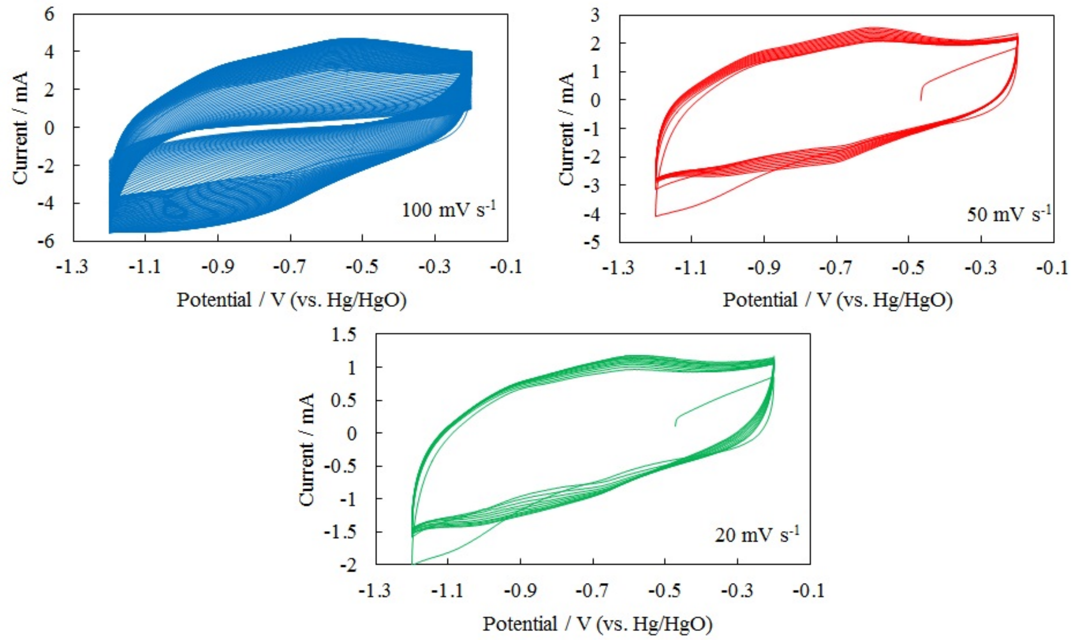

Figure 7.11: Cyclic voltammograms for VN/C samples obtained at 500 °C at the scan rates as labelled in 1 M KOH against Hg/HgO reference electrode.

Table 7.4: Capacitance measurements in F g^{-1} for the samples of VN/C obtained from solvothermal reaction of $V(NMe_2)_4$ and NH_3.

Scan rate (mVs^{-1})	**100**			**50**		**20**	
Scan number	**1**	**10**	**100**	**1**	**10**	**1**	**10**
300 °C	25	21	15	42	30	40	29
400 °C	27	30	17	43	41	39	35
500 °C	39	43	8	52	60	64	72

A graph (Fig. 7.12) below showing the capacitance behaviour of the three VN/C samples run at 100 mV s^{-1} for 100 cycles. A drop in capacitance can be seen from the very first cycle in the lower temperature sample, while the other two samples increased in charge storage up to the 40th cycle.

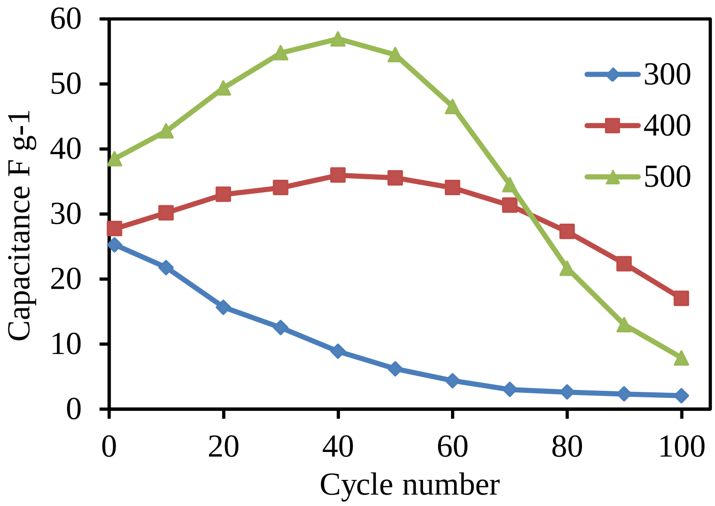

Figure 7.12: Graph of capacitance vs cycle number showing charge storage behaviour up to 100 cycles at 100 mV s^{-1} in 1 M KOH of VN/C samples obtained at the given temperatures (°C).

The sample obtained at 500 °C was also run at a scan rate of 2 mV s^{-1}, where the initial capacitance of 86 F g^{-1} is increased to 103 F g^{-1} from the 1st to 4th cycle and dropped back to 54 F g^{-1} by the10th cycle (Fig. 7.13). The sample retained 63 % of its initial capacitance until the last cycle in the potential window of 1 V as used for other scan rates. The vanadium nitride anode was electrochemically unstable in aqueous solution due to the irreversibility of forming vanadium oxide (VO_x) on the surface.[22-24] The electrochemical reaction mechanism of VN nanoparticles are given in chapter 5.

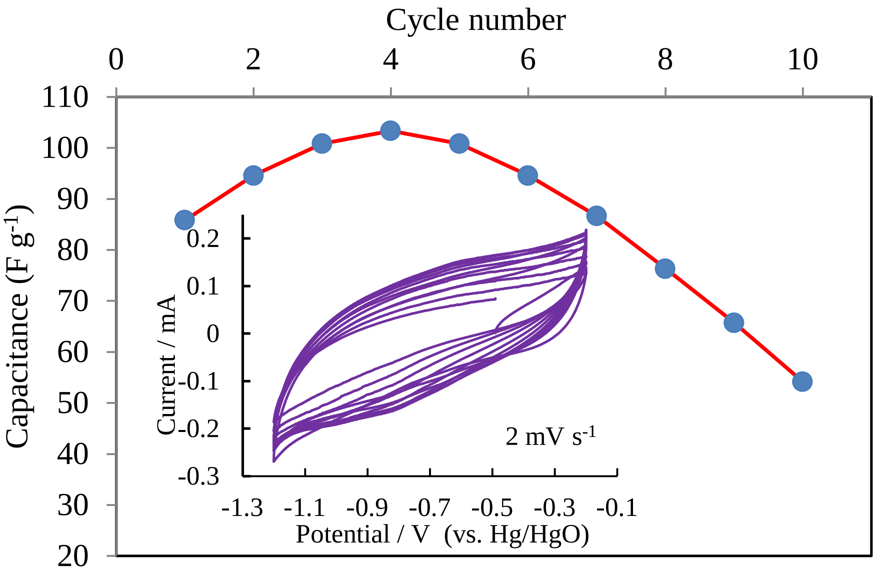

Figure 7.13: Cyclic voltammograms for a VN/C sample obtained at 500 °C run at 2 mV s^{-1} in 1 M KOH, in a potential window of 1 V. The graph above shows capacitance behaviour vs cycle number for the given CV.

A short potential window of 0.7 V was used to analyse the charge storage behaviour up to 300 cycles (Fig. 7.14). For this run a VN/C obtained at 500 °C was run at a scan rate of 100 mV s^{-1}, where the initial capacitance of 37 F g^{-1} increased to 53 F g^{-1} from the 1st to 120th cycle and dropped back to 15 F g^{-1} by the 300th cycle. The sample tends to retained the initial capacitance up to the 200th cycle.

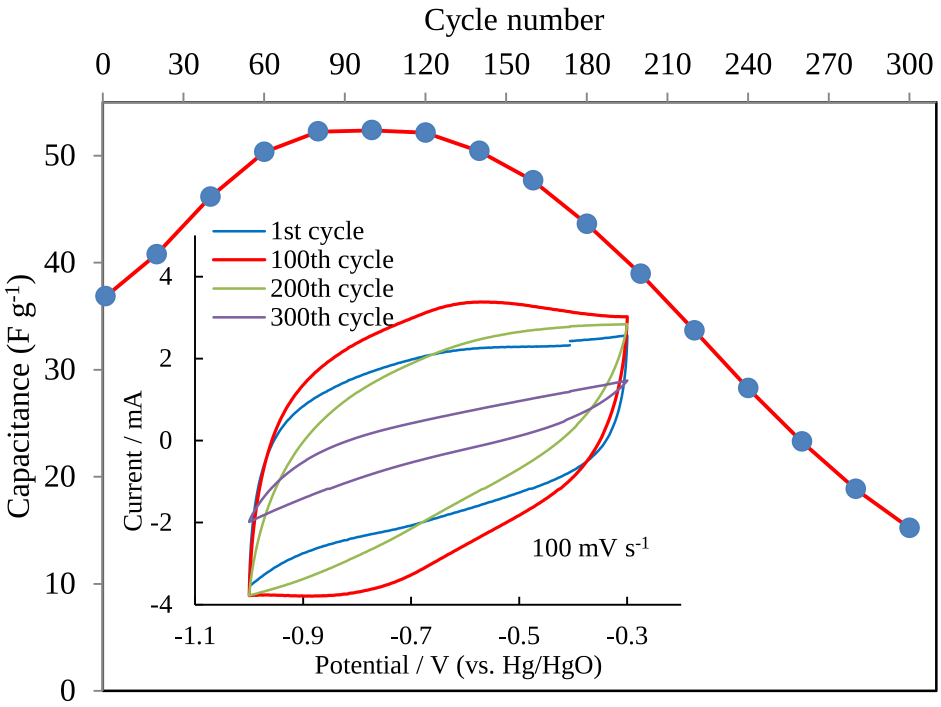

Figure 7.14: 300 cycle run for a VN/C sample obtained at 500 °C with the graph above showing capacitance behaviour vs cycle number.

7.5 Conclusions

Vanadium nitride carbides were prepared through a solvothermal ammonolysis of $V(NMe_2)_4$ in a hydrothermal bomb at three different temperatures 300 – 500 °C. PXD showed the crystallinity of the product increased on increasing the temperature. Diffraction data was fitted to the rock salt VN structure. Combustion microanalysis revealed a high carbon content, with some hydrogen at lower temperature. Thermogravimetric analysis under flowing Ar showed great mass loss in the samples obtained at lower temperature, having more amide residue in the sample. TGA under air showed mass gain in the samples obtained at higher temperature due to oxidation which shows vanadium nitride was present with vanadium carbide. TEM images of the samples has showed tubular carbon were present along with nanostructured VN particles. Grain boundaries of the carbon structures were more distinct in the samples obtained at 500 °C than the other samples. Adsorption/ desorption data showed type IV isotherms for mesoporous structures as confirmed by the pore distribution data.

Cyclic voltammetry discovered the highest capacitances for the sample obtained at 500 °C at any scan rate.

7.6 References

1. P. T. Shaffer, Plenum Press handbooks of high-temperature materials, **vol. 1**, Plenum Press, New York, 1964.
2. X. Chu and S. A. barnett, *Vac. Sci.Technol.*, 1996, **14**, 3124.
3. Z. N. Dai, A. Miyashita, S. Yamamoto, K. Narumi and H. Naramoto, *Thin Solid Films*, 1999, **347**, 117.
4. J. P. Dekker, P. J. Vanderput, H. J. Vering and J. Schoonman, *Mater. Chem.*, 1994, **4**, 689.
5. Y. G. Li, L. Gao, J. G. Li and D. S. Yan., *Am. Ceram. Soc.*, 2002, **85**, 1294.
6. P. S. Herle, M. S. Hegde and N. Y. Vasathacharya, *Solid State Chem.*, 1997, **134**, 120.
7. I. P. Parkin, *Chem. Soc. Rev.*, 1996, **25**, 199.
8. J. Q. Hu, Q. Y. Lu, K. B. Tang, S. H. Yu, Y. T. Qian, G. E. Zhou and X. M. Liu, *Am. Chem. Soc.*, 2005, **127**, 15722.
9. C. M. Ghimbeu, E. Raymundo-Pinero, P. Fioux, F. Beguin and C. Vix-Guterl, *J. Mater. Chem.*, 2011, **21**, 13268.
10. G. Zhao-Hui, Z. Hao, C. G-Ping, H. Min-Fang and Y. Yu-Sheng, *Inorg. Mater.*, 2012, **27**, 1261.
11. W. Yao, M. Gao, S. Yu, J. Dingc and X. Lic., *RSC Adv.*, 2011, **1**, 1489.
12. D. Choi, G. E. Bloomgren and P. N. Kumta, *Adv. Mater.*, 2006, **18**, 1178.
13. X. Zhou, H. Chen, D. Shu, C. He and J. Nan, *Phys. Chem. Sol.*, 2009, **70**, 495.
14. R. B. Von Dreele and A. C. Larson, Generalized structure analysis system, Los Alamos National Laboratory, NM87545, USA, December 2002 release.
15. S. Hosoya, T. Yamagishi and M. Tokonami, *Phys. Soc. Jap.*, 1968, **24**, 363.
16. R. B. Von Dreele and A. C. Larson, GSAS Manual, LANSCE MS-H805, Los Alamos National Laboratory, Los Alamos NM, NM 87545, 2000.
17. B. Mazumder, P. Chirico and A. L. Hector, *Inorg. Chem.*, 2008, **47**, 9684.
18. M. H. Chisholm, V. Baxter, J. Gama, F. Distasi, A. L. Hector and I. P. Parkin, *Chem. Mater.*, 1996, **8**, 1222.
19. K. Nakamoto, Infrared and Raman Spectra of Inorganic and Organic Coumpounds 3rd ed.; J. Wiley: New York, 1978.

20. S. K . Louis, Pang, J. D. Saxby and S. P. Chatfield, *Phys. Chem. Sol.*, 1993, **97**, 3654.

21. N. S. Alhajri, D. H. Anjum and K. Takanabe., *J. Mater. Chem.* , 2014, **2**, 10548.

22. A. M. Glushenkov, D. Hulicova-Jurcakova, D. Llewellyn, G. D. Lu and Q. Chen, *Chem. Mater.*, 2010, **22**, 914.

23. D. W. Choi and P. N. Kumta, *Electrochem. Solid State Lett.*, 2005, **8**, A418.

24. L. Zhang, C. M. B. Holt, E. J. Luber, B. C. Olsen, T. H. Wang, M. Danaie, X. H. Tan, V. W. Lui, W. P. Kalisvaart and D. Mitlin, *J. Phys. Chem.*, 2011, **49**, 24381.

8 Conclusions

Transition metal nitrides can be obtained through various methods as discussed in the introduction chapter. Metal nitrides have been mostly synthesised using the oxide precursor source, due to ease of access and handling feasibility of the precursor in air. Final products from oxide precursors are often contaminated with oxygen and need long annealing time at high temperature. High temperature reactions cause agglomeration of the particles hence reduce the surface area due to sintering effects. Our work aimed to synthesise the metal nitrides from nonoxide precursor sources (metal amides or chlorides) to produce oxygen free nitrides at lower temperatures and short annealing times. Solution phase reactions were the first choice to produce the metal nitrides from a solvothermal route or using polymer synthesis from metal amide or chloride sources. Solvothermal conditions are desirable for metathesis reactions because the heat produced can be absorbed by the solvent, resulting in more controlled growth of small-scale crystallites.[1]

Ammonolysis of a chloride or dialkylamide group results in an amide moiety that can act as a nucleophile towards another metal centre yielding a bridging imide group. A polymeric product containing amide, imide and unreacted chloride or dialkylamide group results, the balance between these varying with reaction conditions. The resultant chloroimide, amide/imide polymer precursor on annealing under ammonia yields the nitride product with the loss of ammonia.[2]

In energy-storage devices supercapacitors bridge the gap between batteries and conventional capacitors with regard to energy/power performance. Supercapacitors have been intensively studied due to their long cycle life, highly reversible charge storage process and high specific power density. Electrode materials for supercapacitors comprise carbon-based materials, conducting polymers and transition metal oxides. Carbon nanotubes, mesoporous carbon spheres and graphene show good electrochemical stability and high electrical conductivity, however they show a low specific capacitance (90 to 250 F g^{-1}), which makes them unsuitable for high energy density SCs.[3, 4] Polyaniline and polypyrrole are the most extensively studied conducting polymers for supercapacitor applications. Polyaniline can reach a specific capacitance of 150-190 F g^{-1} [5, 6] while polypyrrole shows a specific capacitance of 80-100 F g^{-1}.[7, 8]

Since the pseudo-capacitance of conducting polymers is limited by the percentage dopant, that they contains redox stability hinders their use for supercapacitors. In addition, the exchange of anions between polymer and electrolyte usually has a detrimental effect on electric charge density, switching speed and cyclability.[9] Transition metal oxides have also been extensively explored as electrode materials for supercapacitors due to their layered structures and ability to adopt various oxidation states. The charge storage mechanism of metal oxides is pseudo-capacitive in nature. MnO_2 can deliver capacitance of ~ 240 F g^{-1} with capacitance fading with the scan number.[10] Fe_3O_4 shows a poor specific capacitance of 5-7 F g^{-1} in common neutral or basic electrolytes.[11] The highest specific capacity for Fe_3O_4 of 510 F g^{-1} can be achieved by promoting the electrolyte anion species.[11] Among metal oxides ruthenium oxide has been reported to have a very high capacitances of ~ 900 F g^{-1} for hydrous ruthenium dioxide.[12, 13] However the cost of ruthenium oxide makes it impractical for its use in supercapacitors on a commercial scale. Poor conductivity, structural instability and general irreversibility of metal oxides limit their practical application for high energy density supercapacitors.[14, 15] Recently metal nitrides have attracted the researcher's attention as for supercapacitors applications due to their significant advantages. Metal nitrides have excellent much superior electrical conductivity (4000-55500 S cm^{-1}) than most of the metal oxides, and thus can exhibit higher power density,[16] higher specific capacitance[17, 18] and higher mechanical stability compared to carbon and metal oxide electrode materials.[19, 20]

In this project two main precursor sources were used a metal chloride or a metal amide to synthesise the metal nitrides. Materials obtained through chloride precursor sources (MoN_x and Mn_3N_2) were found with fairly high surface area and porous structure at lower temperatures. It could possibly be concluded that salt formation during the reaction of a chloride based system enhances the pore formation and possibly avoids the aggregation of the nitride powders. On the other hand the amide derivatives were generally found to have lower surface area and were often found to be contaminated with the precursor residue at lower temperature. TiN_x samples produced through template infiltration or from ammonolysis of TDMAT were found with high surface areas, although the presence of organic matter was evidence in elemental analysis. High temperature annealing and long annealing time with slow ramp rate caused agglomeration of the particles and might collapse the porosity of the powders.

The electrochemical response of the nitride materials was dependent on the surface area (Fig. 8.1) and the chemical composition of the electrode material. Carbon contamination in transition metal nitrides is an important consideration because it degrades electrical and optical properties and often causes adhesion problems.[21] TiN_x nanoparticles synthesised using the long chain amines were found to be contaminated with the residual organic matter. Nitrides samples where excess of organic residues were observed to be present showed low charge/discharge performance and poor cycling life.

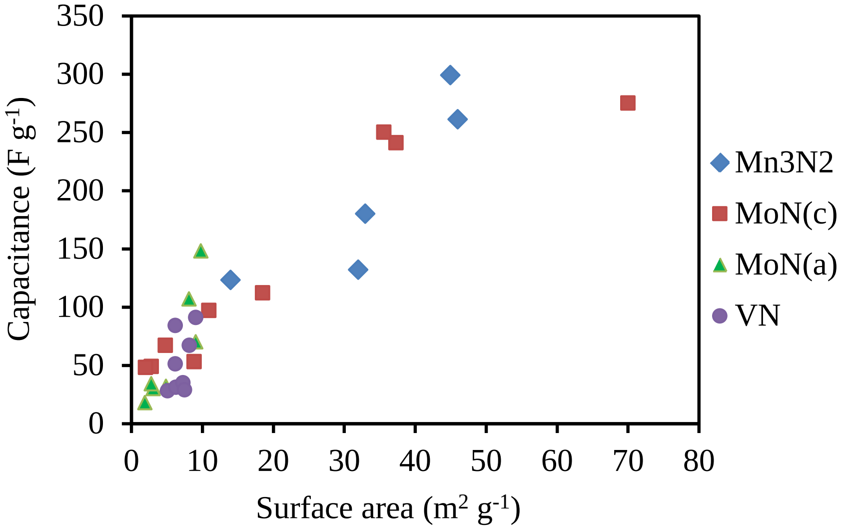

Figure 8.1: A graph showing capacitance vs surface area of Mn_3N_2, MoN (MoN(c) chloride precursor) MoN (MoN(a) (amide precursor) and VN. Mn_3N_2 and VN in 1 M KOH against Hg/HgO and MoN in 0.5 H_2SO_4 against $Hg/HgSO_4$ at 2 mV s^{-1}. 0.18 mg, 2 mg or 0.6 mg electrode material was loaded for Mn_3N_2, MoN or VN respectively.

Manganese nitride was prepared via a solvothermal route from the reaction of $MnCl_2$ and $LiNH_2$. Pure Mn_3N_2 was identified at 500 °C and below while 11 % of Mn_2N phase was produced at 550 °C. HRTEM confirmed nano-tubes of Mn_3N_2 with some graphitic carbon present at 350 °C. Elemental analysis of the samples correlated well with IR and TGA measurements. Samples were found with fairly high surface area and mesoporous in nature when produced at low temperature. Electrochemical data of charge and discharge efficiency suggested that the material was initially stable in the potential window of 0.9 V in 1 M KOH against Hg/HgO. Highest capacitance of 299 F g^{-1} was observed for a sample obtained at 350 °C at 2 mV s^{-1}, or 130 F g^{-1} at 100 mV s^{-1}. This is higher than the MnO_2 capacitance.[22] Voltammograms show prominent redox features common in all the samples at – 0.2 and 0.1 V. The redox process becomes more obvious at lower scan rates. These features the the open circuit value of -0.32 V, suggesting that Mn^{+2} in Mn_3N_2 is oxidised to Mn^{+4} and reduced back to Mn^{+2}. Capacitance of the materials was found to be fading with scan number, with larger drop at lower scan rate. The larger drop of capacitance at lower scan rate can be attributed to the length of time it spends under reducing or oxidising conditions. A sample obtained 550 °C show less drop in capacitance than the other samples. This suggests that the capacitive performance of manganese nitride can be further improved by producing high surface area phase pure Mn_2N.

Molybdenum nitrides were synthesised by annealing a polymeric precursor obtained through solution phase ammonolysis of $MoCl_5$ or $Mo(NMe_2)_4$ under ammonia at various temperatures and time schemes. Choloroimide derivatives were found either hexagonal MoN at 500 °C or rock salt at 700 °C and above, while a mixture of both phases at 600 °C. PXD of imide-derivatives were showed distorted rock salt Mo_2N up to 800 °C while hexagonal MoN was also present at 900 °C and above. Compositions of the molybdenum nitride samples from both the precursors were found to be consistent with TGA and IR data. TEM showed the imide-derivatives to be nanotubes while spherical particles were observed for the chloride derivatives. Fairly high surface areas up to 70 m^2 g^{-1} were calculated for the chloride-derivatives at lower temperature, while imide-derivatives were found with the surface area below 10 m^2 g^{-1}.

Electrochemical charge storage studies of MoN samples were carried out in 0.5 M H_2SO_4 or K_2SO_4 electrolytes. Previous reports of molybdenum nitride-based supercapacitors had used $H_2SO_{4(aq)}$[23-26] or $KOH_{(aq)}$[27] electrolytes. Voltammograms were found slightly tilted in $K_2SO_{4(aq)}$ at higher scan rates, due to $K^+_{(aq)}$ intercalation.[26, 28] Cyclic voltammograms for MoN_x samples obtained through chloroimide precursor route were found to exhibit mainly double layer capacitive behaviour. Redox features were either absent or very broad. The highest capacitance of 275 F g^{-1} was measured at 2 mV s^{-1} in $K_2SO_{4(aq)}$ for a molybdenum nitride sample obtained from choloroimide precursor annealed at 500 °C for 2 h. This value exceeds the previous reported capacitance of molybdenum nitride electrode materials.[23-26] A capacitance of around 200 F g^{-1} was observed for the same sample in $H_2SO_{4(aq)}$ electrolyte, which is again comparable to the literature. Capacitance was drop by ~ 50 % in most of the samples when the scan rate was increased from 2 to 100 mV s^{-1}. Capacitance was also decreased with the annealing temperature as the crystallite size increases and surface area of the sample decreases. Imide-derived samples on the other hand showed three clear redox features in $H_2SO_{4(aq)}$ at all scan rates, while the voltammograms obtained in $K_2SO_{4(aq)}$ at higher scan rate were irregular in shape with a single redox peak. The redox features in imide deratives suggest that the pseudocapacitance behaviour is more prominent in these samples, and shows a very reasonable capacitance of 161 F g^{-1} in $K_2SO_{4(aq)}$ at 2 mV s^{-1} even having small surface area as compared to chloroimide derivative. A chloride-derived sample at 500 °C and imide-derived sample at 600 °C showed a stable capacitances through 100 cycles at 100 mV s^{-1} in both H_2SO_4 or K_2SO_4 electrolytes.

Vanadium nitride samples were obtained through solution phase ammonolysis of $V(NMe_2)_4$ and annealing the precursor at various temperatures. PXD and PDF patterns suggested standard rock salt structure for the samples obtained at high temperatures, while structure distortion was found at lower temperature. Previous reports about such structural distortions in vanadium nitride lattice suggests it to be the low nitridation level[29] or oxygen atoms occupying the vacancies in to the nitride matrix.[18] Chemical compositions suggested nitrogen rich with the precursor residues samples at lower temperatures and so as in the TGA and IR data. BET surface area of the samples were found below 10 m^2 g^{-1}. TEM images show the particles were spherical in shape mostly agglomerated in the size range of 3 – 30 nm.

Cyclic voltammetry was performed in 1 M KOH against Hg/HgO reference electrode in the potential window of 1.2 V (0 to – 1.2 V). Capacitance for the samples obtained at lower temperature were found to drop after few cycles at any scan rate, as these samples were rich in the organic residues of the undecomposed precursor. While the samples obtained at higher temperature showed stable capacitance through 150 cycles where it starts to drop and over 90 % of the capacitance was dropped through 1000 cycles in the maximum potential range of 1.2 V. A stable capacitance through 1000 cycles was achieved only by reducing the potential window to 0.7 V (- 0.3 to – 1 V) as previously reported for vanadium nitride materials.[18] Previous studies show that the vanadium nitride electrode is electrochemically unstable in aqueous solution due to the irreversibility of forming vanadium oxide (VO_x) on the surface.[30-32] Samples were found to be redox active showing prominent redox features. The highest capacitance of 91 F g^{-1} in the first cycle and 128 F g^{-1} in the 20th cycle was observed at 2 mV s^{-1} for the sample obtained at 600 °C.

High surface area TiN_x samples were prepared by synthesising the polymeric precursors through NH_3 condensation over TDMAT or adding structure directing agents i.e. long chain amines. Polymers were then annealed to 500 °C or 800 °C under ammonia. PXD patterns showed the samples to be cubic TiN with broad peaks at lower temperature. Elemental analysis revealed that the TiN samples obtained at 500 °C were contaminated with precursor residues as the surfactants couldn’t be decomposed completely at this temperature. Compositions were also confirmed by TGA and IR analysis. Transmission electron microscopy revealed particle sizes in the range of 3 to 20 nm. The aim of template based synthesis was to obtain high surface area titanium nitride samples. The highest surface area of 319 m^2 g^{-1} was measured for HDA/$PrNH_2$ based polymer annealed at 500 °C, which was reduced by 63 % when annealed at 800 °C.

Investigating the electrochemical capacitive behaviour revealed poor response of the titanium nitride samples in the cell, capacitance was found to be very low and dropped with scan number. This behaviour could be due to the high content of organic residues in the samples that tend to oxidize in the aqueous electrolytes and hence passivate the electrode surface. Previous studies of the effect of organic residues in TiN samples showed that these limited its surface catalytic activities due to passivation and shielding of the outer TiN_x particle.[33] No extensive electrochemical studies were carried out for the TiN samples due to their low capacities and instability during the charge/discharge process.

Vanadium nitride/carbon composite materials were obtained by ammonolysis of $V(NMe_2)_4$ solution in THF. Ammonia was condensed over the amide solution in an autoclave and it was heated at various temperatures overnight. PXD patterns were refined using rock salt vanadium nitride. Combustion microanalysis showed high amount of carbon in the samples. TGA under Ar showed two step mass losses, polymer residue decomposition and ammonia at lower temperature while metal reduction occurred in the 2nd step. TGA under oxygen confirmed the presence of graphitic carbon.

TEM showed the nanostructured VN particles widely dispersed in the carbon nanotube structures. Ink electrodes of the samples were run in 1 M KOH against Hg/HgO reference electrode in the potential window of 1 V (– 0.2 to – 1.2). The highest capacitance of 103 F g^{-1} was measured at 2 mV s^{-1} at 4th scan. Capacitance tends to be reducing with scan number when the electrodes are run for 100 scans at 100 mV s^{-1}. Capacitance drop with scan number was more in the sample obtained at lower temperature.

In summary, some metal nitrides were synthesised and their structures and morphologies were analysed. Cyclic voltammetry was used to assess their charge storage capacities and electrochemical behaviour as supercapacitors. The nitride materials showed promising electrochemical performance relative to many materials in the literature. It is evident that their capacitive abilities can be further improved by optimizing their surface area and composition to improve their surface capability for fast oxidation and reduction processes during charge/discharge.

8.1 References

1. B. Mazumder, P. Chirco and A. L. Hector, *Inorg. Chem.*, 2008, 47, 9684.
2. A. L. Hector, *Chem. Soc. Rev.*, 2007, 36, 1745.
3. P. Simon and Y. Gogotsi, *Nat. Mater*, 2008, 7, 845.
4. J. Chen, N. Xia, T. Zhou, S. Tan, F. Jiang and D. Yuan, *Electrochem. Sci.*, 2009, 4, 1063.
5. F. Fusalba, P. Gouerec, D. Villers and D. Belanger, *Electrochem. Soc.*, 2001, 148, A1.
6. Y. K. Zhou, B. L. He, W. J. Zhou, J. Huang, X. H. Li, B. Wu and H. L. Li, *Electrochem. Acta*, 2004, 49, 257.
7. C. Arbizzani, M. Mastragostion and L. Meneghello, *Electrochem. Acta*, 1996, 41, 21.
8. K. H. An, K. K. Jeon, J. K. Heo, S. C. Lim, D. J. Bae and Y. H. Lee, *Electrochem. Soc.*, 2002, 149, 1058.
9. X. Zhao, B. M. Sanchez, P. J. Dobson and P. S. Grant, *Nanoscale*, 2011, 3, 839.
10. A. J. Roberts and R. C. T. Slade, *J. Mater. Chem.*, 2010, 20, 3221.
11. N. L. Wu, S. Y. Wang, C. Y. Han, D. S. Wu and L. R. Shiue, *J. Power Sources*, 2003, 113, 173.
12. J. W. Long, K. E. Swider, C. I. Merzbacher and D. R. Rolison, *Langmuir*, 1999, 15, 780.
13. D. A. McKeown, P. L. Hagans, L. Swider and D. R. Rolison, *Phys. Chem.*, 1999, 103, 4825.
14. M. Zhi, C. Xiang, J. Li, M. Li and N. Wu, *Nanoscale*, 2013, 5, 72.
15. J. N. Broughton and M. J. Brett, *Electrochem. Acta*, 2005, 50, 4814.
16. x. Lu, M. H. Yu, T. Zhai, G. Wang, S. Xie, T. Lu, c. Liang, Y. X. Tong and Y. Li, *Nano Lett.*, 2013, 13, 2626.
17. X. Lu, T. Liu, T. Zhai, M. Yu, S. Xie, Y. Ling, C. Liang, Y. Tong and Y. Li, *Adv. Energy Mater.*, 2014, 4, 1300994.
18. D. Choi, G. E. Bloomgren and P. N. Kumta, *Adv. Mater.*, 2006, 18, 1178.
19. X. Zhou, H. Chen, D. Shu, C. He and J. Nan, *J. Phys. Chem. Solids*, 2009, 70, 495.
20. D. Choi and P. N. Kumta, *Electrochem. Solid-State Lett.*, 2005, 8, A418.

21. D. M. Hoffman, *Polyhedron*, 1994, 13, 1169.
22. R. N. Reddy and R. G. Reddy, *Electrochem. Acta*, 2005, 50, 4814.
23. S. L. Robertson, D. Finello and R. F. Davis, *J. Appl. Electrochem.*, 1999, 29, 75.
24. T. C. Liu, W. G. Pell, B. E. Conway and S. L. Robertson, *J. Electrochem. Soc.*, 1998, 145, 1882.
25. C. Chen, D. Zhao and X. Wang, *Mater. Chem. Phys.*, 2006, 97, 156.
26. X. L. Li, Y. Xing, H. Wang, H. L. Wang, W. D. Wang and X. Y. Chen, *Trans. Nonferrous Met. Soc. China*, 2009, 19, 620.
27. D. Choi and P. N. KUmta, *J. Am. Ceram. Soc.*, 2011, 94, 2371.
28. R. N. Reddy and R. G. Reddy, *Power Sources*, 2006, 156, 700.
29. M. A. Roldan, V. L. Flores, M. D. Alcala, A. Ortega and C. Real, *J. Europ. Ceram. Soc.*, 2009, 30, 2009.
30. A. M. Glushenkov, D. Hulicova-Jurcakova, G. D. L. D. Llewellyn and Q. Chen, *Chem. Mater.*, 2010, 22, 914.
31. D. W. Choi and P. N. Kumta, *Electrochem. Solid State Lett.*, 2005, 8, 418.
32. L. Zhang, C. M. B. Holt, E. J. Luber, B. C. Olsen, T. H. Wang, M. Danaie, X. H. Tan, V. W. Lui, W. P. Kalisvaart and D. Mitlin, *Phys. Chem.*, 2011, 49, 24381.
33. S. Kaskel, K. Schlichte and T. Kratzke, *J. Mol. Catal.*, 2004, 208, 291.